The Dissertation Committee for Michael Thomas O'Connor Certifies that this is the approved version of the following Dissertation:

Controls Governing Active Layer Thermal Hydrology: How Predictable Subsurface Properties Influence Thaw, Groundwater Flow, and Soil Moisture

Committee:

Meinhard Bayani Cardenas, Supervisor

Ethan T. Coon

George W. Kling

Ashley M. Matheny

Bethany T. Neilson

Daniella M. Rempe

Controls Governing Active Layer Thermal Hydrology: How Predictable Subsurface Properties Influence Thaw, Groundwater Flow, and Soil Moisture

by

Michael Thomas O'Connor

Dissertation

Presented to the Faculty of the Graduate School of

The University of Texas at Austin

in Partial Fulfillment

of the Requirements

for the Degree of

Doctor of Philosophy

The University of Texas at Austin

May 2019

Dedication

For my parents, Tom and Lisa O'Connor. For my father Tom, for his unceasing devotion to his family and certifiably obsessive desire to make sure our lives are better than his was. For my mother Lisa, for being my first and best example of a curious scientist and an inquisitive mind. And to the two of them together, for the perfect example of tenacity and love.

Acknowledgements

My advisor, Bayani Cardenas, deserves a mountain of thanks simply for dealing with me in Austin through both a two-year Masters and a five-year PhD. That's a lot of Mike. I was certainly not a perfect example of a graduate student, especially at the beginning, but thank you so much for committing to me, helping me grow, and teaching me how to be proud of my work. My committee members and affiliated faculty together have created a wonderful professional support network that I am excited to continue to work with. Special thanks goes to my committee member Ethan Coon, and his colleagues Scott Painter and Ahmad Jan of Oak Ridge National Laboratory, for providing me with immeasurable help in the development and analysis of my numerical modeling, both remotely and during a wonderfully productive fall in Knoxville. I particularly hope to continue working with them, as their combination of intelligence and communicative ability is not easily matched. Special thanks also go to Bethany Neilson and George Kling for their initial guidance and financial support as I began my fieldwork in the Arctic. Special thanks also goes to Dr. Tyler King, who unofficially served as my mentor in my first two field seasons at Toolik Field Station. I hope to continue to work with him for years to come.

Graduate school can be a cripplingly lonely process; I am extremely fortunate that a wide and wonderful group of personal and professional friends have ensured that this was not the case for me. I must foremost thank the Cardenas Research Network past: Kevin Befus, Peter Zamora, Lizhi Zhang, and Lichun Wang, for creating a high-performance yet high-support environment that encouraged me to join the group in the first place and also showed me how to lead a group as a senior member. My office-mates, Matt Kaufman, Eric Guiltinan, Kimberly McCormack, Stephen Ferencz, Anna Turețcaia, and Paul Southard,

for truly making me excited to go to work every day. I will miss the hell out of the office both because of the wonderful side banter and for the surprising amount of actual scientific discourse that occurred. Everyone in grad school should be lucky enough to have officemates like you.

A host of friends, roommates, and others also made my time in Austin one I've enjoyed more than any other in my life. Particularly, Peter Carlson, Ed Marshall, Angela Schnelle, Mackenzie Day, Ryan Lichtenfels, Lizzy Lawrence, and the Austin Improv Community deserve credit for dealing with me and helping keep me sane during the times when work tough.

I am finally eternally thankful for the support of not just my nuclear family, but the entire network of O'Connors, Terminis, and related parties. It has been so wonderful to know that I have such a great team rooting for me back in New York. Thank you for that.

This research was funded through the American Geophysical Union Horton Research Grant, the United States Department of Energy Office of Science Graduate Student Research Program, the Geological Society of America Student Grant, the American Association of Petroleum Geologists Grants-In-Aid program, the CUAHSI Pathfinder Research Program, the Geology Foundation of the Jackson School of Geosciences at the University of Texas at Austin, and NSF ARC 1204220, DEB 1637459, 1754835, 1026843, and 0639805, PLR 1504006, and OPP 1107593.

Abstract

Controls Governing Active Layer Thermal Hydrology: How Predictable Subsurface Properties Influence Thaw, Groundwater Flow, and Soil Moisture

Michael Thomas O'Connor, Ph.D.

The University of Texas at Austin, 2019

Supervisor: Meinhard Bayani Cardenas

The hydrology of near-surface arctic soils above continuous permafrost, known as the 'active layer', is controlled by coupled thermal and hydraulic processes that are not well understood. The poorly-quantified spatial variability in active layer soil thermal and hydraulic properties, compounded with continually-migrating aquifer geometries that are not mechanistically understood, cause our current knowledge of arctic hydrology to be limited. Particularly, we do not mechanistically understand which parameters govern arctic groundwater flows, we do not understand how such governing properties vary across the landscape, and we do not understand the ranges that such landscape variability provides on arctic hydrologic processes.

This dissertation investigates these open questions through novel field observations and numerical modeling. In Chapter Two, I show how groundwater flows in the active layer are controlled by highly-variable soil permeability within three variable-thickness soil layers using fieldwork and saturated groundwater flow models. In Chapter Three, I identify how those soil layers and properties vary across the commonly-observed land

surface slopes, dominant vegetation types, and microtopographic features found on the foothills of the Alaskan North Slope through original fieldwork and terrain analysis. In Chapter Four, I show how the thawing and freezing of the active layer, lateral groundwater flow, and soil moisture storage (i.e., dominant thermal hydrologic processes) are controlled by the commonly-observed patterns in soil stratigraphy and soil properties found across the landscape. Finally, in the Conclusion, I lay out a framework for how this information can be leveraged to inform larger-scale arctic thermal hydrology models. In totality, this dissertation provides insight in the understanding of arctic thermal hydrology because of its grounding in observed soil properties and the use of cutting-edge numerical tools.

Table of Contents

List of Tables

List of Figures

Chapter 1: Introduction

1.1 Motivation: The Role of Hydrology in the Arctic Carbon Cycle

Climate change is warming the Arctic twice as fast as the global average (Serreze & Barry, 2011). Such warming has critical implications for the global carbon cycle, as more than half the soil carbon stored on Earth is held in Arctic permafrost (Ping et al., 2008). As the Arctic warms, these stores of once-latent soil carbon can be released into the atmosphere, potentially contributing hundreds of billions of additional tons of CO_2 and CH_4 (Schaefer et al., 2014). However, there is enormous uncertainty in the amount and timing of permafrost soil carbon release to the atmosphere (Schuur et al., 2015), in part because the carbon in newly-thawed soil is hydrologically transported to surface waters where microbial and photochemical processes can produce greenhouse gases (Cory et al. 2014).

One source of uncertainty arises because the complicated and coupled processes controlling hydrology in permafrost environments are currently poorly understood, and the characterization of such processes is oversimplified (Clark et al., 2015; Lawrence et al., 2015). Hydrology regulates the biogeochemical reactions that produce CO_2 or CH_4 within the soil column through soil moisture: CH_4 production dominates in damp or inundated soils, while CO_2 production dominates in drier soils (Anisimov, 2007; Lawrence et al., 2015; Zimov et al., 2006). Understanding which gas is released, and when, is necessary because the greenhouse effect induced by CH_4 is 25 times more potent than CO_2. Hydrology also controls dissolved carbon transport from arctic soils to surface waters by groundwater flow (e.g., Kling et al. 1991; McGuire et al. 2009), but the controls on transport processes are poorly known. Uncertainty in the impact of hydrology on the arctic carbon cycle contribute to a currently-enormous range in published estimates of global permafrost carbon release (between 50 and 400 Pg (Schuur et al., 2015)), resulting in between US$3-166 trillion of economic damage to society (Hope & Schaefer, 2016). Refining this requires better representation of permafrost hydrology within biogeochemical models.

Permafrost hydrology is unique because it involves a host of interacting thermal and hydraulic processes not seen in temperate environments. The 'aquifer' through which groundwater flows in permafrost environments is known as the 'active layer', a thin surficial rind of soil that freezes and thaws each year. Unlike in temperate environments, where the geometry of the aquifer is constant in time, the freeze-thaw cycle of the active layer causes arctic aquifer geometry to become transient in time and dependent on soil temperature. Such transience occurs seasonally, as the thawed zone of the active layer expands and contracts each summer with changing seasons. Transience in aquifer geometry can also occur inter-annually; as the mean annual air temperature rapidly rises in the Arctic (Chapman & Walsh, 2007), it is expected that permafrost active layer thicknesses should increase (Hope & Schaefer, 2016). Such increases provide a second source of transience in aquifer geometry that is not currently represented.

Permafrost hydrology is additionally complicated by the extreme amount of internal variability in the soil properties that govern the heat and water flow through the soil. The near-surface stratigraphy of arctic permafrost terrain is traditionally a thin, richly-organic soil layer atop a thicker, glacially-derived mineral sediment layer (Walker et al., 1989). These layers have starkly different thermal and hydraulic properties that can influence the development of the active layer itself (Jafarov & Schaefer, 2015).

The complexities imposed by a transient, temperature-dependent aquifer geometry within a highly-variable soil column must be understood to predict the hydrology of the active layer and constrain arctic soil carbon release. The questions posed in this dissertation are therefore motivated by the need to understand and quantify these complexities.

1.2 Motivating Questions

Question 1: What are the dominant external drivers and internal controls of thermal hydrology processes within the seasonally-thawed active layer above permafrost?

The combined effects of a transient, temperature-dependent aquifer geometry within a highly-variable soil column complicate near surface soil moisture and

groundwater flow dynamics within permafrost. For example, active layer growth into a deeper, lower-permeability soil layer sets up a hydrologic competition between an increasing aquifer thickness, which would increase lateral groundwater flows, and a decreasing aquifer transmissivity, which would decrease lateral groundwater flows. It is currently unclear which factor dominates across the arctic landscape. This and other interrelated aquifer geometry and properties dynamics have yet to be investigated; for these reasons, we currently do not know which external drivers and internal controls most substantially govern groundwater flow in the active layer.

Question 2: How do active layer soil thermal and hydraulic properties commonly vary across space?

As highlighted above, the high amount of internal variability in soil thermal and hydraulic properties is one reason that permafrost hydrologic processes are complex. While it is broadly known that there is a standard stratigraphy of arctic near-surface soil (organic-rich over a glacially-derived mineral soil layer), scant measurements of the thermal and hydraulic properties of these soils exist. Most published work that models thermal hydraulic processes in permafrost invokes values measured by either Hinzman et al. (1991) or Quinton et al. (2008). While these studies sufficiently describe the properties necessary to represent groundwater flow, soil moisture storage, and active layer development in the locations of measurement, they are limited in their scope. They do not address how such properties might vary across the massive landscape within which active layer thermal hydrologic processes are occurring. This lack of critical data coverage contributes substantially to wide-ranging uncertainties in arctic thermal hydrologic processes, and subsequently, carbon release (Walvoord & Kurylyk, 2016).

Question 3: How are active layer thermal hydrology processes affected by commonly-observed variability in arctic soil thermal and hydraulic properties?

Because the range in thermal and hydraulic properties across soil types is currently unknown, it is also unclear how the hydrologic attributes that contribute to carbon export (i.e., active layer thaw depth, lateral groundwater flows, and soil moisture

storage) are affected by such variability. In addition to knowing how properties commonly vary across space, determining how thermal hydrology is affected by properties variability requires the ability to simultaneously simulate energy and water fluxes in unsaturated soils undergoing freeze/thaw (i.e., incorporating the phase change between liquid water and ice). This capability has only recently been developed (Painter et al., 2016), and has yet to be informed widely with observed thermal and hydraulic properties.

This dissertation combined novel fieldwork, which provided the most comprehensive dataset of active layer thermal and hydraulic properties currently available for the Alaskan arctic, with cutting-edge numerical modeling to quantitatively determine the importance that such properties exerted on thaw, groundwater flows, and groundwater storage. Such insights are necessary for hydrologists, ecologists, climate scientists, and earth system modelers alike because of the integral role that water and heat play in the production and transport of carbon from soils to the atmosphere. It is, however, only a limited step towards an ultimate goal of understanding and predicting the carbon balance of the entire Arctic. This work is limited to the spatial scope of investigation: particularly, the landscape surrounding Toolik Field Station in the North Slope Foothills of Alaska. While many studies have used this location as a point for landscape-wide extrapolation, increased direct observation of active layer soil profiles in areas beyond this scope to better confirm its widespread applicability. The work here is also limited in its applicability to reality. We were unable to verify the groundwater flows calculated in Chapter 2 with flows in reality, because the flows themselves were not measured within the prescribed test grids. Additionally, the idealized geometries and forcing conditions prescribed yielded results that, in some places, directly contradict reality. However, these limitations do not detract from the purpose of the work, which was to quantify and identify the importance of properties on thermal and hydrologic mechanisms.

The investigations embedded in this dissertation have led me to hypothesize that areas with thicker organic layers (i.e. riparian zones and sedges) will be the most

hydrologically active, which will promote the respiration and dissolved transport of soil carbon. These regions will have deeper vadose zones than hillslopes due to more rapid drainage of organic soil, and will also transmit more groundwater due to higher permeability. Such factors will outweigh the deeper thaw that will occur in the thin-organic hillslope regions. The information from this dissertation, and the hypotheses this information creates, will help improve our understanding of the carbon budgets of a future Earth.

Chapter 2: Groundwater flow in a supra-permafrost aquifer: the effects of stratigraphy, water table position, thawing, and micro- and macro-topography

KEY POINTS

- Changes in acrotelm, catotelm, and mineral soil thickness between landscape types cause differences in groundwater flows from active layers.
- Groundwater flow differences become muted when the water table is shallow and within the highly permeable acrotelm.
- Microtopographic features retain groundwater and this is more pronounced in steeper than flatter locations.

2.1 ABSTRACT

The external drivers and internal controls of groundwater flow in the thawed "active layer" above continuous permafrost are poorly defined because they are seasonally dynamic and spatially variable. Understanding these controls is critical because groundwater supplies baseflow to surface water bodies, and carries with it carbon and nutrients. We calculated steady-state three-dimensional groundwater flow from active layer aquifers using high-density measurements of aquifer geometry, saturated thickness, and hydraulic properties collected from two major landscape types at multiple times within the North Slope of Alaska. The position and thickness of the saturated zone, defined by water table fluctuations, is the dominant control of groundwater flow variability between sites and at different time periods. The effect of water table fluctuations on groundwater flow dwarfs the effect of progressively-increasing thaw depth. In landscapes with low land-surface slopes (2-4%), a combination of higher water tables and thicker permeable peat deposits cause relatively constant groundwater flows between the early and late thawed season. Landscapes with larger land-surface slopes (4 -10%) have both deeper water tables and thinner peat deposits; here, the permeability decrease with depth is more pronounced than in flatter areas, and groundwater flows decrease significantly between early and late summer. Groundwater flows are also affected by microtopographic features, which retain groundwater that could otherwise be released as the active layer thickens. The dominant sources of groundwater are likely flatter regions with thick organic layers and high precipitation. This finding informs fluid and solute mass budgets for the present and future arctic.

2.2 INTRODUCTION

The inter-connected hydrology and biogeochemistry of Arctic soils determine the fate of 50% of the world's soil carbon which are present in areas of permafrost (Ping et al., 2008). Global warming is accelerating permafrost thaw which will allow for unknown amounts of groundwater to dissolve and mobilize soil constituents through groundwater flow (Frey & McClelland, 2009; Walvoord & Striegl, 2007). Given the vast volume of carbon in Arctic soils, its transport by groundwater could substantially impact the global carbon cycle (Hobbie & Kling, 2014).

We have an incomplete understanding of groundwater flow in areas of continuous permafrost because the geometry and the properties of the aquifer vary in an often-ignored but important way: the water table and the ice table both migrate into soils of differing permeabilities. Groundwater flow in any saturated porous media is described by Darcy's Law:

$$Q = KA\nabla h \qquad [1]$$

where Q is volumetric groundwater flow [L^3 T^{-1}]; it is controlled by ∇h, the hydraulic head gradient [L L^{-1}], K, the hydraulic conductivity [L T^{-1}], and A, the aquifer cross sectional area [L^2], which is determined by the saturated thickness b [L] and some unit width w [L]. Fluctuations in the water table, driven by precipitation and drainage, change both the thickness and the overall hydraulic conductivity of the aquifer by incorporating (in the case of a rising water table) or excluding (in the case of a falling water table) overlying soil layers with potentially different hydraulic properties than underlying soils. Commonly, these water table fluctuations are negligible when compared to the entire thickness of an aquifer, and are therefore ignored in groundwater flow calculations through the application of the Boussinesq equation (Cardenas, 2010). However, aquifers in near-surface continuous permafrost are typically quite thin: active layer thicknesses in the continuous permafrost found on the North Slope of Alaska and the Yukon Territory in Canada range between approximately 40 and 80 cm (Hinkel & Nelson, 2003; Nelson et al., 1999; Quinton et al., 2005; Smith et al., 2009). Furthermore, previous work showed that saturated K within arctic and boreal peatlands can be two

orders of magnitude higher at the surface than at 30 cm depth (Hinzman et al., 1991; Quinton et al., 2000). Decimeter-scale water table fluctuations in the shallow subsurface of continuous permafrost aquifers can therefore represent substantial changes to both b and K, and by extension, Q, and should not be ignored or approximated.

Ice table fluctuations also drive potentially substantial changes to aquifer b, K, and Q. Unlike in typical aquifers, where the bottom boundary is defined by lithology, the bottom boundary of a permafrost aquifer is defined by a time-variable frozen surface. The temporal migration of that surface, both within a season and between seasons, exposes new and deeper soil layers with hydraulic properties that can differ from the soil above it, and thus affects the hydraulic properties of the entire permafrost aquifer. Few studies consider the impact that ice table migration could have on soil hydraulic properties and subsequent groundwater flows, which has led to wide uncertainty in the prediction of future groundwater flows in the Arctic (Walvoord & Kurylyk, 2016).

It is unclear what effect the migration of the water and ice tables will have on b, K, and Q. As the summer season progresses, the saturated zone within the active layer tends to thicken as the thaw depth increases, which would increase groundwater flows. However, the saturated zone can deepen into less permeable soil, which could decrease flows. The interplay between these factors can be quantified through hydraulic transmissivity [T; L^2 T^{-1}], which is the product of K and b; however, active layer T, and its variation in time and space, is currently uncharacterized because few measurements of K, b, and ∇h have been made in continuous permafrost environments. Previous studies have measured depth-dependent relationships for saturated and unsaturated K (Hinzman et al., 1991; Quinton et al., 2000), but the lateral variability of these parameters across different landscape types is poorly quantified. Additionally, while previous work has characterized both temporal variability and microtopographic variability in b in a permafrost environment (Pomeroy et al., 2007; Quinton et al., 2000, 2005), we do not yet understand how b varies across and within different landscape types such as hillslopes or valley bottoms. Because we lack observations of how K and b vary in time and space,

we cannot yet quantify how the interplay of K and b affect T and, ultimately, groundwater flows.

There have been many previous interrogations of groundwater flows in peat-dominated, continuous permafrost environments using both field methods and numerical methods. However, these studies could not investigate how the impact of K and b interactions affects groundwater flows. For example, field-based studies of active layer groundwater flows have employed baseflow separation (e.g., McNamara et al., 1997; Stieglitz et al., 2003), geochemical methods (e.g., Blaen, 2013; McNamara et al., 1997; Walvoord & Striegl, 2007), and water balance calculations (e.g., Roulet et al., 2010); while these methods can determine groundwater contributions to streamflow, they do not consider the subsurface mechanisms that drive groundwater contributions. Thus, indirect, field-based groundwater flow studies are unable to predict how groundwater flows may change as K and b change; they can only predict the integrated, net effect of those changes. Studies that rely on process-based numerical models to calculate groundwater flows (e.g., Atchley et al., 2015; Frampton et al., 2011; Schuh et al., 2017) inherently consider the effects of changes to K and b, as well as any other groundwater flow parameter. However, these studies are rarely informed by field observations of the water table and the ice table, and they often parameterize K based on small sample sizes (Hinzman et al., 1991; Quinton et al., 2008).

Here we use high-density grids of direct field observations to quantitatively determine how summer seasonal thaw and water table fluctuations impact transmissivity and groundwater flow across multiple landscape and microtopographic settings. We use measurements of b, K, and ∇h to directly calculate groundwater flows from active-layer saturated zones, solving the groundwater flow equation effectively given only one unknown – flow rate. We calculated flows based on measurements collected when the water table was high and the active layer was thin (in mid-June, i.e., the 'Early Season'), when the water table was lower and the active layer was thick (in mid-August, i.e., the 'Late Season'), and at hypothetical instances when the water table was set at intermediate depths between fully-saturated and fully-drained (i.e., 'Variable Moisture' conditions).

Our groundwater flow calculations in the Early and Late Season represent estimates for actual conditions. The ancillary flow calculations across variable moisture (or variable water table depth) scenarios determine the potential contribution to groundwater flow from each progressively-saturated soil layer by differencing the groundwater flows calculated within the saturated zone from successive simulations.

2.3 Study Site and Experimental Design

To test how groundwater flows in the active layer vary across space and through time, we established regularly-spaced, high-density measurement grids within Imnavait Creek Watershed, a 2.2 km^2 first-order watershed (McNamara et al., 1997; Merck et al., 2012) underlain by hundreds of meters of continuous permafrost (Osterkamp & Payne, 1981). The watershed is a representative study site for understanding hydrologic behavior in the Arctic, as it exhibits the geology, climate, and ecology typical of a headwater catchment in the Arctic Foothills (Walker & Walker, 1996). The Arctic Foothills is one of only two USGS-designated physiographic regions (Wahrhaftig, 1965) and EPA-designated ecoregions (Omernik & Griffith, 2014) found in Alaska's North Slope, and thus it represents a large area key to understanding Arctic groundwater flows. The Arctic Foothills is defined largely by topography, containing moderate to steep rolling hills carved by six distinct glaciations in the late Pleistocene (Detterman et al., 1958; Hamilton, 1982a). The Arctic Foothills is bounded to the south by the Brooks Range and to the north by the much flatter Arctic Coastal Plain, and the Coastal Plain is bounded to the north by the Arctic Ocean (Figure 2.2, inset). Summer air temperatures range between 6 and 18°C, and the watershed receives 35 cm of precipitation a year on average, with 60% of that occurring as summer rain (McNamara et al., 1997). The Late Season active layer thicknesses (ALT) measured at Imnavait Creek are approximately 50 cm, but substantial variability exists within the measurements (Nelson et al., 1999).

Walker and Walker (1996) identified two dominant landscape zones, the hillslope and riparian area, which together comprise 90% of Imnavait Creek Watershed. The remaining 10% is largely defined as bare ground and dwarf heath vegetation on ridge

tops, which are typically hydrologically disconnected from the rest of the watershed (Stieglitz et al., 2003). We established multiple observation grids in each zone to capture the variability between and within the zones (Figure 2.2). These landscape zones are topographically distinct: hillslopes have broad and linear 4 to 20% slopes leading to the basin spine, and riparian zone slopes are shallower than 4%. The hillslope zone is asymmetric: the west-facing hillslope is broad, extending over 600 m from the creek to the watershed divide, while the east-facing hillslope has about one-sixth that reach. The hillslope and riparian zones differ substantially in ALT, vegetation composition, and soil stratigraphy (Stieglitz et al., 2003; Walker & Everett, 1991; Walker & Walker, 1996).

Our observation grids include the dominant microtopographic features within each landscape zone (Tables 2.1 and 2.2). Water tracks represent a dominant hillslope zone microtopographic feature (Walker & Walker, 1996). Water tracks are zero-order geomorphic drainage features that funnel substantial water flows from the hillslope (McNamara et al., 1999). These linear drainage features, spaced somewhat regularly in intervals of tens of meters, develop in subtle topographic lows within the landscape (McNamara et al., 1997; Voytek et al., 2016). They are unique to tundra environments in that, while they resemble streams in their morphology and retain moisture for substantially longer periods than the surrounding inter-track areas (Rushlow & Godsey, 2017), they rarely exhibit surface flow because shallow permafrost prevents the erosive processes necessary to carve out a stream channel (McNamara et al., 1999). They therefore are sites of potentially substantial groundwater flows. These features are most easily distinguished by a change in vegetation from sedges that dominate the surrounding tussock tundra to sedges in the water tracks. Our study contained two hillslope zone grids; one included a water track (the 'Water Track grid'), and one did not (the 'Inter-Track grid').

Water tracks are not observed in the riparian zone grids, as the concentrated flow derived from these confined linear features diffuses broadly when the land surface slopes decrease (McNamara et al., 1997). Rather, the dominant microtopographic features in the riparian zone are 'hummocks', small mounds that develop due to frost-heave processes,

and subsequent 'hollows', the depressions found in between hummocks (Quinton et al., 2000). Hummocks vary in size, but serve a similar function as water tracks in that they drive variability in saturation within the grids by concentrating water in local depressions. Our three riparian zone grids contained both small and large hummocks (Table 2.1), allowing us to determine their potential effects on b, K, $\nabla h, T$, and groundwater flow.

We set one grid on either side of the creek within the asymmetric riparian zone (six times more area on the western face). These opposing grids have comparable land surface slopes and size scales of microtopography, and are located at the same distance downstream of one another. This allows for a comparison of hydrologic properties and flows from contributing areas of substantially different sizes.

2.4 METHODS

To understand the factors controlling groundwater flow within active layer aquifers, we collected original field measurements in grids of high spatial resolution at two points in time within the summer of 2016. We employed standard statistical methods to determine spatial and temporal patterns within the data. We then used these data as boundary, geometry, and parameter constraints for 3D groundwater flow calculations to determine the impact of each factor controlling groundwater flow (b, K, $\nabla h, T$).

2.4.1 Field measurements of ground surface, thaw depth, water table, and soil hydraulic properties

Thaw depth and water table elevation data were collected at 61 evenly-spaced measurement points within each grid (Figure 2.2). Thaw depth was measured using a graduated 1.2 m long metal rod that was driven into the ground until refusal. Three measurements were taken near each point and averaged. Water levels were measured within 0.5" and 0.75" diameter PVC piezometers installed at each point, screened over the bottom 20 cm and sealed at the bottom with epoxy. These measurements were taken during the early summer (June 9-15) and late summer (August 7-10) of 2016.

Stratigraphic data were collected within measurement grids during late summer, at a sparser spatial resolution to minimize local disturbance. Measurements were made at

9 equally-spaced points within the original 61 points (see Figure 2.2c). We measured the depths to the contacts between the organic and mineral soil types from a core withdrawn using a 2" diameter, 24" long soil corer (AMS, American Falls, ID), which was driven into the ground until refusal then removed.

Saturated K was measured in the field at various depths within the six sampling grids using three different methods. Multiple methods were necessary to determine K across the depths and locations of the study site due to the requirements for each method. In locations where we were able to isolate a saturated depth segment of soil, we determined K in-situ with slug tests as described by Surridge et al. (2005). We performed 26 total slug tests at depths ranging from 11 to 85 cm. To perform the test, a 2" diameter drive-point piezometer (comprised of a 20 cm screen below 1 m of PVC casing and sealed with epoxy) was driven into the ground to the desired depth of the measurement. Water displacement during a slug test was measured with a fast-response pressure transducer (Aqua Troll 700, In Situ, Fort Collins, CO) placed at the bottom of the well. K was calculated by analyzing the water level recovery recorded by the pressure transducer following the theory of Bouwer and Rice (1976). The slug tests lasted several seconds to a few minutes. Water level logging rates were set at 0.25 s. The K values from the slug test represent the effective horizontal K across the saturated depth segment.

Given that in-situ slug tests must be performed within a fully-saturated aquifer depth segment, the full range of slopes and depths necessary for this investigation was not covered by in-situ tests because there were many locations in which a saturated depth segment was unavailable. To complete the sample set, soil cores from unsaturated locations were extracted and analyzed in the lab using two methods. For intact 5 cm-diameter cores, saturated K was measured using a constant-head test implemented with a KSAT Benchtop Hydraulic Conductivity instrument (UMS Corp., Berlin, DE). Our cores provided the K of the soil over a 5 cm depth segment, and soil depths ranged from 0-50 cm.

For mineral soil samples, the retrieval of an undisturbed, intact 5 cm core was impossible in the field due to the depth of the sample, and the aquifer response to the slug test was too slow to be measured. We therefore used an empirical method based on grain size to estimate K in these samples. Eleven samples of mineral soil were collected from an AMS Soil Corer for grain size analysis using a wet sieve for particles above 74 μm (No. 200 sieve) and laser particle refraction for particles smaller than 74 μm (Liu et al., 2005). The d_{50} (50^{th} percentile) of the grain sizes was then used to predict K via the Carman-Kozeny model (Carman, 1956).

2.4.2 Analysis of soil hydraulic conductivity patterns

Patterns within K measurements were identified by first grouping the measurements with respect to soil type, and then grouping them by depth. We assigned soil types for each of the soil core samples visually, and we assigned the soil types for all slug test samples based on the nearest extracted soil core. We used a two-sample Mann-Whitney U Test to determine if the K values of each soil group were significantly different to a 5% significance level ($p = 0.05$). Within each soil type, we grouped our measurements at 5 cm depth segments and performed a Kruskal-Wallis one-way analysis of variance across all depth segments to determine if there was statistically significant decay in K with depth. We lastly performed linear regressions of K with depth to build a functional relationship.

2.4.3 Spatial and temporal analysis of field measurements

Measurements were categorized by landscape zone and microtopographic position (i.e., the relative vertical position of each point with respect to the average land surface elevation). To determine the landscape zone, we calculated the land surface slope based on a 20-cm spatial resolution DEM of the watershed collected in April 2015 (Fairbanks Fodar, Fairbanks, AK). A slope threshold of 4% delineated between the hillslope and

riparian landscape zones (Figure 2.2); this resulted in three of the six sample grids falling in the hillslope zone and three falling in the riparian zone.

We determined the microtopographic position of each sample point by fitting a linear, first-order polynomial surface to the land surface elevation measurements collected at each of the 61 grid points. This surface represented the average land surface slope of the entire grid. We then identified individual measurement points as either a local elevation high or a low based on the difference between the actual measured elevation and the elevation of each point based on the calculated average land surface slope. A positive difference between actual and average elevation denoted a local high and a negative difference denoted a local low.

We determined average ∇h for each grid by fitting a linear, first-order polynomial surface to the measured water table elevations. The slope of that surface represented the average ∇h within each plot.

Using the above criteria, we compared how measurements of active layer thickness, $\nabla h, b, K, T,$ and estimated groundwater flows varied across landscape zones, microtopography, and season. Comparisons were performed using non-parametric statistical tests in which each measurement was grouped into populations based on landscape zone, microtopographic size, or season. We determined the uniqueness of these populations using a two-sample Mann-Whitney *U* Test when comparing two populations and a Kruskal-Wallis one-way analysis of variance when comparing more than two populations. Any *p*-value below 0.05 determined from these tests is considered statistically significant.

2.4.4 Transmissivity calculations

Transmissivity (T) describes the lateral K of a sample across a known aquifer b. When K is depth-dependent, the equation for T is:

$$T|_{z_1}^{z_2} = \int_{z_1}^{z_2} K(z)dz \qquad [2]$$

where z_1 and z_2 are the bottom and top of the aquifer saturated zone (or any two arbitrary vertical points), respectively [L]. We applied $K(z)$ relationships established from

measurements (described above) along with the depths of the water table (z_2) and ice table (z_1) to analytically compute T at every measurement point on the landscape. We then compared the computed T at these measurement points between landscape zones and microtopographic position based on the same statistical tests described in section 3.3.

2.4.5 Groundwater flow calculations from observed and variable moisture modeling scenarios

2.4.5.1 Model development

We constructed a series of 3D, steady-state saturated groundwater flow models to calculate groundwater flows from each of the measurement grids for the Early Season and Late Season time periods and at arbitrarily-assigned water table positions ('Variable Moisture') (Figure 2.3). As stated above, the groundwater flow equation can be solved given prescribed hydraulic conductivity, hydraulic head distribution, and cross-sectional area at a fine spatial resolution and result in estimates of groundwater flow through each grid. Conventional applications of groundwater models require parameter tuning to correctly calculate the position of the water table or soil hydraulic conductivity in unknown locations (Wang & Anderson, 1995); however, in our models both the water table position and the hydraulic conductivity are well-defined at a sufficiently fine spatial resolution and do not require adjustment. We can therefore directly apply these measurements to the model to solve for groundwater flow.

The general construction of the model used to perform the calculations is described below. The geometry, boundary conditions, and hydraulic properties for each calculation were informed by the measurements described previously. The equation for 3D saturated groundwater flow in a system with locally isotropic K and no sink or source terms is:

$$\nabla \cdot -K(z)\nabla h = 0 \qquad [3]$$

While the absolute values of hydraulic properties and boundary conditions for the model are not identical between grids, the method we used to apply them to each grid is

consistent. The hydraulic heads at the top boundary and all side boundaries were fixed at the elevation of the measured water table:

$$h_{top,sides} = z_{wt} \quad [4]$$

where z_{wt} is the observed water table elevation at all grid measurement points. The bottom boundary in each model, i.e., the thaw depth, was assigned as a no-flow boundary:

$$n \cdot -K(z)\nabla h = 0 \quad [5]$$

where n is the vector normal to that bottom boundary. K was defined using the depth function described in section 3.1 (Figure 2.4). The groundwater flow equation was solved within quadrilateral mesh elements that were narrowest at the top of the domain (the water table) and grew in a geometric sequence to the bottom (the ice table) (Figure 2.3). This meshing framework was used to represent the high variability in K observed near the ground surface, at the top of the model domain. The calculation was performed using the finite-element modeling software COMSOL Multiphysics.

For all calculations, we used a Lowess Regression to interpolate a smooth surface based on our measured water table elevations (Trexler & Travis, 1993). This step was necessary to smooth out peaks and valleys within the water table measurements that caused the groundwater flow field to develop large, anomalous, and nonphysical groundwater sink and source locations. Such locations are likely the result of easily-deformable ground affecting the accuracy of land surface survey measurements. This happened rarely; the goodness-of-fit coefficient for the Lowess Regressions exceeded 0.9 for all models.

We determined the total groundwater flow out of the domain by integrating the groundwater flow through the down-slope boundary:

$$\int [n \cdot -K\nabla H] = Q_{out} \quad [6]$$

where n is the vector normal to the down-slope boundary; this face is represented in Figure 2.3.

2.4.5.2 Scenario definition

We calculated groundwater flow for scenarios defined by differing water table and ice table positions to investigate how groundwater flows evolve across a range of anticipated seasonal ice dynamics and intermittent precipitation dynamics. Two scenarios were based entirely on observations: the Early Season scenario calculated groundwater flows from each grid based on water table and thaw depth observations made in June; it therefore resulted in one calculation per grid. The Late Season scenario calculated groundwater flows from each grid based on water table and thaw depth observations made in August; it also resulted in one calculation per grid.

The third scenario, Variable Moisture, calculated groundwater flows from each grid based on shifting the measured August water table upwards and downwards in 5 cm increments. This Variable Moisture scenario was designed to calculate the incremental contribution of groundwater flow of discrete 5 cm depth segments of soil within each grid. While the water table elevations we prescribed are not directly informed by measurements, our own field data, as well as published observations (e.g., Schramm et al., 2007, Figure 2.9) show that the water table within the active layer does range from fully-saturated to fully-drained; thus, these imposed scenarios represent realistic, observed conditions. This scenario used the thaw depth measured in August as the bottom boundary, and manually shifted the water table measured in August upwards to full active layer saturation and downwards to full drainage in 5 cm increments. These scenarios resulted in approximately ten calculations per grid. The number of calculations per grid was not identical because the mean thaw depth for each grid was different. The incremental contribution of groundwater flow for each 5 cm depth segment was computed by taking the difference in groundwater flow between model runs at successive water table depths. For example, the groundwater contribution of the depth segment between 5 and 10 cm was determined as the difference between the groundwater flow computed with a 5 cm deep water table and with a 10 cm deep water table.

2.5 RESULTS

Our findings showed that variability in active layer stratigraphy, b, and saturated zone position based on landscape zone cause important differences in T and groundwater flow. Particularly, the thick, low-gradient riparian zone is able to transmit groundwater water for the duration of the summer, while the thinner-soiled hillslope only briefly provides flow.

2.5.1 Hydraulic conductivity variability

Three distinct soil layers were found consistently across all grids: acrotelm (living or recently dead, but not decomposing peat (Holden & Burt, 2003)), catotelm (decomposing and compressed peats (Morris et al., 2011)), and loess (wind-blown, fine-grained sediments (Walker & Everett, 1991)) (Figure 2.4). These layers have been identified across the Arctic Foothills in previous work (Walker et al., 2003). The K of these materials differed significantly both between and within soil types. The K of the acrotelm and catotelm deposits decayed significantly with depth, whereas the K in loess did not. Broadly speaking, the most surficial acrotelm is very permeable because its high porosity creates little to no resistance to flow (Quinton et al., 2008). K measured in these soils can exceed 800 m d^{-1} (equivalent to marble-sized gravel). However, peat soils compact readily as they degrade (van Asselen et al., 2009) and thus the K also decreases in time, and correspondingly with depth (Beckwith et al., 2003a). We observed two distinct patterns of K decay in the acrotelm and catotelm. Acrotelm K decay was most substantial; K dropped three orders of magnitude from the surface to the base of the acrotelm layer, and porosity decreased 30% in that same interval (Figure 2.4). The decay in K observed in the catotelm was less prominent, dropping approximately 60% between the top and the base of the catotelm; however, porosity decay continued, decreasing approximately 50% over the same depths (Figure 2.4). The slopes of K decay with depth in the catotelm are similar to those observed in previous work in both arctic and temperate zone locations (Beckwith et al., 2003; Quinton et al., 2008). We observed no

differences in K decay with depth across different landscape zones or microtopographic locations.

The K of the loess soils changes little with depth and is consistently very low. The average K of such deposits was 0.004 m d^{-1} (Figure 2.4), two orders of magnitude lower than the deepest catotelm samples. We did not observe significant variability in loess soil K across grids. The K values we measured fall within typical ranges for loess soils (Freeze & Cherry, 1979).

We conducted a series of linear regressions to determine a piecewise relationship between K and depth:

$$K(z) = \begin{cases} 10^{-19.17z+2.937}, & z < z_a \\ 10^{-0.35z}, & z_a < z < z_m \\ 10^{-2.39}, & z > z_m \end{cases} \quad [7]$$

where z is the depth of the soil [meters, m], z_a is the depth to the inflection point in the K-depth curve (established to be 0.15 m, Figure 2.4), z_m is the depth to the catotelm base (if observed) [m], and K is in [m d^{-1}]. z_a approximately represents the contact between acrotelm and catotelm soils, although as described below, the contact depths between acrotelm and catotelm soils change with landscape type and microtopographic position. When the catotelm base was not observed, Equation 7 is limited to only the upper two sections.

2.5.2 Hydrostratigraphic variation

Given the variation in K observed both between and within soil types, an accurate determination of groundwater flows in this landscape requires knowing where each soil contact lies, especially in relation to the water table. The measurements show that the thickness and depth of the soil layers differ predictably both between and within landscape zones.

The total peat thickness (acrotelm plus catotelm) increases across grids as the grid position migrated down-slope. The measured total peat thickness in the low-slope riparian sites (48 ± 18 cm) was significantly larger than in the two steepest hillslope sites

(23 ± 9 cm) (Figure 2.5). The Slope Break grid, which sits in the hillslope zone but near the transition from hillslope to riparian, had an intermediate total peat thickness (30 ± 8 cm). The peat thicknesses observed in most riparian sites are underestimates because we reached frozen ground before we reached the bottom of the catotelm; thus, we expect the actual total peat thickness to be larger than what we reported here. The overall increase in peat thickness observed between the hillslope and riparian zone was driven mainly by increases in the catotelm rather than in the acrotelm (Figure 2.5). A mean acrotelm thickness of 17 cm was observed across both zones; the mean catotelm thickness was significantly larger in riparian settings (33 vs. 8 cm, respectively). We assumed that the riparian sites without thawed loess (i.e., the thaw depth was always above the loess) were comprised entirely of peat, and therefore we excluded those data from further stratigraphic analysis.

The variability in peat thickness within hillslope sites is caused by the presence and scale of microtopographic features. Microtopographic features are approximately the same size in both hillslope and riparian grids (7.0 and 6.5 cm, respectively; Figure 2.6); however, within hillslope grids the stratigraphy underneath local highs differs significantly from that under local lows. This difference arises mainly from changes in acrotelm thickness; local highs have acrotelm thicknesses approximately 1.7 times larger than local lows (Figure 2.6), while catotelm thicknesses are approximately equal (11.3 cm underneath local highs vs. 11.2 cm underneath local lows). This results in slightly thinner total peat columns underneath microtopographic lows than highs. Water tracks seem to exacerbate this relationship; acrotelm thicknesses within water tracks is less than one third of that outside water tracks (7.0 vs. 20.3 cm, respectively), and catotelm thickness within and outside of water tracks is approximately equal.

In the riparian zone, we observed the mean peat thickness underneath local highs (35.5 cm) to be slightly thinner than the mean peat thickness underneath local lows (40.8 cm); however, these differences were not statistically significant ($p = 0.4$). Despite the lack of statistical significance, there is evidence that microtopography influences total peat thickness; we observed a strong correlation between grid microtopography feature

size and peat thickness variability ($R^2 = 0.98$). Although cryoturbation has been reported in this and other similar landscapes (Bockheim, 2007; Michaelson et al., 1996), we did not uncover any samples in which the acrotelm-catotelm-loess stratigraphy was interrupted or reversed by freeze-thaw or any other process.

2.5.3 Saturated thickness and ice and water table depths

As described above, quantifying the thickness of the saturated zone (b) requires identifying the time-varying depths of both the upper boundary (the water table) and the lower boundary (the ice table as determined by thaw depth). Our overall findings from the Early and Late Season measurements of those boundaries confirm that aquifer saturated zones are thin, disconnected, and at shallow depths in the soil column in the Early Season, and they are significantly thicker, connected, and deeper in the soil column in August (Figure 2.5, Table 2.2). Our findings also show that the Early Season saturated zone is significantly thicker in the riparian area than on the hillslope (Figure 2.5, Table 2.2), and that inter-grid microtopography causes the vertical position of b to shift substantially across very short distances.

2.5.3.1 Hillslope saturated thicknesses, thaw depths, and water table depths

The early season saturated zone in the hillslope was essentially nonexistent, with pockets of saturation surrounded by mostly 'dry' soil (Figure 2.6c). Among all sites, the mean b was approximately 1 cm; however, 69% of those sites were 'dry', meaning that the thaw and water table were at the same depth. Among the sites that were not dry, the mean b was approximately 5 cm, with a maximum observed b of 13 cm occurring within the water track portion of the Water Track grid (Figure 2.6). The vertical position of the saturated zone was very near the surface; the mean thaw depth had only reached 12 cm, and the mean observed water table depth was only 7 cm below the land surface elevation. Local highs were more likely to be dry than local lows (76 vs. 61% of sites, respectively); this is consistent with other findings in the literature (Quinton et al., 2000). However, there was no observed difference in the thaw depth between the highs and lows (11 cm

underneath both highs and lows). Because the thaw depth was so shallow, all the saturation in June occurred within the acrotelm.

The saturated pockets within the hillslope became connected by the Late Season because the saturated zone expanded and deepened substantially (Figure 2.5, Table 2.2). The net expansion in the saturated zone occurred because the thaw depth expanded more than the water table deepened; the thaw depth increased by an average of 45 cm across hillslope sites between June and August (Table 2.2), while the water table only deepened by an average of 10 cm (Table 2.2). Expansion in b was not homogeneous across the hillslope, however. The populations of b measured within each grid were statistically different ($p < 0.0001$), with the average b increasing most in the Water Track grid (to 52 cm), less in the Slope Break grid (to 39 cm), and less still in the Inter-Track grid (to 23 cm). The Water Track grid thawed anomalously deep in the Late Season, and this increased thaw occurred both directly in the water track and in the nearby area. We measured the Late Season average thaw depth within the water track portion of the Water Track grid at 95 cm; the average thaw depth in all other areas of this grid was significantly less (67 cm). However, even the water-track-adjacent portion of the Water Track grid had significantly deeper thaw than any other location within the hillslope zone. Deep thaw in water tracks has been observed previously (McNamara et al., 1999; Rushlow & Godsey, 2017).

Despite grids having significantly different b values, the vertical position of the saturated zone within Late Season hillslope grids occurred consistently within the loess. The average measured water table elevation (21 cm) equaled the mean depth to loess in these sites. We observed no significant difference between the b underneath local highs (36 ± 16 cm) and local lows (41 ± 20 cm).

2.5.3.2 Riparian zone saturated thicknesses, thaw depths, and water table depths

Excluding the water track points within the Water Track grid, the thickest saturated layers were consistently observed in the riparian zone (Figure 2.5, Table 2.2). b in the riparian zone averaged 6.3 cm in June, due mainly to a deeper observed thaw depth

in the riparian zone than on the hillslope (15.6 cm vs. 11.1 cm, respectively). The mean water table depth in the riparian zone was also shallow (9 cm). Unlike in the hillslope, less than 10% of riparian sites measured were dry. However, like in the hillslope, we observed significant variability in saturated zone thickness and vertical position due to microtopography. b under local lows was approximately three times larger than b under local highs (9.7 vs. 3.6 cm, respectively), and the percentage of dry sites was much lower (6 vs. 18%, respectively). However, the thaw depths underneath local highs and local lows were approximately equal (15.4 vs. 16.3 cm, respectively). As in the hillslope, all the saturation in the Early Season occurred within acrotelm, as the catotelm and loess had yet to be thawed.

The b in the riparian zone also increased between June and August, but not as substantially as hillslope b did. The mean b observed in the riparian zone grew 450%, to 35 cm (Table 2.2). The net expansion in the saturated zone occurred because the thaw depth expanded more than the water table deepened; the thaw depth expanded by 218%, from 16 to 51 cm, while the water table depth only increased by 67%, from 9 to 15 cm.

The net expansion of the saturated zone was greatest under local topographic highs. Although local lows still exhibited significantly larger b than under local highs (43 cm vs. 28 cm), the seasonal increase in b was much larger underneath local highs than local lows (560% vs. 302%, respectively). Additionally, a significant disparity in thaw depth arose in the Late Season, with thaw underneath local highs averaging 6 cm less than thaw under local lows (48 vs. 54 cm, respectively). Excluding the Water Track grid, the Late Season data show a progression of increasing b with decreasing land surface slope (Figure 2.5).

2.5.4 Transmissivity calculated from observed water table elevations

We used measurements of K with the position and thickness of the saturated zone to calculate T for all grid points. Such calculations show that spatial and temporal variability in active layer T is substantial across very small distances. T variability occurred because K decreased approximately five orders of magnitude within a depth of

about 60 cm, and the vertical position of the saturated zone varied significantly within that depth across grids and throughout the season. Because we observed lateral consistency of K across soils of the same type, we could calculate T (equation 2) using the measured soil contact depths, soil K, water table elevations, and thaw depths from our grids. The integral in equation 2 is a piecewise function; the three components reflect the different K observed in the acrotelm (a function that decays with depth), catotelm (a function that decays with depth), and loess (a constant). Based on the linear regressions of K measurements with depth (Equation 7), we determined T to be:

$$T = \begin{cases} 19.6e^{-44.1z_a} - 19.6e^{-44.1z_1}, & z < z_a \\ 1.24e^{-0.81z_m} - 1.24e^{-0.81z_a}, & z_a < z < z_m \\ 10^{-2}(z_2 - z_m), & z > z_m \end{cases} \quad [8]$$

where z_1 is the depth of the water table [m], z_2 is the depth to thaw [m], z_a is the depth to the inflection point in the K-depth curve (established to be 0.15 m, Figure 2.4), z_m is the depth to the catotelm base (if observed) [m], and T is expressed in [m^2 d^{-1}]. In instances where the catotelm base was not observed, $z_m = z_2$ and the piecewise equation is limited to only the first two items.

The riparian zone was consistently more transmissive than the hillslope (Figure 2.7e, Table 2.2). In June, the mean hillslope T was 1.17 m^2 d^{-1}, and the riparian T was significantly larger (2.13 m^2 d^{-1}). This difference widened in August, when riparian T increased slightly to 2.9 m^2 d^{-1}, while hillslope T decreased over an order of magnitude to 0.10 m^2 d^{-1}. The factors that limited T in the hillslope changed between June and August; in June, the average hillslope T was low largely because many locations were 'dry' and thus had a T = 0. The average T among only saturated hillslope sites was 1.95 m^2 d^{-1}, which is comparable to the average T in the riparian sites. In August, hillslope T was not influenced by unsaturated sites, because saturation was ubiquitous across all grids. Hillslope T was low in the Late Season because 96% of the saturation that occurred was in the low-permeability loess. The low K of this soil overwhelmed the increases in b observed, causing the steep seasonal drop in T.

We did not observe a decline in riparian zone T between Early Season and Late Season. Rather, increases in b drove slight increases in T, from 2.13 to 2.9 $m^2 d^{-1}$. Increases in b were not overwhelmed by a K decrease because most riparian sites lack a thawed, low-permeability loess layer and because the seasonal thickening of the saturated zone was not accompanied by substantial deepening. The water table depth measured in June across riparian sites (7.6 cm) only fell 4 cm in August (11.7 cm); such shallow saturation ensured that higher-permeability soils were incorporated in the aquifer, keeping the T high.

Microtopographic features caused inter-grid T variability to span five orders of magnitude (Figure 2.7a-d). Variability in T was most prominent in the Early Season because local highs were either unsaturated or minimally saturated. For example, the average Early Season riparian zone T in a local high was an order of magnitude lower than T in a local low (0.36 vs. 3.21 $m^2 d^{-1}$, respectively); in the hillslope, the difference was nearly two orders of magnitude (0.07 $m^2 d^{-1}$ in local highs vs. 2.24 $m^2 d^{-1}$ in local lows). In the Late Season, saturation occurred underneath both local highs and lows, so the disparity between T underneath local highs and local lows shrank significantly (Figure 2.8). The T in local highs tripled in the riparian zone, to 1.10 $m^2 d^{-1}$, while the T in local lows remained constant (3.30 $m^2 d^{-1}$). Inter-grid T variability remained substantial throughout the Late Season in the hillslope. The difference between T in local highs and local lows decreased (0.03 $m^2 d^{-1}$ in local highs vs. 0.16 $m^2 d^{-1}$ in local lows); however, even in the Late Season, the difference between T in local highs and local lows was significant because both b and the saturated zone position varied largely between such microtopographic features.

2.5.5 Measured groundwater head gradients and calculated groundwater flows based on Early and Late Season scenarios

The measured water table elevations produced a planar surface whose slope mimicked that of the regional topographic gradient (Table 2.2). Hydraulic head gradients

within the riparian zone ranged between 1.5 and 3.9%. Hydraulic head gradients in the hillslope ranged between 5.5 and 11.8%.

We applied our measured hydraulic head gradients and the $K(z)$ function computed above (Equation 7) to inform 3D groundwater flow calculations based on the Early Season and Late Season water table and thaw depth measurements (Figure 2.9). Each groundwater flow calculation in this study represents the flow through a 20 m long strip of soil perpendicular to the mean slope, reflecting the dimensions of the study grids (Figure 2.3). These calculations showed that hillslope groundwater flows are largest in the Early Season and diminished substantially as the season progressed (Figure 2.7f, Table 2.2). Groundwater flows in low-gradient riparian zone sites are maintained throughout the entire season (Figure 2.7f, Table 2.2).

Hydraulic head gradients seemed to have no appreciable effect on groundwater flows, because the highest-gradient grid, the Inter-Track, had the least groundwater flow in both June and August. The lowest-gradient grid, the Near-Stream East (2.7% gradient), yielded the third-highest groundwater flow in June and the second-highest flow in August (Figure 2.7f). We found no strong correlation, either positive or negative, between hydraulic head gradient and groundwater flow (Table 2.2) during the conditions when data were collected.

There was, however, a strong correlation between T and groundwater flow (R^2 = 0.7) that we observed by comparing the grids within each season. In June, when T is high, the groundwater flow across all grids is high as well (Figure 2.7). There is only a small difference between groundwater flows out of hillslope grids (through the 20 m downslope boundary), which averaged 1.21 m^3 d^{-1}, and the groundwater flows out of riparian grids, which averaged 1.74 m^3 d^{-1}. Hillslope T plummeted in August, and correspondingly so did groundwater flows. The mean flow from hillslope grids decreased two orders of magnitude to 0.075 m^3 d^{-1}. In the riparian grids, where T

remains relatively constant throughout the season, groundwater flows increased slightly between June and August.

2.5.6 Transmissivity and groundwater flow calculated based on variable moisture scenarios

Both T and groundwater flow were dominated by the highly-permeable acrotelm, with the catotelm contributing small flows and the loess providing negligible flow (Figure 2.10). The T of the upper 15 cm of soil is 10 times larger than the T of remaining riparian zone catotelm (11.4 vs. 1.1 m^2 d^{-1}, respectively), and 12 times larger than that in the hillslope catotelm and mineral soil (11.4 m^2 d^{-1} vs. 0.94 m^2 d^{-1}, respectively).

High acrotelm T promotes high groundwater flows. A saturated acrotelm can yield approximately 92% of the total flow from a completely-thawed column in the hillslope and 91% of the total flow from a completely-thawed column in the riparian area (12.1 m^3 d^{-1} and 5.1 m^3 d^{-1}, respectively). Groundwater flows from the high-gradient hillslope acrotelm are more than twice as large as those in the low-gradient riparian zone (Figure 2.10).

The commonly accepted conceptual structure of peat states that acrotelm generally sits above the long-term mean water table, and catotelm is below (Morris et al., 2011). Our water table observations also show that the acrotelm was rarely fully saturated during our data collection periods. While the acrotelm could be a regular component of the active layer saturated zone during rain events, excluding it from transmissivity calculation by considering a column of peat saturated from the long-term water table average (i.e., the acrotelm-catotelm boundary) to the August thaw depth shows that near-surface flow still overwhelms deeper flow. For example, in the hillslope the T of the approximately 10 cm-thick catotelm layer exceeds the T of the entire loess by 30 times (0.9 m^2 d^{-1} vs. 0.03 m^2 d^{-1}, respectively), and the catotelm generates 98% of the total flow (1.04 m^3 d^{-1} vs. 0.03 m^3 d^{-1}). A similar but more muted relationship is observed in the riparian zone, despite the absence of loess. Low K at depth causes the T of the upper 10 cm of catotelm (15 to 25 cm depth) to be approximately 4.8 times larger

than T in the remaining thickness of the column (from 25 cm depth to the bottom of the active layer thickness of approximately 51 cm). The disparity in T with depth causes 83% of the total column flow to be generated within the upper 10 cm of the catotelm (0.52 m^3 d^{-1} vs. 0.08 m^3 d^{-1}). The steeper gradients of the hillslope still cause flow from that landscape zone to be approximately twice the flow from the riparian zone at this depth at the time of our measurements.

2.6 DISCUSSION

This study quantitatively shows that the thickening of the active layer has no appreciable control on groundwater flows. Rather, groundwater flows from the active layer are controlled by the position of the saturated zone within the soil column. While this has been suggested before (Wright et al., 2009), our analysis provides the first quantitative assessment of this impact, and shows it to be true across multiple times and landscape zones. Active layers that contain near-surface saturated zones will transmit much more groundwater than active layers with deep saturated zones. Our variable-moisture calculations show that the upper 10 cm of active layer soil, within the acrotelm, can transmit over 600% more water than the rest of the thawed column, despite being one fifth the size. The position of the saturated zone dominates groundwater flows because the saturated zone is imposed on a K profile that decays exponentially with depth, which strongly decreases both T and groundwater flow. The observed decrease in K with depth agrees well with patterns observed in continuous permafrost environments (Hinzman et al., 1991; Quinton et al., 2000), boreal environments (Quinton et al., 2004; Quinton et al., 2008), and other peat-dominated environments lacking permafrost (Beckwith et al., 2003a). However, our results reveal a steeper decay over a shorter depth interval than other studies in similar settings.

Hillslopes and riparian zones transport equal volumes of groundwater in the Early Season, but riparian zones are substantially better at transporting groundwater than hillslopes in the Late Season. This is because landscape zone (i.e., hillslope zone and riparian zone) determined the position of the saturated layer within the soil column,

which correspondingly determined groundwater flows. We observed the saturated zone in the riparian zone to be near the surface across both the Early and Late Season, whereas the hillslope saturated zone deepened significantly in the Late Season. The average riparian saturated zone position dropped only 6 cm across the season (from 9 ± 4 cm to 15 ± 7 cm), while in the hillslope the water table dropped twice as much (from 9 ± 4 cm to 21 ± 7 cm). Even in the Late Season, therefore, 50% of the sites measured in the riparian zone have a saturated zone that sits in the highly-permeable acrotelm. In contrast, only 15% of the sites measured on the hillslope have a saturated zone in the acrotelm, and thus much more of the flow occurs in the less permeable, deeper soils. The continuous position of a saturated zone in the near surface provides a mechanistic explanation for why riparian groundwater flows remained constant across the season, while hillslope groundwater flows decreased by an order of magnitude.

Our data show that seasonal thaw may result in a deepening of the saturated zone, but almost always causes a thickening of the saturated zone. Thaw provides the potential for shallow groundwater to migrate downward, but only if there is available void space within those deeper, thawing soils. Thaw into an already-saturated loess column would not cause any downward migration of shallow groundwater; however, that thaw would substantially increase saturated zone thickness (b). Thawing into deeper, unsaturated soils, which typically have lower porosity than soils near the surface (Figure 2.4), could also increase b incrementally, because the same volume of water occupies a larger volume of lower porosity soil. While we do observe a pronounced downward shift in the hillslope saturated zone between seasons, it is unlikely that such shifting is due to the downward migration of shallow groundwater. The K of deeper soils is quite low, which limits the ability for these soil layers to drain within a season. Saturation is likely a persistent condition in these deep soils, and our observed aquifer deepening is more likely due to draining of much higher-K organic soils and thawing into saturated loess layers.

These results capture two temporal snapshots of active layer saturated zones, and it has been shown that in seasonally-thawed active layers, precipitation and drainage can cause the water table to fluctuate substantially in short time periods (Quinton & Gray,

2003; Roulet et al., 2010; Woo & Steer, 1983; Wright et al., 2009). This study does not attempt to model the effect of such fluctuations on groundwater flow, but multiple lines of evidence suggest that the spatial and temporal patterns we observed in saturated zone thickness and position are representative. For example, in the Early Season the saturated zone will exclusively occur in the acrotelm in both hillslope and riparian landscape zones, because it is the only soil type that is thawed at that time. In the Late Season, it is likely that frequent, summer precipitation events could cause the acrotelm in the riparian zone to partially or completely saturate, and to influence hillslope saturation conditions or groundwater export. One such event occurred during our Late Season measurements. This event, on August 7, 2016, led to approximately 4 mm of rainfall at Toolik Field Station, which falls just above the average amount of a daily rainfall event calculated from all rain events from 2011 to 2017 (3.56 mm per day, Toolik Field Station, Environmental Data Center, https://toolik.alaska.edu/edc/). The precipitation that fell on the watershed that day elevated the riparian zone water table into the acrotelm, saturating the soil nearly to the surface and increasing groundwater flows. Precipitation failed to elevate the water levels on the hillslope over the time scales that we were able to measure; rather, the high land surface slopes on the hillslope likely led to rapid down-slope transport of this precipitation into the riparian zone. This connectivity between hillslope and riparian zone has been demonstrated in the past (Stieglitz et al., 2003). The hillslope provides a source of water necessary to maintain late-season b that can include the highly-permeable acrotelm, and the low slope of the riparian zone prevents it from draining out rapidly. Given that the rain event magnitude we observed was slightly above the mean rain event magnitude, we could expect riparian zone acrotelm flow to be a common occurrence; this also supports our conclusion that riparian zones are substantially better at transmitting water in the Late Season than hillslopes.

We also observe different results between the hillslope and riparian zones in the effect of the continually-deepening depth of thaw (ice table) on both b and groundwater flow. These different results occur because of the distinct stratigraphy between the zones. In the riparian zone, only a two-layer soil stratigraphy was observed, where

highly permeable acrotelm overlaid less permeable catotelm. Only in the hillslope does extremely low-K loess exist within the depth that is thawed, and the Late Season b in the hillslope deepens into that loess while the Late Season b in the riparian zone remains entirely in peat. The small K of hillslope loess leads to an approximate order of magnitude decrease in flow compared to catotelm peat at the same depth in the riparian zone (Figure 2.10). The presence of this loess, in conjunction with a lack of acrotelm flow, explains why T and groundwater flow in the hillslope are significantly smaller than in the riparian zone in the Late Season, despite similar increases in b from the Early Season conditions (Figure 2.6). Loess, which originated as the first post-glacial sedimentary deposit across wide areas of the North Slope of Alaska, has been observed ubiquitously across the region (Walker & Everett, 1991). The widespread distribution of loess across the landscape, combined with its distinctly different hydraulic properties from catotelm, suggests that loess may provide a strong limitation on deep groundwater flow rates across the region, and highlights the importance of identifying the loess-catotelm contact to build a complete understanding of groundwater flows in the region.

The ice table depth does not substantially influence groundwater flows in the Late Season in either landscape zone due to low-permeability soils at depth, but the ice table depth does exert a strong control on Early Season groundwater flows by causing subsurface flow barriers that withhold groundwater within microtopographic features. Microtopographic surface features drive variability in the thaw depth, and this variability creates pockets of saturation disconnected from flowpaths, temporarily trapping water in place (Figures 2.6, 2.9). Water in these pockets is unable to move because it is surrounded by 'dry' local highs. Such microtopographic withholding is landscape-specific, with more withholding occurring in the hillslope zone than in the riparian zone. The thaw depth difference under local highs between the two landscape zones was minimal; however, in the hillslope, the water table depths were, on average, 2 cm below the ice table of a local high (Figure 2.6). Groundwater is therefore commonly retained within local lows on the hillslope. While there was variability in thaw depth between

local highs and lows in the riparian zone, the water table still sat above the thaw depth in most locations, leading to fewer isolated pockets.

Microtopography-induced withholding of groundwater has been observed at local scales in permafrost settings (Quinton et al., 2000), and at basin scales where an uneven bedrock bottom can cause groundwater to be similarly withheld behind bedrock dams (Tromp-van Meerveld & McDonnell, 2006), and has strong implications for groundwater age. Water in a local low that exists deeper than a nearby ice dam is effectively disconnected from the free-flowing surface layer unless there is a substantial upward component of deeper groundwater flow directing it towards the free-flowing surface layer. Because generation of such an upward component is difficult, the deeper, trapped water is therefore only free to flow once the ice barrier thaws. Given that we observed microtopography-driven variability in the thaw depth to increase over the summer season, there are always depths at which water underneath local lows is trapped by ice barriers underneath local highs. While this water cannot flow laterally, it is possible that future warming or mechanical processes such as frost wedging could alter ice dams (Liljedahl & Hinzman, 2012; Zhang, 2014) and potentially allow the trapped water to escape. This could lead to a threshold influx of unexpectedly old groundwater into connected flow pathways.

2.7 IMPLICATIONS

Future climate warming will increase the active layer thickness of continuous permafrost environments (Lawrence et al., 2011) such as the Imnavait Creek Watershed. There is widespread debate within the literature on the impact of this active layer thickening on future groundwater flows. Many previous studies suggest that thickening of the active layer may increase groundwater flows (Evans & Ge, 2017; Kurylyk et al., 2016; Walvoord & Kurylyk, 2016; Walvoord & Striegl, 2007), while others suggest that soil compaction could decrease baseflows (Koch et al., 2014). Our results suggest that the impact of active layer thickening will depend on location in the watershed. For example, we show that groundwater increases due to active layer thickening are

negligible in loess-dominated locations such as the hillslope zone, and moderate in catotelm-dominated locations such as the riparian zone. However, these changes are dwarfed by precipitation-driven groundwater flow increases, because precipitation introduces new water at the top of the soil column where hydraulic conductivities are highest. It has been shown that the streams in such basins are supplied nearly entirely by groundwater flowing through or exchanging with this high-K zone (Neilson et al., 2018). It is therefore necessary to know how K changes with depth across space, and how precipitation will change in the future, to predict the impact of climate change on groundwater flow.

A thicker, thawed soil column has a relatively large effect on groundwater flows through catotelm, but an insignificant effect if the soils are loess. Results from our models representing variable moisture conditions show current groundwater contributions from loess in the hillslope to be ~0.029 m^3 d^{-1} (across our 20-m wide downslope grid boundary); assuming loess hydraulic properties are constant with depth, expanding the thawed loess column by 300% results in a flow of 0.09 m^3 d^{-1}, and increase of ~0.06 m^3 d^{-1}. Comparatively, in the riparian area, a 300%-thicker catotelm column would increase groundwater flows approximately ten times more (~0.6 m^3 d^{-1}), from 0.49 m^3 d^{-1} to 1.13 m^3 d^{-1}, assuming a decrease in K with depth extrapolated from our measurements (Figure 2.4, Equation 8). It is therefore necessary to identify the location and depth of the contact between loess and peat soil in watersheds to better predict future groundwater contributions as thaw increases. In areas with relatively thin peat layers underlain by loess, it is unlikely that groundwater flows will be affected by active layer expansion; in areas with thick peat sequences, substantial flow increases are possible.

The decrease in K with depth currently provides a limitation to groundwater flows that will likely continue into the foreseeable future. Loess soils provide a much stronger limitation than catotelm soils because K in the deepest, most compressed peat was still two orders of magnitude greater than K in the most permeable loess. This pattern likely continues beyond the depths we measured because peat compaction at depth, due both to the weight of overbearing soil and the microbial degradation of the organic material, can

extend tens of meters deep (e.g., Beckwith et al., 2003). If we extrapolate the increase in compaction (i.e., decrease in K) with depth in the riparian soils, the K of peat would exceed that of loess until a depth of approximately 5.75 m. It is unlikely that such deep soils will be thawed soon. Simulations of active layer dynamics in continuous permafrost near Barrow, AK predict that rising temperatures could drive an approximately 300% expansion in active layer thickness in the next 100 years (Atchley et al., 2015). This thaw expansion would result in future active layer thicknesses that range between 1.3 and 2.2 m if applied to the current thaw depths measured in our grids—depths well short of the 5.75 m necessary for peat K to equal loess K.

2.8 Conclusions

Our study shows that active layer groundwater flows are dominated by thin, near-surface saturated zones, with saturated zones at greater depth playing a minimal role. Therefore, water table fluctuations occurring at the top of the soil column exert a stronger control on groundwater fluxes than do ice table fluctuations. Water table fluctuations near the land surface translate into active-layer aquifer K values that vary multiple orders of magnitude because the observed K-depth decay profile declines most sharply in these shallow acrotelm and catotelm soils. Conversely, ice table fluctuations occur at the base of the aquifer where the K-depth decay profile is declining less rapidly in riparian zones, or within constant but low-K loess soils in hillslopes. Therefore, changes in thaw depth alone exert minimal impact on groundwater flow, despite causing potentially significant changes to the position or the thickness of the saturated zone. In other words, our observations illustrated that the effect of decreasing K due to saturated zone deepening dominates over increasing b due to thaw, and that this pattern is likely to continue as the climate warms.

Significant spatial patterns in both the position of the active layer saturated zone and the shape of the K-depth decay profile were found, and such patterns caused groundwater flows across the watershed to vary between but not within the riparian or hillslope zones. Within hillslope soils, a low-K loess layer at approximately 25 cm depth

caused groundwater flows from below that depth to be insignificant in comparison to flows from equal depths within the riparian zone, which lacked this loess layer. Steep hillslopes therefore only transport significant quantities of groundwater for brief periods because high-K surface soils rapidly drain. Shallower-slope riparian areas provide both low enough gradients that groundwater can remain longer, keeping water tables high, and contain thick catotelm soils whose intermediate K allows for persistent flow across the season.

Groundwater flows were also strongly influenced by microtopography. Microtopography creates significant variability in b and T at the meter scale by retaining groundwater behind ice dams. This phenomenon happened more readily in hillslopes than in riparian zones. Microtopographic retention may exert a substantial effect on the age distribution of groundwater in the basin.

2.9 TABLES FOR CHAPTER 2

Grid Name	Landscape Zone	Land Surface Slope [%]	Average microtopography peak-to-trough height [cm]	Notable Features
Inter-Track	Hillslope	10.57	7.49	No anomalous land surface slope or microtopography characteristics
Water Track	Hillslope	6.69	6.53	Grid bounded on the south edge by a continually wet, but rarely flowing water track
Slope Break	Hillslope	5.56	7.12	Grid reflects hillslope topography; however, it sits just above the abrupt transition between Hillslope and Riparian
Broad Riparian	Riparian	3.93	5.13	No anomalous land surface slope or microtopography characteristics
Near-Stream East	Riparian	2.96	7.33	Microtopography is more present; grid bisects the stream on its western face
Near-Stream West	Riparian	3.16	7.07	Water track on southern border; grid bisects stream on its eastern face

Table 2.1: Description of study grids within Imnavait Creek Watershed

		Inter-Track		Water Track		Slope Break		Broad Riparian		Near-Stream East		Near-Stream West	
		μ	σ	μ	σ	μ	σ	μ	σ	μ	σ	μ	σ
Land surface slope [%]		10.5	1.5	6.6	1.2	5.5	1.1	3.9	1.1	2.9	1.2	3.1	1.3
Microtopography height [cm]		7.4	1.3	6.5	-0.2	7.1	0.0	5.1	0.5	7.3	2.0	7.0	1.8
Depth to catotelm [cm]		12.0	6.3	23.6	10.6	18.0	8.1	18.6	7.7	18.6	7.7	12.6	10.6
Depth to loess [cm]		21.3	3.7	20.9	7.9	24.7	3.8	N/A	N/A	N/A	N/A	34.8	10.4
Water table depth [cm]	June	11.3	3.3	7.7	3.3	9.3	6.2	8.3	5.5	8.6	4.5	10.0	5.7
	August	21.0	3.5	20.9	7.9	17.9	8.6	8.4	9.1	15.7	13.3	21.4	10.0
Thaw depth [cm]	June	11.9	3.7	10.2	3.9	14.7	6.7	15.7	4.3	15.1	4.7	16.7	6.1
	August	43.7	8.1	73.9	18.4	55.7	11.4	46.8	8.8	51.9	11.8	53.6	9.6
Saturated thickness [cm]	June	0.5	1.7	2.4	3.9	5.6	6.0	7.4	5.2	6.5	7.5	6.2	6.4
	August	22.9	8.7	52.0	19.5	38.6	13.2	39.2	8.4	36.2	22.3	31.6	15.3
Transmissivity [m^2 d^{-1}]	June	0.4	1.5	2.2	4.2	1.0	2.6	2.9	4.8	1.3	3.1	0.9	2.3
	August	0.1	0.8	0.0	0.3	0.1	0.5	2.9	4.2	2.7	4.5	0.7	2.2
Hydraulic Gradient [%]	June	10.7	1.8	6.8	1.1	5.3	1.3	4.0	0.6	2.6	1.1	3.2	0.9
	August	10.2	1.1	6.6	2.2	5.7	1.0	4.2	0.9	2.7	0.6	4.4	2.0
Groundwater Flow [m^3 d^{-1}]	June	0.5	0.0	1.8	0.3	0.6	0.1	1.5	0.2	0.4	0.2	0.3	0.1
	August	0.1	0.0	0.0	0.0	0.1	0.0	1.6	0.3	0.9	0.2	0.4	0.1

Table 2.1: Summary of means (μ) and standard deviations (σ) of measurements and calculations from each measurement grid. The grid locations are depicted in Figure 2.2.

2.10 FIGURES FOR CHAPTER 2

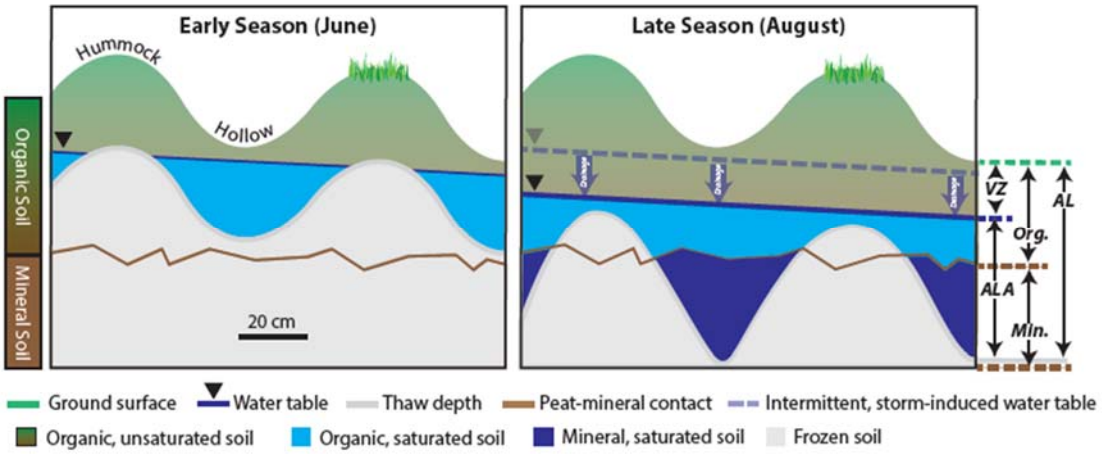

Figure 2.1: Conceptualized cross section of groundwater flow in the active layer in Early Season (left panel) and Late Season (right panel). The panels highlight the potential spatial variability of the active layer saturated zone (ALA), both in position and in thickness, as well as the temporal variability in both those factors. Although it is not depicted, flow comes into and out of the plane illustrated as the system is three-dimensional; such flow connects seemingly isolated pools observed in the Early Season (June) panel. Note that in this conceptual model, the water table is shown as planar, rather than as a subdued replica of topography, as is often the case in groundwater hydrology illustrations. Our observations did not support a water table reflecting topography, and studies conducted in similar settings also observe a planar water table despite undulating topography (e.g., Figure 2.2, Quinton et al. 2000).

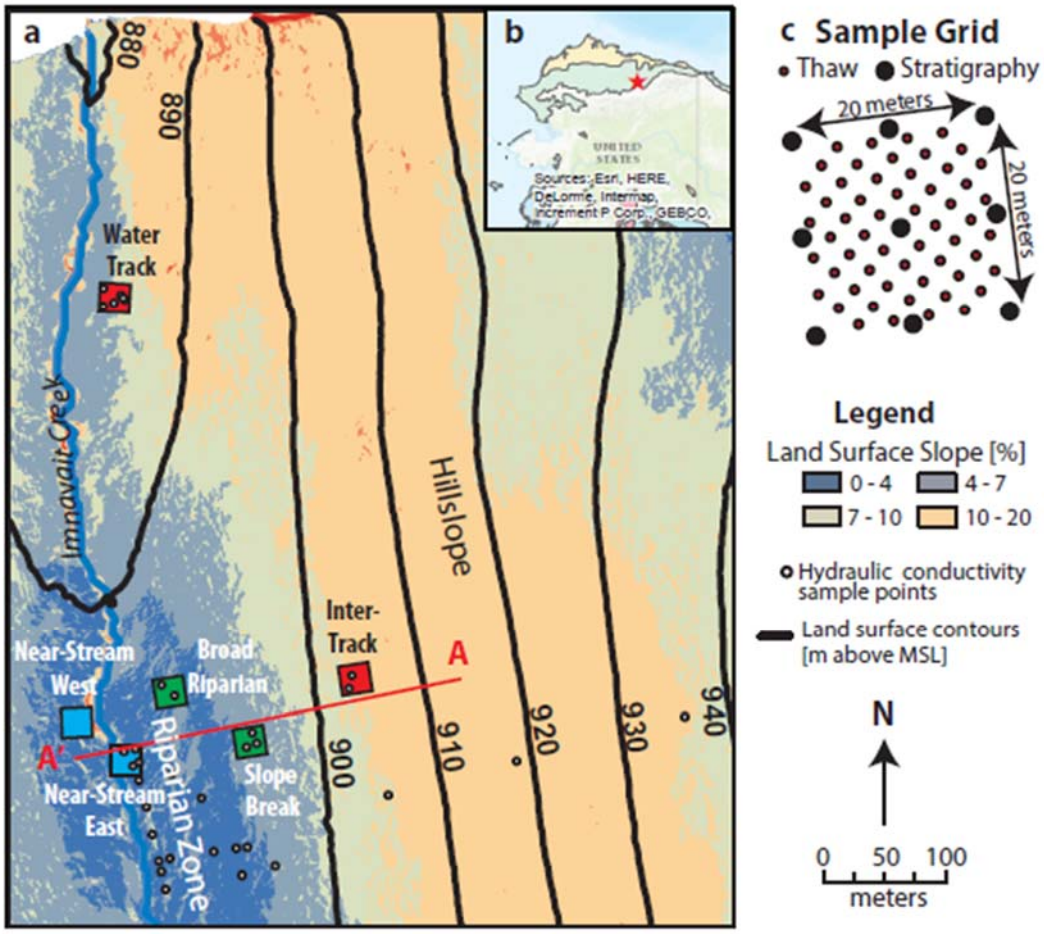

Figure 2.2: Map of field site. Clockwise from top right: (a) Locations of the six sample grids within Imnavait Creek Watershed, underlain by topographic slope; (b) Map of Alaska, showing location of Imnavait Creek (red star) and the two EPA Ecoregions of the North Slope, the Foothills (green) and Coastal Plain (yellow); (c) locations of individual sample points within each grid. The Riparian Zone is indicated by the darkest blue section of the map; the Hillslope represents all other colors.

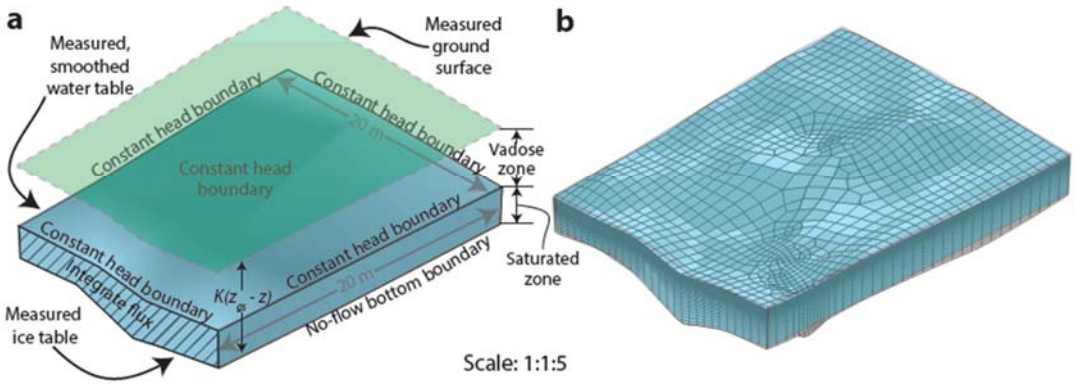

Figure 2.3: Schematic of 3D saturated groundwater flow models constructed to calculate groundwater flows. (a) Model domain, boundary conditions, and hydraulic conductivity parameterization. The green surface represents the measured ground surface elevation, which provided the reference for calculating depth-dependent K. The blue box represents the saturated model domain, bounded above by a Lowess Regression-smoothed water table and below by the measured ice table of each grid. The water table defines the constant head boundary on all sides and the top of the domain; the bottom boundary condition is no flow. Assignment of K and boundary conditions is consistent throughout all the models in this study; however, the position of the ground surface, water table, and ice table vary due to grid location and study time. The 'Early Season' model series employed the June measured surfaces; the 'Late Season' model series employed the August measured surfaces; the 'Variable Water Table' model series employed the August ground surface and ice table, and shifted the August water table in 5 cm increments between those two boundaries. (b) Unstructured mesh illustration used in the groundwater flow models. We employed 3D quadrilateral elements whose z-dimension thickness increased in a geometric sequence from the water table to the ice table in order to capture the steep depth-dependent K decay observed at shallow depths.

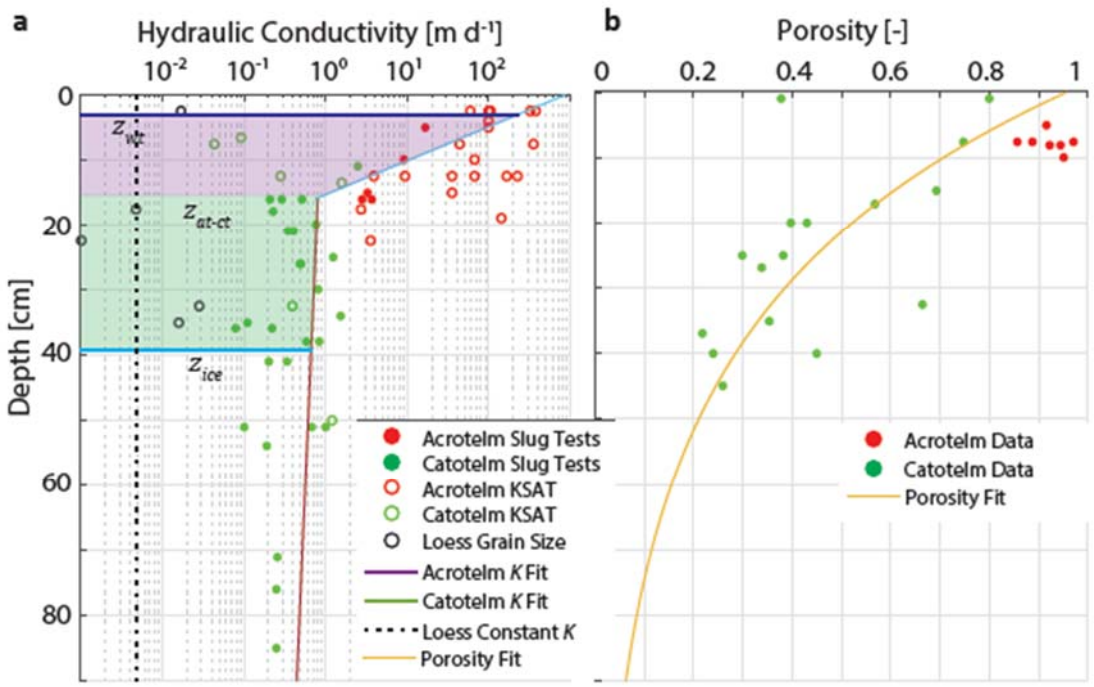

Figure 2.4: Depth distribution of measured (a) K and (b) porosity of all samples. The solid lines are fitted curves or piecewise lines. All mineral soil samples were analyzed via the grain size method (open black circles); among catotelm and acrotelm samples, open circles denote measurements taken in the laboratory with a constant-head test apparatus, and filled circles represent measurements taken in-situ via slug tests. The purple and green shaded boxes graphically represent the T of the acrotelm and catotelm segment of the profile.

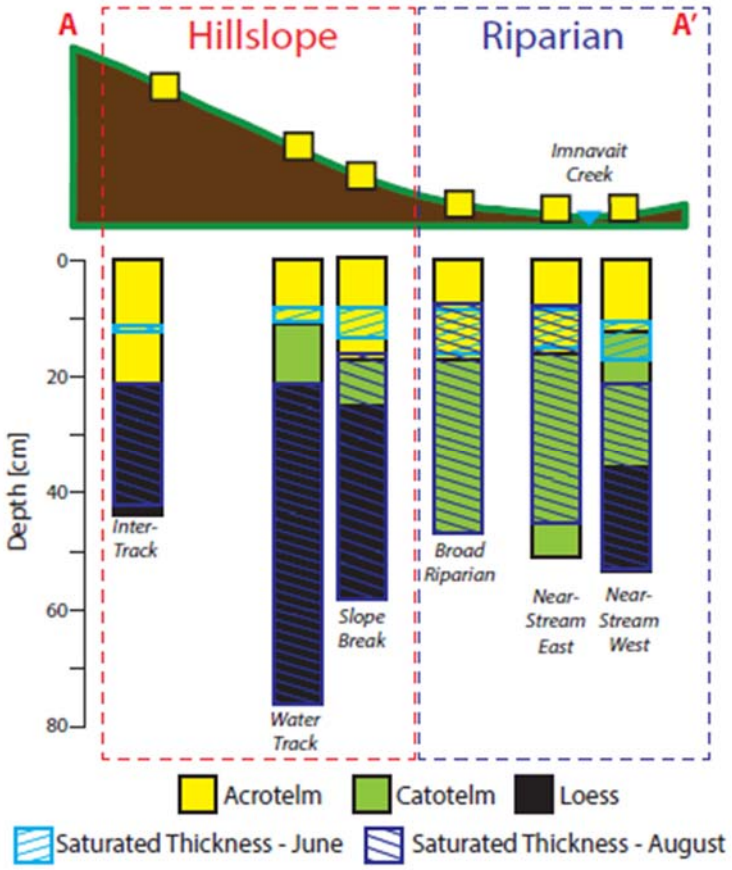

Figure 2.5: Average thickness of the acrotelm, catotelm, and loess (when present) within each of the six sampling grids, with June and August saturated thicknesses superimposed on the columns. The bottom boundary of each saturated thickness is defined by the ice table at the time of measurement. Grids are represented by yellow squares on the cross-section above; the cross-section A-A' can be found on Figure 2.2. The water track grid, which does not fall within the A-A' cross section, is included here at its approximate position downslope from its nearest ridge.

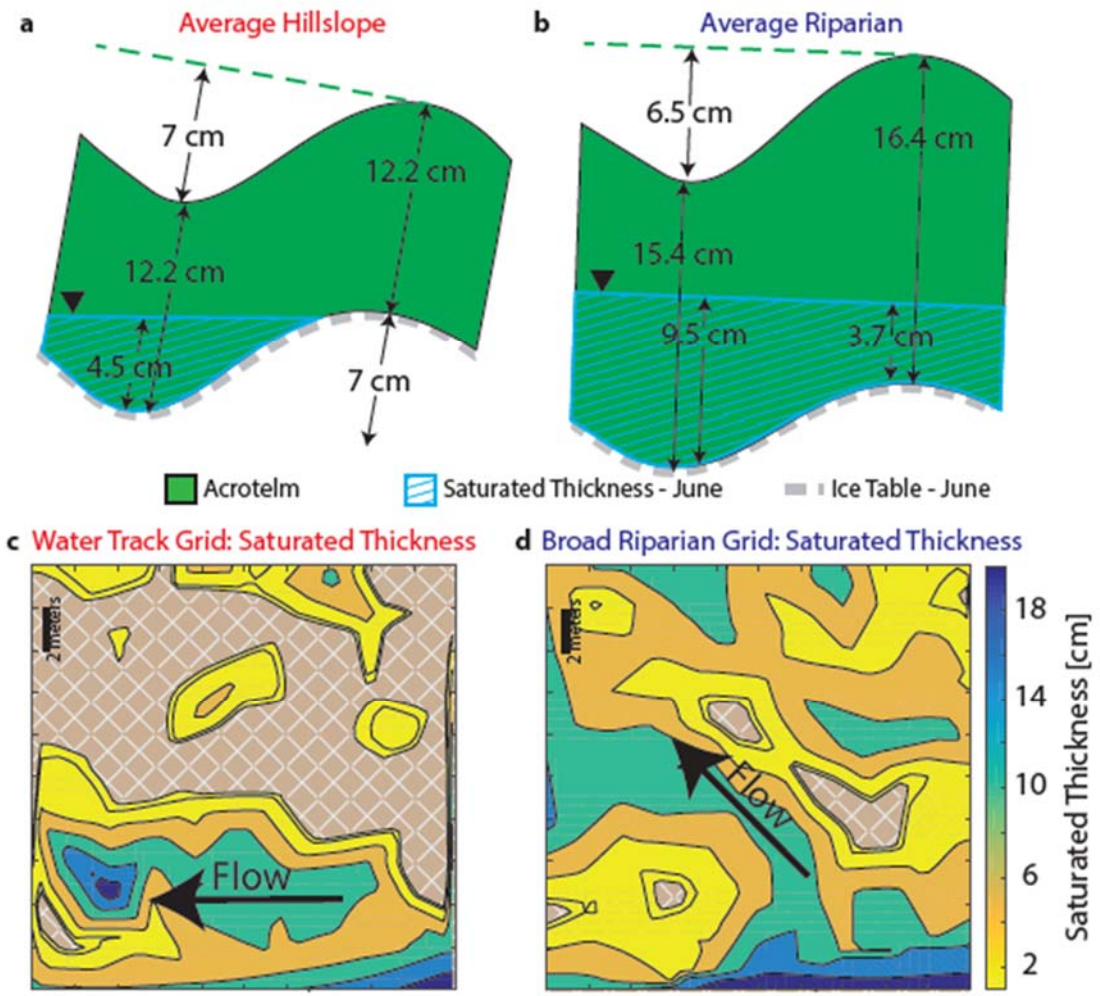

Figure 2.6: Schematic representations of microtopography size and land surface slope, and their influence on stratigraphy, saturated thickness, and thaw in the Early Season. (a) Average of measurements in the three hillslope grids; (b) average of measurements in the three riparian zone grids. Observed saturated thicknesses in the (c) Water Track grid on the hillslope, and the (d) Broad Riparian grid in the riparian area. Black arrows represent the general groundwater flow direction in each grid. Brown hatched pattern represents completely unsaturated soil.

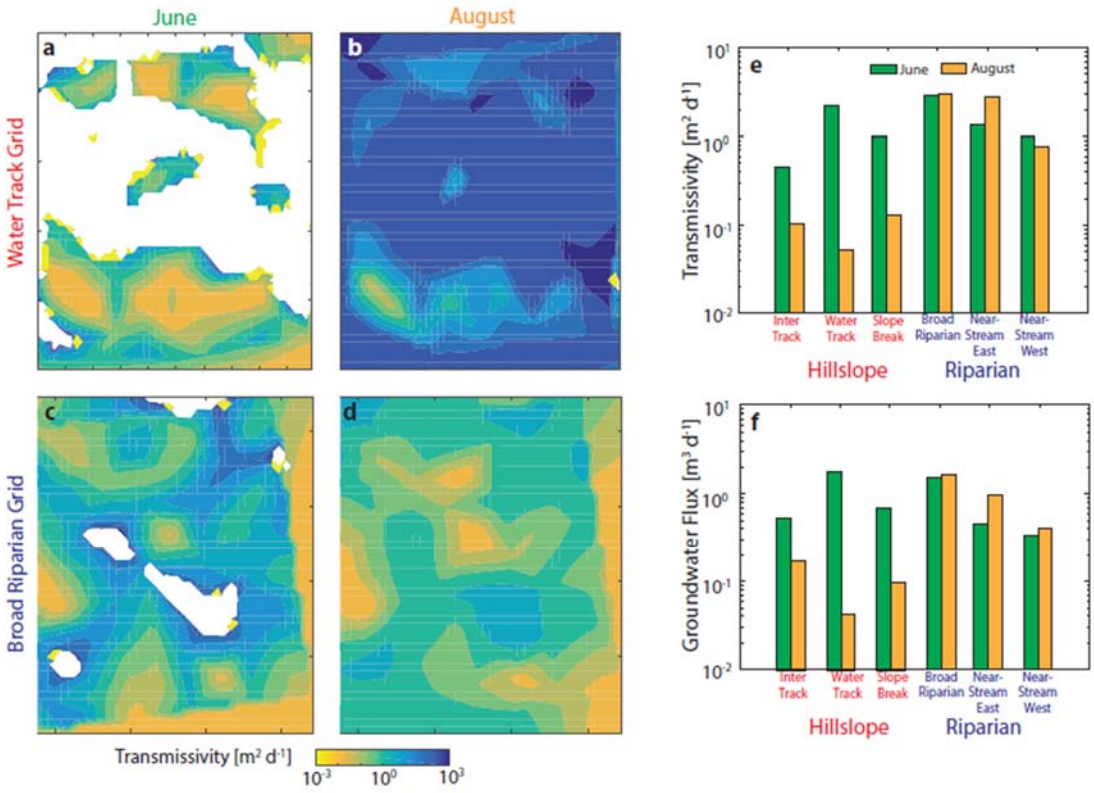

Figure 2.7: Spatial patterns and temporal snapshots of T and groundwater flow within the study grids. Upper panels show the calculated transmissivities of (a) the Water Track grid in June, (b) the Water Track grid in August, (c) the Broad Riparian grid in June, and (d) the Broad Riparian grid in August. (e) Mean T of each grid in June (green bar) and August (orange bar); (f) total groundwater flow leaving each grid through the 20 m downslope boundary in June (green bar) and August (orange bar).

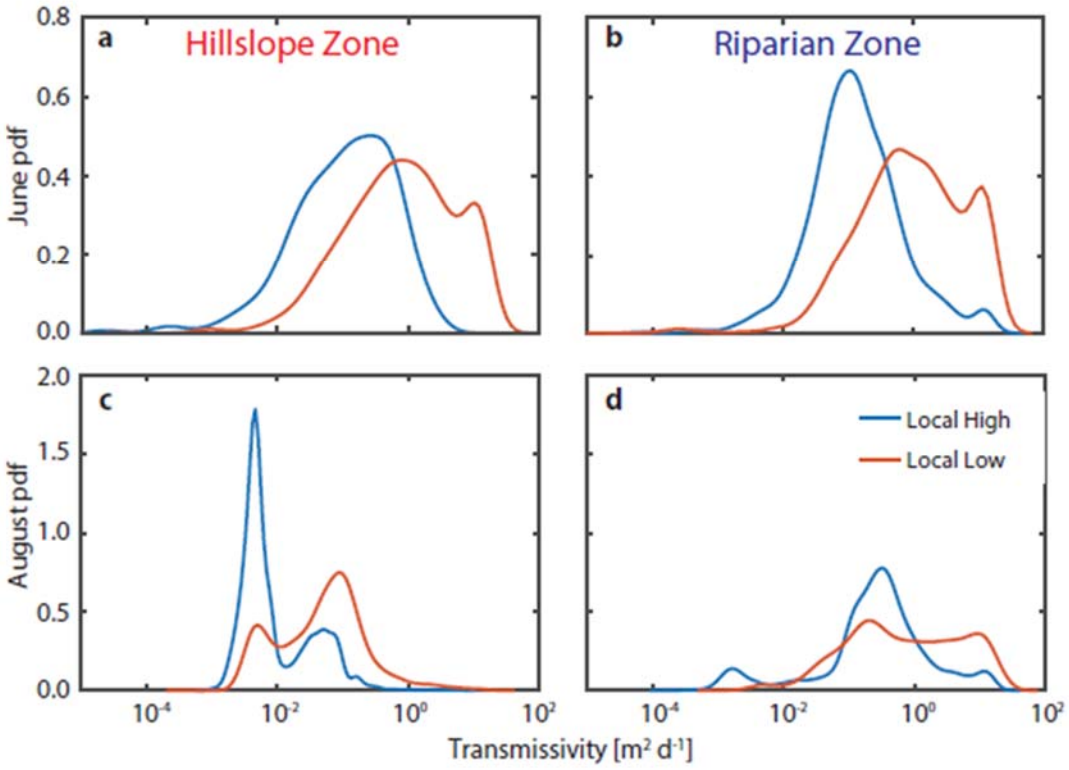

Figure 2.8: Probability density of calculated T in local highs (blue lines) and local lows (red lines). (a) and (b) show calculated values based on June observations; (c) and (d) show calculated values based on August observations. Left hand column represents all data points in the hillslope zone; right hand column represents all data points in the riparian zone.

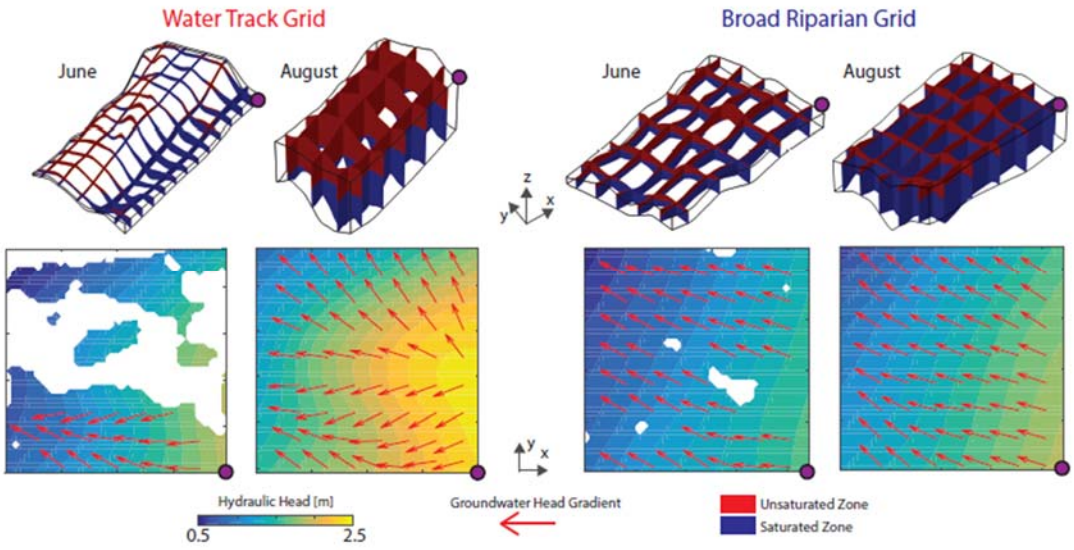

Figure 2.9: 3D saturated groundwater flow model results. Top row shows the location of the water table within the domain; bottom row shows the plan view groundwater hydraulic head distribution (contours) and gradients (red arrows). White gaps in the contour fields represent completely dry locations. Purple circles in the corner of the 3D grids correspond to the same purple circles on the 2D fields. Black ovals denote the water track within the Water Track grid.

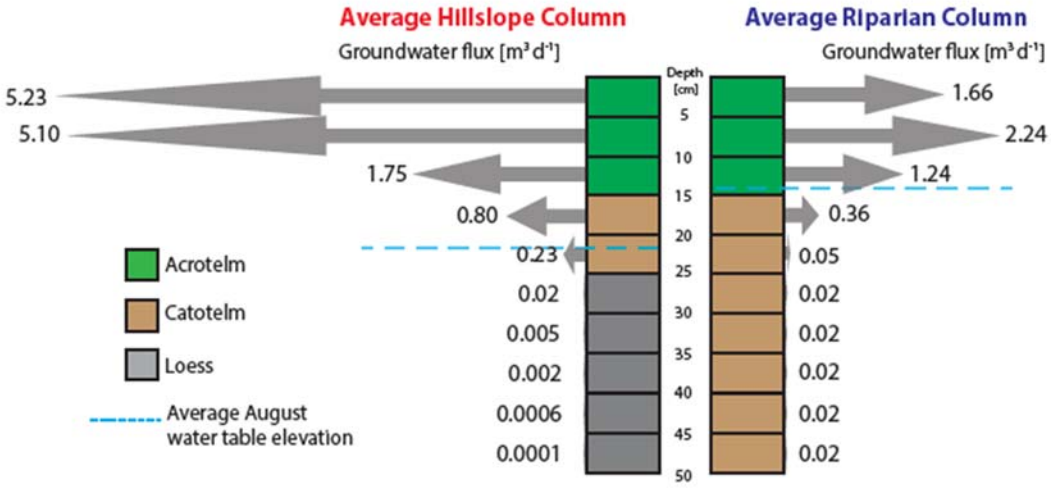

Figure 2.10: Average groundwater flow rate for individual 5 cm slices of a column of (left) the average hillslope active layer and (right) the average riparian active layer. Groundwater flows are based on a column of soil with a length of 20 m, a width of 20 m, a depth of 5 cm, and porosity determined from observations (see Figure 2.4).

Chapter 3: The similarity and predictability of soil stratigraphy, hydraulic properties, and thermal properties of supra-permafrost soils in the arctic Alaska foothills

KEY POINTS

- Soil stratigraphy and the properties of different horizons (acrotelm, catotelm, and mineral soil) were mapped for representative areas with different slopes and vegetation cover along the North Slope of Alaska.
- The stratigraphy of supra-permafrost active layer soils in arctic Alaska is predictable based on land surface slope and dominant vegetation type.
- The three main horizons (acrotelm, catotelm, and mineral soil) have systematic differences in organic matter content and in thermal and hydraulic properties.

3.1 ABSTRACT

Global climate change is driving rapid increases in Arctic temperatures, which is thawing shallow permafrost and exposing vast amounts of soil carbon to biogeochemical and hydrologic processes. The impact of such thaw on the global carbon cycle is uncertain. The uncertainty stems from a lack of information on the spatial variability of soil hydraulic and thermal properties. Through analysis of strategically distributed soil samples, we show that soil stratigraphic variability, represented by three horizons (acrotelm, catotelm, and mineral soil), is systematic and predictable based on vegetation cover and land surface slope. Each horizon has predictable hydraulic and thermal properties and organic matter content. In addition, the physical properties can be predicted solely from soil bulk density independent of horizon type. These findings are crucial for advancing the prediction of coupled hydrologic, thermal and biogeochemical processes in the Alaskan arctic. They directly inform both local flow and transport models and regional Earth system models.

3.2 INTRODUCTION

Climate change is warming the Arctic twice as fast as the global average (Serreze & Barry, 2011). Such warming has critical implications for the global carbon cycle, as more than half the soil carbon stored on Earth is held in Arctic permafrost (Ping et al., 2008). As the Arctic warms, these stores of once-latent soil carbon can be released into the atmosphere, contributing hundreds of billions of additional tons of CO_2 and CH_4 (Schaefer et al., 2014). However, there is enormous uncertainty in the amount and timing of permafrost soil carbon release to the atmosphere (Schuur et al., 2015). One source of uncertainty arises because current global models simplify the complicated and coupled processes controlling the hydrological transport of carbon in permafrost environments (Clark et al., 2015; Lawrence et al., 2015).

Hydrology regulates the biogeochemical reactions that produce CO_2 or CH_4 within the soil column through soil moisture: CH_4 production dominates in damp or inundated soils, while CO_2 production dominates in drier soils (Lawrence et al., 2015). Constraining which gas is released, and when, is necessary because the greenhouse effect induced by CH_4 is 25 times more potent than CO_2. Hydrology also controls dissolved carbon transport from arctic soils to surface waters (e.g., Kling et al. 1991; McGuire et al. 2009), but the controls on transport processes are poorly known. Uncertainty in the impact of hydrology on the carbon cycle contributes to a broad range in published estimates of global permafrost carbon release (between 50 and 400 Pg (Schuur et al., 2015)), resulting in between US$3-166 trillion of economic damage to society (Hope & Schaefer, 2016). Refining this requires a better representation of permafrost hydrology.

Hydrologic, thermal, and biogeochemical processes are tightly coupled in supra-permafrost soils. These processes are controlled by thermal and hydraulic properties of the soil which co-depend on each other. Very little is known about how the properties vary across the landscape, and what impact this variability exerts on hydrology (Walvoord & Kurylyk, 2016). While substantial understanding exists regarding the near-surface sedimentology (Walker & Everett, 1991; Walker & Walker, 1996) and soil

structure (Bockheim et al., 1998a; Bockheim, 2007; Ping et al., 2008; Walker et al., 2003) of continuous permafrost terrain, only a handful of studies interrogate the properties necessary to understand soil hydraulic and thermal processes (Hinzman et al., 1991; Quinton et al., 2008). The dearth of reported data inhibits the understanding of how these properties—particularly hydraulic conductivity K [L T^{-1}], thermal conductivity k [M L T^{-3} t^{-1}], and the saturation dependence of water retention capacity and hydraulic conductivity via the van Genuchten α [L^{-1}] and n [-] parameters—vary across the landscape.

It is impossible to accurately predict how climate warming will affect terrestrial hydrologic and thermal budgets without knowledge of the above properties. Particularly, it is unclear if the intense warming occurring in arctic areas will cause the region to become wetter or drier (Hodson et al., 2013; Kattsov et al., 2005). Determining this trajectory is critical because it is generally accepted that a wetter arctic will result in substantially more CH_4 production with a larger greenhouse impact, and a drier arctic will result in more CO_2 production with a lesser greenhouse impact. Two metrics are commonly used to assess the 'wetness' of the landscape: 1) soil water content and 2) baseflow. The amount of volumetric soil moisture present is a direct result of the water retention and transmission behavior of the soils, which are largely unknown for arctic soils. This gap has additional implications that reach beyond hydrology, as the moisture content of the soil is a direct control on soil thermal conductivity, which controls seasonal active layer development and long-term thawing. Models have interrogated the impact of variable soil moisture on active layer development by performing sensitivity analyses on various hydraulic and thermal input parameters within experimental domains (Harp et al., 2015; Jafarov & Schaefer, 2015). These studies have found that active layer development is highly sensitive to the soil hydraulic properties that control soil moisture; however, the ranges used for such sensitivity analyses are not informed by data, thus they do not accurately reflect the soils we observe in the landscape.

The fate of baseflow, the proportion of streamflow contributed by inflowing groundwater, in permafrost terrain undergoing intense warming is a subject of substantial debate (Neilson et al., 2018; Walvoord & Kurylyk, 2016). Competing factors are at play—as the soils warm, the active layer thickens, which increases the potential volume of liquid water available to be stored and to flow. However, because the K of arctic soils decays sharply with depth, flow rates decrease sharply as the active layer deepens (Chapter Two). Predicting future baseflows requires proper consideration of these competing factors at the landscape scale, which is only possible if the hydraulic and thermal properties of the soil are constrained at that scale.

This study uses field measurements and terrain analysis to answer the following questions necessary to build a landscape-based understanding of the supra-permafrost subsurface: *1)* How do arctic soil thermal and hydraulic properties vary within each unique soil layer; *2)* Are there correlations that can be employed to interpolate these hard-to-measure soil properties from simple ones; *3)* How do the thicknesses of these unique soil layers vary based on land surface characteristics; and *4)* Do the thermal and hydraulic properties of active layer soils also vary based on land surface properties? The results presented here improve our understanding of the arctic subsurface, and lay the groundwork for both local and landscape-scale, data-driven arctic hydrology predictions, which will substantially reduce the uncertainty that currently exists for permafrost carbon release.

3.3 Methods and Study Site

Soil stratigraphic data were collected from 192 sites within the Kuparuk River Watershed and the Itkillik River Watershed in the North Slope of Alaska (Figure 3.1) over two summer field seasons (2017-18). We classified each site based on the observed surface landscape properties (dominant vegetation type, slope, and microtopographic position) that we observed in the field. From these 192 sites, 136 soil cores were collected for which the hydraulic and thermal properties were analyzed in the laboratory.

Statistical methods were then used to determine significantly unique distributions of soil stratigraphy and properties for each classification.

3.3.1 Description of study site

Our study site spanned two watersheds which capture the most common landscape features observed across the Arctic Foothills. The Arctic Foothills, one of only two USGS-designated physiographic regions (Wahrhaftig, 1965) and US EPA-designated ecoregions (Omernik & Griffith, 2014) found in Alaska's North Slope, represents a large area key for understanding Arctic thermal hydrology. The Arctic Foothills is defined largely by topography, containing moderate to steep rolling hills carved by six distinct glaciations in the late Pleistocene (Detterman et al., 1958; Hamilton, 1982a). The Arctic Foothills is bounded to the south by the Brooks Range and to the north by the much flatter Arctic Coastal Plain, and the Coastal Plain is bounded to the north by the Arctic Ocean (Figure 3.1, inset). Summer air temperatures range between 6 and 18°C, and the watershed receives 35 cm of precipitation a year on average, with 60% of that occurring as summer rain (McNamara et al., 1997).

3.3.2 Classification of sample sites based on landscape criteria

The landscape classification of each site was determined by inspection. The landscape classifications we created combined three easily-identified surface criteria: dominant vegetation type, land surface slope, and microtopographic position. Thresholds that defined categories within each criteria were either previously established in literature or, in the case of microtopographic position, obvious in the field. The classification scheme we developed was hierarchical: we first identified the landscape zone, defined based on the land surface slope. Within each landscape zone, the dominant vegetation type was then identified, and finally, within each vegetation type, microtopographic position was determined.

Landscape zone was identified based on the classification used by Walker and Walker (1996). They identified two dominant landscape zones, the hillslope zone and

riparian zone—these two zones comprised approximately 90% of their study site and are defined based on a combination of topography and distance to a stream. Riparian zones are flatter (<10%) slopes that border creeks; Hillslope zones are steeper (>10%) and often feed into Riparian zones.

Four types of dominant vegetation were observed: woody shrubs, tussocks, sedges, and lichens. Substantial work has been performed to identify and further sub-classify vegetation types within the Toolik Lake Region (Hahn et al., 1996; Walker et al., 2003; Walker & Walker, 1996), the North Slope (Payne, 2013), and in arctic continuous permafrost terrain in general (Stow et al., 2004). Different vocabulary has been used across disciplines to describe different classifications and sub-classifications of this landscape, and in particular, the North Slope Science Initiative has used a vegetation-based approach to divide the landscape into 25 categories, 8 of which are found in our study extent. Here, we introduce umbrella categories that are meant to simplify these particular sub-classifications based on a common, simple criteria. We use 'Sedge' to describe any wet to saturated, graminoid-dominated plot; 'Woody Shrubs' to describe any plot whose extent is dominated by plants with woody stems (i.e. birch, willow, and alder); 'Tussock Tundra' to describe any plot with tussock cottongrass (genus *Eriophorum*) present, and 'Lichens' to describe any plot with matted lichen vegetation or bare ground. These four categories include all the dominant land cover types in the North Slope Foothills of Alaska.

The North Slope Science Initiative (NSSI)-developed Land Cover Classification (Payne, 2013) identifies sub-classifications that would fit within our broad umbrella terms: 'Woody Shrubs' encapsulates 'Birch Ericaceous Low Shrub', 'Low-Tall Willow', and 'Alder'; 'Sedge' encapsulates 'Carex Aquatillis', 'Wet Sedge' and 'Wet Sedge – Sphagnum'; 'Tussock Tundra' encapsulates both 'Tussock Tundra' and 'Tussock Shrub Tundra', and 'Lichens' includes 'Bare Ground', 'Sparsely Vegetated', 'Dwarf Shrub', and 'Mesic Sedge – Dwarf Shrub'. However, we correctly hypothesized in our study design that soil property differences across sub-classifications within an umbrella class

would be insignificant. We therefore based our vegetation characterization on umbrella classes.

Our observations of dominant vegetation sometimes disagreed with the classification imposed on a given plot by the NSSI Land Cover Data Product (Figure B1). Disagreements most frequently occurred in plots identified in the Hillslope landscape zone, as 'Sedge' or 'Woody Shrubs'. These vegetation types often grow in linear, down-slope tracks with narrow widths ("water tracks"). Both sedge-type and woody shrub-type vegetation have been described in previous literature as identifiers of water tracks. Water tracks are important hydrologic conduits that differ from the surrounding tussock tundra; although they rarely appear in the NSSI Land Cover Data Product, they have been identified by Walker & Walker (1996) as a landscape zone distinct from the 'Hillslope' in this region. Water tracks are zero-order geomorphic drainage features that funnel substantial water flows from the hillslope (McNamara et al., 1999). These linear drainage features are spaced somewhat regularly in intervals of tens of meters and have narrow widths (1 to 3 meters), and they occur in subtle topographic lows within the landscape (McNamara et al., 1997; Voytek et al., 2016). They are unique to tundra environments in that, while they resemble streams in their morphology and retain moisture for substantially longer periods than the surrounding inter-track areas (Rushlow & Godsey, 2017), they rarely exhibit surface flow because shallow permafrost prevents the erosive processes necessary to carve out a stream channel (McNamara et al., 1999). We frequently observed water tracks comprised of sedge vegetation, and lined on each subtle topographic 'ridge' by woody shrubs. Such narrow features are difficult to detect given the 25-m resolution of the Landsat imagery that informs the NSSI Land Cover Map (Payne, 2013); thus, there was frequent disagreement between the observed vegetation cover type and the NSSI-imposed land cover type at these locations.

Microtopographic position was established visually by comparing the local elevation of the sample site to the surrounding elevation points. Microtopographic variability ranged from 20 to 50 cm in our study site, and these elevation changes occur

approximately 1 m apart from one another. They therefore present substantial relief at the meter-scale, especially in the Riparian Zone, where microtopographic relief (20 to 50 percent) is orders of magnitude larger than the regional land surface relief (1 to 5 percent). Microtopography was pervasive in Tussock Tundra vegetation in the Hillslope and in Sedge vegetation in the Riparian Zone. We did not observe obvious microtopography in Hillslope Sedge vegetation, as these locations fell within water tracks, and water tracks naturally occur in microtopographic lows. We also did not observe obvious microtopography in Hillslope Woody Shrubs for the opposite reason—woody shrubs tend to grow in more drained areas, and microtopographic highs are drier than microtopographic lows (Quinton et al., 2000). Across all plots, we did not assign a microtopographic position when it could not be clearly determined in the field.

Our classification resulted in the creation of eight categories: Tussock Tundra High and Low, Sedge Hillslope (i.e., Water Tracks), Woody Shrubs Hillslope (i.e., Water Track-Adjacent), Woody Shrubs Riparian Zone, Sedge High and Low, and Lichens.

Our sample sites also spanned a well-accepted ~80,000 year old glacial divide between the Itkillik I and Sagivinirktok glaciations (Hamilton, 1982b). However, all Student's T Tests performed to compare differences between stratigraphy and properties across the glacial divide failed; therefore, glacial age was not considered as a defining characteristic for developing classifications. This finding is counter to other studies that show soils on the younger side of the glacial divide to have thinner total organic layers than soils on the older side of the glacial divide (Bockheim et al., 1998a).

3.3.3 In-situ measurements of soil stratigraphy, active layer thickness, and water table depth

An approximately 30×30 cm square section of tundra soil was extracted using a bread knife and then returned in place. This window exposed the soil stratigraphy at that site (Figure 3.1, inset). We delineated the contact depth between obviously different soil layers through multiple qualitative criteria. First, to identify the acrotelm/catotelm contact, we measured the depth at which recently-dead roots, leaves, and fibers were no

longer present in the soil (Figure 3.1). These features are commonly present in young, less-degraded acrotelm peat (Agus et al., 2011; Holden & Burt, 2003). We employed a color- and texture-based criteria to identify the catotelm/mineral soil contact: catotelm and mineral soil were often starkly different colors (catotelm being a dark brown or black, whereas mineral soils were a very light brown or grey), and physically, mineral soils were cohesive and rarely compress, while catotelm peats are loose and compressible. The depth at which this transition occurred was recorded as the catotelm/mineral soil contact depth. We also used a quantitative approach to test the validity of the qualitative classification - this approach is listed in the last section of the Methods.

Both the active layer thickness and the water table depth were measured at each site. Active layer thickness was measured using a graduated 1.2 m long metal rod that was driven into the ground until refusal. Three measurements were taken near each point and averaged. The water level within the pit was measured after 30 minutes from when the pit was dug, which allowed the water level to return to a static condition. Additionally, in-situ soil k was measured using a KD2 Thermal Analyzer (METER Group, Pullman, WA), and in-situ soil water content was measured using a time-domain reflectometry probe ('Theta' Probe, METER Group, Pullman, WA). Multiple k and water content measurements were taken at each pit, and their depths were recorded to build a profile at each pit.

3.3.4 Laboratory measurements of soil hydraulic and thermal properties

We extracted a 5 cm diameter soil core from a subset of sample sites to be returned to the laboratory for analysis. In the laboratory, we measured K, k, porosity φ, bulk density ρ_b, and percent loss-on-ignition (LOI) for each core. For a further subset, we analyzed water retention parameters α, n, residual water content, and saturated water content (which equals φ) of the van Genuchten model (1980). K was measured using a constant-head test implemented with a KSAT Benchtop Hydraulic Conductivity instrument (UMS Corp., Berlin, DE). k was measured in each soil core at both full water

saturation and total dryness using the two-pronged thermal diffusivity probe attachment on a KD2 Thermal Analyzer (METER Group, Pullman, WA). Dryness was achieved during the measurement of φ: the cores, which were a known volume, were weighed at saturation, placed in an oven at 105°C to dry for 24 hours, and re-weighed. The difference in weight represented the volume of water lost within the sample, and that volume divided by the total soil volume represents the porosity.

A direct estimation of organic matter (OM) content was attained from the samples by using loss on ignition (LOI) analysis. In this method, a sample is fully dried at 105 °C to remove water and a known mass is ignited in a muffle furnace at 375 °C for 24 hours (Ball, 1964). The difference in mass before and after ignition is a proxy for percent of OM within the sample. Soil water retention properties were determined through the evaporation method (at relatively high soil suctions) and the dew point technique (for relatively low soil suctions). We performed the evaporation method using the HYPROP, which is described in detail in Schindler et al. (2010). The HYPROP builds a real-time soil water retention curve by simultaneously measuring the pressure gradient between two tensiometers at different heights in a soil core and the soil water weight. The evaporation method is limited by tensiometer cavitation when the hydraulic connection to the soil pores is broken, which occurs at relatively high soil suctions. Thus, to complete the soil water retention curve at high suctions, we used a WP4C Dew Point Potentiometer (METER Group, Pullman, WA), which measured the humidity of the air in a small chamber in equilibrium with a sample of dried soil, as described in Leong et al. (2003). For each sample, we included three WP4C points; these points provided the information necessary to complete the soil water retention curve at high suctions. The closed-form equation developed by van Genuchten (1980) was fitted to the experimental soil water retention curves:

$$s_*\{p\} = s_r + (1 - s_r)[1 + (\alpha p)^n]^m \qquad \text{[Eq. 1]}$$

where s_* [-] is water content, p [Pa] is pressure, α [m^{-1}] represents an air-entry pressure and is related to pore throat size, n [-] is a shape parameter, $m = 1 - 1/n$, and s_r [-] is soil residual water content.

3.3.5 Hierarchical characterization of soil types, stratigraphy, and properties

Our laboratory measurements allowed for a robust classification of soil samples that was not possible in the field. We used soil bulk density and loss on ignition percent measurements to group our soils into three unique layers. We first differentiated organic soil from mineral soil through an LOI threshold established in Agus et al. (2011): soils with less than 40 percent organic content by mass were considered 'mineral soil', whereas soils above were considered organic soil. This threshold represents the lower standard error of the LOI percent of the most mature peat soils (Sapric) in Agus et al. (2011). To further differentiate the organic soils, we applied a dry bulk density criteria also established by Agus et al. (2011). Organic soil samples were considered least degraded (i.e., acrotelm) if their dry bulk density fell below 0.15 g cm^{-3}, and more degraded (i.e., catotelm) if dry bulk density fell above that. This threshold represents the upper standard error in measured dry bulk density of immature (Fibric) peats in Agus et al. (2011).

To develop a landscape-based characterization of soil stratigraphy and properties, our observations were grouped into populations based on the landscape-driven criteria we developed in section 2.2. A one-sample Kolmogorov-Smirnov test was implemented on each dataset to confirm normal distribution of the data. A series of one-way ANOVA and T-tests were then performed to determine if the variability in acrotelm thickness, catotelm thickness, K, k, φ, LOI, α, and n was larger between categories than within categories. The categories tested were: landscape zone (Hillslope vs. Riparian), vegetation type (Sedge vs. Tussock Tundra vs. Woody Shrubs vs. Lichens), microtopography (local high vs. local low), and all categories together (Tables B3-B5). This testing scheme allowed us to determine which category of factors exerted the most substantial control on properties. In instances where a population had fewer than five

samples, comparisons were withheld. For all analyses, we denoted statistical significance at a *p*-value less than 0.05.

3.4 RESULTS

The measurements of soil stratigraphy (Table B1) and properties (Table B2) yielded and confirmed the three distinct soil types: less-degraded acrotelm peat, more-degraded catotelm peat, and glacial till or loess-type mineral soil. These classifications or variants of them have been identified previously in the literature (Hinzman et al., 1991; Neilson et al., 2018; Quinton et al., 2008; Woo & Marsh, 2005a). In this study, we quantified how their hydraulic and thermal properties vary systematically both between and within soil types, and between and within landscape classes. The pervasiveness of these three soil types, combined with the uniqueness of the observed hydraulic and thermal behavior of each type, and the relatively narrow range of properties observed within landscape classes, opens many possibilities to better understand how heat and water flow through arctic tundra across wider areas.

3.4.1 Mean soil properties

As has been shown in other work, the degradation state of organic soil has a substantial effect on its properties (Boelter, 1969; Holden & Burt, 2003). Less-degraded acrotelm peat has very low average ρ_b, and that low ρ_b results in extremely high average φ (Figure 3.2, Table B2). The high acrotelm average φ we observe is consistent with values measured in other peat studies in temperate and boreal locations (Agus et al., 2011; Beckwith et al., 2003b; Boelter, 1969; Hinzman et al., 1991). More-degraded catotelm soils have significantly higher average ρ_b but only slightly lower average φ, and they have significantly lower average K and α. Acrotelm K was measured at 0.0016 +/- 0.001 m s^{-1}, whereas catotelm average K is approximately 100 times lower (Table B4). Catotelm average K ranges more than acrotelm K in log scale; however, the absolute range of acrotelm K is much larger than catotelm.

Less-degraded acrotelm soils retain very little porewater in comparison to catotelm (Figure 3.3, Figure B2). Acrotelm has a significantly higher van Genuchten n shape parameter than catotelm (Table B4), and acrotelm α is a 4.5 times higher than catotelm α. Acrotelm α is very high (Figure 3.3), both in comparison to the other soils observed in this site and, more broadly, in comparison to commonly-observed soils in nature (Hillel, 1998). Despite having a low water retention ability, when driest, acrotelm residual water content (θ_r) is significantly higher than that of catotelm (Table B4).

Although distinct hydrologically, acrotelm and catotelm soils are thermally much more similar. The average saturated k of both soil types is approximately 0.6 W m^{-1} K^{-1}, which is similar to the thermal conductivity of water. This is because the porosities of both acrotelm and catotelm soils are quite high, ranging between 85 and 95%, so water comprises the bulk of the saturated soil sample. Similarly, the average dry thermal conductivity of both acrotelm and catotelm soil is quite low (0.07 W m^{-1} K^{-1}), approaching the thermal conductivity of air (0.03 W m^{-1} K^{-1}).

The KD2 Thermal Analyzer measures soil effective k, which is the thermal conductivity of the volume-weighted average of the soil grains, water, and air immediately surrounding the heat pulse probe (Devices, 2006). Given the very high φ measured for both organic soil types, the effective k of organic soils is highly dependent on its saturation, because as those soils dry, relatively-high-k soil porewater is replaced with substantially lower-k air. We clearly observed this dependence in our data (Figure 3.3, Figure C2). The relationship between k and saturation is relatively constant across all the organic soils measured (average of 0.52 +/- 0.14 W m^{-1} K^{-1} per percent saturation lost, Figure 3.3), despite substantial variability in φ and LOI. However, the average k of acrotelm at a given water content is slightly lower than the average k of catotelm at that same water content. The saturated and dry k that we measured in our organic soils, as well as the rate of change in k due to saturation, generally fall slightly above values reported for other organic soils in the literature (e.g., Becker et al., 1992; O'Donnell et al., 2009, Figure B3).

The soil properties we measured from our mineral soil samples were not normally distributed; thus, their average properties are not representative of the dataset as a whole. However, overall, mineral soils are more thermally conductive (higher k), less porous (lower φ), less permeable (lower K), and retain more porewater (lower α, higher n, and higher θ_r) than both acrotelm and catotelm soils. Two distinct groupings of mineral soil properties could be derived from the overall data, and we present them here based on their relative organic matter contents: 'high-organic' and 'low-organic'. High-organic mineral soils are also high φ, high K, and lower k relative to the other, 'low-organic' mineral samples (Figure 3.2). Despite the high variability observed in mineral soil K, the values we observed were approximately two orders of magnitude lower than mineral soil K values measured by Hinzman et al. (1991) in Imnavait Creek Watershed, which is included in the study extent for this work.

3.4.2 Bulk density as a predictor of soil properties and a factor in variability

Soil dry bulk density alone correlates well with the other observed soil properties in supra-permafrost soils (Figure 3.4). These correlations are useful both for estimating the average thermal and hydraulic properties of supra-permafrost soils and for predicting and explaining variability in those thermal and hydraulic properties within a soil type. ρ_b best predicts the variability of properties in mineral soils, and is progressively worse at predicting the variability of properties within catotelm and acrotelm soils, respectively. ρ_b is particularly useful for predicting the properties of mixed soils whose ρ_b falls between two unique soil types. The regression models used to create the relationships described below are found in Table B6.

Dry bulk density (ρ_b) can be used to estimate φ using a first-order polynomial function ($R^2 = 0.88$, respectively). As ρ_b increases, φ decreases linearly. This relationship is strongest in mineral soils ($R^2 = 0.93$), significant but weaker in catotelm soils ($R^2 = 0.50$), and poor in acrotelm soils ($R^2 = 0.14$). There is also a strong overall linear trend between ρ_b and dry soil k ($R^2 = 0.84$). As was found for φ, the relationship

between ρ_b and k is strongest when only mineral soils are considered ($R^2 = 0.92$), weaker but significant for catotelm samples ($R^2 = 0.54$), and poor in acrotelm soils ($R^2 = 0.11$).

ρ_b also affects the dependence of k on saturation. The slope of the linear relationship between soil k and water content increases with ρ_b ($R^2 = 0.76$) (Figure 3.3). However, the slope of that linear relationship is not well correlated to ρ_b or any other soil properties within organic soils alone. Rather, the relationship between k and water content is relatively constant across all the organic soils measured.

ρ_b can be used to predict LOI percent using a first-order exponential function ($R^2 = 0.88$). This relationship is useful for explaining the LOI percentages of outliers within both catotelm and mineral soil populations. Similar relationships between LOI and ρ_b are commonly observed in a variety of soil types, including peat soils (Huntington et al., 1989; Périé & Ouimet, 2008; Post & Kwon, 2000; Prévost, 2004), and our observed relationship agrees well with such other published relationships (Figure 3.4).

Soil ρ_b can be used in our site to estimate both K and van Genuchten α using first-order power functions ($R^2 = 0.73$ and 0.80, respectively). Unlike our other measured properties, the relationship between ρ_b and K is weaker when considering each soil type individually than when considering all soil types together. There is relatively wide variability (~3 orders of magnitude) in mineral soil K that is not well-explained by ρ_b trends; however, ρ_b trends better explain the K of catotelm outlier sample points. Although a limited sample size exists, the dependence of α on ρ_b is significant.

3.4.3 Definition of landscape classes based on unique soil stratigraphies determined by bulk density and in-situ criteria

Soil stratigraphy varies predictably based on the vegetation cover type, the landscape zone, and the microtopographic position of the land surface (Figure 3.5, Table B3). These patterns held across a glacial age divide that spanned approximately 80,000 years (Hamilton, 1982b, Figure 3.1)

Landscape zone exerts the strongest control on catotelm thickness but has no significant effect on acrotelm thickness. Overall, riparian zone sites exhibited a 150 percent larger mean catotelm column thickness than hillslope zone sites (Table B3). The combination of a statistically similar acrotelm, combined with significantly larger catotelm, cause the total organic layer thicknesses in riparian zone sites to be significantly larger than the total organic layer thicknesses in hillslope sites (21 +/- 5 cm in hillslopes versus 30 +/- 9 cm in riparian zones).

The total organic layer thicknesses observed across all hillslope sites were similar; however, the distribution of acrotelm and catotelm thicknesses within those similar organic columns varied significantly based primarily on vegetation type and secondarily on microtopography. Sedge-dominated water tracks, which were the most saturated, have the thinnest acrotelm and thickest catotelm (Figure 3.5). Woody Shrub sites, which commonly had the deepest water tables, have the thickest acrotelm and subsequently the thinnest catotelm. Tussock Tundra sites exhibit intermediate-thickness acrotelm and catotelm when microtopography is ignored; however, when considered, significant patterns emerge that reflect the moisture and vegetation relationships described above. Local highs, which are commonly dry and contain small woody shrubs, exhibit similar stratigraphies to our Woody Shrubs sites in that they have relatively thicker acrotelm compared with a relatively thinner catotelm. Local lows, which are commonly flooded and populated with sedges and mosses, have relatively thinner acrotelm atop relatively thicker catotelm—this is similar to the pattern observed in the perennially-flooded and sedge-dominated Water Track sites.

The total organic thickness across riparian sites did vary substantially. This substantial difference was largely due to anomalously large catotelm under sedge vegetation; catotelm columns in riparian sedges are 210 percent thicker than the rest of the catotelm columns observed (Table B3). Additionally, microtopography correlates strongly with acrotelm thickness in this zone; sedges in the relatively less saturated local

highs have thicker acrotelm than sedges in local lows. Microtopography does not substantially affect the thickness of catotelm, however.

3.4.4 Variability in soil properties within soil layers across landscape classes

The hydraulic and thermal properties of acrotelm remained consistent across the observed classifications (Figure 3.6, Table B5). However, the K of Woody Shrub Hillslope acrotelm is substantially but not significantly lower than the K of all other acrotelm sites.

Variability in catotelm properties can be further constrained when landscape-driven catotelm properties patterns are considered. ANOVA tests across catotelm samples grouped by landscape class showed that the LOI, K, k, φ, and ρ_b in Woody Shrub Riparian sites and Tussock Tundra High sites are significantly different from the rest of the catotelm sample population (Figure 3.6, Table S4). T-tests that we conducted by grouping catotelm soils of Woody Shrub Riparian and Tussock Tundra High against catotelm soils of all other plots confirmed this: the first group, which contained catotelm in the Woody Shrub Riparian and Tussock Tundra High classes, exhibits significantly lower LOI, K, k, and φ than catotelm in the second group, which contained all other plots. The first group of soils (Woody Shrub Riparian and Tussock Tundra High) also have significantly higher ρ_b than all other plots.

The inter-population variability in overall mineral soil properties is much larger than that of both acrotelm and catotelm soil properties (Figure 3.6, Table B4). However, as is the case for catotelm soils, that variability can be further constrained when the patterns of landscape-driven properties are considered. Soils in Woody Shrubs and Tussock Tundra Highs in the Hillslope zone exhibited elevated K, φ, and LOI, and lower k, in comparison to mineral soils from all other plots. However, we did not have enough samples from any one category in order to establish significance between these different landscape classes.

3.5 DISCUSSION

This study presents the first hydrologic characterization of landscape-based soil stratigraphy patterns. Many previous studies have used similar landscape-driven approaches to identify patterns in subsurface properties such as soil texture (Walker & Everett, 1991), soil organic thickness (Bockheim et al., 1998a; Shelef et al., 2017), and active layer thickness (Walker et al., 2003), but by developing a landscape-driven approach to describe thermal and hydraulic soil properties both across space and with depth, we open the door for the first landscape-scale, process-based, field-informed arctic thermal hydrology studies to be developed. By connecting landscape-based stratigraphy to readily available remote sensing products such as the NSSI Land Cover Map (which describes the dominant vegetation cover based on Landsat Imagery (Payne, 2013)) and the ArcticDEM (Morin et al., 2016), it is possible to expand this knowledge regionally.

We employed a previously-used characterization of organic soil types that simplifies the continuum of soil degradation states that can occur in peats into two categories: acrotelm (less degraded), and catotelm (more degraded). In peat soils, it is commonly known that ρ_b increases with degradation (Boelter, 1969). Furthermore, many studies have observe that in peat deposits, such degradation increases with depth, which drives depth-decay in φ and K (Beckwith et al., 2003b; Quinton et al., 2008). While we observe a range of ρ_b in our samples, both sample populations are normally distributed about a mean value, rather than uniformly distributed along a range of ρ_b values, suggesting that although a range of degradation states was observed, two such states dominate. The data for soil hydraulic and thermal properties are also similarly distributed, and there are only weak trends between ρ_b and most soil properties within organic soils. This suggests that a two-layer characterization of organic soils, rather than a continuum characterization, is representative of the system we observed.

Unlike the organic soil samples we measured, mineral soil data was not normally-distributed. Mineral soil properties varied many times more than did either acrotelm or catotelm soil properties (Figure 3.2). Thus, a single characterization of 'mineral soil' to

describe these wide-ranging deposits across the landscape is likely not appropriate. Our study instead found that mineral soil variability was better explained when divided into respective low-density and high-density populations. The mean properties of low-density and high-density mineral soil datasets varied by as much or more than the mean properties of catotelm and low-density mineral soils did; such variability should be considered in an accurate representation of subsurface properties of these systems.

ρ_b is a good overall predictor of soil properties in our site (Figure 3.4). Many studies have established functional relationships between ρ_b and other soil physical properties, such as φ (Boelter, 1969), K (Assouline, 2006; Boelter, 1969; Branham & Strack, 2014; Jaynes & Tyler, 1984; Morris et al., 2019), k (Becker et al., 1992; Lu et al., 2014; Ochsner et al., 2001; O'Donnell et al., 2009), organic carbon content (Adams, 1973; Boelter, 1969; Huntington et al., 1989; Périé & Ouimet, 2008; Prévost, 2004), and water retention (Ghanbarian-Alavijeh et al., 2010; Vereecken et al., 1990; Rawls et al., 1998). Such trends are desirable to identify because the ρ_b is substantially easier and cheaper to measure, and more widely reported than most hydraulic and thermal properties. However, K, k, organic carbon content, water retention, and φ are all necessary to build a mechanistic understanding of thermal or hydraulic processes.

Usually, ρ_b alone is not enough information to determine other soil hydraulic or thermal properties. For example, the studies above that predict K, k, φ, or water retention often also require an understanding of the grain size distribution of the sample in question. However, our predictive relationships achieve high correlation coefficients (greater than or equal to 0.8) despite lacking grain size information. These high and significant correlation coefficients based simply on bulk density imply that there is little variability in sample grain size distribution, which could further imply that the acrotelm, catotelm, and mineral soils we observe here originated from a common source due to common mechanisms. Previous geomorphology work has identified that the watersheds included in this study endured similar glacial histories, albeit separated by a period of approximately 80,000 years (Hamilton, 1982b). Our findings here suggest that this gap

in time does little to affect the properties of the soil types on either side of the glacial divide.

Our predictive trends were based on soil ρ_b that ranged from 0.01 to 2 g cm^{-3}; however, as mentioned above, acrotelm and catotelm ρ_b are relatively well-constrained and quite low. Thus, within organic soil types, the ρ_b trends we identify are relatively weak, as there is only a small range of ρ_b values upon which to build these trends. It has been well-established that peat ρ_b increases as it degrades and that peat ρ_b is well-correlated with thermal and hydraulic properties (Agus et al., 2011; Beckwith et al., 2003b; Boelter, 1969; Morris et al., 2019; Weiss et al., 1998). It has also been well-established that peat degradation generally increases with depth (Boelter, 1969; Morris et al., 2011). However, the greater depths upon which these ρ_b relationships are built are not found in the sites we investigated (Figure 3.5). The maximum active layer thickness that we measured was 98 cm, and in almost all sites, the catotelm-mineral soil contact occurred well above that depth. Because peat thicknesses observed at our sites is substantially abbreviated in comparison to the thicker peat deposits observed in other, more temperate locations, there is likely less opportunity for a degradation profile to develop. Thus, trends based on ρ_b, which also rely on degradation state, would be relatively weak. Abbreviated peat thicknesses within our observed landscape could also help explain why there was no measurable difference in soil properties on either side of the glacial divide; there was not enough time to develop a profile with differences.

Predictive trends between ρ_b and hydraulic and thermal properties are much stronger within mineral soils. Such trends help explain the wide variability in mineral soil properties. Wide variability arises because our data includes many samples whose bulk density and organic matter concentration sits between catotelm and mineral soil. These ‘in-between’ soils are outliers in both catotelm and mineral soil property distributions, but their properties are well-described by overall, predictive ρ_b relationships.

Differences observed in soil layer thicknesses between landscape classes imply that these classes underwent different geomorphological histories. For example, one of the clearest landscape-driven trends observed was the substantial difference in catotelm thickness between Hillslope zone sites, which had small thicknesses, and Riparian zone sites, which had relatively larger thicknesses. This pattern has been observed in other permafrost-dominated hillslopes. One possible explanation for such increased thicknesses has been attributed to slow, down-slope migration of organic soils aided by frost heave (Shelef et al., 2017). Our simulations show that the water table frequently sits at the contact between catotelm and mineral soil, and field observations have shown that this contact is commonly a location for preferential flow (Hinzman et al., 1996). Therefore, the contact is commonly saturated when the active layer re-freezes in late summer. The freezing of this porewater forces an approximately 10 percent volume expansion, which jacks the organic soil overlying that contact upwards in a well-studied thermo-hydro-mechanical process called frost heave (Bryan, 1946). This continual mechanical lift of organic soil reduces cohesion at that contact, making the overlying organic soil free to slide, slowly, downhill.

Another clear stratigraphic pattern emerged between microtopographic highs and lows: acrotelm made up a larger share of the total active layer in local highs, and catotelm made up a larger share of the total active layer in local lows. Previous work has identified this, and has also found that local lows are more saturated than local highs (Chapter Two; Quinton et al., 2000b). These two concurrent findings agree well with the traditionally-accepted conceptual model of permafrost, which states that acrotelm develops above the long-term average water table, and catotelm develops below that depth (Morris et al., 2011).

3.6 Conclusions

Soils in the active layer above continuous permafrost in the North Slope of Alaska exhibit broadly similar hydraulic and thermal properties across wide areas. There are three laterally continuous soil layer categories found ubiquitously across the landscape.

Acrotelm soils are the most organic, porous and permeable, the least thermally conductive, and retain less water than catotelm and mineral soil. Mineral soil is the least organic, porous and permeable, the most thermally conductive, and retains the most water. Catotelm soils fall in between. The composition and properties of these soil types are largely unique, but some overlap occurs between catotelm and mineral soil composition and properties in specific landscape locations.

The stratigraphy of these three unique soil types is broadly predictable based on the land surface gradient, vegetation cover type, and microtopographic position. . Hillslope zone soils have thin total organic layers (acrotelm and catotelm combined) in comparison to Riparian zone soils. Microtopographic highs have relatively thicker acrotelms and thinner catotelms than microtopographic lows. Woody shrubs tend to have thick acrotelms with thin catotelms, and sedge locations, both in the hillslope as water tracks and in the riparian zone, exhibit the opposite trend.

Soil bulk density is sufficient for predicting porosity, saturated hydraulic conductivity, dry thermal conductivity, organic mass lost on ignition, and soil retention curve coefficients. The lack of predictability of these factors has been a major gap for accurately describing and forecasting the hydrologic, thermal, and biogeochemical state of supra-permafrost soils. Our extensive measurements allow for data-driven predictions of soil hydraulic, thermal, and compositional profiles across the Alaskan North Slope Hillslope.

3.7 FIGURES FOR CHAPTER 3

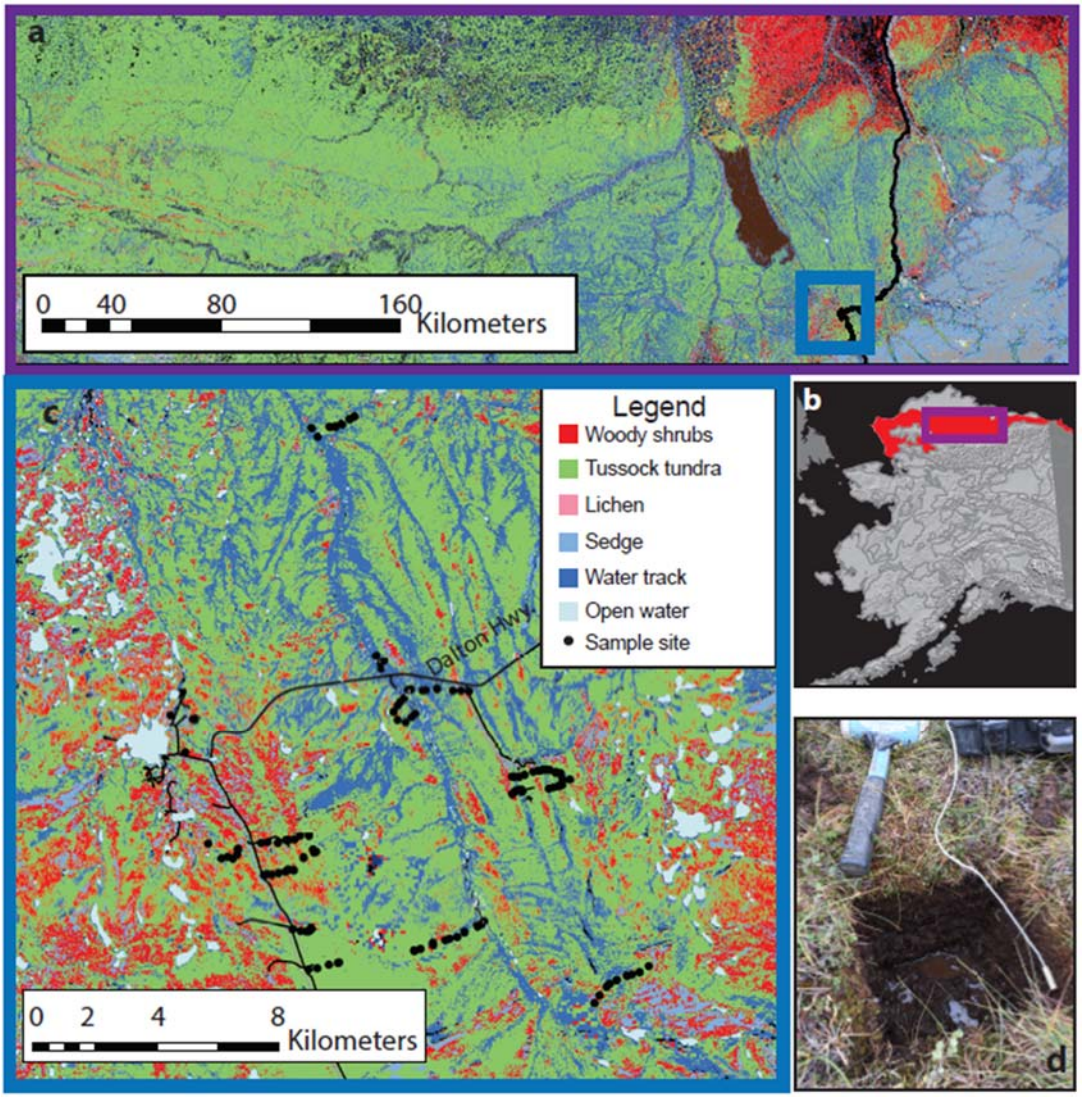

Figure 3.1: Site description and context of study within Alaska. Panel a) North Slope Science Initiative (NSSI) Landcover Data Map for a large section of the North Slope Foothills Ecoregion highlighted in red in Panel b). Panel c) Extent of the study site used in this work. Stars represent soil sampling locations, and the map is underlain by the NSSI Landcover Data Map. Panel d) An example soil pit from one site, with a standard kitchen breadknife for scale.

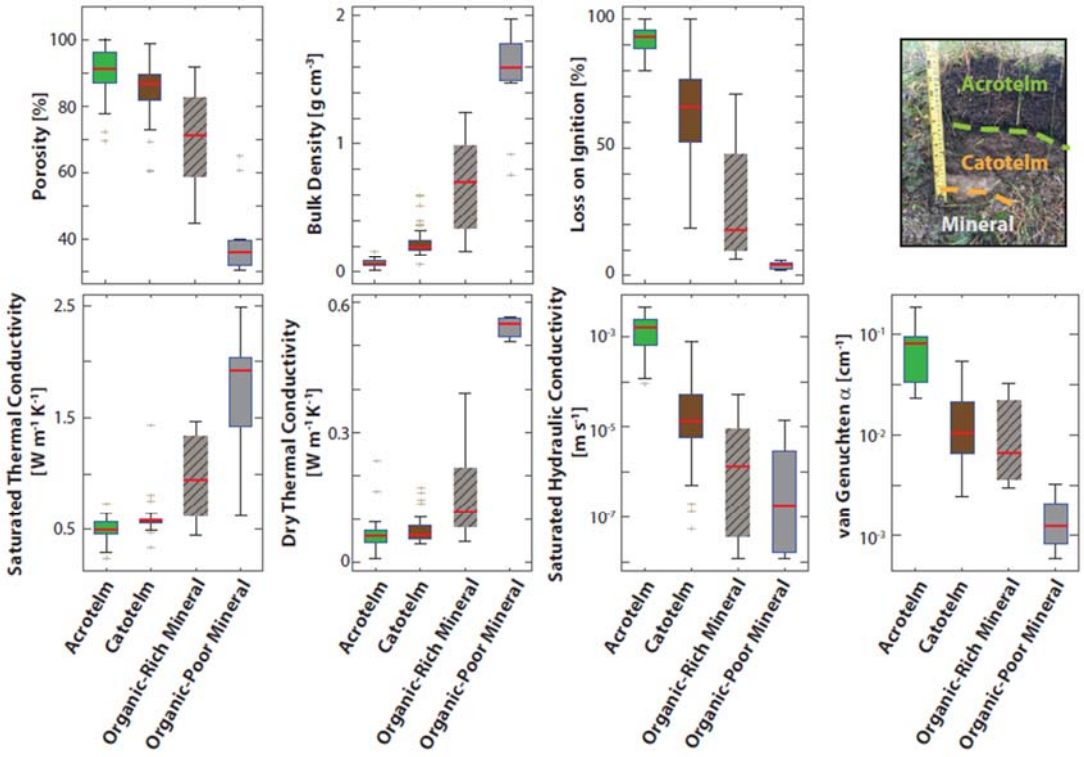

Figure 3.2: Distributions of measured soil compositional properties (top row) and thermal and hydraulic properties (bottom row) for each of the soil types we observed, across all landscape classes. Red lines represent the population median, and shaded boxes describe the interquartile range of each property.

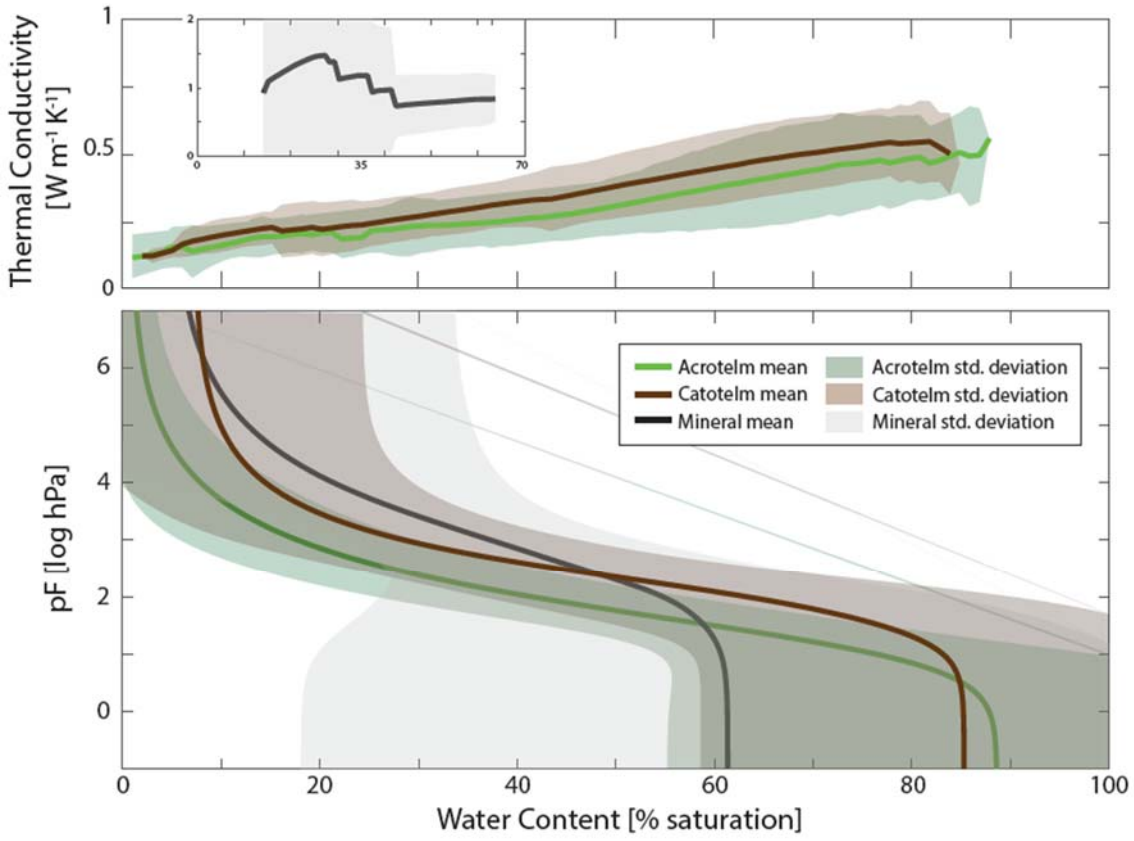

Figure 3.3: Measured soil thermal conductivity (top panel) and soil water suction pressure (bottom panel) as a function of water content from HYPROP evaporation experiments. The solid green lines represent the average thermal conductivity and soil water suction of all analyzed acrotelm soils at a given water content, respectively; the solid blue lines represent average thermal conductivity and soil water suction of all analyzed catotelm samples; and the solid black lines represent average thermal conductivity and soil water suction of all analyzed mineral soil samples. Surrounding shaded areas represent +/- 2 standard deviations from the mean in each plot. Averages of thermal conductivity and soil water suction were only calculated at water contents achieved by all soils in a given group.

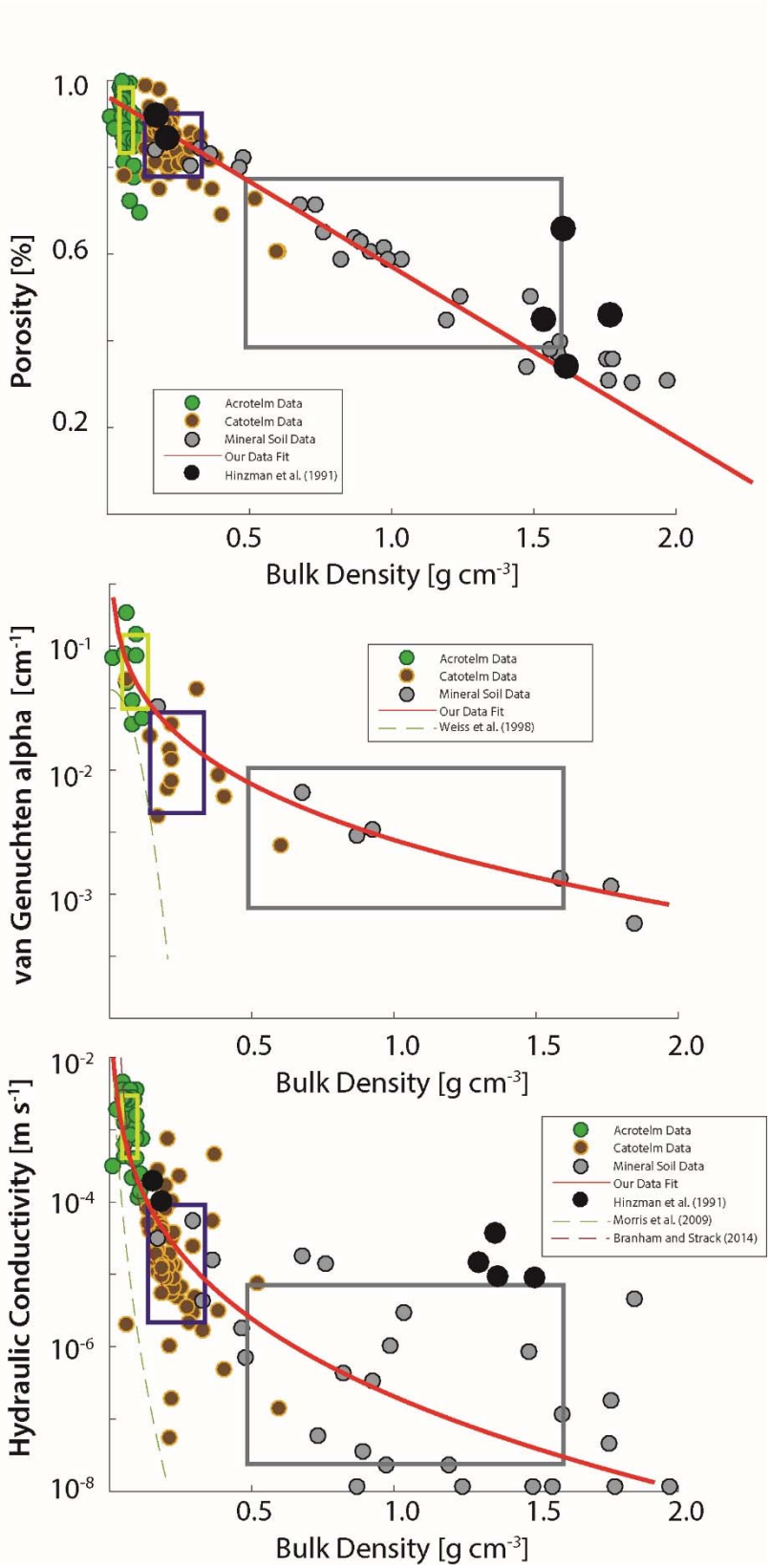
Porosity [%]
1.0
0.6
0.2
0.5
1.0
1.5
2.0
Bulk Density [g cm-3]
Acrotelm Data
Catotelm Data
Mineral Soil Data
Our Data Fit
Hinzman et al. (1991)
van Genuchten alpha [cm-1]
10-1
10-2
10-3
Bulk Density [g cm-3]
Acrotelm Data
Catotelm Data
Mineral Soil Data
Our Data Fit
Weiss et al. (1998)
Hydraulic Conductivity [m s-1]
10-2
10-4
10-6
10-8
Bulk Density [g cm-3]
Acrotelm Data
Catotelm Data
Mineral Soil Data
Our Data Fit
Hinzman et al. (1991)
Morris et al. (2009)
Branham and Strack (2014)

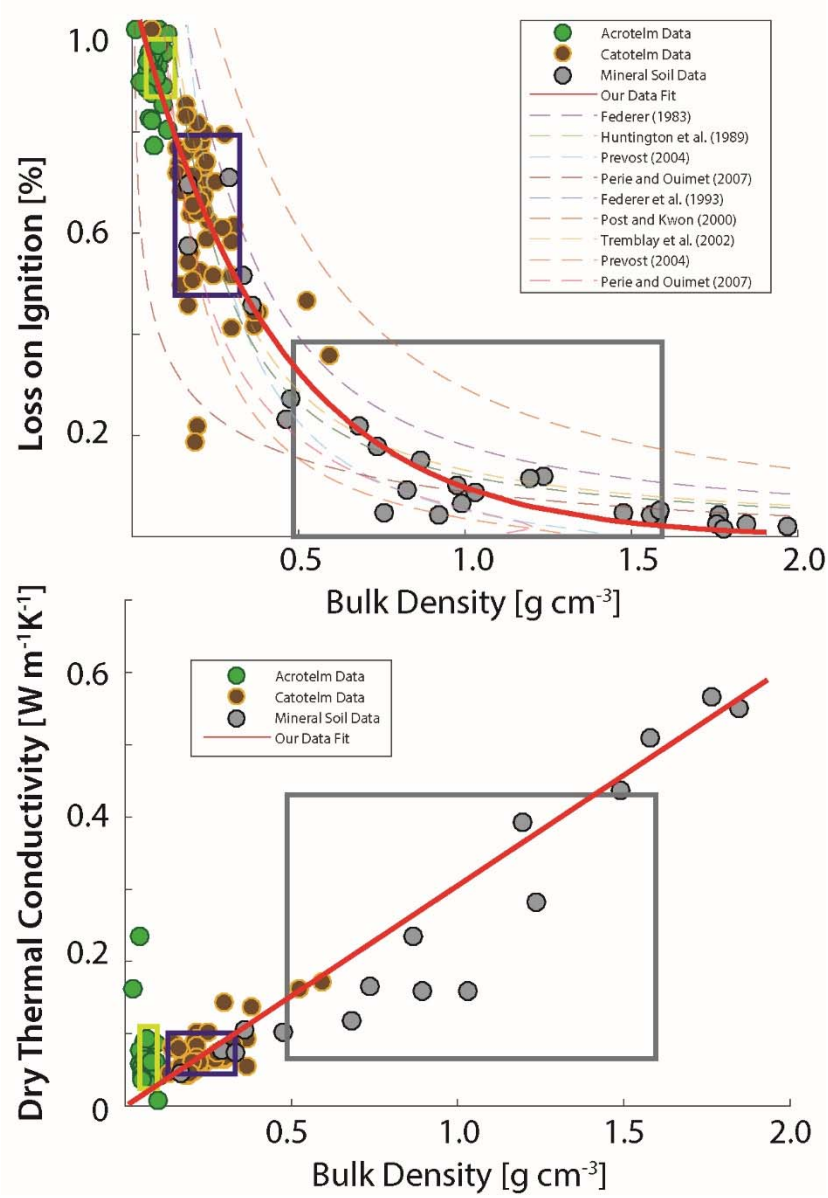

Figure 3.4: Statistically-significant trends in in soil porosity, loss-on-ignition percentage, saturated hydraulic conductivity, van Genuchten shape parameter α, and dry thermal conductivity based on bulk density. Comparable literature values are presented where available. Equations representing these predictive models are presented in Table B6.

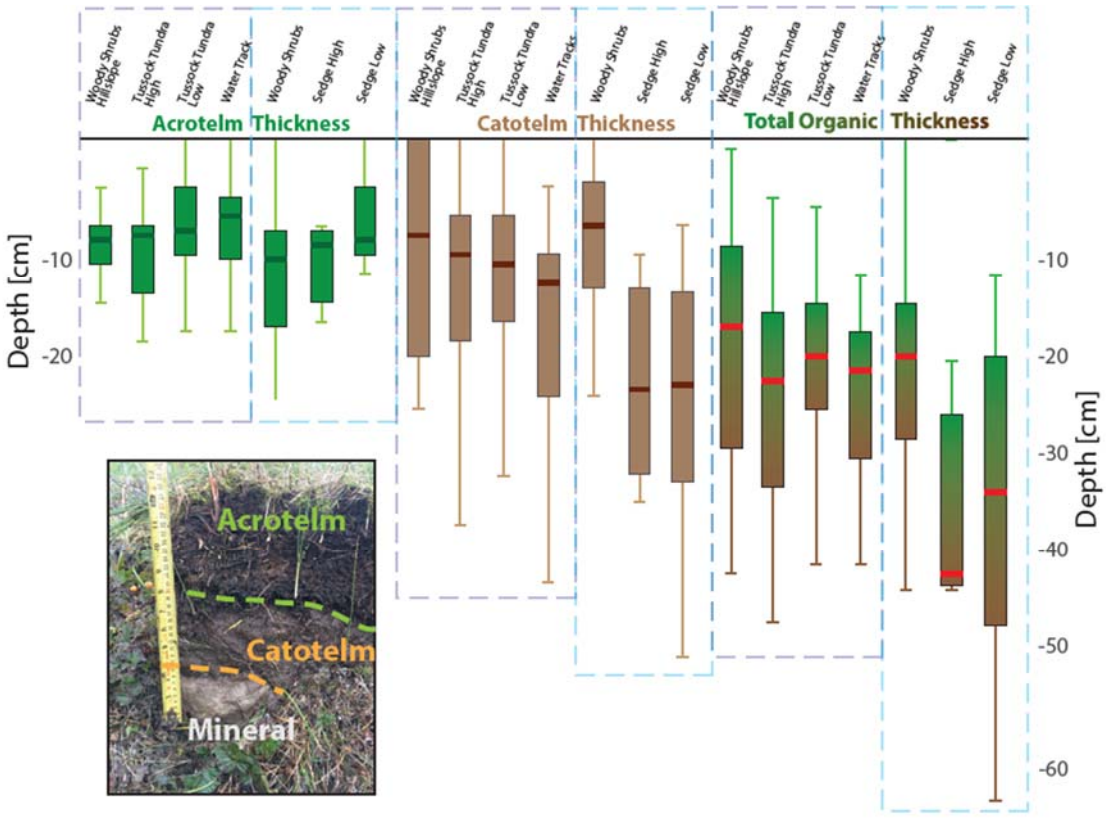

Figure 3.5: Distributions of the measured soil stratigraphies within each of the landscape classes we defined. Thick green and white lines represent the median acrotelm and catotelm soil contact depths, respectively, and dark green and brown shaded boxes represent the interquartile range of those contact depths. Plots found in the Hillslope landscape zone are on the left hand side, and plots found in the Riparian landscape zone are on the right hand side.

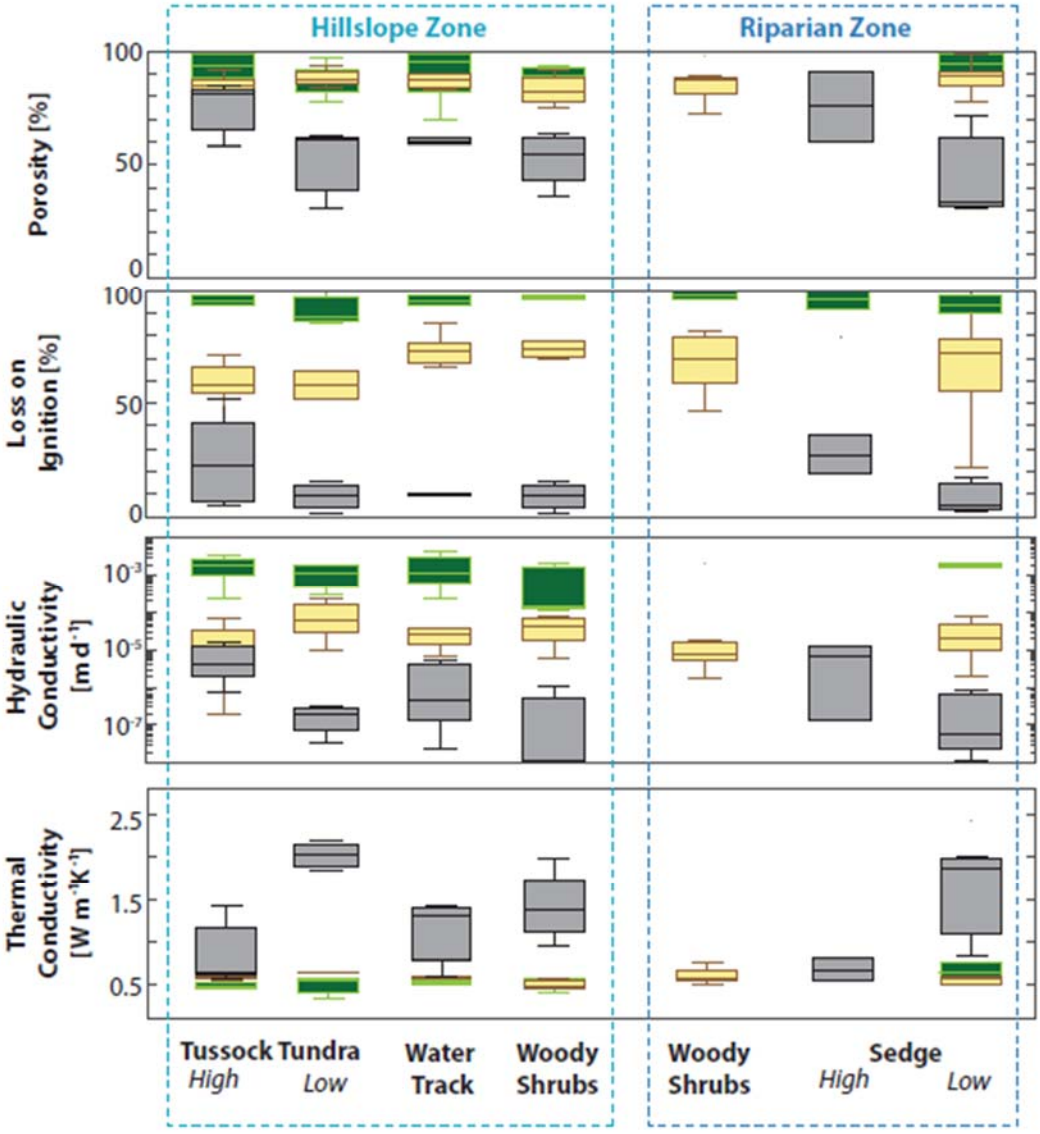

Figure 3.6: Observed soil properties, grouped by our observed stratigraphy. Green boxes represent acrotelm soils, brown boxes represent catotelm soils, and grey boxes represent mineral soils. Central line of each box represents the median of the data, and box edges represent the interquartile range. Populations with fewer than 5 samples were excluded from analysis.

Chapter 4: Observed soil stratigraphic variability controls arctic thermal hydrology

KEY POINTS

- I investigated how groundwater flow rates, soil moisture storage, and thaw depth vary across commonly-observed soil stratigraphies, hydraulic properties, and thermal properties using a fully-coupled, variably-saturated thermal hydrology model informed with field-observed soil properties.
- The magnitude and rate of active layer development, and the amount of water stored in the soil versus released through lateral flows, is significantly influenced by stratigraphic variability.
- Stratigraphic variability, which is spatially predictable based on landscape characteristics, should be considered in future models designed to predict thermally-mediated arctic hydrologic processes.

4.1 ABSTRACT

Landscapes underlain by continuous permafrost exhibit predictable soil stratigraphy that create substantial variability in soil hydraulic and thermal properties profiles. However, it is currently unknown how such variability affects active layer development, lateral groundwater flows, and soil moisture storage. Here we identify those effects by comparing the thawed zone thickness, lateral groundwater flow rates, and total soil moisture storage across a suite of fully-coupled thermal hydrology hillslope models. We varied the soil hydraulic and thermal properties of these hillslope models based on the profiles commonly observed throughout the North Slope Foothills in Northern Alaska, and kept model geometries, initial conditions, and boundary conditions constant. Simulations were run for one year using average meteorological conditions.

Thaw dynamics are mutually governed by soil physical properties and water content. The two high-porosity, low-thermal-conductivity organic soil layers overall insulate the deeper mineral soil, and the variability in the thicknesses of the organic layers observed in the field significantly affects the active layer daily thaw rate, maximum depth, and daily freeze-up rate. However, differences in water retention between easily-drained upper organic 'acrotelm' and less-easily-drained lower organic 'catotelm' cause acrotelms to be relatively dry throughout the summer and thus insulate well, and catotelms to retain more water and insulate less well.

Soil moisture storage and lateral groundwater flows are also dually controlled by soil physical properties and soil water inputs. Higher-porosity organic soils are capable of storing more soil moisture within thicker unsaturated zones; thus, more soil moisture storage was observed in hillslopes with thicker organic layers. However, organic soils also require more water to raise the water table because there is more void space to fill. Because the average meteorological data used to force our models rarely provided sufficient precipitation to induce saturation in these high-porosity organic soil layers, the saturated zone was relegated to the lowest-permeability organic soils, and lateral groundwater flows were mostly negligible. The few instances in which lateral groundwater flows were not negligible occurred in hillslopes with the thinnest organic

layers, where the comparatively little void space allowed the organic soil layers to saturate.

These findings highlight the importance that field-variable soil stratigraphy exerts on hydrologic processes. However, it also highlights the important compounding role that soil moisture plays on these processes. To accurately predict future arctic thermal hydrologic metrics such as thaw, lateral groundwater flow, and soil moisture storage, both soil properties profiles and water inputs must be well-characterized.

4.2 INTRODUCTION

The processes that govern the thaw, groundwater flow, and soil moisture storage within the seasonally-thawed 'active layer' above continuous permafrost are poorly constrained. While the physical laws governing heat and water fluxes through variably-saturated soil are known, it is unclear which of the many parameters that control these fluxes dominate. Particularly, it is unclear if variability in soil hydraulic and thermal properties commonly observed across continuous permafrost landscapes can exert enough of an impact on heat and water fluxes that thaw, groundwater flow, and soil moisture storage will also significantly vary across space.

Two major reasons have inhibited our understanding of spatial variability in thaw, groundwater flow, and soil moisture storage across the landscape: a lack of capability to properly simulate heat and water fluxes above the water table, and a lack of real-world data needed to inform these models (Walvoord & Kurylyk, 2016). Simulation capability is lacking because the heat and water fluxes occurring above the water table have been ignored or oversimplified. It is known that heat flow and water flow are tightly coupled in permafrost soils: the introduction or removal of water from soil alters the thermal properties of that soil, which affects its phase state (i.e., whether the soil porewater is frozen or not) and in turn governs the availability of liquid porewater that is able to flow.

However, the numerical methods needed to simultaneously solve the nonlinear unsaturated phase change and groundwater flow equations have been, until recently, computationally prohibitive (Frampton et al., 2011; Kurylyk & Watanabe, 2013). Studies have avoided employing a full coupling between heat and water flow through a variety of simplification methods. One method, commonly used for landscape-scale investigations, imposes one-dimensional heat conduction models to thaw or freeze soil porewater. These models may be analytical solutions, rooted in the Stefan equation (i.e., Hayashi et al., 2007; Kurylyk & Hayashi, 2016; Lawrence et al., 2015; Riseborough et al., 2008; Woo et al., 2008), or numeric solutions (i.e., Gouttevin et al., 2012; Zhang et al., 2013). Another method, employed by many studies that investigate lateral groundwater flows, simplify the unsaturated soil and overlying surface system through empirical equations

that relate soil temperature and saturation to surface conditions (i.e., Bense et al., 2012; Evans & Ge, 2017; McKenzie & Voss, 2013; Zhang et al., 2013), or couple a surface and unsaturated zone thermal model to a saturated subsurface model (Kurylyk et al., 2016).

These simplified approaches are unable to mechanistically capture how soil hydraulic and thermal properties act in concert to affect thaw, groundwater flow, and soil moisture storage. For example, failure to include this coupling can lead to erroneous estimates of deeper-surface soil temperature, and subsequently active layer thickness, because such approaches would fail to represent how the potentially substantial insulating effects of the organic soil layers vary with moisture content (Koven et al., 2009; Lawrence & Slater, 2008), which has been shown empirically to exert a substantial effect on active layer thickness (Quinton et al., 2000a). Subsequently, it is impossible to understand hydrologic processes within the active layer, such as groundwater flow and soil moisture storage, if the active layer itself is not mechanistically represented. Simplification of coupled thermal hydrology makes it impossible to mechanistically understand the thermal hydrologic processes occurring in a variably-saturated active layer.

A second major reason why active layer thermal hydrology is poorly understood is because there are scant measurements of the spatial distribution of permafrost thermal and hydraulic properties in the literature (Walvoord & Kurylyk, 2016). Active layer soils in continuous permafrost environments are traditionally conceptualized as having a single organic soil layer comprising of dead and decaying plant organic matter atop a layer of glacially-derived mineral soil (Hinzman et al., 1991; Lawrence & Slater, 2005; Tarnocai et al., 2009). These soil types have diametrically different porosities, hydraulic and thermal conductivities, and water retention capacities (Hinzman et al., 1991; Neilson et al., 2018; Chapter Three), and the contact between them represents a significant discontinuity in the profiles of soil hydraulic and thermal properties. Furthermore, there is often a clear transition between young, recently-dead organic soil (‘acrotelm’) and organic soil with substantially more substantial decay (‘catotelm’) (Morris et al., 2015). The formational difference between these two soil layers causes another stark

stratigraphy discontinuity within the organic soils themselves, from more permeable soils with a low water retention capability above to significantly less permeable soils with a high water retention capability below (Chapter Two; Chapter Three; Woo & Marsh, 2005). As stated above, organic soil thickness can be directly related to seasonal active layer development (Jafarov & Schaefer, 2015; Lawrence et al., 2008); however, it is unclear if that influence is important in reality, both because a two-layer organic soil structure is rarely considered, and because we only recently have begun to understand how these two organic soil layers are distributed across continuous permafrost landscapes (Chapter Three). We therefore do not know how the regular, predictable variability in acrotelm and catotelm thickness can influence active layer thermal hydrologic processes.

Advancements in both simulation capability and knowledge of soil properties now allow for answers to these and other thermal hydrology questions in permafrost environments. Recent advances in the simulation of thermal hydrology provide us with a completely mechanistic numeric representation of unsaturated soil heat and water flow in soils undergoing freeze-thaw (Atchley et al., 2015; Endrizzi et al., 2014; Frampton & Destouni, 2015; Painter et al., 2016). Such models can better answer questions and unknowns about important mechanisms governing active-layer dynamics and function. Recent advances in understanding the spatial distribution of soil layer thicknesses, hydraulic properties, and thermal properties at the landscape scale (Chapter Three) provide the ability to determine if the variability in thermal hydrology processes incurred by stratigraphy is significant.

This study leverages the above advancements in simulation capability and soil properties knowledge to investigate how observed variability in soil hydraulic and thermal properties profiles affects active layer development, soil moisture storage, and lateral groundwater flow during a fabricated year built from decadally-averaged meteorological conditions. This investigation is performed by simulating water and energy fluxes using the Advanced Terrestrial Simulator ("ATS", Painter et al., 2016), the only currently available variably-saturated, fully-coupled energy and water balance numerical model. We simulated water and energy fluxes through a suite of 2D hillslopes

parameterized with commonly-observed soil hydraulic and thermal properties profiles found in the Arctic Foothills region of the North Slope of Alaska. The experimental design and tools employed for this study allows us to answer questions necessary to build a more complete picture of arctic thermal hydrologic processes throughout the year: *1)* How does the thawed zone thickness, lateral groundwater flow rate, and soil moisture storage within a hillslope active layer respond to seasonality in atmospheric forcings; *2)* How and why does soil stratigraphy affect those thaw and freeze-up responses; and *3)* How and why does soil stratigraphy affect those flow and storage responses? Such findings identify the sensitivity of thermal hydrology predictions to field-scale variability in properties, which help constrains currently-vast uncertainty in arctic thermal hydrologic processes.

4.3 METHODS

4.3.1 Model physics

The numerical experiments in this study were performed using the Arctic Terrestrial Simulator (ATS, Painter et al. (2016)). ATS represents a particular construction of the multiphysics software Amanzi (Coon et al., 2016) designed for variably-saturated arctic thermal hydrology (Jan et al., 2018). The model includes four 'process kernels' (PKs) that each represent a physical process necessary to understand heat and water flow through the surface above the active layer and the active layer itself. A description of the governing equations used in the model is below. All the variable symbols are explained, and prescribed values are provided, in the Table of Symbols. For clarity, curly brackets are used to denote functional relationships, and parentheses are used to denote multiplication and order of operations. The descriptions of surface and subsurface thermal hydrology provided below are also presented in greater detail in Painter et al. (2016), and the descriptions of the surface energy balance are provided in greater detail in Atchley et al. (2015).

4.3.1.1 Subsurface coupled water and energy balance including phase change

In order to simulate the total conservation of mass and heat in a variably-saturated soil, all phases present in a variably-saturated medium (ice, liquid, and air) must be represented. The conservation of water mass in a transient, variably-saturated soil is governed by the Richards equation, which is expanded here to account for all these phases and expressed in molar form:

$$\frac{\partial}{\partial t}\left[\varphi\left(\sum_{P=l,i,g}\omega_P\eta_P s_P\right)\right] = -\nabla\cdot[\eta_l V_l] + q_W \qquad \text{[Eq. 1]}$$

where φ is porosity [-], P represents substance phase (with l as liquid phase, i as ice phase, and g as gas phase), ω is mole fraction [-], η is molar density [mol m^{-3}], s is saturation percent [-], and q_w is a fluid source [mol m^{-3} s^{-1}]. Note that $s_g + s_l + s_i = 1$, not φ. Because both ice and liquid water are assumed to be pure-component phases (i.e., both ice-phase air and dissolved air are ignored), $\omega_l = 1$ and $\omega_i = 1$. ω_g is defined as:

$$\omega_g = \frac{e_{sat}\{T\}}{p_g} \qquad \text{[Eq. 2]}$$

where $e_{sat}\{T\}$ is the saturation vapor pressure at a given temperature T [Pa], calculated from the Clausius-Clapeyron Equation, and p_g is the gas partial pressure, assumed to be 101325 Pa.

ATS assumes that the change of mass is governed only by the movement of liquid phase water (i.e., no vapor or ice transport). The Darcy velocity V_l [m s^{-1}] is therefore defined through an expression of Darcy's Law:

$$V_l = -\frac{k_{r,l}k}{\mu_l\{T\}}(\nabla p_l + \rho_l\{T\}g\hat{z}) \text{ [Eq. 3]}$$

where $k_{r,l}$ is the relative permeability [-], k is intrinsic permeability [m^2], $\mu_l\{T\}$ is liquid water dynamic viscosity [Pa s], p_l is pore pressure [Pa], $\rho_l\{T\}$ is liquid water mass density [kg m^{-3}], g is acceleration due to gravity [m s^{-2}], and $\hat{z}$ is the z dimension unit vector [m].

The water mass balance equation is tightly coupled to the energy balance equation for unsaturated soil, which is constructed assuming local thermal equilibrium between all phases:

$$\frac{\partial}{\partial t}\left[\varphi \sum_{p=l,g,i}\left(\eta_p s_p u_p\right) + (1-\varphi)C_{v,soil}T\right] = -\nabla \cdot (\eta_l h_l V_l) + \nabla \cdot \left(\kappa_{eff}\nabla T\right) + Q_{g-gw} + Q_{Ess} \quad \text{[Eq. 4]}$$

where u_l is the specific internal energy of liquid water [J mol^{-1}], u_i is the specific internal energy of ice [J m^{-3}], u_g is the specific internal energy of gas [J mol^{-1}], $C_{v,soil}$ is the volumetric heat capacity of the soil matrix [J m^{-3} K^{-1}], h_l is the specific enthalpy of liquid water [J mol^{-1}], κ_{eff} is effective thermal conductivity [W m^{-1} K^{-1}], Q_{g-gw} is the convected heat source from the ground [W m^{-3}], and Q_{Ess} is the conducted heat source from the ground [W m^{-3}].

Unlike in the water mass balance, conduction and convection of heat from multiple phases are considered in the total energy balance. The dependent variables in the system of equations created by Eq. 1, 3, and 4 are p and T. Tight couplings exist between the thermal and water mass balances due to changing saturation indices s and fluid advection V_l. Tight couplings also exist between the surface and subsurface systems: the top thermal and hydraulic boundary conditions in the subsurface component of the model are assigned as flux boundaries informed by the solution of the ground surface component of the model (see Section 2.1.2, below).

The inclusion of phase change into thermal hydrology models introduces additional tight couplings between the water and energy balances. Freeze/thaw in porous media is governed by the capillary forces between the phases present: ice, water, and air (Fisher, 1923). Tensile capillary forces between air, ice, and water can depress the freezing point temperature (T_f) in porous media, because water molecules that are more tightly-adhered to the soil matrix due to capillary forces will require more energy to change phase (Dall'Amico, 2010). Thus, the partitioning between s_l, s_i, and s_g is a function of both temperature and pressure. To account for this additional coupling, ATS

employs an explicit adaptation of the Clapeyron equation which describes the relationship between temperature, capillary pressure, and freezing point depression in variably-saturated soils (Painter & Karra, 2014):

$$s_l = \begin{cases} s_*\{-\beta\rho_l L_f \vartheta\}, & \vartheta < \vartheta_f \\ s_*\{p_g - p_l\}, & \vartheta \geq \vartheta_f \end{cases} \qquad \text{[Eq. 5]}$$

$$\vartheta_f = -\frac{1}{\beta L_f \rho_l} p_*\{1 - s_g\} \qquad \text{[Eq. 6]}$$

$$s_i = 1 - \frac{s_l}{s_*\{p_g - p_l\}} \qquad \text{[Eq. 7]}$$

where L_f is the latent heat of fusion of water [J kg^{-1}], ϑ [-] is a dimensionless temperature $(T - T_0)/T_0$, p_g is the capillary pressure of the gas phase [Pa], and p_l is the capillary pressure of the liquid phase [Pa]. β [-] is a coefficient related to soil quality: $\beta = 1$ for colloidal soils (i.e., granular soils with substantial grain-to-grain contact), and $\beta = \gamma_{i-l}/\gamma_{l-g}$ for noncolloidal soils (i.e., soils with substantial grain-water-grain contacts), where γ_{i-l} is the surface tension between ice and liquid phases, and γ_{l-g} is the surface tension between liquid and gas phases (Koopmans & Miller, 1966).

Any coupling between soil capillary pressures and saturation states requires a constitutive relationship between pressure and saturation; in hydrology, these relationships are most commonly reported as soil moisture retention curves. Soil moisture retention curves are unique for individual soils, and many models have been developed to empirically describe the soil moisture retention curve as a function of soil properties. ATS employs the van Genuchten soil moisture retention model (van Genuchten, 1980) both because it is widely accepted in literature and produces a continuous, differentiable soil moisture retention curve. It is presented here in both its forms (saturation as a function of pressure and pressure as a function of saturation):

$$s_*\{p\} = s_r + (1 - s_r)[1 + (\alpha p)^n]^m \qquad \text{[Eq. 8]}$$

$$p_*\{s\} = \frac{1}{\alpha}\left[\left(\frac{s - s_r}{1 - s_r}\right)^{-1/m} - 1\right]^{1/n} \qquad \text{[Eq. 9]}$$

where $m = 1 - 1/n$, and α [m^{-1}] , n [-], and s_r [-] are all either experimentally derived or assumed parameters based on soil texture. In current state-of-the-art thermal hydrology models, it is assumed that the capillary forces that adhere porewater to grains in a drying, unsaturated soil are analogous to capillary forces that adhere liquid porewater to grains as an unsaturated soil freezes (Kurylyk & Watanabe, 2013). Thus, the soil moisture retention curve, which describes how capillary forces affect the drying of a soil, is assumed to be analogous to the 'soil freezing curve', which describes how capillary forces affect the freezing of the soil (Koopmans & Miller, 1966).

The freezing-as-drying approximation also is employed in determining the relative permeability k_r of a variably-saturated porous medium. ATS employs a constitutive relation that combines the van Genuchten and Mualem models (van Genuchten, 1980):

$$k_r = (s_l)^{1/2}[1 - \left(1 - (s_l)^{\frac{1}{m}}\right)^m]^2 \quad \text{[Eq. 10]}$$

ATS also assumes that gas is highly mobile and its concentration is linearly related to the saturation content s_g.

ATS calculates the effective thermal conductivity of each model cell κ_{eff} based on a ratio of saturated, dry, frozen, and unfrozen phases:

$$\kappa_{eff} = Ke_f * \kappa_{sat} + Ke_u * \kappa_{sat} + (1 - Ke_f - Ke_u \kappa_{dry}) \quad \text{[Eq. 11]}$$

where κ_{sat} is the thermal conductivity of the saturated soil [W m^{-1} K^{-1}], κ_{dry} is the thermal conductivity of the dry soil [W m^{-1} K^{-1}], and the Kersten number Ke is a ratio between partially saturated to fully saturated thermal conductivity [-], calculated as:

$$Ke_u = {s_l}^{\tau_u} \quad \text{[Eq. 12]}$$

$$Ke_f = {s_i}^{\tau_f} \quad \text{[Eq. 13]}$$

where τ is an empirical fitting parameter that varies for the frozen and unfrozen states [-] (Karra et al., 2014).

4.3.1.2 Ground surface coupled water and energy balance including phase change

ATS employs a system of energy balance equations to allow for 'icy overland flow':

$$\frac{\partial}{\partial t}[(\chi\eta_i + (1-\chi)\eta_i)d_w] + \nabla\cdot(\chi\eta_l d_w U_w) = q_{rain} + q_{melt} - q_{evap} - q_{g-gw} \text{[Eq. 14]}$$

$$U_w = -\frac{(\chi d_w)^{\frac{2}{3}}}{N(\|\nabla z_s\|+\delta)^{\frac{1}{2}}}\nabla(z_s + d_w) \quad \text{[Eq. 15]}$$

$$\frac{\partial}{\partial t}[(\chi\eta_l u_l + (1-\chi)\eta_i u_i)d_w] + \nabla\cdot(h_l\chi\eta_l d_w U_w) - \nabla\cdot[(\chi\kappa_l + (1-\chi)\kappa_i)d_w\nabla T_s] =$$
$$Q_{s-g} + Q_{rain} + Q_{melt} - Q_{evap} - Q_{g-gw} - Q_{Ess} \quad \text{[Eq. 16]}$$

where h_l is the specific enthalpy of liquid water [J mol^{-1}], N is the Manning's Roughness coefficient [s m$^{-1/3}$], δ is a numerical surface velocity fitting parameter [-], U_w is the lateral surface water flow [m s^{-1}], q represents mass fluxes of water [mol s^{-1} m^{-2}] and Q represents energy fluxes to the surface [W m^{-2}]. The energy balance of the surface cell (Eq. 16) depends on both the mass and the energy fluxes of water sources from above and below, because the total heat flux Q is the product of the mass flux in moles, q, and the enthalpy of the system h, which depends on temperature.

The mass balance component solves for ponded water depth (d_w) using a hybrid of the kinematic and diffusion wave approximations (Eq. 14-15). The hybrid form both approximates the diffusion wave equation on sloping ground and provides physically reasonable results on flat ground. The fluid source term that couples surface water flow to groundwater flow, q_{g-gw}, is determined by employing the mass-conservative boundary condition strategy described in Kollet & Maxwell (2006). This approach uses the surface flow equations (Eq. 14-15) as flux boundary conditions for the subsurface flow equations.

The energy balance component (Eq. 16) includes the advection of heat due to lateral surface water flow U_w. It also includes phase change through the inclusion of a liquid-ice partitioning factor χ. This factor is represented as smoothed step function with

a prescribed width τ [K] that empirically assigns liquid and ice fractions based solely on soil temperature, T_s (Table C1). This approximation is appropriate for shallow water depths (i.e., a well-mixed water column with no substantial vertical stratification in surface water temperature distributions) but fails in deeper water columns as it does not allow for depth-variable freezing. In this system of equations, water mass is represented in molar form, as this allows for the volumetric expansion of water as it freezes from liquid to ice.

4.3.1.3 Surface energy balance, including snowmelt

The surface energy balance employed in ATS, in a general form, is:

$$Q_{s-g} = Q_{sw}^{in} + Q_{lw}^{in} + Q_{lw}^{out}\{T\} + Q_h\{T\} + Q_e\{T\} \quad \text{[Eq. 17]}$$

$$Q_{s-g} = Q_{Ess} + Q_c \quad \text{[Eq. 18]}$$

The right-hand side of this energy balance represents incoming shortwave and longwave radiation $Q_{sw}^{in} + Q_{lw}^{in}$ (provided by forcing data) and outgoing longwave radiation $Q_{lw}^{out}\{T\}$, sensible heat flux $Q_h\{T\}$, and latent heat flux $Q_e\{T\}$ (calculated based on temperature, see below). All energy fluxes presented in Equations 17 and 18 are in [W m^{-2}].

The left-hand side of this energy balance, Q_{s-g}, represents heat transferred from the surface to the ground. Q_{s-g} is the sum of bare-ground conductive heat flux (Q_{Ess}) and snowpack conductive heat flux (Q_c) (Eq. 18). ATS assumes that if a snowpack is present, it is in equilibrium with all energy fluxes going into and out of the snowpack; therefore, the term representing residual heat conducted from the surface to the ground, Q_{Ess}, equals zero. This does not mean that heat transfer between the surface and the ground cannot occur, but such heat transfer is controlled by the conduction of heat through the snowpack Q_c, which ATS directly calculates based on the thickness, density, and temperature of the snowpack (see below). Conversely, if a snowpack is absent, conductive snowpack heat transfer does not occur, so $Q_c = 0$. Without a snowpack, no

thermal equilibrium can be assumed, and Q_{Ess} is calculated as the residual of the right-hand-side energy balance terms. Snowpack conduction Q_c is important for the accurate representation of arctic thermal hydrology, as it can be a controlling factor in ground temperature and active layer development (i.e., Abolt et al., 2018; Atchley et al., 2016; Woo & Marsh, 2005).

The radiative components of the surface energy balance (incoming Q_{sw} and Q_{lw}) are supplied as forcing data. The initial Q_{sw} supplied by the user is corrected to account for ground surface albedo a [-] (Table C1). Given that a changes with surface temperature due to the shifting exposure of snow, ponded water, or bare ground, a is assigned based on the current surface conditions.

Outgoing longwave radiation Q_{lw}^{out} is calculated based on snow or surface temperature T_s:

$$Q_{lw}^{out} = -\varepsilon_s \epsilon T_s^4 \qquad \text{[Eq. 19]}$$

where ε_s, surface emissivity [-], varies with ground cover as a does (Table C1), and ϵ is the Stefan-Boltzman constant [W m^{-2} K^{-4}].

The non-radiative components (latent heat Q_e, sensible heat Q_h, and conduction Q_c or Q_{gf}) are dependent on soil or snow temperature T_s. Q_h is expressed as:

$$Q_h = \rho_g C_p D_{eh} \xi (T_a - T_s) \qquad \text{[Eq. 20]}$$

where ρ_g is the mass density of gas [kg m^{-3}] and C_p is the specific heat of water [J kg^{-1} K^{-1}]. T_a, air temperature, is provided as forcing data. D_{eh}, the turbulent exchange of latent and sensible heat, is:

$$D_{eh} = \frac{0.1681 U_s}{(\ln(\frac{z_r}{z_0}))^2} \qquad \text{[Eq. 21]}$$

where wind speed U_s [m s^{-1}] is provided as forcing data, z_r is the reference height of the wind speed measurement [m], and z_0 is a prescribed roughness length [L]. The stability function ξ from Equation 20 is:

$$\xi = \begin{cases} \frac{1}{1+10R_i}, & T_s \leq T_a \\ 1 - 10R_i, & T_s > T_a \end{cases} \quad \text{[Eq. 22]}$$

which itself depends on the atmospheric stability parameter R_i:

$$R_i = \frac{gz_r(T_a - T_s)}{T_a {U_s}^2} \quad \text{[Eq. 23]}$$

where g is the acceleration due to gravity [m s^{-2}].

Latent heat Q_e is calculated slightly differently depending on if there is a snowpack present or absent. The porosity of the top subsurface cell is used when no snowpack exists, whereas with a snowpack, there is no subsurface influence:

$$Q_e = \begin{cases} \rho_g \lambda_s E_r \left(0.622 \frac{e_a - e_s}{p_{atm}}\right), & z_s \geq 2\ cm \\ \varphi_{z=0} \rho_g \lambda_e E_r \left(0.622 \frac{e_a - e_s}{p_{atm}}\right), & z_s < 2\ cm \end{cases} \quad \text{[Eq. 24]}$$

where λ_s is the latent heat of sublimation for snow [J kg^{-1}], e_a and e_s are the vapor pressures of the atmosphere and the snow or soil, respectively [Pa], p_{atm} is atmospheric pressure [Pa], which is provided as forcing data, and λ_e is the latent heat of evaporation from the ground surface [J kg^{-1}]. Evaporation resistance E_r [m s^{-1}] is the inverse of the air and soil resistance sums R_{air} [s m^{-1}] and R_{soil} [s m^{-1}], defined as:

$$E_r = \frac{1}{R_{air} + R_{soil}} \quad \text{[Eq. 25]}$$

Air resistance is the inverse of turbulent exchange (Eq. 21) and atmospheric stability (Eq. 22):

$$R_{air} = \frac{1}{D_{eh} \xi} \quad \text{[Eq. 26]}$$

Soil resistance R_{soil} is the ratio of the length that vapor must travel from the point of evaporation L [m] to empirically-calculated vapor diffusion D [m^2 s^{-1}]:

$$R_{soil} = \frac{L}{D} \quad \text{[Eq. 27]}$$

$$L = d_1 \frac{\exp[(1-s_l/\varphi)^w]-1}{e_v-1} \quad \text{[Eq. 28]}$$

$$D = D_0\, \varphi^2 (1 - \frac{s_r}{\varphi})^{2+3m} \quad \text{[Eq. 29]}$$

where e_v is air vapor pressure and φ, s_r, and m are taken from the soil properties of the most surficial subsurface cell.

As highlighted above, ATS solves for conductive heat flux through the snowpack when it exists:

$$Q_c = \begin{cases} \frac{\kappa_s(T_s - T_{ground})}{z_s}, & z_s \geq 2\ cm \\ 0, & z_s < 2\ cm \end{cases} \quad \text{[Eq. 30]}$$

The thermal conductivity of the snowpack κ_s is calculated empirically through the function established in Ling & Zhang (2004):

$$\kappa_s = 2.9 * 10^{-6} \rho_{snow}^2 \quad \text{[Eq. 31]}$$

and the total mass density of the snowpack ρ_{snow} [kg m^{-3}] is the volume-weighted average of fresh snow ($\rho_{snow,fresh}$, assigned at 100 kg m^{-3}), ice from condensation ($\rho_{snow,cond.}$, assigned at 200 kg m^{-3}), and older snowpack that settles over time ($\rho_{snow,settled}$), which is calculated based on snow age in days (Martinec, 1977):

$$\rho_{snow,settled} = \rho_{snow,fresh} (age_{snow})^{0.3} \quad \text{[Eq. 32]}$$

The total snow density is then used with the cell dimensions to calculate the snow height z_s. With snow height and density, ATS then calculates snow water equivalent (SWE):

$$SWE = \frac{z_s}{\rho_{snow}} \quad \text{[Eq. 33]}$$

As both water fluxes and energy fluxes are necessary to solve the ground energy and mass balance (see section 2.1.2), ATS calculates water fluxes from the surface to the subsurface after calculating the energy balance. ATS iterates to solve for the meltwater contribution to the system: if the energy balance calculation determines that snow temperature T_s is above freezing, then ATS sets T_s to freezing (273.15 K) and the surface

energy balance is re-calculated. In this case, all the excess energy that would have gone to increasing snow temperature is then bulk redistributed to snowmelt energy Q_{melt}. This allows for ATS to calculate the flux of snowmelt into the subsurface:

$$q_{melt} = \frac{Q_{melt}}{\rho_l L_f}\left(\frac{\rho_w GFW_w}{1000}\right) \quad \text{[Eq. 34]}$$

where GFW_w is the gram formula weight of water [g mol^{-1}].

The physics of vertical and lateral flow rates of meltwater within snowpack are not calculated. Water loss due to both evaporation and sublimation from the snowpack is also calculated, based on the latent heat flux Q_e:

$$q_{evap} = \frac{Q_e}{\rho_l \lambda_s}\left(\frac{\rho_w GFW_w}{1000}\right) \quad \text{[Eq. 35]}$$

In both equations 34 and 35, the conversion factor $\left(\frac{\rho_w GFW_w}{1000}\right)$ is applied so that the mass fluxes of water are expressed in [mol m^{-2} s^{-1}].

4.3.2 Model development

4.3.2.1 Geometry and discretization

This study uses the ATS model but imposes a range of soil layer thicknesses and permeabilities on otherwise uniform hillslope domains. Each 2D domain is 300 m long, 40 m deep, and inclined at a 5 percent slope (Figure 4.1). Although the area of interest in each domain is only the top meter of the hillslope, the model extends 40 m because that is beyond the depth where borehole data has shown that annual fluctuations in soil temperature do not occur, and thus a constant-temperature boundary condition can be applied (Atchley et al., 2015).

Each model cell is 10 m long. Given that the area of interest is between the land surface and the organic/mineral soil transition, the thickness of model cells in organic soil is very small and thicknesses increase geometrically with depth. At the surface, within the acrotelm, each model cell is 1 cm thick. Below that, within the catotelm, each model

cell is 2 cm thick. The next 20 cell thicknesses increase in a geometric sequence with a factor of 1.1, and the thicknesses of all cells deeper than that increase in a geometric sequence with a factor of 1.2. Because the thicknesses of the organic soil layers varies between models (see section 2.2.4), the discretization of the model domains is not consistent across models.

4.3.2.2 Boundary conditions

ATS couples surface meteorological processes to the subsurface; thus, surface meteorology must be provided as the top hydraulic and thermal boundary condition. To develop the surface meteorology boundary condition dataset, an 'average' year of meteorological forcings was derived from the MIROC5 climate model historical input data (Watanabe et al., 2010). The daily-averaged precipitation, longwave and shortwave radiation, wind speed, relative humidity, and air temperature between 1986 and 2006 was computed for the MIROC5 model cell (grid resolution 1.4° Latitude and Longitude) that includes Toolik Field Station on the North Slope of Alaska (68.63°N, 149.60°W) (Figure C1). That average year was repeated continuously for the duration of each simulation (see 'Initial Condition and Spin-Up', Section 2.2.3).

Thermal and hydraulic boundary conditions were prescribed for the bottom, left, and right edges of each hillslope domain (Figure 4.1). The bottom of each domain was assumed to remain at a constant temperature of 268.15 K and no water flow was permitted:

$$0 = -\nabla \cdot \left[\eta_{l_{z=-40}} V_{l_{z=-40}}\right] \cdot \hat{n} \qquad \text{[Eq. 36]}$$

$$268.15 = T_{z=-40} \qquad \text{[Eq. 37]}$$

The right-hand side of the domain (up-slope) was assigned a symmetry boundary (i.e., it is assumed that an identical mirror image of this domain existed opposite it); thus, no fluxes of water or heat were permitted through that side:

$$0 = -\nabla \cdot \left[\eta_{l_{x=300}} V_{l_{x=300}}\right] \cdot \hat{n} \qquad \text{[Eq. 38]}$$

$$0 = [-\nabla \cdot \left(\eta_{l_{x=300}} h_{l_{x=300}} V_{l_{x=300}}\right) + \nabla \cdot \left(\kappa_{eff_{x=300}} \nabla T_{x=300}\right)] \cdot \hat{n} \quad \text{[Eq. 39]}$$

The left-hand side of the domain (down-slope) was prescribed a seepage condition as to simulate a creek with a constant water surface elevation at the bottom of the hillslope. If the hydraulic head of the left-most cell fell more than 20 cm below the ground surface, a constant head boundary was assigned, with the water table set at 20 cm below the ground surface as to mimic the time-invariant height of a stream. However, if the head exceeded that depth, the boundary condition switched to zero-flux boundary. The thermal boundary condition for this side was zero flux:

$$\begin{cases} -\nabla \cdot \left[\eta_{l_{x=0}} V_{l_{x=0}}\right] \cdot \hat{n} < 0, & -\nabla \cdot \left[\eta_{l_{x=0}} V_{l_{x=0}}\right] \cdot \hat{n} = 0 \\ H_{p_{x=0}} > 0.2\ m, & H_{p_{x=0}} = 0.2\ m \end{cases} \quad \text{[Eq. 40]}$$

$$0 = [-\nabla \cdot \left(\eta_{l_{x=0}} h_{l_{x=0}} V_{l_{x=0}}\right) + \nabla \cdot \left(\kappa_{eff_{x=0}} \nabla T_{x=0}\right)] \cdot \hat{n} \quad \text{[Eq. 41]}$$

4.3.2.3 Initial conditions and spin up

A multi-step initialization was employed to spin up the hillslope domains. In the first step, only a hydraulic initial condition in a 1D column was assigned, in the form of an initial pore pressure:

$$p_{t=0} = 76461\ Pa \quad \text{[Eq. 42]}$$

This pore pressure set the water table approximately 2.5 m below the ground surface in the initial column. The column was then frozen from below: cells were all assigned an initial temperature of 293.15 K, and then a bottom fixed-temperature thermal boundary condition was applied to drive freezing:

$$T_{t=0,z=-40m} = 268.15\ K \quad \text{[Eq. 43]}$$

Freezing from below, although nonphysical, helps ensure that liquid porewater is not trapped within a freezing lens, which could create substantial overpressures. The freezing of the column caused the water table to rise substantially due to the volumetric expansion that occurs when water freezes to ice; thus, the new position of the frozen

water table was between 10 and 30 cm below the ground surface, and that depth varied with the organic layer thicknesses assigned to the domain.

That column was then draped on the 2D hillslope domain, which provided an initial pressure and temperature field for the entire domain. These 2D domains were then forced with the complete set of boundary conditions described in section 2.2.2 (Figure C1). Each model ran for 10 years, with the first 9 years designated as 'spin-up' time. This period was used to ensure that each domain exhibited the heat and water flux representative of steady-state condition between years, rather than the dynamic fluxes of model domains progressing towards a steady state between years. We considered inter-annual steady state to be achieved when the average over-winter ice table depth varied by less than 1 cm between years; this occurred between years 3 and 5 of each hillslope spin-up period. The 10th and final year of simulation was considered and analyzed for this study.

4.3.2.4 Design of numerical experiments

Five parameters varied across the suite of models created: acrotelm thickness b_{ac}, catotelm thickness b_{ct}, acrotelm hydraulic conductivity K_{ac}, catotelm hydraulic conductivity K_{ct}, and mineral soil hydraulic conductivity K_{mn} (Table 4.1). These parameter values were determined from Chapter Three, which classified the stratigraphy and subsurface properties of the Arctic Foothills based on seven unique landscape classes. These classes reflect the dominant land surface slope, vegetation type, and microtopographic position above an active layer soil column. Four landscape classes describe steeper-topography hillslopes: Tussock Tundra in local highs (Tussock Tundra High), Tussock Tundra in local lows (Tussock Tundra Low), Water Tracks, and Woody Shrubs. Three landscape classes describe shallow-sloping riparian zones: Sedges in local highs (Sedge High), Sedges in local lows (Sedge Low), and Woody Shrubs.

Within each landscape class, the 25th and 75th percentiles of b_{ac}, b_{ct}, K_{ac}, K_{ct}, and K_{mn} were used; this resulted in 32 parameter combinations per landscape class, and a

total of 224 total parameter combinations across all landscape classes. For the parameters measured in Chapter Three that were not varied within landscape classes (φ, κ, and van Genuchten fitting parameters $\alpha, n,$ and $s_{l,r}$), the median value reported for each landscape class was used. For parameters necessary for ATS but not measured in Chapter Three, the default values prescribed in ATS were used. All parameter values can be found in Table 4.1.

This study is informed by measurements of hydraulic conductivity K rather than intrinsic permeability k. We therefore converted reported K measurements to k:

$$K = \frac{k*\rho_l*g}{\mu_l} \qquad \text{[Eq. 44]}$$

assuming the ρ_l and μ_l of the water at 293.15 K.

4.3.2.5 Metrics for comparing across different hillslope simulations

Trends in thaw depth, total groundwater storage, and lateral flow (both in the surface and the subsurface) were determined for each model domain. Thaw depth within each model was determined as the depth of the deepest ice-free cell within each column. As lateral variability in thaw depth within each model was not observed, the thaw depth of all the columns was averaged in order to create one value for each hillslope at each point in time:

$$z_{thaw_t} = \frac{\sum_{x=0}^{300} \max(z_{x,t}\{s_{i,t}\}=0)}{30} \qquad \text{[Eq. 45]}$$

Total groundwater storage at each point in time was calculated as the sum of the total volume of ice and liquid in each cell at each point in time:

$$S_t = \sum_{x=0}^{300} \sum_{z=0}^{40} s_{i_{x,z,t}} \varphi dxdz + s_{l_{x,z,t}} \varphi dxdz \qquad \text{[Eq. 46]}$$

Total lateral groundwater flow was calculated as the sum of all flows normal to the down-slope boundary:

$$q_{out_t} = \sum_{z=0}^{40} \hat{n} \cdot -v_{x=0,z,t} \qquad \text{[Eq. 47]}$$

To mechanistically describe the trends observed in thaw depth, groundwater storage, and flow within and between hillslope models, we also analyzed how intrinsic properties within the models, such as thermal conductivity, vary with time. For such calculations, the thermal conductivity of all the cells within a soil layer was spatially averaged across the entire length of the domain.

4.3.2.6 Analysis

The hydrologic cycle in permafrost watersheds is commonly divided into four seasons of unequal length defined by the position of the ice table: 'Freshet', 'thaw', 'freeze-up', and 'over-winter' (Carey & DeBeer, 2008; Hinkel & Nelson, 2003; Kane et al., 2004; Neilson et al., 2018). The goal of this study is to identify how stratigraphic variability affects thermal hydrology processes within hillslopes; we thus wanted to compare the thermal hydrologic responses that occur within each season to each other. Our simulations clearly exhibited these four seasons; however, an intermittent 'stagnation' season was also observed, in which the active layer was neither freezing nor thawing. This period was examined independent of the thaw and freeze-up seasons, leading to a total of five unique seasons defined by active layer position (Figure 4.2, Table 4.2). We created explicit definitions for these seasons based on the thermal hydrologic response of each hillslope: the Freshet lasted from the day that surface water flows first exceeded zero to the day that groundwater flows q_{out} returned to pre-freshet flow levels; Active Layer Development lasted from the end of the Freshet to the first day the thaw depth z_{thaw} reaches its annual maximum depth; Active Layer Stagnation lasted from the end of Active Layer Development to the last day that z_{thaw} was at its maximum depth; Freeze-Up lasted from the end of Active Layer Stagnation to the first subsequent day that $z_{thaw} = 0$, and Over-Winter was all other days.

4.4 RESULTS

The rate and the depth that the active layer thaws and re-freezes is controlled by observed stratigraphy, but the timing of these processes is not (Figures 4.2 and 4.3). The

active layer does not continually grow and shrink over the thaw cycle; rather, its thickness stagnates at the maximum for approximately one month, and while stratigraphy governs the depth at which that stagnation occurs, it exerts no control over its duration.

Groundwater flow and storage are also controlled by stratigraphic variability. Because substantial differences in porosity between organic and mineral soils exist, more porewater can be stored within organic soils than mineral soils, and more water is required for the water table to rise in organic soil than in mineral soil. We observed that the variability in stratigraphy tested here exerts significant controls on the amount of groundwater storage, water table depth, and groundwater flow rates.

The averaging of a decade of rain events led to a continual, yet low rate of input precipitation; these rates were frequently overwhelmed by evaporation, which caused the model hillslopes to be relatively dry (i.e., saturation in organic soils was rarely achieved). Because organic soils were rarely saturated, lateral groundwater flows, which occurred mostly through the low-permeability mineral soils, were negligible, and evaporation was the primary outward groundwater flux. This flux was most dominant during Active Layer Development; decreasing radiation and air temperature, coincident with increased precipitation, drove a net re-saturation of the active layer in the second half of the summer.

Table 4.2 summarizes the observed thermal hydrology trends that occur within each season, and how stratigraphic changes affect these trends. A more detailed description of the thermal hydrologic processes within each season is presented below.

4.4.1 Freshet thaw and groundwater flow

Although the active layer is thinnest during the Freshet season, subsurface processes are active and affected by stratigraphy. Thaw is minimal during the Freshet (Figure 4.5); however, the largest subsurface flows observed throughout the year occur in this narrow thawed zone (Figure 4.4). The median subsurface flows in the Freshet are

between 4 and 5 orders of magnitude higher than the median subsurface flows in any other season (Figure 4.4).

Substantial groundwater infiltration occurs during this time because of the thin thawed thickness of the active layer. Initially during the Freshet, the total groundwater storage in the aquifer increases rapidly due to the infiltration of meltwater (Figures 4.3 and 4.6). However, soon following that rise, there is an equally rapid and substantial loss of groundwater storage. This loss occurs as the thawed zone deepens and the shallowest stored soil moisture is released as drainage. This causes the active layer to experience a small net loss of groundwater during the Freshet season (Figure 4.4).

Stratigraphy—particularly catotelm thickness— controls the partitioning of water between surface runoff and subsurface storage. Less surface runoff (i.e. overland flow) occurs over soils containing thick catotelms than thin ones (Figure 4.7, top row), while more groundwater is stored in thick catotelms than thin ones (Figure 4.7, top row). Stratigraphy did little to control groundwater fluxes in the Freshet season, and exerted no noticeable influence on the thaw rate during this time.

4.4.2 Active layer development and desiccation

The early-season hydrology of the hillslopes is defined by a steady, stratigraphy-dependent thawing of the active layer, minimal but steadily-increasing groundwater flows that are coincident with a protracted desiccating of the organic soil layers (Figures 4.3, 4.5, and 4.6). The acrotelm layer is already thawed by the time this period begins; however, the thawing of the remaining two frozen soil layers in the active layer occurs at two different rates depending on if the ice table was in the catotelm or the mineral soil. Catotelm thaw occurred at an average rate of 0.68 +/- 0.4 cm d^{-1}, and mineral soil thaw occurred slightly faster, at a rate of 0.82 +/- 0.3 cm d^{-1}.

The rate at which both the catotelm and mineral soils thaw is governed by stratigraphic variability, but such stratigraphic effects are not equally strong in both layers. The thicknesses of the different organic layers have conflicting effects on

catotelm thaw rate: catotelm thaw rate is negatively related to acrotelm thickness, yet catotelm thaw rate is positively related to catotelm thickness. Thus, catotelm thaw rate does not have a significant dependence on total organic thickness (Figure 4.7, second row). Conversely, both acrotelm thickness and catotelm thickness are inversely related with mineral soil thaw rate; thus their combined effect strengthens that negative relationship (Figure 4.7, second row). Given that total organic soil thicknesses are small in most hillslope active layers, mineral soil thaw tends to happen faster and deeper in hillslope sites than riparian sites (Figures 4.7, 4.8).

Substantial losses of soil moisture occur during Active Layer Development because evaporation overwhelms precipitation (Figure 4.3). The drying of the active layer occurs mostly in the catotelm—the acrotelm drained fully during the Freshet, and the mineral soil layer remains saturated perennially (Figure 4.6). Unlike in the Freshet, where catotelm thickness promoted groundwater storage, there is no significant relationship between organic layer thicknesses and groundwater storage (losses). However, stratigraphy does affect the rate at which the catotelm dries—thicker catotelms dry faster than thin ones (Figure 4.6).

The minimal but increasing groundwater flows during Active Layer Development are affected both by stratigraphy and soil properties, however. Active Layer Development groundwater flows are significantly inversely related to total organic thickness (Figure 4.8). Other soil properties also exert a controlling effect: approximately two orders of magnitude more groundwater flow occurs in hillslopes with higher-K mineral soils than otherwise-identical lower-K hillslopes (Figures 4.3 and 4.8).

4.3.3 Active layer stagnation

In the Active Layer Stagnation, which is defined as the length of time that the change in thawed zone thickness is less than 2 cm, the ice table reaches its nadir and remains there for a period of approximately 35 days (Figure 4.3, Table 4.2). The depth of this maximum thaw (i.e., active layer thickness, ALT) ranged between 45 and 105 cm

across all runs; however, the average ALT was 70 +/- 17 cm. These values fall within the commonly-observed ALTs in the continuous permafrost found on the North Slope of Alaska and the Yukon Territory in Canada, which range between 40 and 80 cm (Hinkel & Nelson, 2003; Nelson et al., 1999; Quinton et al., 2005; Smith et al., 2009). No lateral (down-slope) trends in active layer thickness were observed.

The ALT is strongly controlled by both organic soil thicknesses (Figure 4.7). ALT is strongly negatively related to both acrotelm thickness and catotelm thickness, and the relationship improves when both organic soil layers are considered (R^2 = 0.26, 0.46, and 0.81 when comparing ALT to acrotelm thickness, catotelm thickness, and total organic thickness, respectively).

Although there is no appreciable change to the thickness of the thawed zone over this season, the shift from net evaporative loss to net precipitation gain causes groundwater storage to increase (Figure 4.3). This elevates the water table (Figure 4.3), increases groundwater storage (Figures 4.4 and 4.6), and increases groundwater flows (Figures 4.3 and 4.4). Groundwater storage universally increases, and the water table rises because the losses caused by the increase in lateral groundwater flows are orders of magnitude less than the gains incurred due to a net positive surface water budget. Total groundwater flows are weakly, inversely related to organic matter thickness (R^2 = 0.17). Total changes to groundwater storage during this season do not vary significantly with stratigraphy; but the thinnest catotelms re-saturate more rapidly than the thickest catotelms (Figure 4.6).

4.4.4 Freeze-up

The ‘Freeze-Up’ season is characterized by the collapse of the thaw zone (Figures 4.3 and 4.5). The overall rate at which these soil columns freeze is approximately twice as fast as the rate at which active layers thaw (Figure 4.4). Active layers freeze at a constant rate, excluding a brief inflection point roughly halfway through the season (Figure 4.3). The imposed meteorological conditions cause the hillslope models to freeze both from the top-down and the bottom-up during the study year (Figure 4.5). The

freezing, particularly from the top-down, causes input precipitation water to freeze in place rather than evaporate; this induces sharp increases in the saturation of the acrotelm (Figure 4.6). The now relatively saturated and frozen acrotelm functions as a cap above the middle and still-thawed lens of catotelm soil that substantially reduces the connection between the surface hydrologic inputs (precipitation and evaporation) and the subsurface (Figure 4.3).

As is the case during Active Layer Development, the daily rate that these domains re-freeze is affected by organic matter thickness. The beginning and end of the Freeze-up season occurs at approximately the same time across all hillslopes, but since the maximum thaw depths vary substantially based on organic matter thickness, freeze-up rates are also controlled by organic thickness (Figure 4.7). Thus, hillslopes with the thickest organic layers have less soil thickness to freeze in the same amount of time as hillslopes with the thinnest organic layers, so they have the lowest freeze-up rates (Figure 4.3). The consistent timing of Freeze-Up across all hillslopes also causes the thawed 'lens' of soil between the top-down and the bottom-up freezing fronts to exist for approximately the same duration across all hillslope models.

Groundwater flows continue to increase in this season (Figure 4.3). Median total groundwater flows during this season are the highest among all non-Freshet seasons (Figure 4.4). Stratigraphy exerted a slight control on variability: organic thickness exhibits the same weak but significant negative relationship with groundwater flows in this season as it did during Active Layer Stagnation (Figure 4.9, $R^2 = 0.16$).

Groundwater flow increases correspond to net groundwater storage decreases within catotelm (Figures 4.5 and 4.6). However, simultaneously, these flows also correspond to groundwater storage increases within acrotelm (Figures 4.5 and 4.6). The increases to groundwater storage in acrotelm outweigh the decreases in catotelm, resulting in a net increase in total groundwater storage (Figure 4.4).

4.4.5 Over-winter subsurface storage and storm-water dynamics

The 'Over-Winter' season is defined by a fully-frozen yet variably-saturated soil in the region of the previous summer's maximum active layer. Over-winter total (solid) water content ranges substantially across hillslope models: the total water contents range between 60 and 90 percent in the acrotelm, between 45 and 95 percent in the catotelm, and always near 100 percent in the mineral soil (Figure 4.6). Total organic soil thickness explains much of the variance in total, areal (depth-integrated) void space: hillslope models with higher total organic thickness have more over-winter void space than hillslope models with lower total organic thickness (Figure 4.13).

Despite being frozen, groundwater flow can still occur and total groundwater storage can change substantially in the Over-Winter season (Figure 4.4). These situations occur largely because of a winter rainfall event early in the Over-Winter season (mid-October) (Figure 4.3). Although frozen, groundwater storage can increase due to this input if soils were not fully saturated at freeze up (Figure 4.4). Unlike in the freeze-up season, the amount of groundwater storage increase that occurred due to winter rainfall is strongly negatively correlated to the organic thickness in the hillslope (Figure 4.10).

The average time series of precipitation included a late-season rainfall event, and this precipitation only induced a groundwater response in the model. There was no surface water response, because even though the soil was fully frozen it was unsaturated and infiltration occurred. The amount of groundwater flow that occurred due to this rainfall input ranged over five orders of magnitude (Figure 4.10). This groundwater flow variability can be explained with the (frozen) water table depth: hillslopes in which the water table was nearest to the surface transported the extremely high groundwater flows due to higher hydraulic conductivity of the near-surface soils (Figure 4.10). The water table depth was unrelated to groundwater flow rates beyond a depth of approximately 40 cm, however.

4.5 DISCUSSION

4.5.1 Seasonal response of thawed zone thickness, lateral groundwater flow rate, and soil moisture storage to atmospheric forcings

Our numerical experiment revealed overall consistency in time-dependent trends of thaw, freeze-up, groundwater flow, and groundwater storage across hillslopes with varying soil hydraulic and thermal properties profiles. Five distinct periods were identified in which these trends behaved consistently, and these periods occurred simultaneously across all models (Table 4.2). The Freshet was characterized by rapid acrotelm thaw and high groundwater flows. Active Layer Development was characterized by continual and constant-rate thaw in which groundwater flows were low but increasing and evaporation outweighed precipitation, incurring groundwater losses. Active Layer Stagnation was characterized by non-detectable changes in the thaw zone depth at its maximum, a switch from net groundwater losses to net groundwater gains, and further-increasing groundwater flows. Freeze-Up was characterized by the shrinking of the thawed zone from above and below, continual groundwater gains, and further-increasing flows. Over-Winter was characterized by a frozen yet unsaturated active layer and widely-ranging groundwater flows triggered from storm events.

Our findings identified that both soil properties and input moisture exert complimentary controls on thaw, lateral flows, and soil moisture storage. Because air is much more thermally insulative than water, soil moisture is a critical component of soil thermal conductivity (Figure 4.11), which is control on heat transfer and thus thaw. Lateral flows are governed by soil permeability (Chapter 2), which is many orders of magnitude higher in organic soils than in mineral soils (Table 4.1). However, in order for lateral flow to occur in organic soils, saturation must be attained within those soils; thus, lateral flow rates within active layer aquifers also depend on soil moisture. Soil moisture itself depends not only on the water retention capability of the soils, but also on the amount of precipitation input into the system.

Input precipitation is therefore an additional critical control on thaw, lateral flow, and soil moisture storage. Thus, the trends in thaw, groundwater flow, and soil moisture

storage observed within each of these periods occurred in part because of the meteorological data chosen to force these models, and such data was compiled based on the averages of daily data rather than daily data itself. While many of the overall trends observed within these models are consistent with observation (i.e. the rates and depths of simulated active layers fall within the ranges of those observed), some do not reflect reality as well. For example, saturation is almost never achieved within organic soil, so groundwater flows are relegated to the low-permeability mineral soil and are thus negligible in comparison to other fluxes. Divergence between saturation and groundwater flows that are simulated versus observed likely occurred for two reasons: first, because the precipitation time series data used to force the models was a decadal average, which mutes rainfall peaks. By muting peaks, evaporation rates are able to consistently match precipitation rates, and organic soils are continually drying. Secondly, by only representing a 2D slice of a hillslope, there is no potential input of the surrounding contributing areas. These areas are particularly important in water tracks, which have been shown to focus flow laterally (Voytek et al., 2016), and riparian zones, which sit at the down-slope end of hillslopes and thus receive up-slope input (Stieglitz et al., 2003). These combined effects led to hillslope groundwater models that were drier, particularly within organic soils, than is commonly observed in reality.

We did not observe any significant down-slope trends in thawed zone thickness. This is strong evidence that, given the conditions we prescribed, thaw is dominated by vertical conduction, rather than lateral advection of heat with groundwater. As highlighted above, our hillslope models had relatively dry organic soil layers; thus, for most of the simulated year, flow in all model domains was occurring mainly within the mineral soil. Such flows were minimal and quite slow, due to the low permeability of mineral soil. For heat transfer by groundwater advection to overwhelm heat transfer by vertical conduction, groundwater flow velocities must be relatively faster than the conduction rate (Kurylyk et al., 2016). With the Darcy velocities observed in the mineral soil, that cannot be achieved. It should however be noted that the predominantly low groundwater flow rates observed in these hillslopes likely would differ in a wetter environment, as a wetter hillslope would

have a higher water table, which would allow for flow in the more-permeable organic soil. If the saturated thickness sits within the higher-K organic soil, groundwater flow rates can be orders of magnitude higher (Chapter Two), and in that case, lateral advection of heat could become significant. A different precipitation forcing could cause this behavior.

4.5.2 Stratigraphic impact on thaw, lateral flows, and soil moisture storage

Although the hydrologic conditions represented in our hillslope models were not always reflective of reality, a reflection of reality is not necessary to identify the mechanistic importance of particular parameters. Our experimental design, which kept all parameters except soil thicknesses and properties constant, allowed us to isolate and test how the variability in the thicknesses of soil layers with starkly different hydraulic and thermal properties affected thaw, lateral groundwater flow, and soil moisture storage within the meteorological condition provided. Although the meteorology will vary from year to year, soil properties, and the physical relationships that they influence, will not. This study therefore provides a useful investigation into the mechanisms that govern thaw, groundwater flow, and soil moisture storage.

4.5.2.1 Stratigraphic impacts on thaw rate, active layer thickness, and freeze-up rate

The two organic soil layers, acrotelm and catotelm, have very different water retention properties (Table 4.1); they thus exert opposite controls on the rate that catotelm thaws. The rate that the catotelm thaws is inversely related to acrotelm thickness, meaning it functions as an insulator. However, catotelm thaw rate is positively related to catotelm thickness, meaning it functions as a conductor of heat. The difference occurs because all acrotelm soils are typically drained after the Freshet season, whereas much of the catotelm soils are still wet to saturated (Figures 4.5 and 4.6). Thus, a hillslope with a thick, dry acrotelm layer will be well-insulated because most of the substantial porosity in acrotelm soils will be filled with air, driving down thermal conductivity (Figure 4.11). Low thermal conductivity lowers the thaw rate. Simultaneously, the frozen yet still wet

catotelm has a respectively higher thermal conductivity, which does not inhibit thaw as strongly as the thawed, dry acrotelm.

Unlike catotelm thaw, which was oppositely controlled by each organic soil layer, the mineral soil thaw rate, the ultimate active layer thickness, and the freeze-up rate all were inhibited in concert by both organic soil layers. This is because, in our simulations, the catotelm drained soon after it thawed. This drainage caused a wholesale lowering of catotelm thermal conductivity such that it functioned similarly to acrotelm (Figure 4.11). Once the catotelm thawed and subsequently drained, both relatively dry organic soil layers insulate the deeper mineral soil. The large variability observed in active layer saturation over winter collapsed by the middle of Active Layer Development: acrotelm total water saturation converged at approximately 40 percent, and catotelm water saturation converged between 60 and 70 percent. The consistent saturation within these soils across hillslopes causes acrotelm and catotelm bulk soil thermal conductivity to also collapse at a very low value (Figure 4.11), because the bulk soil volume in both acrotelm and catotelm is now comprised of low-thermal-conductivity air. Because the thermal properties of these organic soils are homogeneous and insulating, variations in their thicknesses alone directly control the overall thaw rate of the soil.

4.5.2.2 Stratigraphic impacts on lateral groundwater flows and soil moisture storage

Stratigraphy governs both soil moisture storage and groundwater flow, and such governance is linked. Stratigraphy governs soil moisture storage simply because stratigraphy dictates the amount of available void space within the active layer (Figures 4.5, 4.10c). The increased soil moisture storage that occurs within thick-organic hillslopes during the freshet occurs because there is more available void space to fill with meltwater. However, the water table does not rise as rapidly in thick-organic hillslopes as thin-organic ones. In order for the water table to rise, all available pore space must be filled; that means that more water is necessary to raise the water table in thick-organic hillslopes (where void space is plentiful) than thin ones (where void space is limited). The water table responds less to water inputs in thick organic layers because there is

more unsaturated pore space for the input water to be stored in, due to the high porosity of organic soil (Figure 4.3). Because of this, substantial groundwater flows are only observed in thin-organic hillslope models, where the water input is able to generate saturation in organic soil (Figure 4.3). Such flows are fleeting; because these zones also drain well, the saturation disappears quickly once the input water source ceases.

Although groundwater flows overall were extremely low throughout the simulated year, they still varied substantially between models. Groundwater flow during non-event-flow conditions occurred mainly within the saturated mineral soils, which have a very low *K*. However, mineral soil K did vary across hillslope models, and that variability in K caused approximately two orders of magnitude of variability in groundwater flow during the baseflow-dominated Active Layer Development and Active Layer Stagnation times (Figures 4.3, 4.8, and 4.9). Variability in mineral soil *K* is rarely quantified or considered. The broad category of 'mineral soil' is recognized in the arctic soil science community as having substantial heterogeneity in compositional properties (Bockheim et al., 1998; Everett, 1980; Ping et al., 2008). However, hydraulically, mineral soil is often treated as one homogeneous soil deposit (Lawrence et al., 2011), largely because no known studies have investigated variability in mineral soil hydraulic properties in this region. Furthermore, most of the mineral soil K values used in this study are substantially lower than mineral soil *K* reported in the widely-referenced Hinzman et al. (1991) study. Although flows from mineral soil are low volumetrically, they could potentially be conveying deep, ancient carbon (Shelef et al., 2017); it is therefore important to update our understanding of how water flows through this soil layer.

Our results demonstrate that subsurface properties (i.e. organic soil layer thicknesses and properties) exert an effect on processes commonly assumed to be limited to the surface. The Freshet, in particular, is frequently considered a surface flow phenomenon because so little of the active layer is thawed when it occurs. However, the highest overall groundwater flows occur during the freshet, and the stratigraphy of the subsurface helps control how much water flows out versus is retained in the active layer.

Such surface-subsurface connections during the high-flow Freshet can help explain the similarly high fluxes of dissolved soil carbon that can be observed during that time (Neilson et al., 2018)

4.6 CONCLUSIONS

The thaw, groundwater flow, and groundwater storage responses to forcings within each of the five seasons modeled for active layer hillslopes are substantially affected by regularly-observed sequences of soil stratigraphy and properties. During the spring snowmelt thaw ('Freshet'), the volume of void space within the mostly-frozen active layer exhibits a substantial control on the partitioning of meltwater between flow and storage, and that void space volume is controlled by (a) the varying porosity different layers in the soil (i.e., stratigraphy) and by (b) the extent of saturation during freeze up the previous year. Under the precipitation conditions prescribed from average meteorological conditions, soil organic layers slow the growth of the active layer, limit the ultimate active layer thickness, and slow the freeze-up of the active layer because they have consistently low thermal conductivities.

The surface water and energy balance can exert a dominant control on the subsurface water balance, as precipitation and evaporation fluxes overwhelmed lateral, down-slope groundwater flows throughout the season. As the active layer thawed, evaporation dominated, and there was a net loss of water from the hillslope domains both downslope and mainly to the atmosphere. As the active layer re-froze later in the season, however, precipitation dominated and resulted in a net gain of soil water. During this re-saturation, the response of the water table was governed by the amount of available void space. The response of the water table to re-saturation controlled how input water was partitioned between groundwater storage and groundwater flow due to the location of the water table in either less permeable mineral soil or in the overlying and more permeable organic soil. Variability in the water table position could explain up to five orders of magnitude of variability in lateral groundwater flow.

4.7 TABLES FOR CHAPTER 4

Landscape Class:		Tussock Tundra Hi		Tussock Tundra Low		Water Track		Woody Shrubs Hillslope		Sedge High		Woody Shrubs Riparian		Sedge Low	
		Low	*High*	*Low*	*High*	*Low*	*High*	*Low*	*High*	*Low*	*High*	*Low*	*High*	*Low*	*High*
b_{ac}	cm	9	17	7	12	5	10	10	20	8	16	10	17	3	12
b_{ct}	cm	6	13	6	16	14	25	0	12	10	19	20	34	18	45
k_{ac}	m^2	9E-11	3E-10	4E-11	2E-10	6E-11	3E-10	1E-11	2E-10	1E-11	2E-10	1E-11	2E-10	1E-11	2E-10
k_{ct}	m^2	2E-13	3E-12	3E-12	1E-11	1E-12	4E-12	2E-12	6E-12	5E-13	1E-12	2E-12	6E-12	8E-13	4E-12
k_{mn}	m^2	2E-03	1E-12	7E-15	3E-14	1E-14	4E-13	1E-15	7E-14	1E-15	8E-14	1E-15	7E-14	1E-15	8E-14
φ_{ac}	%	94%		89%		95%		90%		98%		90%		92%	
φ_{ct}	%	85%		88%		88%		83%		87%		83%		89%	
φ_{mn}	%	81%		61%		60%		50%		32%		50%		32%	
Sat. κ_{ac}	$W\ m^{-1}\ K^{-1}$	0.56													
Sat. κ_{ct}	$W\ m^{-1}\ K^{-1}$	0.67													
Sat. κ_{mn}	$W\ m^{-1}\ K^{-1}$	1.65													
Dry κ_{ac}	$W\ m^{-1}\ K^{-1}$	0.08													
Dry κ_{ct}	$W\ m^{-1}\ K^{-1}$	0.09													
Dry κ_{mn}	$W\ m^{-1}\ K^{-1}$	0.40													
α_{ac}	m^{-1}	5.87E-04													
α_{ct}	m^{-1}	1.14E-04													
α_{mn}	m^{-1}	2.00E-05													
n_{ac}	-	1.39													
n_{ct}	-	1.52													
n_{mn}	-	1.58													
$s_{r_{ac}}$	%	5%													
$s_{r_{ct}}$	%	5%													
$s_{r_{mn}}$	%	20%													

Table 4.1: User-defined parameters used in ATS simulations. $b_{ac}, b_{ct}, K_{ac}, K_{ct}$, and K_{mn} varied within landscape classes, $\varphi_{ac}, \varphi_{ct}$, and φ_{mn} varied across landscape classes, and all other parameters varied across soil types.

		Avg. Start	Length [days]		Overall AL Dynamics				Impact of Stratigraphy or Properties on AL Dynamics			
			μ	σ		Variable	μ	σ		x	y	R2
1	Freshet	13-May	11	1	Acrotelm thaws completely and rapidly	ac. thaw rate [m/d]	0.007	0.001	Thaw rate in acrotelm is weakly, positively correlated to acrotelm thickness	bac	thaw rate	0.192
2	AL Dev.	25-May	79	3	Active layer thaws to its maximum depth at two distinct rates depending on where thaw occurs. Catotelm thaw happens slower than mineral soil thaw	cat. thaw rate [m/d]	0.007	0.004	Thaw in the catotelm is weakly negatively correlated to bac, but positively correlated to bct	bac	cat thaw rate	0.09
						min. thaw rate [m/d]	0.008	0.003		bct		0.21
3	AL Stag.	13-Aug	33	6	Thaw stagnates at its maximum	ALT [m]	0.7	0.17	ALT is inversely correlated to all OM thicknesses	bac	ALT	0.26
										bac		0.46
										bct		0.81
4	Freeze-up	17-Sep	33	6	Simultaneous freezing from above and below at constant rates within each layer.	freeze rate [m/d]	-0.02	-0.01	Freeze-up rate is inversely correlated to all OM thicknesses	bac	freeze rate	0.17
										bac		0.32
										bct		0.56
5	Over-winter	20-Oct	204	9	Active layer is fully frozen but unsaturated	n/a	n/a	n/a	n/a	n/a	n/a	n/a

		Avg. Start	Length [days]		Overall Groundwater Flow Dynamics				Impact of Stratigraphy or Properties on Flow Dynamics			
			μ	σ		Variable	μ	σ		x	y	R2
1	Freshet	13-May	11	1	Substantial spike in both surface water flows and groundwater flows.	Qsw [m3]	22.9	2.13	Surface water flow is inversely correlated to all OM thicknesses	bac	Qsw	0.129
						Qgw [m3]	1.80E-02	2.10E-02		bct		0.36
										bom		0.58
2	AL Dev.	25-May	79	3	Very low but constantly-increasing groundwater flows	Qgw [m3]	1.70E-06	3.10E-06	Groundwater flow rate is directly correlated to total organic thickness	bom	Qgw	0.31
3	AL Stag.	13-Aug	33	6	Groundwater flows quickly increase	Qgw [m3]	7.19E-07	1.26E-06	Weak negative relationship between bom and total groundwater flow	bom	Qgw	0.17
4	Freeze-up	17-Sep	33	6	Increasing and higher groundwater flows; approximately twice as much flow over half as long a period	Qgw [m3]	2.42E-07	6.52E-07	Weak negative relationship between bom and total groundwater flow	bom	Qgw	0.151
5	Over-winter	20-Oct	204	9	Spikes at a highly variable value due to the late-season storm	Qgw [m3]	0.00458	0.014	n/a	n/a	n/a	n/a

		Avg. Start	Length [days]		Overall Groundwater Storage Dynamics				Impact of Stratigraphy or Properties on Storage Dynamics			
			μ	σ		Variable	μ	σ		x	y	R2
1	Freshet		11	1		dS [m3]	-1.88	-1.34		bct	dS	0.33

		13-May			Near-inundation of all soil, then rapid acrotelm drainage and, ultimately, a net loss of water				Direct relationship between groundwater storage changes and both bct and total om	bom		0.39
2	**AL Dev.**	25-May	79	3	Steady drying of the organic soil layers and decrease of the water table	dS [m3]	-15.47	3	Positive relationship between bac and gw storage, but negative relationship between bct and gw storage	bac	dS	0.1
										bct		0.2
3	**AL Stag.**	13-Aug	33	6	Re-saturation of the organic soil layers and an increase in the water table	dS [m3]	8.41	1.36	n/a	n/a	n/a	n/a
4	**Freeze-up**	17-Sep	33	6	Re-saturation of acrotelm (first) and then catotelm (second)	dS [m3]	5.35	1.29	Weak positive relationship between bct, bom and groundwater storage increases	bct	dS	0.08
5	**Over-winter**	20-Oct	204	9	Increases due to late-season storm	dS [m3]	3.56	1.55	Negative relationship between bom and groundwater stlorage increases	bom	dS	0.38

Table 4.2: Qualitative and quantitative summary of how thaw, groundwater flow, and groundwater storage vary both between seasons and within seasons due to stratigraphy and soil properties. The symbol μ denotes a population mean, and the symbol σ denotes the standard deviation.

4.8 FIGURES FOR CHAPTER 4

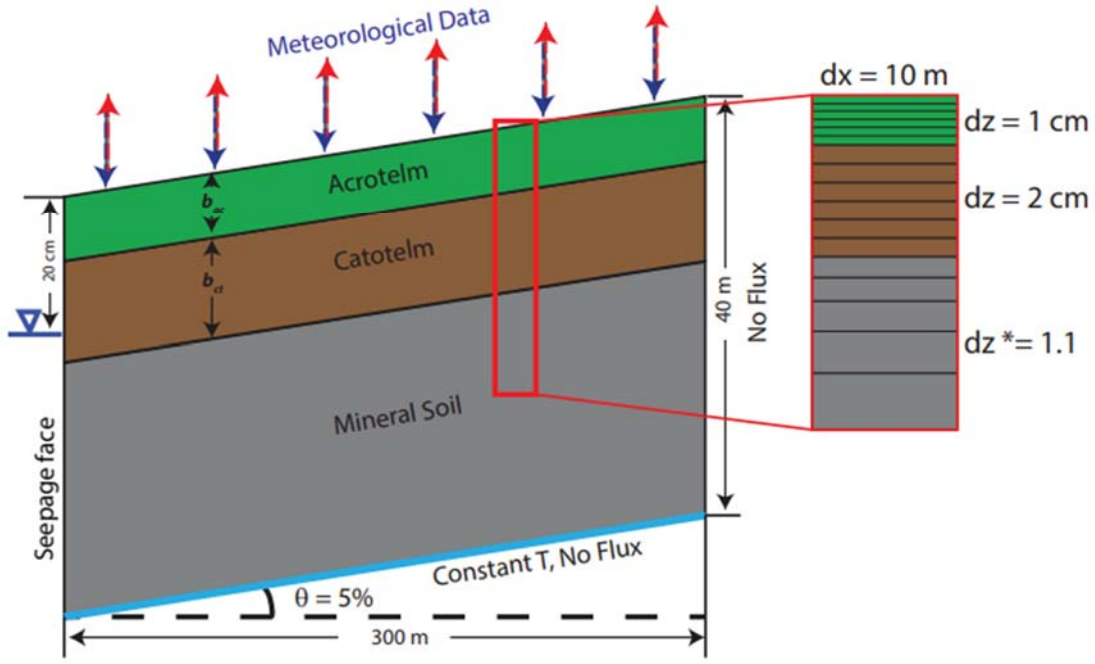

Figure 4.1: Schematic for the geometry, discretization, boundary conditions, and initial conditions for the hillslopes used in numerical experiments. The varying parameters were $b_{ac}, b_{ct}, K_{ac}, K_{ct}$, and K_{mn}.

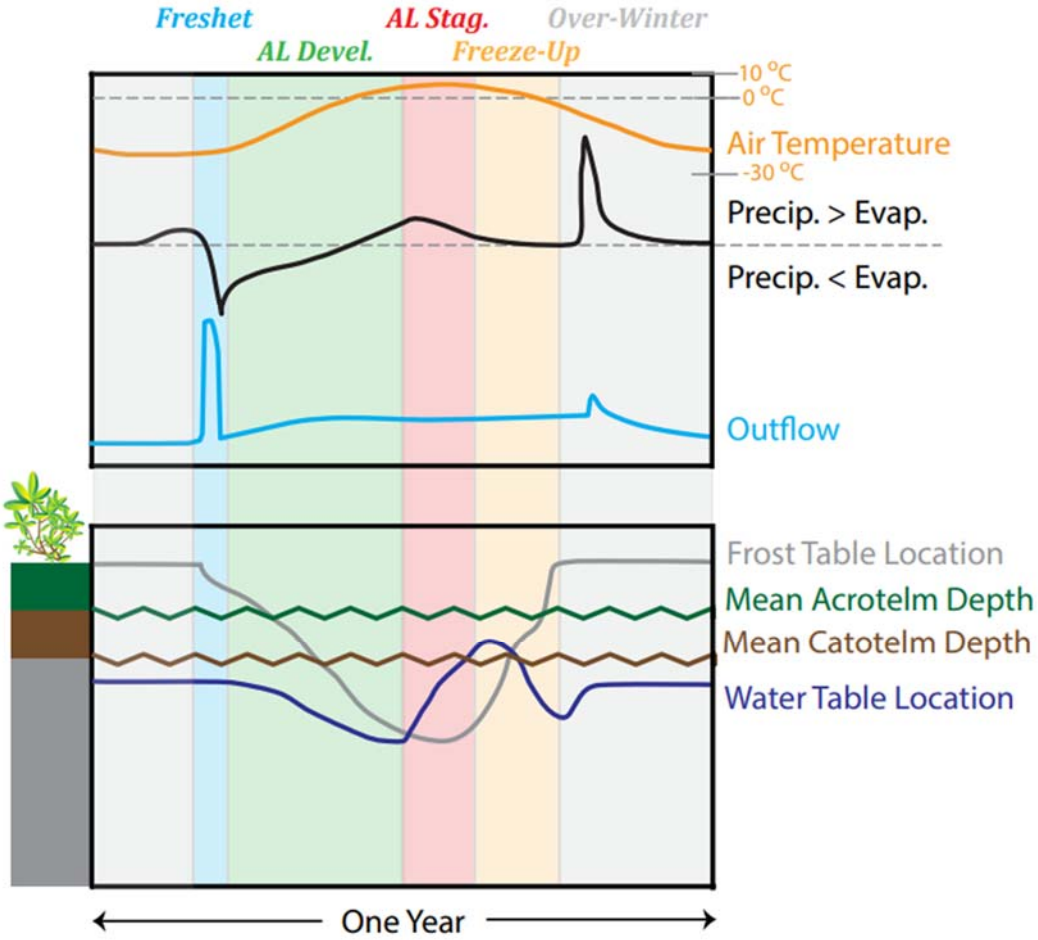

Figure 4.2: Conceptual figure of the hydrologic cycle in hillslope active layers. Top panel: air temperature (orange), net gain or loss of water to the subsurface due to precipitation or evaporation (black), and groundwater flow (blue). Bottom panel: depth to the first fully-frozen cell (grey), approximate b_{ac} (green and jagged), approximate b_{ct} (brown and jagged), and the depth to the first fully-saturated cell (blue). Shaded colors represent the five seasons within the hydrologic year, with the 'Over-Winter' season wrapping around from the end of the previous year to the beginning of the next one.

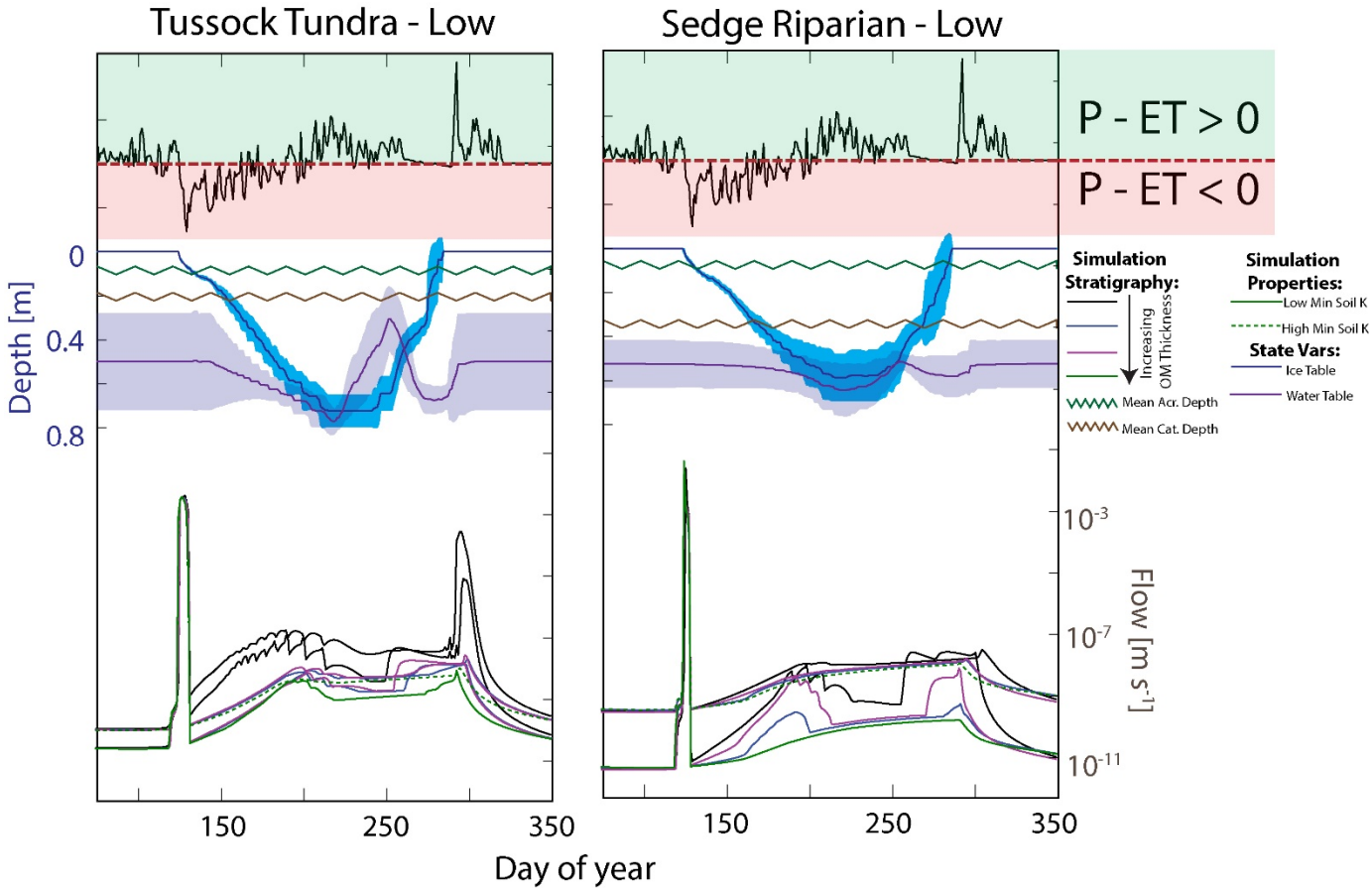

Figure 4.3: Simulated hydrologic fluxes and state variables for the stratigraphy and properties for two of the seven major landscape types in the North Slope Foothills. These two landscape types represent the end-members of total organic thickness. Top panel: net gain (green shading) or loss (red shading) of water to the subsurface due to precipitation or evaporation. Middle panel: depth to the first fully-frozen cell (blue), approximate b_{ac} (green and jagged), approximate b_{ct} (brown and jagged), and the depth to the first fully-saturated cell (purple). Shading around the ice table and water table depths represent the 95% confidence bounds from the 32 simulations within each landscape class. Bottom panel: lateral groundwater flow from each grid. Line colors denote the organic matter thicknesses, and line dashing denotes either high or low mineral soil K. The data for all seven major landscape types are presented in the appendix (Figure C2).

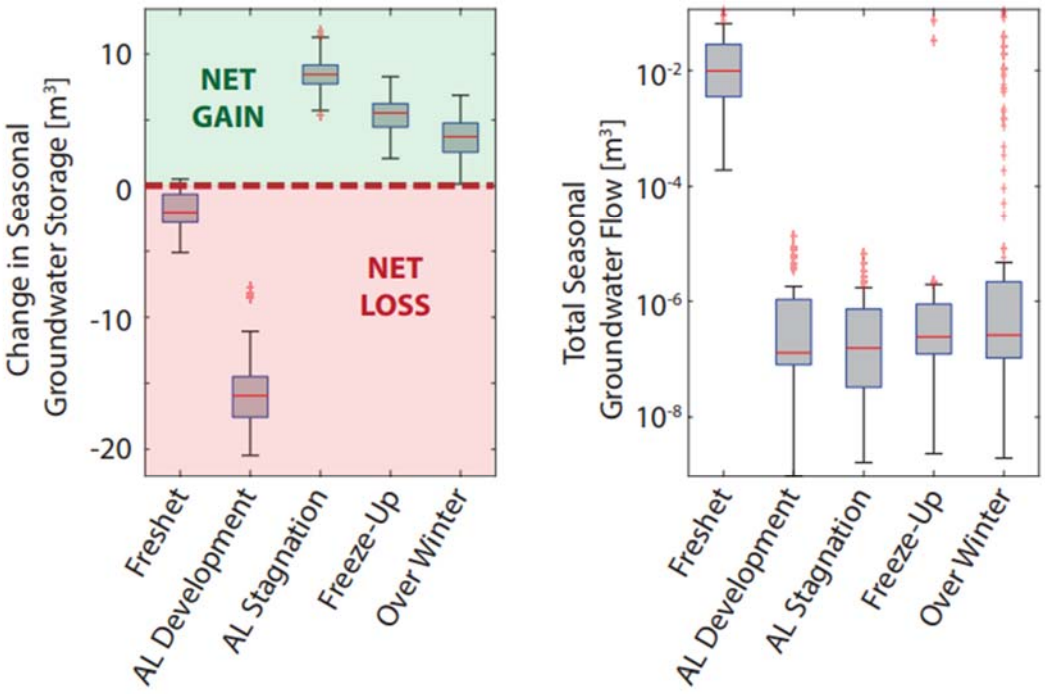

Figure 4.4: Boxplots showing (left panel) the net change in groundwater storage for each season for all simulations, and (right panel) the total groundwater flow in each season for all simulations. Boxes represent the interquartile range, with the red line representing the median. Red '+' signs denote outliers that fall outside the interquartile range.

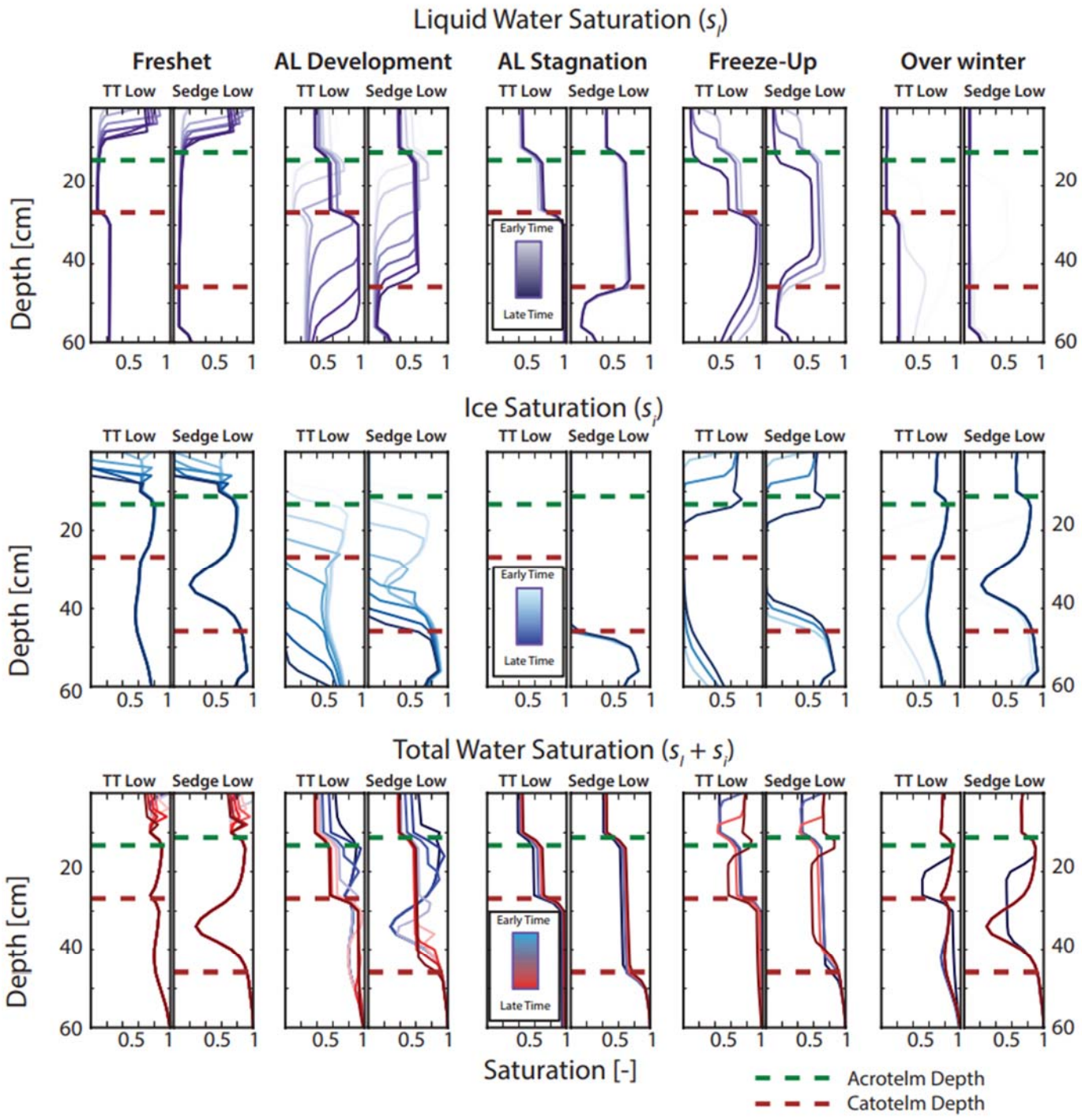
Liquid Water Saturation (s_l)
Freshet
AL Development
AL Stagnation
Freeze-Up
Over winter
TT Low
Sedge Low
Depth [cm]
20
40
60
0.5
1
Early Time
Late Time
Ice Saturation (s_i)
Total Water Saturation ($s_l + s_i$)
Saturation [-]
Acrotelm Depth
Catotelm Depth

Figure 4.5: Vertical profiles in (top panel) s_l, (middle panel) s_i, and (bottom panel) $s_l + s_i$ for two selected model runs. The profile was selected at the node closest to the eastern, down-slope boundary of the model. The left panel represents a run with high values of $b_{ac}, b_{ct}, K_{ac}, K_{ct}$, and K_{mn} for the Tussock Tundra Low landscape class, and the right panel represents a run with high values of $b_{ac}, b_{ct}, K_{ac}, K_{ct}$, and K_{mn} for the Sedge Low landscape class. Shaded colors get darker as time increases.

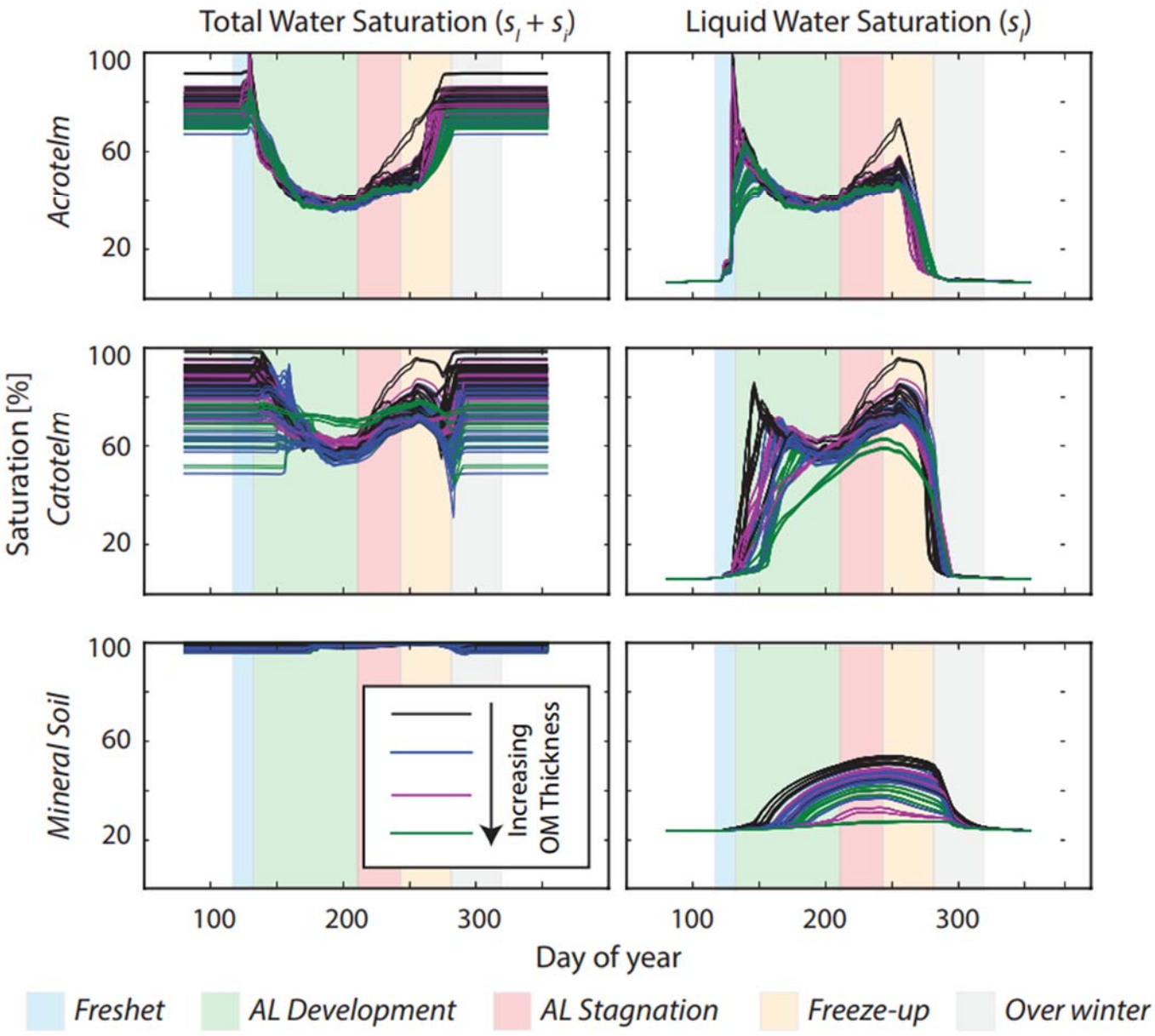

Figure 4.6: (Left column) total water saturation values and (right column) total liquid water saturation values for (top row) all acrotelm soil, (middle row) all catotelm soil, and (bottom row) all mineral soil over the course of the simulated year for all simulations. Shaded colors represent the five seasons denoted in the manuscript.

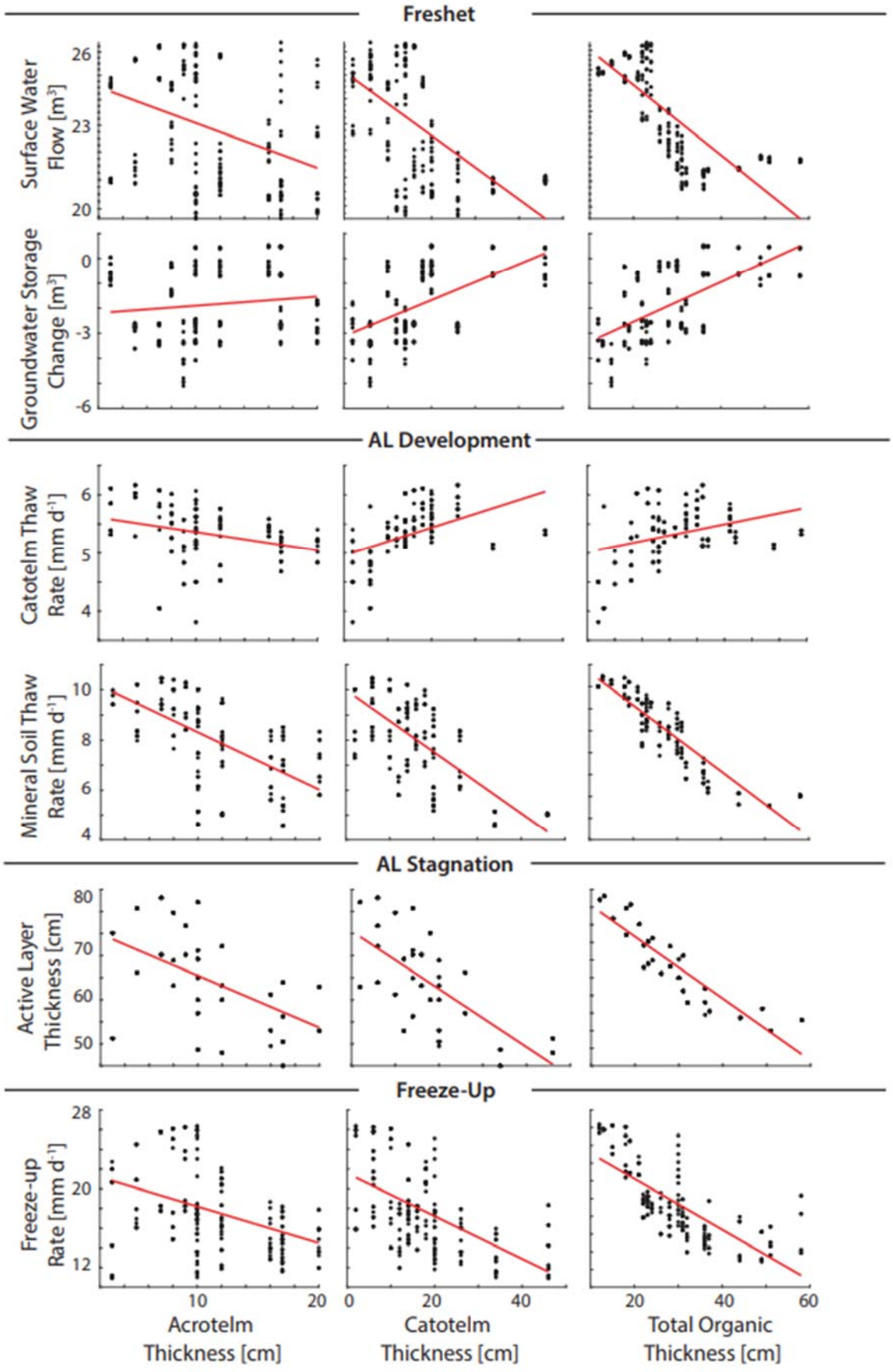
Freshet
Surface Water Flow [m³]
26
23
20
Groundwater Storage Change [m³]
0
-3
-6
AL Development
Catotelm Thaw Rate [mm d⁻¹]
6
5
4
Mineral Soil Thaw Rate [mm d⁻¹]
10
8
6
4
AL Stagnation
Active Layer Thickness [cm]
80
70
60
50
Freeze-Up
Freeze-up Rate [mm d⁻¹]
28
20
12
10
20
Acrotelm Thickness [cm]
0
20
40
Catotelm Thickness [cm]
20
40
60
Total Organic Thickness [cm]

Figure 4.7: Scatterplots showing how hydrology is affected by variability in (left column) b_{ac}, (middle column) b_{ct}, and (right column) $b_{ac} + b_{ct}$ (i.e. b_{om}) within each specified time period. Scatter plots are separated to show the pertinent relationship within each season specified in the manuscript.

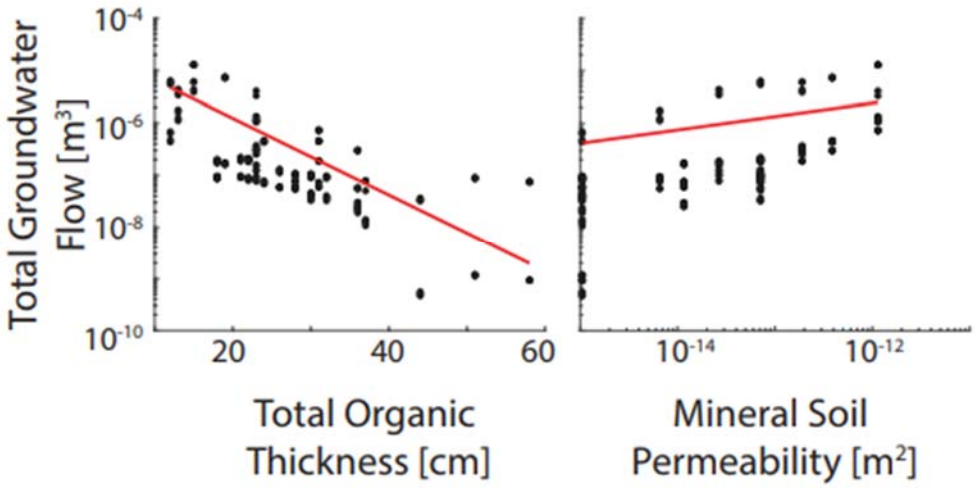

Figure 4.8: Scatterplots showing the relationship between total groundwater flow and (left panel) total organic thickness and (right panel) mineral soil *K* during the Active Layer Development season.

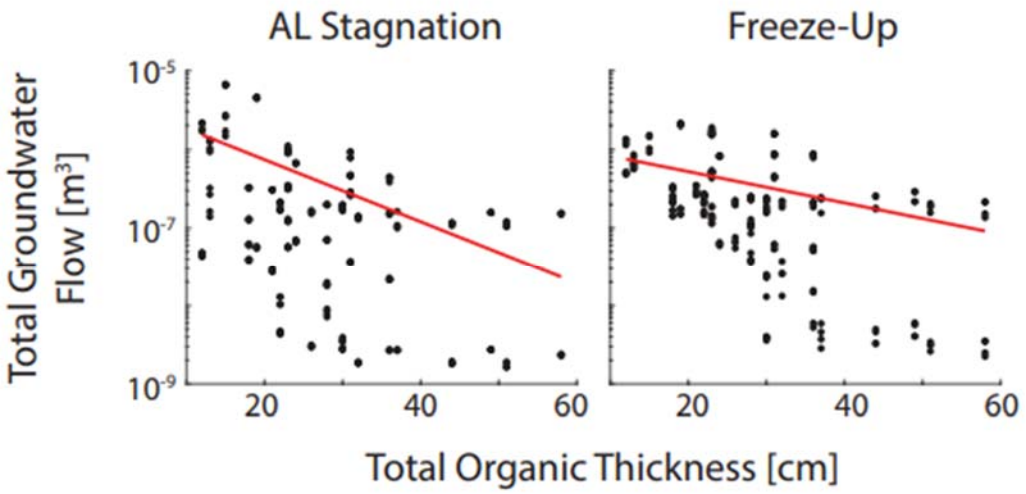

Figure 4.9: Scatterplots showing how total groundwater flows are affected by total organic thickness during (left panel) Active Layer Development and (right panel) Freeze-Up.

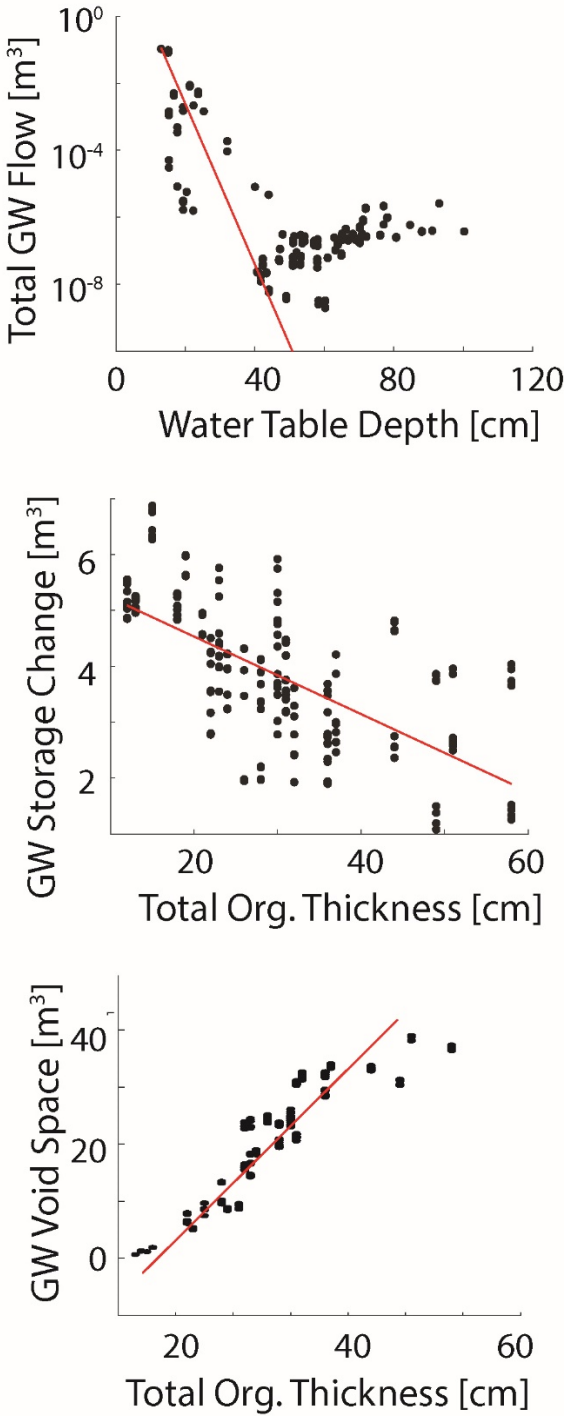

Figure 4.10: Scatterplots showing how groundwater flow, change in storage, and total void space are affected by water table depth and total organic thickness during Over-Winter.

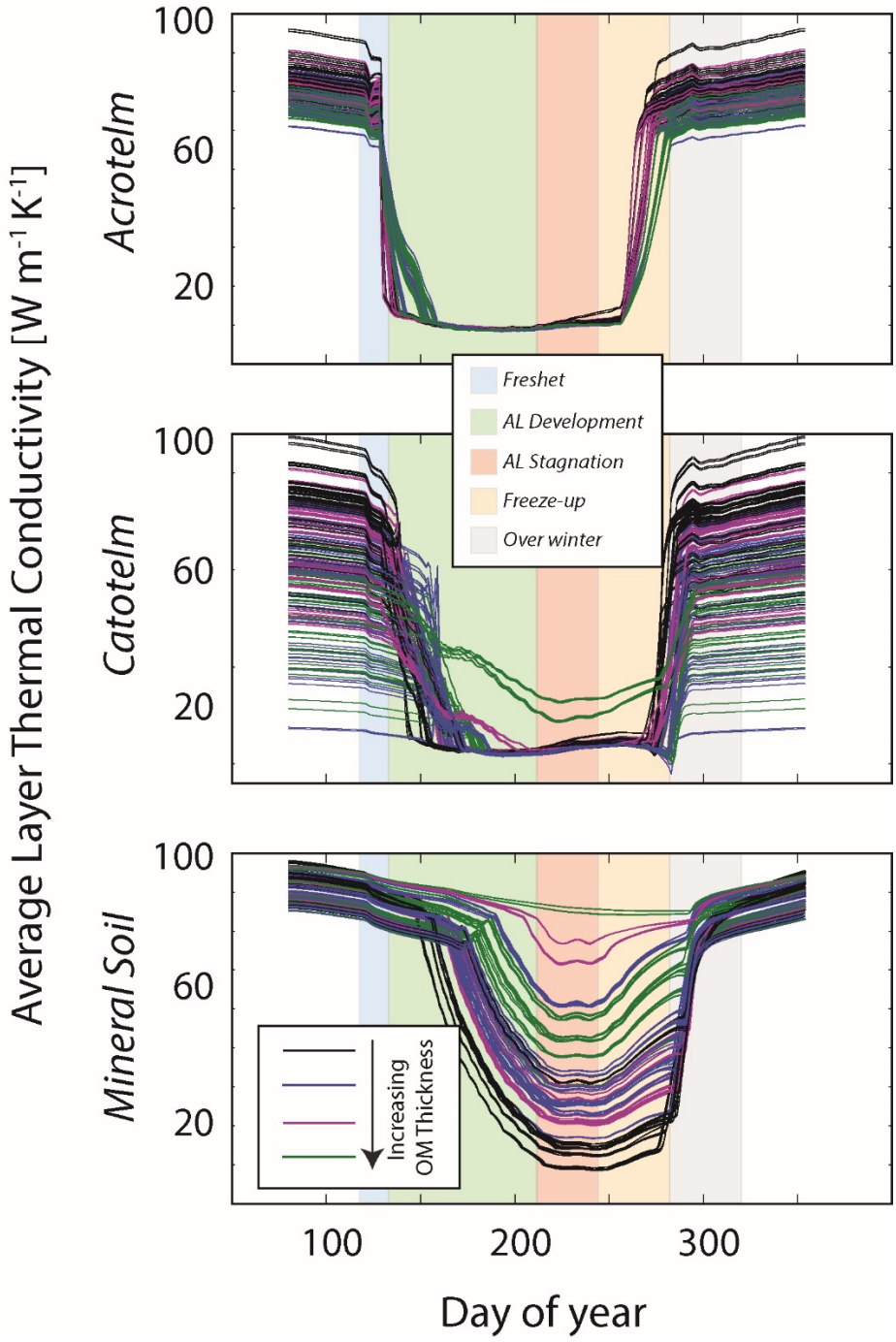

Figure 4.11: Total effective thermal conductivity of (top row) all acrotelm soil, (middle row) all catotelm soil, and (bottom row) all mineral soil over the course of the simulated year for all simulations. Shaded colors represent the five seasons denoted in the manuscript.

Chapter 5: Conclusions

5.1 Synthesis

This dissertation provides, in sequence, some of the answers necessary to understand the complexities of permafrost hydrology. It determines the dominant controls of groundwater flow in arctic landscapes, identifies how those controls commonly vary across space, and determines how thermal hydrologic processes are affected by the variability of soil properties. These investigations provide insight necessary to help predict the future of arctic carbon in permafrost environments.

This dissertation began in Chapter Two with a field exercise designed to determine the dominant external drivers and internal controls that governed groundwater flow in the active layer. Using Darcy's Law as the framework, I built six hydrologic monitoring grids within two topographically distinct landscape zones, and within each grid I measured all the components necessary to calculate groundwater flows: head gradient, aquifer saturated thickness, and aquifer permeability. I took these measurements both in the early summer when the active layer was thin, and in the late summer when the active layer was thick. I found that the subsurface stratigraphy, which describes the permeability structure of the active layer, governs groundwater flows. In steeper-sloping terrains, groundwater flows are strongly controlled by the stark decay in permeability that occurs within the narrow depth of the active layer, between the more-permeable overlying organic soil and the less-permeable underlying mineral soil. In shallow terrains, however, organic soil layers are substantially thicker, and groundwater flows are controlled both by permeability-depth decay and aquifer thickening due to thaw.

Chapter Two highlighted the primary importance that soil layer thicknesses, and the properties of those soil layers, exert on groundwater flows. Chapter Three was therefore designed to understand how those properties and thicknesses varied across the landscape. I hypothesized that commonly-accepted patterns of vegetation and relief observed on the land surface would similarly yield predictable subsurface stratigraphic

patterns with normally-distributed and predictable thermal and hydraulic properties. To test this hypothesis, I measured the stratigraphy, hydraulic properties, and thermal properties of active layer soil across the common vegetation types, land surface slopes, and microtopographic positions found in the North Slope Foothills in Alaska. These measurements found that stratigraphic patterns were predictable based on surface properties, and that the hydraulic and thermal properties of each of the two organic-rich layers were normally distributed and varied little across landscape classes. I also found that the often-overlooked mineral soil layer exhibits a much wider range in properties than previously considered.

Finally, Chapter Four determined if thermal hydrologic processes that help govern soil carbon transport in the Arctic (thaw, groundwater flow, and soil moisture storage) are significantly affected by the stratigraphy and variability of soil properties found in Chapter Three. I performed a numerical experiment in which I compared the active layer development, lateral groundwater flow, and soil moisture storage across a suite of model hillslopes with identical geometries and atmospheric forcings. The model hillslopes varied in that I imposed the measured ranges in soil layer thicknesses, hydraulic properties, and thermal properties determined for each of the seven landscape types identified in Chapter Three. The results from the numerical experiment showed primarily that active layers are significantly shallower, groundwater flows are significantly lower, and groundwater storage is significantly higher in hillslopes with thicker organic layers. These results also showed that mineral soil permeability, often overlooked, exerts a significant control on lateral groundwater flows, and that the differentiation between acrotelm and catotelm within the organic soil layer affects the volumes of groundwater that are transported laterally versus stored.

5.2 "WHAT ARE WE GOING TO DO NOW? THE SAME THING WE DO EVERY NIGHT…TRY TO TAKE OVER THE WORLD!"

The insight provided by this dissertation is of wide interest across multiple communities because of the groundwork it provides for reality-based upscaling of

thermal hydrology processes to regional and global models. This dissertation helps navigate a primary challenge to representing permafrost hydrology in global models: how to accurately represent computationally-intensive and local-scale processes that are critical to the outcome, such as freeze-thaw in spatially-variable unsaturated soils, without necessarily computing all the physical processes. The movement of soil moisture is an example of one such highly-localized, yet critically-important physical process because soil moisture content in the unsaturated zone regulates biogeochemical reactions (Holden & Fierer, 2005; Lawrence et al., 2015), and also acts as an insulative 'blanket' that can inhibit permafrost thaw (Atchley et al., 2016; Jafarov & Schaefer, 2015).

This dissertation has shown that the thermal hydraulic processes in the active layer vary substantially due to local-scale heterogeneity in soil properties; it also shows that the soil properties that govern these processes are readily predictable based on land surface characteristics. The next step of this work, therefore, is to implement this characterization of soil properties across wide areas for a large-scale estimate of active layer thermal hydrology.

The representation of locally-variable yet critically important soil thermal and hydraulic properties across wide areas requires that two problems be addressed: the physics of the larger landscape must be simplified, and that larger landscape must be accurately parameterized. The physics of unsaturated freeze/thaw are too computationally intensive to fully implement across large areas. However, if the large areas are broken down into smaller, independent units, they can be effectively represented. Such an approach is detailed in Jan et al. (2018), and any Arctic upscaling model should follow that approach. In the Arctic Foothills, where the dissertation focused, the independent 'unit' that should be employed is a water track-hillslope complex. 'Water tracks' are slight topographic lows that serve as the central spine of mini-watersheds that drain arctic hillslopes. Each unit should comprise a water track in the center, and will extend to the midpoint between adjacent water tracks (Figure 5.1). It is possible to delineate these units using currently-available remote sensing data products of the topography, geometry, and vegetation type of the North Slope Foothills (Figure

5.1) (Morin et al., 2016; Payne, 2013). These data products also address the second problem, parameterization. By knowing the topography, geometry, and dominant vegetation type of wide areas, the relationships established in Chapter Three of this Dissertation can be employed to parameterize the subsurface. The combination of a physically-based simplification of computationally-intensive physics and broad, physically-based parameterization of the subsurface provides a complete blueprint for regional and pan-Arctic thermal hydrology simulations.

5.3 Final Thoughts

This dissertation identified what is important in an unknown environment, characterized how those important properties vary across space, and quantified the impact that those properties can have on processes we care about. This process is the result of letting new questions arise from old ones, and allowing those questions to guide the next step of research. The openness with which the dissertation was conducted is directly responsible for this clear train of logic. Given this experience, I highly encourage future advisors and doctoral students to allow themselves the freedom to let their research follow the questions. This type of scientific process both ensures the questions remain relevant and keeps the investigators interested. I am thankful that in this dissertation, I feel I've been able to do both.

5.4 FIGURES FOR CONCLUSION

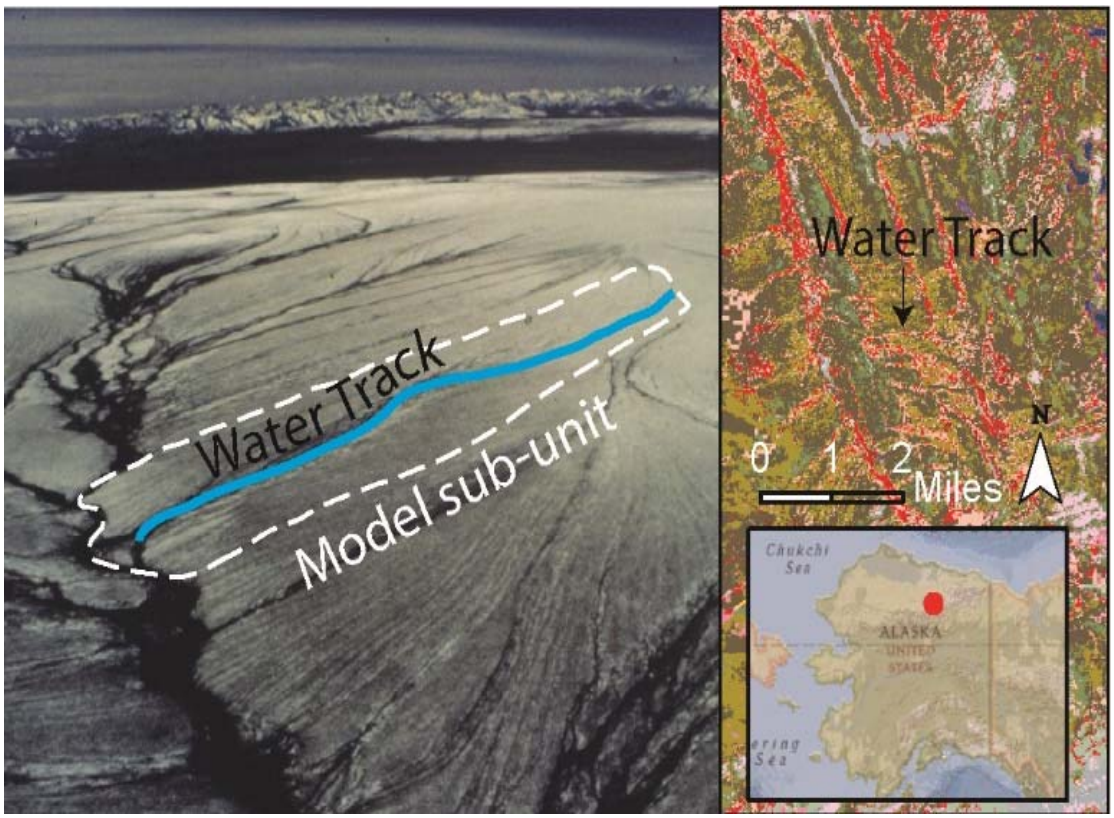

Figure 5.1: Example of a water track-hillslope unit from aerial imagery (left panel) and as shown on the NSSI Land Cover Map (right panel).

Appendices

APPENDIX A: SUPPLEMENTAL MATERIALS FOR CHAPTER 2

Table A1: All field data collected for analysis in Chapter Two during the 2016 Summer at Imnavait Creek

		UTM zone 6N [m]	UTM zone 6N [m]	NAVD88 [m]	NAVD88 [m]	[cm]	[cm]	[cm]	[cm]	[cm]	[cm]	[-]
Grid ID	Well ID	Easting	Northing	Top of Casing Elev.	Ground Surface Elev.	Thaw Depth 1	Thaw Depth 2	Thaw Depth 3	Depth to Water	Height of Well Stickup	Well Length	Local High or Low
fvb	1	405746.2	7612806.2	889.064	888.01	16	14	16	19.5		120	H
fvb	2	405746.1	7612802.7	889.032	888.01	21	19	20	19		120	L
fvb	3	405745.7	7612798.7	889.202	888.13	22	20	16	13		120	L
fvb	4	405745.5	7612794.8	889.311	888.31	21	23	23	15.5		120	H
fvb	5	405744.9	7612790.9	889.437	888.34	17	16	16	3.5		120	H
fvb	6	405744.0	7612786.9	889.092	888.37	23	24	23	13		90	H
fvb	7	405742.2	7612788.9	889.242	888.28	29	29	30	24		120	L
fvb	8	405742.8	7612792.7	889.199	888.23	28	28	28	27		120	L
fvb	9	405743.3	7612796.7	889.267	888.20	15	13	14	8		120	L
fvb	10	405743.6	7612800.7	889.081	888.03	17	19	18	14		120	L
fvb	11	405744.0	7612804.6	888.975	887.86	17	19	18	20		120	L
fvb	12	405742.2	7612806.3	888.697	887.94	17	17	16	1		90	L
fvb	13	405741.9	7612803.1	888.73	887.97	20	20	21	17		90	L
fvb	14	405741.3	7612799.4	888.848	888.10	20	20	19	16		90	L
fvb	15	405740.7	7612795.0	889.159	888.29	13	10	9	2		90	H
fvb	16	405740.1	7612791.2	889.588	888.45	10	9	10	1		120	H
fvb	17	405740.1	7612786.8	889.166	888.37	15	16	15	3.5		90	L
fvb	18	405738.4	7612788.6	889.311	888.49	10	11	12	0		90	H
fvb	19	405738.9	7612793.1	889.197	888.38	14	15	15	2		90	H
fvb	20	405739.5	7612797.2	889.238	888.50	18	20	22	1		90	H
fvb	21	405739.7	7612801.1	888.756	888.05	23	24	22	18		90	H
fvb	22	405740.2	7612804.8	888.809	888.02	16	16	16	9		90	L
fvb	23	405738.2	7612806.5	888.794	888.01	14	15	14	5		90	H
fvb	24	405738.1	7612803.4	888.797	888.03	17	18	18	11		90	L
fvb	25	405737.5	7612799.8	888.954	888.13	12	12	16	0		90	H
fvb	26	405737.4	7612795.2	888.981	888.16	13	13	13	3		90	H
fvb	27	405736.9	7612791.3	889.15	888.31	10	11	10	2		90	H
fvb	28	405736.1	7612786.6	889.003	888.21	12	13	14	4		90	L
fvb	29	405734.6	7612789.0	889.036	888.23	13	14	10	1		90	H
fvb	30	405735.1	7612793.3	889.174	888.34	10	15	12	1		90	H
fvb	31	405735.9	7612797.6	888.932	888.11	10	10	11	0		90	L
fvb	32	405736.3	7612801.3	888.826	888.00	12	12	11	2		90	L
fvb	33	405736.5	7612804.9	889.148	888.37	17	17	17	0		90	H
fvb	34	405734.2	7612806.6	888.888	887.79	11	13	12	8		120	L
fvb	35	405733.9	7612802.5	888.719	887.96	15	16	17	11		90	L

fvb	36	405733.5	7612798.4	888.875	888.06	10	11	11	0		90	H
fvb	37	405732.9	7612794.4	888.974	888.18	9	10	11	1		90	H
fvb	38	405732.5	7612790.4	889.111	888.30	13	12	13	0		90	H
fvb	39	405731.9	7612786.5	889.503	888.39	10	11	11	0		120	H
fvb	40	405730.2	7612788.5	889.208	888.13	14	13	13	0		120	L
fvb	41	405730.8	7612792.4	889.281	888.17	12	11	10	1		120	L
fvb	42	405731.3	7612796.4	888.904	888.10	12	11	11	4.5		90	L
fvb	43	405731.7	7612800.4	888.856	888.02	14	13	13	1		90	L
fvb	44	405732.0	7612804.4	889.254	888.12	10	10	9	0		120	H
fvb	45	405730.2	7612806.6	888.935	887.86	13	14	13	0		120	H
fvb	46	405729.9	7612802.1	889.237	888.14	10	10	10	1		120	H
fvb	47	405729.2	7612798.4	889.311	888.24	14	13	14	0		120	H
fvb	48	405728.7	7612794.3	888.951	888.17	13	13	12	2		90	L
fvb	49	405728.4	7612790.5	889.209	888.09	15	16	17	2		120	L
fvb	50	405726.8	7612792.7	889.003	888.20	12	13	12	1		90	H
fvb	51	405727.4	7612796.7	889.299	888.20	10	10	12	1		120	H
fvb	52	405727.9	7612800.4	889.097	887.99	10	9	10	3		120	H
fvb	53	405728.1	7612804.5	888.641	887.84	11	12	11	3.5		90	H
fvb	54	405726.3	7612806.6	888.499	887.69	10	11	12	0		90	H
fvb	55	405726.0	7612803.0	888.586	887.80	16	17	16	6.5		90	L
fvb	56	405725.5	7612799.0	888.744	887.93	12	13	12	0		90	H
fvb	57	405725.2	7612795.1	888.875	888.09	13	12	13	2		90	H
fvb	58	405724.9	7612791.0	889.039	887.96	17	15	16	12		120	L
fvb	59	405723.6	7612792.8	888.653	887.88	20	19	19	22		90	L
fvb	60	405723.9	7612796.8	888.783	887.97	8	9	8	0		90	H
fvb	61	405724.0	7612800.7	888.788	887.72	16	17	17	13		120	L
fvb	62	405724.1	7612804.8	888.54	887.78	16	17	16	0		90	H
fvb	63	405722.3	7612806.5	888.26	887.60	29	30	29	20		90	L
fvb	64	405722.3	7612802.1	888.393	887.57	20	22	23	20		90	L
fvb	65	405721.6	7612795.8	888.592	887.84	18	17	17	9		90	L
fvb	66	405721.0	7612790.3	888.719	887.96	18	16	18	11.5		90	L
svb	1	405733.3	7613224.0	880.415	879.58	13	11	12	7		90	L
svb	2	405733.3	7613221.8	880.063	879.82	10	10	8	0		90	H
svb	3	405733.3	7613217.9	880.321	880.12	10	10	10	0		90	H
svb	4	405733.2	7613213.9	880.707	880.19	8	8	10	0		120	L
svb	5	405732.9	7613209.9	880.511	880.26	4	6	6	0		90	L
svb	6	405733.0	7613205.8	880.597	880.36	8	6	6	0		90	H
svb	7	405732.9	7613202.0	880.611	880.12	15	16	15	11		120	L
svb	8	405731.0	7613203.7	880.535	880.05	14	12	15	6		120	L
svb	9	405731.1	7613207.7	880.382	880.12	8	10	6	0		90	H
svb	10	405731.2	7613211.7	880.296	880.08	10	10	10	2		90	L
svb	11	405731.4	7613215.6	880.402	880.17	10	10	10	0		90	H
svb	12	405731.4	7613219.7	880.496	879.93	6	2	2	0		120	H
svb	13	405729.7	7613221.5	879.839	879.58	7	6	9	0		90	L
svb	14	405729.5	7613217.4	879.992	879.76	10	9	10	0		90	L
svb	15	405729.5	7613213.6	880.482	879.98	10	10	10	0		120	H
svb	16	405728.9	7613209.5	880.279	880.03	8	9	8	0		90	H
svb	17	405729.1	7613205.4	880.38	879.83	10	9	10	4		120	L

svb	18	405729.1	7613201.6	880.395	879.95	17	17	15	6		120	L
svb	19	405727.1	7613203.2	879.86	879.74	15	17	17	13		90	L
svb	20	405727.2	7613207.3	880.408	879.93	13	15	15	1		120	H
svb	21	405727.2	7613211.3	880.125	879.95	11	13	13	0		90	H
svb	22	405727.5	7613215.2	880.1	879.86	5	6	4	0		90	H
svb	23	405727.6	7613219.3	879.705	879.45	9	9	8	0		90	L
svb	24	405728.0	7613223.5	879.907	879.36	9	8	7	0		120	L
svb	25	405725.8	7613221.1	879.577	879.32	5	5	6	0		90	H
svb	26	405725.5	7613217.0	879.839	879.61	10	10	10	0		90	H
svb	27	405725.5	7613213.4	879.952	879.73	8	6	8	0		90	H
svb	28	405725.0	7613209.1	879.963	879.75	9	9	10	0		90	H
svb	29	405725.2	7613205.0	880.036	879.55	9	11	10	10		120	L
svb	30	405725.1	7613201.2	880.112	879.66	15	13	14	5		120	L
svb	31	405723.1	7613202.9	879.654	879.46	13	11	13	7		90	L
svb	32	405723.3	7613206.8	879.694	879.48	13	12	13	8		90	L
svb	33	405723.2	7613210.9	880.006	879.75	6	13	8	4		90	H
svb	34	405723.5	7613214.7	879.772	879.56	12	14	13	0		90	H
svb	35	405723.7	7613218.9	879.561	879.30	4	4	5	0		90	L
svb	36	405724.0	7613222.8	879.413	879.15	6	6	7	0		90	L
svb	37	405721.8	7613220.6	879.271	879.02	6	7	6	0		90	L
svb	38	405721.6	7613216.5	879.605	879.40	6	7	8	0		90	H
svb	39	405721.6	7613212.9	879.68	879.44	10	11	10	0		90	L
svb	40	405721.1	7613208.7	880.011	879.48	14	13	12	1		120	H
svb	41	405721.3	7613204.7	879.788	879.28	13	12	14	12		120	L
svb	42	405721.2	7613200.7	879.955	879.53	19	20	17	5		120	L
svb	43	405719.1	7613202.4	879.557	879.27	6	8	8	0		90	L
svb	44	405719.3	7613206.4	879.752	879.27	22	21	22	4		120	L
svb	45	405719.3	7613210.5	879.618	879.42	12	10	12	0		90	H
svb	46	405719.6	7613214.3	879.587	879.36	10	11	12	2		90	H
svb	47	405719.7	7613218.4	879.359	879.17	8	8	7	0		90	H
svb	48	405720.1	7613222.3	879.519	878.95	2	4	4	1		120	L
svb	49	405717.9	7613220.2	879.185	878.92	6	7	8	0		90	L
svb	50	405717.6	7613216.1	879.369	879.14	10	10	11	0		90	H
svb	51	405717.6	7613212.3	879.798	879.24	7	6	7	0		120	H
svb	52	405717.1	7613208.2	879.7	879.14	8	6	10	1		120	L
svb	53	405717.2	7613204.3	879.213	879.04	24	16	17	11		90	L
svb	54	405717.3	7613200.2	879.719	879.28	13	18	16	9		120	L
svb	55	405715.1	7613202.0	879.693	879.22	15	15	16	3		120	H
svb	56	405715.3	7613206.1	879.122	878.93	14	15	13	12		90	L
svb	57	405715.3	7613210.1	879.263	879.03	6	10	9	0		90	L
svb	58	405715.5	7613214.0	879.66	879.13	10	11	11	1		120	H
svb	59	405715.7	7613218.0	879.174	878.93	6	6	6	1		90	L
svb	60	405714.2	7613221.8	878.994	878.82	16	15	16	1		90	L
svb	61	405713.8	7613219.9	879.055	878.78	8	7	8	0		90	L
svb	62	405713.6	7613215.8	879.448	878.94	6	8	10	1		120	H
svb	63	405713.8	7613211.9	879.223	878.96	12	8	8	0		90	L
svb	64	405713.6	7613207.9	879.418	878.91	8	10	10	2		120	L
svb	65	405713.7	7613203.9	879.301	879.05	8	7	8	0		90	H

svb	66	405713.5	7613199.8	879.559	879.09	17	17	17	11		120	L
sb	1	405852.8	7612823.9	892.308	891.47	11	12	13	7		90	L
sb	2	405853.4	7612819.9	892.471	891.62	12	11	13	0		90	L
sb	3	405854.1	7612816.0	892.662	891.89	14	17	15	0		90	H
sb	4	405855.1	7612812.1	892.596	891.50	12	12	14	11		120	L
sb	5	405855.8	7612808.2	892.869	891.71	8	9	7	0		120	H
sb	6	405856.8	7612804.4	892.927	891.83	17	16	15	2		120	H
sb	7	405854.5	7612806.1	892.42	891.67	21	17	22	0		90	H
sb	8	405853.7	7612809.8	892.309	891.57	22	15	17	0		90	L
sb	9	405852.8	7612813.7	892.277	891.46	17	12	17	7		90	L
sb	10	405851.9	7612817.7	892.388	891.58	14	12	10	0		90	L
sb	11	405851.2	7612821.6	892.198	891.39	17	17	14	6.5		90	L
sb	12	405849.0	7612823.1	892.062	891.21	17	15	13	10		90	L
sb	13	405849.8	7612819.3	892.121	891.26	8	10	6	6		90	L
sb	14	405850.5	7612815.3	892.603	891.47	11	9	13	1		120	H
sb	15	405851.2	7612811.4	892.121	891.38	20	20	22	10		90	H
sb	16	405852.0	7612807.7	892.262	891.44	15	15	15	6		90	L
sb	17	405852.9	7612803.7	892.78	891.68	17	15	16	0		120	H
sb	18	405850.6	7612805.4	892.18	891.33	12	12	13	5		90	L
sb	19	405849.7	7612809.2	892.513	891.40	9	13	11	0		120	H
sb	20	405848.9	7612813.1	892.178	891.31	10	12	8	0		90	H
sb	21	405848.1	7612817.1	892.285	891.45	14	13	15	0		90	H
sb	22	405847.4	7612820.7	892.03	891.19	12	12	11	3		90	L
sb	23	405845.0	7612822.6	892.129	891.09	28	33	26	13		120	H
sb	24	405845.9	7612818.7	892.468	891.31	12	9	10	0		120	H
sb	25	405846.6	7612814.7	892.079	891.21	13	12	10	0		90	H
sb	26	405847.3	7612810.8	891.94	891.17	20	21	26	11		90	L
sb	27	405848.2	7612807.1	892.175	891.40	20	25	20	0		90	H
sb	28	405849.1	7612803.1	892.143	891.34	12	12	17	5		90	L
sb	29	405846.6	7612804.6	891.982	891.21	18	19	18	7		90	L
sb	30	405845.8	7612808.7	892.373	891.24	10	12	13	0		120	H
sb	31	405844.8	7612812.4	892.246	891.09	12	15	11	3.5		120	L
sb	32	405844.2	7612816.5	891.721	890.87	6	8	7	18		90	L
sb	33	405843.3	7612819.9	892.01	891.21	13	12	14	0		90	H
sb	34	405841.0	7612821.9	891.709	890.99	23	24	22	9		90	H
sb	35	405841.9	7612818.1	892.309	891.16	12	10	12	0		120	H
sb	36	405842.6	7612814.1	891.785	891.06	17	117	18	5		90	L
sb	37	405843.5	7612810.2	892.099	891.05	20	19	19	10		120	H
sb	38	405844.2	7612806.3	891.988	891.19	19	16	17	0		90	H
sb	39	405845.1	7612802.5	892.316	891.18	6	6	6	3		120	L
sb	40	405842.7	7612804.0	891.888	891.20	20	21	22	5		90	H
sb	41	405841.8	7612808.0	891.975	890.83	12	12	13	13		120	L
sb	42	405841.1	7612811.8	891.921	890.79	13	15	12	15		120	L
sb	43	405840.2	7612815.9	892.197	891.01	13	15	12	0		120	H
sb	44	405839.4	7612819.2	891.63	890.86	13	12	12	9		90	L
sb	45	405837.0	7612821.3	891.502	890.84	23	26	25	12		90	H
sb	46	405838.0	7612817.4	891.688	890.87	11	9	10	0		90	H
sb	47	405838.7	7612813.5	891.566	890.75	14	15	12	10		90	L

sb	48	405839.4	7612809.7	891.663	890.92	20	20	19	9		90	H
sb	49	405840.3	7612805.6	891.814	890.96	11	14	9	0		90	H
sb	50	405841.1	7612801.8	892.089	891.30	10	12	10	0		90	H
sb	51	405838.8	7612803.5	891.674	890.85	10	11	13	7		90	L
sb	52	405837.9	7612807.3	891.891	890.86	20	20	22	10		120	H
sb	53	405837.1	7612811.1	891.67	890.79	3	6	4	0		90	H
sb	54	405836.3	7612815.2	891.516	890.69	13	12	14	3		90	L
sb	55	405836.2	7612818.9	891.695	890.56	8	10	8	17		120	L
sb	56	405833.2	7612820.9	891.755	890.65	10	8	11	3		120	H
sb	57	405834.1	7612816.9	891.836	890.68	8	9	8	0		120	H
sb	58	405834.8	7612813.0	891.442	890.65	14	15	16	10		90	L
sb	59	405835.7	7612809.1	891.774	890.72	18	20	18	11		120	L
sb	60	405836.4	7612805.2	891.564	890.76	17	17	15	8		90	L
sb	61	405837.3	7612801.3	892.051	890.92	8	7	7	1		120	H
hil	1	405946.7	7612880.4	900.402	899.61	18	17	17	0		90	H
hil	2	405947.8	7612876.6	900.64	899.53	14	15	13	7		120	L
hil	3	405948.9	7612872.7	900.752	899.61	9	13	12	0		120	L
hil	4	405949.5	7612868.8	900.437	899.61	14	11	17	0		90	L
hil	5	405950.6	7612864.9	900.701	899.61	13	16	12	0		120	L
hil	6	405951.8	7612861.1	900.433	899.58	14	14	8	0		90	L
hil	7	405949.2	7612862.4	900.491	899.34	10	11	10	1		120	L
hil	8	405948.3	7612866.4	900.294	899.46	8	7	9	0		90	H
hil	9	405947.2	7612870.2	900.267	899.40	10	10	10	0		90	H
hil	10	405946.3	7612874.1	900.211	899.38	13	14	12	0		90	L
hil	11	405945.4	7612878.1	900.51	899.36	T8	9	10	3.5		120	L
hil	12	405943.0	7612879.6	900.362	899.20	4	10	10	0		120	L
hil	13	405943.8	7612875.7	900.032	899.26	15	21	20	4		90	H
hil	14	405944.7	7612871.8	900.13	899.35	11	8	18	0		90	H
hil	15	405945.6	7612868.0	900.347	899.27	15	15	12	0		120	H
hil	16	405946.5	7612864.1	899.978	899.16	13	12	12	0		90	L
hil	17	405947.6	7612859.4	900.007	899.18	11	10	12	0		90	L
hil	18	405945.1	7612861.5	899.736	898.96	8	10	7	0		90	L
hil	19	405944.0	7612865.4	900.111	898.97	5	5	6	0		120	H
hil	20	405943.2	7612869.5	899.863	899.00	10	5	5	0		90	L
hil	21	405942.3	7612873.4	899.831	899.01	12	13	12	0		90	L
hil	22	405941.3	7612877.3	899.888	899.18	20	21	21	0		90	H
hil	23	405939.0	7612878.6	899.557	898.68	8	8	6	0		90	L
hil	24	405939.9	7612874.8	899.602	898.78	13	14	11	4		90	L
hil	25	405940.8	7612870.9	899.952	898.90	18	15	17	0		120	H
hil	26	405941.7	7612867.0	899.894	898.86	17	17	21	0		120	H
hil	27	405942.4	7612863.2	899.817	898.65	11	10	8	0		120	L
hil	28	405943.9	7612858.0	899.547	898.70	5	8	6	0		90	L
hil	29	405941.3	7612860.8	899.387	898.54	16	18	13	0		90	H
hil	30	405940.3	7612864.6	899.692	898.53	6	10	6	0		120	L
hil	31	405939.4	7612868.5	899.455	898.61	8	10	7	0		90	L
hil	32	405938.6	7612872.4	899.461	898.71	13	13	13	0		90	H
hil	33	405937.8	7612876.3	899.424	898.65	14	17	15	0		90	L
hil	34	405935.2	7612877.7	899.536	898.38	10	8	8	0		120	L

hil	35	405936.2	7612873.9	899.535	898.38	10	9	15	2		120	H
hil	36	405936.9	7612870.0	899.268	898.43	14	13	11	0		90	L
hil	37	405937.9	7612866.1	899.223	898.38	13	12	14	0		90	H
hil	38	405938.8	7612862.3	899.037	898.29	12	20	23	11		90	H
hil	39	405939.9	7612857.6	899.08	898.21	8	11	8	3.5		90	L
hil	40	405937.5	7612859.8	899.081	898.22	8	9	9	0		90	H
hil	41	405936.5	7612863.6	898.958	898.10	10	8	10	0		90	L
hil	42	405935.7	7612867.5	898.966	898.10	9	10	10	0		90	L
hil	43	405934.6	7612871.8	898.995	898.10	15	14	15	0		120	L
hil	44	405933.8	7612875.3	899.358	898.23	10	11	12	0		120	L
hil	45	405931.3	7612876.9	899.115	897.97	12	10	11	0		120	H
hil	46	405932.3	7612872.9	899.077	898.01	12	17	12	0		120	H
hil	47	405933.2	7612869.1	899.171	898.05	14	11	12	0		120	L
hil	48	405934.2	7612865.2	899.188	898.04	12	10	10	0		120	L
hil	49	405935.2	7612861.3	898.912	898.04	6	7	8	0		90	L
hil	50	405936.1	7612857.5	898.746	898.07	18	20	24	6		120	H
hil	51	405933.7	7612859.0	898.649	897.83	12	13	10	1		120	H
hil	52	405932.8	7612862.9	898.961	897.81	8	8	7	0		120	L
hil	53	405931.9	7612866.8	899.086	897.92	18	18	17	0		120	H
hil	54	405930.9	7612870.7	898.754	897.96	12	12	11	0		90	H
hil	55	405929.9	7612874.6	898.825	897.96	8	8	10	0		90	H
hil	56	405927.7	7612876.4	898.477	897.68	18	19	16	0		90	H
hil	57	405928.3	7612872.5	898.749	897.60	12	12	12	5		120	L
hil	58	405929.3	7612868.6	898.51	897.63	10	9	10	0		90	L
hil	59	405930.2	7612864.8	898.547	897.70	10	11	12	0		90	L
hil	60	405931.2	7612860.9	898.485	897.62	7	8	8	0		90	L
hil	61	405932.1	7612857.1	898.764	897.67	17	13	17	0		120	L
rip	1	405780.1	7612867.7	889.514	888.36	9	8	7	4		120	L
rip	2	405780.6	7612863.8	889.369	888.50	13	11	11	0		90	H
rip	3	405781.1	7612859.8	889.344	888.60	16	21	18	9		90	H
rip	4	405781.6	7612855.9	889.411	888.58	10	13	10	10		90	L
rip	5	405782.1	7612851.9	889.476	888.65	13	15	14	5.5		90	H
rip	6	405782.7	7612848.0	889.695	888.62	17	17	16	15		120	L
rip	7	405780.6	7612849.7	889.406	888.59	11	13	13	11		90	L
rip	8	405780.0	7612853.6	889.706	888.64	18	20	17	2		120	H
rip	9	405779.5	7612857.6	889.281	888.53	24	26	20	13		90	H
rip	10	405779.0	7612861.5	889.506	888.43	14	14	17	6		120	H
rip	11	405778.4	7612865.4	889.192	888.33	8	8	8	2		90	L
rip	12	405776.3	7612867.2	889.096	888.30	15	16	15	0		90	H
rip	13	405776.8	7612863.3	889.127	888.41	20	20	21	4		90	H
rip	14	405777.2	7612859.3	889.486	888.38	12	14	14	8.5		120	L
rip	15	405777.7	7612855.3	889.627	888.50	9	12	11	0		120	H
rip	16	405778.1	7612851.4	889.378	888.60	17	17	19	7.5		90	H
rip	17	405778.8	7612847.5	889.338	888.58	20	18	17	15		90	L
rip	18	405776.6	7612849.1	889.237	888.43	13	17	15	9.5		90	L
rip	19	405776.0	7612853.1	889.363	888.69	26	25	27	1		90	H
rip	20	405775.5	7612857.0	889.183	888.38	21	24	28	5		90	
rip	21	405775.0	7612860.9	889.112	888.34	20	19	19	6		90	H

rip	22	405774.4	7612864.9	888.97	888.14	16	17	17	7		90	H
rip	23	405772.4	7612866.6	888.817	888.07	16	16	17	11		90	H
rip	24	405772.7	7612862.7	889.239	888.11	8	6	8	7		120	L
rip	25	405773.2	7612858.7	888.972	888.16	10	13	12	9		90	L
rip	26	405773.7	7612854.7	889.233	888.44	13	15	16	0		90	H
rip	27	405774.1	7612850.7	889.214	888.45	19	18	18	6		90	H
rip	28	405774.8	7612847.0	889.21	888.49	20	21	19	12		90	H
rip	29	405772.6	7612848.7	889.095	888.33	18	16	18	12		90	L
rip	30	405772.1	7612852.6	889.012	888.30	21	19	22	15		90	L
rip	31	405771.6	7612856.4	889.346	888.24	12	12	11	1		120	H
rip	32	405771.2	7612860.5	888.92	888.15	17	17	17	9		90	H
rip	33	405770.7	7612864.4	889.151	888.07	17	16	20	5		120	H
rip	34	405768.4	7612866.1	888.695	887.89	18	20	15	6		90	H
rip	35	405769.0	7612862.1	889.077	887.95	17	14	18	6		120	L
rip	36	405769.3	7612858.1	889.259	888.19	15	14	15	0		120	H
rip	37	405769.7	7612854.2	889.241	888.25	25	25	26	12		120	H
rip	38	405770.2	7612850.2	889.383	888.26	13	11	11	5		120	
rip	39	405770.9	7612846.3	889.351	888.30	20	20	19	23		120	L
rip	40	405768.6	7612847.9	889.385	888.28	12	13	14	5		120	L
rip	41	405768.2	7612852.0	888.99	888.24	20	20	20	5		90	H
rip	42	405767.6	7612855.9	889.061	888.07	24	23	26	14		120	H
rip	43	405767.1	7612859.8	888.827	887.99	13	15	12	1		90	H
rip	44	405766.8	7612863.7	888.639	887.82	12	15	12	8.5		90	L
rip	45	405764.6	7612865.6	888.811	887.71	14	15	15	12		120	L
rip	46	405765.0	7612861.7	888.701	887.88	17	17	18	5		90	H
rip	47	405765.5	7612857.7	888.708	887.95	17	20	19	10.5		90	L
rip	48	405765.9	7612853.7	889.084	887.95	10	10	9	8		120	L
rip	49	405766.5	7612849.8	889.022	888.24	12	15	15	0		90	H
rip	50	405766.9	7612845.9	889.001	888.34	18	19	19	18		90	H
rip	51	405764.7	7612847.8	888.96	888.19	16	16	15	7		90	H
rip	52	405764.3	7612851.7	888.869	888.04	14	12	11	0		90	H
rip	53	405763.8	7612855.7	888.643	887.81	10	12	11	11		90	L
rip	54	405763.3	7612859.5	888.93	887.80	10	10	8	7		120	L
rip	55	405762.8	7612863.6	888.919	887.81	14	15	14	1		120	H
rip	56	405760.6	7612865.2	888.722	887.56	10	9	9	9		120	L
rip	57	405761.0	7612861.2	888.817	887.71	15	16	16	10		120	L
rip	58	405761.5	7612857.3	888.554	887.86	22	23	25	16		90	L
rip	59	405761.9	7612853.4	888.608	887.82	15	12	13	14		90	L
rip	60	405762.5	7612849.3	888.848	888.06	15	15	13	0		90	H
rip	61	405763.0	7612845.4	888.86	888.09	15	16	16	11		90	L
wes	1	405698.5	7612838.7	0	887.39	8	12	11	4		90	L
wes	2	405698.9	7612834.7	888.73	887.61	11	11	12	0		120	H
wes	3	405699.5	7612830.9	888.421	887.45	27	28	29	18		120	L
wes	4	405699.9	7612826.9	888.402	887.59	11	15	12	0		120	H
wes	5	405700.3	7612823.0	888.397	887.64	19	18	16	6		90	H
wes	6	405700.6	7612819.0	888.438	887.76	43	41	40	14		90	H
wes	7	405698.7	7612821.0	888.788	887.73	20	22	21	6		120	H
wes	8	405698.2	7612824.9	888.716	887.74	24	24	24	16		120	H

wes	9	405697.7	7612828.8	888.396	887.59	23	20	19	0		90	H
wes	10	405697.2	7612832.7	888.303	887.62	28	24	29	6		90	H
wes	11	405697.0	7612836.8	888.77	887.71	20	22	19	0		120	H
wes	12	405695.0	7612838.8	888.236	887.52	26	26	25	9.5		90	L
wes	13	405695.2	7612834.9	888.643	887.85	15	16	15	0		90	H
wes	14	405695.5	7612830.7	888.256	887.55	24	26	26	17		90	L
wes	15	405695.9	7612826.8	888.412	887.67	19	22	20	10		90	H
wes	16	405696.5	7612822.8	888.736	887.72	21	22	21	14.5		120	H
wes	17	405696.7	7612819.0	888.55	887.78	13	14	15	9		90	H
wes	18	405694.7	7612821.1	888.784	887.82	25	27	24	12		120	H
wes	19	405694.3	7612824.8	888.423	887.71	23	21	24	14		90	L
wes	20	405693.9	7612828.8	888.311	887.57	20	22	19	17		90	L
wes	21	405693.3	7612832.7	888.358	887.58	18	17	19	7		90	L
wes	22	405692.9	7612837.1	888.176	887.44	19	19	20	19		90	L
wes	23	405690.9	7612838.7	888.628	887.82	15	13	15	0		90	H
wes	24	405691.1	7612834.8	888.408	887.60	15	14	13	0		90	H
wes	25	405691.6	7612830.6	888.72	887.60	10	15	9	4		120	L
wes	26	405692.1	7612826.7	888.675	887.61	16	16	18	17		120	L
wes	27	405692.5	7612822.7	888.492	887.71	16	16	15	12		90	L
wes	28	405692.8	7612819.0	888.582	887.80	17	17	14	10		90	L
wes	29	405690.7	7612820.9	888.827	887.75	15	16	17	15		120	L
wes	30	405690.3	7612824.8	888.789	887.72	17	16	18	13		120	L
wes	31	405690.0	7612828.8	888.424	887.73	26	26	25	14		90	H
wes	32	405689.3	7612832.6	888.468	887.64	11	13	12	0		90	H
wes	33	405689.1	7612837.1	888.515	887.67	11	9	11	0		90	H
wes	34	405687.1	7612838.8	888.788	887.73	16	15	14	0		120	H
wes	35	405687.3	7612834.7	888.714	887.86	10	10	11	0		90	H
wes	36	405687.5	7612830.6	888.697	887.84	10	10	11	0		90	H
wes	37	405688.1	7612826.8	888.497	887.71	12	14	13	8		90	L
wes	38	405688.5	7612822.8	888.845	887.78	15	17	17	11		120	L
wes	39	405688.8	7612819.0	888.907	887.86	19	20	20	14		120	L
wes	40	405686.7	7612821.1	888.618	887.83	19	18	20	11		90	L
wes	41	405686.3	7612824.8	888.538	887.73	13	12	11	13		90	L
wes	42	405685.9	7612828.6	888.718	887.87	9	10	9	0		90	H
wes	43	405685.4	7612832.7	888.457	887.73	14	15	15	9		90	L
wes	44	405685.1	7612837.1	888.74	887.71	19	24	23	8		120	H
wes	45	405683.0	7612838.9	888.591	887.75	11	10	10	0		90	H
wes	46	405683.3	7612834.8	888.528	887.76	19	18	21	3		90	H
wes	47	405683.6	7612830.7	888.621	887.81	15	14	13	0		90	H
wes	48	405684.1	7612826.7	889.037	887.95	14	15	14	0		120	H
wes	49	405684.7	7612822.8	888.896	888.08	15	14	16	0		90	H
wes	50	405684.8	7612819.0	889.009	888.03	23	27	24	10		120	H
wes	51	405682.8	7612821.1	888.909	888.12	11	10	10	0		90	H
wes	52	405682.3	7612825.0	888.995	887.87	8	10	8	6		120	L
wes	53	405682.0	7612828.4	888.799	888.01	12	12	13	0		90	H
wes	54	405681.5	7612832.8	888.929	887.80	8	10	11	0		120	L
wes	55	405681.1	7612836.9	888.664	887.85	10	10	10	0		90	H
wes	56	405679.3	7612838.8	888.763	887.92	10	12	10	0		90	H

wes	57	405679.4	7612834.8	889.01	887.92	19	19	17	0		120	H
wes	58	405679.6	7612830.6	888.78	887.96	12	10	12	0		90	H
wes	59	405680.2	7612826.7	888.943	888.16	17	16	17	0		90	H
wes	60	405680.7	7612822.8	888.956	888.11	10	10	8	0		90	H
wes	61	405681.0	7612819.1	889.289	888.16	13	12	12	1		120	H
fvb	1	405746.2	7612806.1		887.97	58	62	65	56	62	120	H
fvb	2	405746.2	7612802.7		888.02	65	62	65	61	31	90	L
fvb	3	405745.8	7612798.8		888.12	65	66	66	64	30	90	L
fvb	4	405745.5	7612794.8		888.26	70	70	69	65	24	90	H
fvb	5	405744.9	7612790.8		888.30	65	64	65	61	56	120	H
fvb	6	405744.1	7612787.0		888.33	65	66	65	59	56	120	H
fvb	7	405742.3	7612788.8		888.29	63	65	63	62	28	90	L
fvb	8	405742.8	7612792.8		888.23	70	72	72	72	22	90	L
fvb	9	405743.3	7612796.7		888.17	59	60	62	55	34	90	L
fvb	10	405743.6	7612800.8		888.05	59	58	56	59	66	120	L
fvb	11	405744.0	7612804.7		887.90	58	60	62	57	68	120	L
fvb	12	405742.0	7612806.6		887.92	67	68	67	52	31	90	L
fvb	13	405741.9	7612803.1		887.99	65	66	67	62	58	120	L
fvb	14	405741.3	7612799.4		888.11	73	80	80	72	46	120	L
fvb	15	405740.7	7612795.0		888.28	63	63	62	45	36	90	H
fvb	16	405740.1	7612791.0		888.39	53	54	52	30	45	90	H
fvb	17	405740.3	7612786.9		888.35	ROCK			18	62	90	L
fvb	18	405738.4	7612788.6		888.45	35	35	34	0	57	90	H
fvb	19	405738.9	7612793.1		888.37	48	56	44	15	50	90	H
fvb	20	405739.6	7612797.2		888.48	50	53	52	4	43	90	H
fvb	21	405739.7	7612801.1		888.03	70	70	72	70	50	120	H
fvb	22	405740.1	7612804.8		887.98	62	65	60	47	71	120	L
fvb	23	405738.1	7612806.5		887.95	48	48	50	39	44	90	H
fvb	24	405738.2	7612803.4		888.04	55	56	56	45	68	120	L
fvb	25	405737.5	7612799.8		888.13	48	48	46	34	45	90	H
fvb	26	405737.4	7612795.3		888.17	40	40	39	25	81	120	H
fvb	27	405736.9	7612791.4		888.24	32	33	30	7	64	90	H
fvb	28	405736.1	7612786.7		888.19	42	42	44	30	49	90	L
fvb	29	405734.5	7612789.0		888.20	49	44	46	32	47	90	H
fvb	30	405735.1	7612793.3		888.32	50	48	45	20	42	90	H
fvb	31	405736.0	7612797.7		888.05	51	54	51	43	42	90	L
fvb	32	405736.2	7612801.3		888.00	39	40	40	29	56	90	L
fvb	33	405736.5	7612805.0		888.38	40	42	38	2	83	120	H
fvb	34	405734.2	7612806.6		887.83	45	46	48	37	45	90	L
fvb	35	405733.9	7612802.5		887.95	53	54	55	46	41	90	L
fvb	36	405733.4	7612798.4		888.03	55	56	57	39	43	90	H
fvb	37	405732.8	7612794.5		888.13	42	41	38	4	84	120	H
fvb	38	405732.4	7612790.5		888.25	40	35	35	7	86	120	H
fvb	39	405732.0	7612786.5		888.33	42	44	46	8	47	90	H
fvb	40	405730.3	7612788.5		888.12	42	47	46	28	76	120	L
fvb	41	405730.8	7612792.5		888.13	38	39	38	17	54	90	L
fvb	42	405731.3	7612796.4		888.09	40	39	40	21	53	90	L
fvb	43	405731.7	7612800.4		887.99	42	41	38	27	84	120	L

fvb	44	405732.0	7612804.3		888.06	46	44	41	8	47	90	H
fvb	45	405730.3	7612806.5		887.84	42	45	45	22	80	120	H
fvb	46	405729.8	7612802.3		888.08	47	39	38	7	84	120	H
fvb	47	405729.2	7612798.2		888.20	47	46	44	0	43	90	H
fvb	48	405728.8	7612794.4		888.11	38	38	38	3	70	90	L
fvb	49	405728.3	7612790.5		888.10	46	44	49	31	50	90	L
fvb	50	405726.8	7612792.7		888.15	45	45	46	21	47	90	H
fvb	51	405727.4	7612796.7		888.12	40	38	39	8	54	90	H
fvb	52	405727.8	7612800.7		887.98	35	36	35	10	86	120	H
fvb	53	405728.2	7612804.6		887.82	43	41	44	26	53	90	H
fvb	54	405726.3	7612806.6		887.67	40	45	45	24	52	90	H
fvb	55	405726.0	7612802.9		887.80	55	55	55	42	36	90	L
fvb	56	405725.6	7612799.0		887.94	46	50	45	25	48	90	H
fvb	57	405725.2	7612795.0		888.04	40	40	41	23	81	120	H
fvb	58	405724.8	7612790.9		887.96	53	52	54	51	69	120	L
fvb	59	405723.6	7612792.8		887.89	62	62	63	64	60	120	L
fvb	60	405723.9	7612796.8		887.94	43	45	46	24	49	90	H
fvb	61	405723.9	7612800.7		887.77	53	52	53	49	70	120	L
fvb	62	405724.2	7612804.8		887.77	56	52	59	34	37	90	H
fvb	63	405722.0	7612806.4		887.59	90	89	91	69	16	90	L
fvb	64	405722.2	7612802.0		887.62	65	64	63	65	67	120	L
fvb	65	405721.6	7612795.9		887.85	60	63	62	67		120	L
fvb	66	405720.9	7612790.2		887.97	55	54	53	75	65	120	L
sb	1	405852.7	7612823.8		891.52	42	45	45	37	48	90	L
sb	2	405853.6	7612819.8		891.62	47	47	48	30	49	90	L
sb	3	405854.1	7612816.0		891.87	66	62	68	7	68	120	H
sb	4	405855.0	7612812.1		891.50	47	52	54	48	46	90	L
sb	5	405855.8	7612808.2		891.74	57	57	56	16	46	90	H
sb	6	405856.8	7612804.3		891.88	47	47	46	16	46	120	H
sb	7	405854.5	7612806.0		891.65	43	46	47	17	76	90	H
sb	8	405853.6	7612809.8		891.52	52	57	55	30	36	120	L
sb	9	405852.8	7612813.7		891.48	59	48	50	39	73	90	L
sb	10	405851.9	7612817.7		891.59	36	37	39	9	54	90	L
sb	11	405851.3	7612821.6		891.42	53	53	51	24	68	120	L
sb	12	405849.0	7612823.1		891.25	45	46	50	19	45	90	L
sb	13	405849.3	7612819.0		891.37	38	38	37	19	87	120	L
sb	14	405850.5	7612815.2		891.50	38	38	40	14	82	120	H
sb	15	405851.3	7612811.3		891.40	52	53	55	40	41	90	H
sb	16	405852.0	7612807.7		891.43	47	47	49	34	46	90	L
sb	17	405853.0	7612803.6		891.70	37	38	39	6	56	90	H
sb	18	405850.6	7612805.3		891.38	42	40	40	36	82	120	L
sb	19	405849.7	7612809.1		891.36	56	53	51	36	41	90	H
sb	20	405848.9	7612813.0		891.33	64	65	63	14	28	90	H
sb	21	405848.1	7612817.0		891.43	63	65	59	4	44	90	H
sb	22	405847.4	7612820.6		891.22	54	51	52	27	38	90	L
sb	23	405845.1	7612822.5		891.11	60	60	63	26	35	90	H
sb	24	405845.9	7612818.6		891.30	45	45	46	5	51	90	H
sb	25	405846.6	7612814.7		891.24	48	48	44	34	45	90	H

sb	26	405847.3	7612810.5		891.22	55	57	61	42	65	120	L
sb	27	405848.2	7612807.0		891.43	38	37	40	7	87	120	H
sb	28	405849.1	7612803.0		891.33	55	56	57	45	35	90	L
sb	29	405846.6	7612804.5		891.22	56	57	60	31	33	90	L
sb	30	405845.8	7612808.5		891.17	70	75	75	41	24	90	H
sb	31	405844.8	7612812.3		891.09	60	60	58	52	35	90	L
sb	32	405844.2	7612816.4		890.91	37	39	40	42	87	120	L
sb	33	405843.4	7612819.8		891.20	57	59	60	9	37	90	H
sb	34	405841.2	7612822.2		890.97	68	65	64	42	61	120	H
sb	35	405841.9	7612818.1		891.18	36	37	35	1	61	90	H
sb	36	405842.6	7612814.0		891.03	61	62	63	26	32	90	L
sb	37	405843.4	7612810.2		891.07	67	73	68	57	53	120	H
sb	38	405844.2	7612806.2		891.22	54	55	53	36	36	90	H
sb	39	405845.2	7612802.4		891.20	40	42	39	31	57	90	L
sb	40	405842.5	7612804.1		891.17	67	67	67	36	33	90	H
sb	41	405841.9	7612807.9		890.88	48	48	50	37	42	90	L
sb	42	405841.1	7612811.8		890.83	50	51	52	47	42	90	L
sb	43	405840.2	7612815.8		891.01	46	50	47	21	49	90	H
sb	44	405840.2	7612818.9		891.01	59	60	60	30	62	120	L
sb	45	405837.1	7612821.3		890.87	70	71	72	59	20	90	H
sb	46	405838.1	7612817.4		890.87	52	56	55	38	68	120	H
sb	47	405838.7	7612813.4		890.77	71	69	73	37	60	120	L
sb	48	405839.5	7612809.6		890.89	78	81	80	67	43	120	H
sb	49	405840.3	7612805.5		890.95	73	74	76	26	30	90	H
sb	50	405841.3	7612801.8		891.16	52	50	49	5	80	120	H
sb	51	405838.8	7612803.4		890.86	53	57	60	30	69	120	L
sb	52	405837.9	7612807.2		890.81	79	78	77	28	17	90	H
sb	53	405837.1	7612811.1		890.78	78	78	75	66	50	120	H
sb	54	405836.3	7612815.2		890.70	64	58	62	69	29	90	L
sb	55	405836.3	7612818.9		890.58	50	52	54	50	74	120	L
sb	56	405833.3	7612820.8		890.64	58	64	60	10	37	90	L
sb	57	405834.1	7612816.9		890.68	61	66	64	58	31	90	H
sb	58	405834.9	7612813.0		890.67	71	70	70	24	27	90	L
sb	59	405835.6	7612809.0		890.69	70	73	73	51	23	90	L
sb	60	405836.4	7612805.1		890.76	72	70	70	48	52	120	L
sb	61	405837.2	7612801.2		890.93	54	54	55	32	38	90	H
hil	1	405946.7	7612880.5	900.374	899.77	38	35	35	12	60.4	120	L
hil	2	405947.8	7612876.5	900.236	899.69	38	42	41	0	54.7	120	L
hil	3	405948.8	7612872.7	900.372	899.82	38	39	36	0	55.7	90	L
hil	4	405949.4	7612868.9	900.233	899.75	47	46	49	12	48.4	90	L
hil	5	405950.6	7612865.0	900.327	899.77	38	36	39	3	56.1	90	L
hil	6	405951.8	7612861.2	900.684	899.78	40	41	40	11	90.5	120	L
hil	7	405949.2	7612862.4	900.273	899.48	43	43	44	0	79.8	120	L
hil	8	405948.4	7612866.4	900.155	899.60	47	44	47	2	55.2	90	H
hil	9	405947.2	7612870.2	900.168	899.57	40	46	47	3	59.8	90	H
hil	10	405946.3	7612874.1	900.444	899.55	32	30	32	6	89.1	120	L
hil	11	405945.5	7612878.0	900.134	899.48	49	52	52	5	65.5	90	L
hil	12	405943.1	7612879.6	900.204	899.33	40	40	36	0	87.6	120	L

hil	13	405943.7	7612875.8	900.092	899.41	58	55	56	0	68.5	120	H
hil	14	405944.7	7612871.8	900.26	899.49	50	44	45	3	76.6	120	H
hil	15	405945.7	7612868.0	899.884	899.39	44	42	43	2	49.4	90	H
hil	16	405946.5	7612864.2	899.836	899.34	39	38	38	0	49.9	90	L
hil	17	405947.7	7612859.3	899.998	899.36	30	27	30	2	63.6	90	L
hil	18	405944.9	7612861.8	899.673	898.92	45	45	45	0	75.6	120	L
hil	19	405943.9	7612865.5	899.587	899.03	35	35	35	1	55.4	90	H
hil	20	405943.1	7612869.8	899.582	899.03	35	39	38	0	55.4	90	L
hil	21	405942.2	7612873.6	899.593	899.06	43	42	41	14	52.9	90	L
hil	22	405941.2	7612877.4	899.619	899.14	60	66	60	0	47.5	90	H
hil	23	405938.9	7612878.7	899.534	898.68	39	38	41	0	85.5	120	L
hil	24	405939.7	7612875.0	899.53	898.79	50	46	49	1	74.4	120	L
hil	25	405940.7	7612871.0	899.449	898.94	48	43	45	6	51.1	90	H
hil	26	405941.6	7612867.2	899.433	898.93	40	40	42	0	50.8	90	H
hil	27	405942.3	7612863.3	899.583	898.71	33	34	33	9	87.3	120	L
hil	28	405943.8	7612858.2	899.232	898.72	40	40	36	18	51.4	90	L
hil	29	405940.9	7612861.0	899.02	898.55	42	44	46	0	47.5	90	H
hil	30	405940.1	7612864.9	899.034	898.61	49	46	49	0	42.6	90	L
hil	31	405939.2	7612868.6	899.16	898.63	43	39	41	0	52.9	90	L
hil	32	405938.3	7612872.5	899.513	898.75	42	41	43	0	76.4	120	H
hil	33	405937.6	7612876.5	899.156	898.68	45	48	46	0	48.1	90	H
hil	34	405935.1	7612877.9	898.881	898.41	44	44	46	0	47.4	90	L
hil	35	405936.0	7612874.1	899.174	898.39	45	46	45	6	78.4	120	H
hil	36	405936.7	7612870.2	899.064	898.45	25	26	28	9	61.6	90	L
hil	37	405937.8	7612866.2	899.22	898.43	48	42	43	1	79.3	120	H
hil	38	405938.7	7612862.5	899.042	898.31	40	38	39	21	72.8	120	H
hil	39	405939.7	7612858.0	898.966	898.21	49	45	44	18	75.9	120	L
hil	40	405937.4	7612860.0	898.724	898.25	56	54	55	29	47.4	90	H
hil	41	405936.3	7612863.8	898.756	898.17	49	39	37	1	58.5	90	L
hil	42	405935.6	7612867.8	898.735	898.20	36	38	35	0	53.3	90	L
hil	43	405934.5	7612872.1	898.819	898.12	31	30	28	12	70.1	90	L
hil	44	405933.6	7612875.5	898.667	898.18	48	45	51	0	48.7	90	L
hil	45	405931.1	7612877.1	898.362	897.67	67	68	65	30	68.9	120	H
hil	46	405932.1	7612873.2	898.472	897.65	48	49	48	0	81.8	120	H
hil	47	405933.0	7612869.3	898.255	897.74	38	40	37	0	51.8	90	L
hil	48	405934.1	7612865.3	898.132	897.68	46	45	48	0	45.4	90	L
hil	49	405934.9	7612861.4	898.166	897.90	43	43	43	0	26.5	90	L
hil	50	405935.9	7612857.4	898.312	897.89	54	50	50	2	42.7	90	H
hil	51	405933.4	7612859.2	898.225	897.76	47	47	45	16	46.5	90	H
hil	52	405932.7	7612863.1	898.376	897.76	36	38	34	8	61.4	90	L
hil	53	405931.8	7612866.9	898.348	897.90	47	48	45	19	44.8	90	H
hil	54	405930.8	7612870.9	898.584	897.87	53	58	55	0	71.9	120	H
hil	55	405929.9	7612874.7	898.181	897.84	58	66	70	0	34.4	90	H
hil	56	405927.5	7612876.6	898.251	897.60	60	63	60	0	64.8	120	H
hil	57	405928.2	7612872.7	898.037	897.57	45	45	44	2	47.2	90	L
hil	58	405929.1	7612868.7	898.532	897.58	33	33	30	5	94.8	120	L
hil	59	405930.1	7612864.8	898.367	897.67	50	48	50	1	70	120	L
hil	60	405931.1	7612861.0	897.829	897.58	43	38	43	5	25.2	90	L

hil	61	405932.0	7612857.2	898.118	897.67	44	43	44	5	44.9	90	L
rip	1	405780.3	7612867.7		888.37	42	45	45	35	52	90	L
rip	2	405780.7	7612863.8		888.53	35	35	36	19	57	90	H
rip	3	405781.2	7612859.8		888.59	45	47	47	35	49	90	H
rip	4	405781.7	7612855.9		888.60	42	42	41	40	51	90	L
rip	5	405782.2	7612851.9		888.67	48	49	48	44	43	90	H
rip	6	405782.9	7612848.2		888.68	48	43	45	43	52	90	L
rip	7	405780.6	7612849.7		888.62	44	46	44	40	51	90	L
rip	8	405780.1	7612853.6		888.66	59	55	59	41	40	90	H
rip	9	405779.6	7612857.6		888.57	54	55	51	40	74	120	H
rip	10	405779.0	7612861.5		888.49	44	44	40	47	50	90	H
rip	11	405778.5	7612865.6		888.36	34	36	35	30	88	120	L
rip	12	405776.4	7612867.1		888.34	41	42	46	25	79	120	H
rip	13	405777.2	7612863.2		888.36	53	54	50	33	73	120	H
rip	14	405777.5	7612859.2		888.43	43	39	39	36	81	120	L
rip	15	405777.9	7612855.3		888.54	43	42	46	40	47	90	H
rip	16	405778.3	7612851.4		888.60	51	48	50	32	74	120	H
rip	17	405778.8	7612847.7		888.58	51	52	52	47	74	120	L
rip	18	405776.4	7612849.1		888.45	45	47	43	40	80	120	L
rip	19	405776.1	7612853.0		888.69	55	58	57	33	34	90	H
rip	20	405775.7	7612857.0		888.38	50	53	52	44	41	90	
rip	21	405775.2	7612861.0		888.37	51	50	51	36	44	90	H
rip	22	405774.5	7612864.9		888.22	48	46	45	32	46	90	H
rip	23	405772.5	7612866.6		888.11	48	49	48	35	48	90	H
rip	24	405772.9	7612862.7		888.12	40	40	38	78	85	120	L
rip	25	405773.4	7612858.7		888.21	45	45	48	41	50	90	L
rip	26	405773.8	7612854.7		888.46	48	46	46	28	43	90	H
rip	27	405774.3	7612850.8		888.46	50	51	53	40	71	120	H
rip	28	405775.0	7612847.2		888.48	55	53	57	35	38	90	H
rip	29	405772.7	7612848.7		888.38	50	53	58	47	42	90	L
rip	30	405772.2	7612852.6		888.34	49	51	53	45	40	90	L
rip	31	405771.8	7612856.5		888.24	48	42	41	50	79	120	H
rip	32	405771.3	7612860.5		888.16	53	52	53	45	42	90	H
rip	33	405770.9	7612864.4		888.10	49	48	52	48	45	90	H
rip	34	405768.6	7612866.1		887.92	49	51	48	38	77	120	H
rip	35	405769.1	7612862.1		888.01	48	46	47	39	46	90	L
rip	36	405769.4	7612858.2		888.20	45	47	45	35	75	120	H
rip	37	405769.9	7612854.2		888.29	59	61	62	43	39	90	H
rip	38	405770.3	7612850.2		888.28	41	42	42	20	67	90	
rip	40	405768.7	7612848.0		888.29	47	48	49	40	44	90	L
rip	41	405768.3	7612852.0		888.24	50	51	52	36	40	90	H
rip	42	405767.8	7612855.9		888.12	58	56	58	45	38	90	H
rip	43	405767.3	7612859.8		888.02	47	46	45	33	48	90	H
rip	44	405766.8	7612863.8		887.87	48	46	45	32	49	90	L
rip	45	405764.8	7612865.6		887.77	48	45	44	42	47	90	L
rip	46	405765.2	7612861.7		887.92	45	48	48	39	49	90	H
rip	47	405765.7	7612857.8		887.96	48	49	50	42	75	120	L
rip	48	405766.1	7612853.7		887.98	35	36	37	39	59	90	L

rip	49	405766.6	7612849.9		888.25	48	47	48	31	43	90	H
rip	50	405767.1	7612845.9		888.36	71	70	69	50	24	90	H
rip	51	405764.8	7612847.8		888.18	48	45	51	44	40	90	H
rip	52	405764.4	7612851.8		888.04	52	51	49	38	71	120	H
rip	53	405763.9	7612855.7		887.85	47	41	40	41	54	90	L
rip	54	405763.4	7612859.6		887.84	37	38	39	35	83	120	L
rip	55	405763.0	7612863.5		887.86	45	46	43	34	76	120	H
rip	56	405760.8	7612865.2		887.61	37	36	36	38	39	90	L
rip	57	405761.2	7612861.2		887.75	48	45	43	42	79	120	L
rip	58	405761.6	7612857.3		887.90	63	60	60	52	61	120	L
rip	59	405762.1	7612853.4		887.86	49	48	49	46	47	90	L
rip	60	405762.6	7612849.4		888.09	46	45	46	33	78	120	H
rip	61	405763.2	7612845.5		888.13	50	47	46	43	75	120	L
wes	1	405698.6	7612838.7		887.40	38	39	37	20	59	120	H
wes	2	405699.0	7612834.8		887.60	35	37	36	7	60	90	H
wes	3	405699.5	7612830.9		887.42	59	64	61	19	33	90	H
wes	4	405699.9	7612826.8		887.58	32	34	32	16	60	90	H
wes	5	405700.4	7612822.9		887.66	52	48	50	38	78	120	H
wes	6	405700.8	7612818.8		887.73	67	67	67	65	31	90	H
wes	7	405698.6	7612820.9		887.78	54	55	58	26	64	90	L
wes	8	405698.3	7612824.8		887.71	55	55	56	39	69	120	L
wes	9	405697.7	7612828.7		887.63	58	59	56	39	35	90	L
wes	10	405697.3	7612832.6		887.61	69	67	66	60	27	90	L
wes	11	405697.0	7612836.8		887.67	46	46	48	11	83	120	L
wes	12	405695.0	7612838.7		887.54	62	60	60	21	65	90	L
wes	13	405695.2	7612834.8		887.83	34	36	33	5	92	120	L
wes	14	405695.6	7612830.7		887.55	67	67	67	59	27	90	L
wes	15	405696.1	7612826.7		887.65	57	54	58	44	42	90	H
wes	16	405696.5	7612822.7		887.72	59	59	58	40	37	90	H
wes	17	405696.8	7612818.9		887.76	44	46	46	38	80	120	L
wes	18	405694.7	7612821.0		887.81	59	58	60	46	38	90	H
wes	19	405694.3	7612824.8		887.69	59	60	58	49	34	90	H
wes	20	405693.9	7612828.7		887.60	63	62	66	60	31	90	H
wes	21	405693.4	7612832.6		887.59	63	65	65	16	56	120	H
wes	22	405692.9	7612836.9		887.47	53	52	54	46	70	120	L
wes	23	405690.9	7612838.7		887.83	39	36	40	0	54	90	H
wes	24	405691.2	7612834.8		887.61	52	51	49	0	43	90	L
wes	25	405691.6	7612830.5		887.61	52	55	55	11	40	90	H
wes	26	405692.2	7612826.3		887.60	61	60	58	44	31	90	H
wes	27	405692.6	7612822.6		887.71	55	53	54	53	40	90	H
wes	28	405692.9	7612818.9		887.80	50	48	50	42	43	90	L
wes	29	405690.9	7612820.7		887.75	55	53	54	53	40	90	H
wes	30	405690.4	7612824.7		887.69	60	61	59	33	34	90	H
wes	31	405690.0	7612828.9		887.72	68	68	68	4	23	90	L
wes	32	405689.3	7612832.5		887.67	45	41	43	6	50	90	L
wes	33	405689.0	7612836.9		887.70	34	35	36	14	60	90	H
wes	34	405687.0	7612838.7		887.66	43	42	45	1	84	90	L
wes	35	405687.3	7612834.6		887.85	39	38	35	0	64	90	L

wes	36	405687.6	7612830.5		887.85	45	43	45	0	53	90	H
wes	37	405688.1	7612826.8		887.69	51	49	51	8	46	90	H
wes	38	405688.6	7612822.7		887.77	59	61	60	55	66	120	H
wes	39	405688.9	7612818.9		887.86	62	61	64	53	37	90	H
wes	40	405686.7	7612820.9		887.83	60	57	64	30	64	120	L
wes	41	405686.3	7612824.7		887.75	57	52	48	2	43	90	L
wes	42	405686.0	7612828.5		887.87	47	44	46	13	76	120	L
wes	43	405685.4	7612832.5		887.72	49	51	53	7	43	90	L
wes	44	405685.1	7612836.9		887.73	63	66	66	37	57	120	H
wes	45	405683.0	7612838.7		887.75	57	56	58	5	38	90	H
wes	46	405683.3	7612834.6		887.77	59	58	60	7	37	90	H
wes	47	405683.7	7612830.5		887.80	54	55	55	13	69	120	H
wes	48	405684.1	7612826.7		887.93	54	56	53	0	41	90	L
wes	49	405684.6	7612822.7		888.10	45	50	55	7	76	120	L
wes	50	405684.8	7612818.9		887.99	68	73	73	0	19	90	H
wes	51	405682.7	7612821.1		888.12	35	38	38	4	54	120	H
wes	52	405682.3	7612824.8		887.86	45	47	45	3	72	120	H
wes	53	405682.0	7612828.3		887.96	68	65	67	2	55	120	H
wes	54	405681.5	7612832.8		887.80	58	58	56	5	64	120	H
wes	55	405681.1	7612836.8		887.83	55	53	52	0	69	90	L
wes	56	405679.3	7612838.7		887.89	56	58	61	2	34	90	H
wes	57	405679.4	7612834.7		887.91	56	57	59	0	35	120	H
wes	58	405679.7	7612830.5		887.93	61	60	61	0	62	90	L
wes	59	405680.3	7612826.6		888.16	65	67	66	0	27	120	L
wes	60	405680.7	7612822.7		888.10	43	40	45	0	84	90	H
wes	61	405680.9	7612818.9		888.18	54	50	53	0	84	90	L
svb	1	405733.0	7613223.9		879.68	95	95	95	95	11		L
svb	2	405732.6	7613221.2		879.88	108	108	108	108	4		H
svb	3	405732.7	7613217.7		880.11	83	83	83	83	13		H
svb	4	405732.6	7613213.6		880.18	65	65	65	65	37		L
svb	5	405732.6	7613210.0		880.27	63	63	63	63	34		L
svb	6	405732.6	7613205.8		880.39	54	54	54	54	41		H
svb	7	405732.4	7613202.1		880.17	90	90	90	90	37		L
svb	8	405730.5	7613203.7		880.06	82	82	82	82	43		L
svb	9	405730.7	7613207.7		880.18	52	49	54	51.67	70		H
svb	10	405730.7	7613211.7		880.13	75	72	72	73	59		L
svb	11	405731.0	7613215.5		880.19	83	84	83	83.33	12		H
svb	12	405730.7	7613220.0		879.84	57	58	53	56	34		H
svb	13	405729.3	7613221.5		879.61	65	68	62	65	29		L
svb	14	405729.0	7613217.4		879.80	55	57	60	57.33	38		L
svb	15	405729.0	7613213.7		880.03	72	70	72	71.33	22		H
svb	16	405728.4	7613209.4		880.08	50	52	54	52	44		H
svb	17	405728.7	7613205.4		879.91	68	65	66	66.33	59		L
svb	18	405728.7	7613201.6		879.96	95	95	95	95	24		L
svb	19	405726.6	7613203.2		879.77	97	97	97	97	26		L
svb	20	405726.8	7613207.2		879.97	58	58	57	57.67	35		H
svb	21	405726.6	7613211.3		879.96	57	56	57	56.67	57		H
svb	22	405727.0	7613215.2		879.87	81	80	79	80	14		H

svb	23	405727.1	7613219.3		879.52	58	62	57	59	26		L
svb	24	405727.3	7613223.4		879.38	97	97	97	97	5		L
svb	25	405725.4	7613221.1		879.35	56	56	56	56	66		H
svb	26	405724.9	7613217.0		879.63	66	62	72	66.67	30		H
svb	27	405725.1	7613213.0		879.76	55	54	53	54	40		H
svb	28	405724.4	7613209.1		879.77	53	53	55	53.67	43		H
svb	29	405724.6	7613205.1		879.59	74	75	82	77	42		L
svb	30	405724.6	7613201.2		879.69	96	96	95	95.67	33		L
svb	31	405722.6	7613202.9		879.47	79	75	75	76.33	44		L
svb	32	405722.7	7613206.8		879.55	85	95	89	89.67			L
svb	33	405722.7	7613210.8		879.74	77	74	74	75	20		H
svb	34	405723.1	7613214.7		879.60	58	59	62	59.67	47		H
svb	35	405722.6	7613218.8		879.25	37	37	37	37	56		L
svb	36	405723.2	7613222.7		879.20	65	62	65	64	33		L
svb	37	405721.1	7613220.7		879.07	46	46	46	46			L
svb	38	405721.0	7613216.6		879.39	44	50	47	47	48		H
svb	39	405721.0	7613213.0		879.48	59	60	60	59.67	39		L
svb	40	405720.5	7613208.7		879.56	79	80	80	79.67	11		H
svb	41	405720.7	7613204.7		879.33	98	98	98	98	7		L
svb	42	405720.7	7613200.8		879.49	94	99	100	97.67	11		L
svb	43	405718.4	7613202.5		879.25	87	106	94	95.67			L
svb	44	405718.8	7613206.4		879.32	105	105	105	105	12		L
svb	45	405718.7	7613210.5		879.45	53	50	50	51	43		H
svb	46	405719.1	7613214.3		879.39	62	62	62	62	34		H
svb	47	405719.1	7613218.3		879.16	90	90	90	90	6		H
svb	48	405719.5	7613222.3		879.02	55	55	55	55	36		L
svb	49	405717.4	7613220.3		878.96	41	49	41	43.67	46		L
svb	50	405717.1	7613216.2		879.14	65	71	65	67	13		H
svb	51	405717.0	7613212.4		879.31	58	59	60	59	35		H
svb	52	405716.5	7613208.3		879.19	84	83	87	84.67	10		L
svb	53	405716.6	7613204.4		879.07	104	104	104	104	44		L
svb	54	405716.8	7613200.3		879.29	100	100	101	100.3	24		L
svb	55	405714.7	7613202.0		879.19	87	87	87	87	7		H
svb	56	405714.8	7613206.1		878.95	102	102	102	102	20		L
svb	57	405714.8	7613210.1		879.05	74	76	76	75.33	28		L
svb	58	405715.1	7613214.0		879.15	60	64	63	62.33	31		H
svb	59	405715.3	7613218.3		878.93	86	80	84	83.33	41		L
svb	60	405713.6	7613221.8		878.85	69	67	66	67.33			L
svb	61	405713.3	7613220.0		878.83	78	78	74	76.67	21		L
svb	62	405713.1	7613215.8		878.93	58	60	62	60			H
svb	63	405713.2	7613211.9		878.96	69	70	68	69	60		L
svb	64	405713.0	7613207.8		878.95	96	98	98	97.33	30		L
svb	65	405713.2	7613204.0		879.05	104	104	104	104	16		H
svb	66	405712.9	7613199.9		879.11	90	91	91	90.67	31		L

APPENDIX B: SUPPLEMENTAL MATERIALS FOR CHAPTER 3

Table B1: All stratigraphy and water table data collected from the two field campaigns in 2017 and 2018.

Site ID	Easting [UTM Zone 6N]	Northing [UTM Zone 6N]	Elevation [m above MSL]	Landscape Zone	Observed Dominant Vegetation	Micro-topographic Position	bAC [cm]	bCT [cm]	Thaw Depth [cm]	Estimated Water Table Depth [cm]
UKP_001	402607	7616459	743.04	Riparian	Woody Shrubs		10	10	40	20
UKP_002	402696	7616472	746.56	Hillslope	Woody Shrubs	High	20	10	58	30
UKP_004	403063	7616387	778.66	Hillslope	Tussocks	High	8	12	41	20
UKP_005	403174	7616384	780.96	Hillslope	Sedges		15	29	65	5
UKP_006	403536	7616377	794.51	Hillslope	Tussocks	High	10	26	47	26
UKP_201	404049	7616272	839.83	Hillslope	Woody Shrubs		12	1	46	12
UKP_202	404308	7616247	859.28	Hillslope	Sedges		11	23	>120	34
UKP_203	404557	7616188	849.42	Hillslope	Woody Shrubs	Low	10	15	57	10
UKP_003	402700	7616460	746.78	Hillslope	Woody Shrubs	Low	20	13	77	11
UKP_005*	403174	7616384	780.96	Hillslope	Sedges	Low	15	29	65	5
UKP_007	403541	7616404	795.46	Hillslope	Woody Shrubs	Low	16	25	47	10
UKP_101	402447	7616197	743.91	Riparian	Woody Shrubs	High	5	10	40	20
UKP_102	402440	7616192	743.78	Riparian	Sedges	Low	3	17	44	10
UKP_106	402322	7616101	751.83	Hillslope	Tussocks	Low	5	15	51	11
UKP_109	402208	7615986	773.36	Hillslope	Woody Shrubs	High	3	16	67	18
UKP_110	402064	7615790	808.15	Ridge	Lichen		4	0	82	5
UKP_112	402161	7615518	804.00	Hillslope	Sedges	Low	8	14	47	13
UKP_114	402747	7615653	750.54	Riparian	Sedges		1	54	55	3
UKP_115	402624	7615560	758.03	Hillslope	Tussocks		6	13	45	13
UKP_116	402407	7615417	792.11	Hillslope	0	High	11	13	82	24
UKP_301	401680	7617690	726.99	Riparian	Woody Shrubs		1	0	>120	0
UKP_302	401807	7617438	730.02	Riparian	Woody Shrubs		11	0	56	0
UKP_303	401810	7617247	732.43	Hillslope	Sedges	Low	14	46	124	49
UKP_304	401940	7617488	731.13	Hillslope	Woody Shrubs		20	11	29	16
UKP_305	401699	7617689	727.61	Riparian	Woody Shrubs		10	0	42	0
UKP_401	409329	7606554	1109.01	Ridge	Woody Shrubs		10	20	51	5
UKP_403	409018	7606377	1090.28	Hillslope	Tussocks	High	10	8	57	10
UKP_404	408759	7606342	1069.82	Hillslope	Tussocks	High	3	17	48	5
UKP_406	408588	7606308	1054.04	Hillslope	Tussocks	High	8	3	46	12
UKP_407	408252	7606212	1034.98	Hillslope	Woody Shrubs	High	7	6	72	7
UKP_409	408017	7606114	1018.72	Hillslope	Tussocks	High	12	15	66	11

UKP_411	407901	7606037	1009.12	Hillslope	Tussocks	High	16	8	49	10
UKP_412	407636	7605772	981.51	Hillslope	Woody Shrubs		3	20	>120	8
UKP_413	407460	7605540	936.91	Hillslope	Tussocks		5	22	43	27
UKP_402	409018	7606391	1090.31	Hillslope	Sedges	Low	10	10	58	0
UKP_405	408588	7606324	1054.42	Hillslope	Sedges	Low	6	14	93	2
UKP_408	408248	7606217	1035.46	Hillslope	Sedges	Low	11	12	79	2
UKP_410	407905	7606027	1008.46	Riparian	Sedges	Low	30	30	76	2
UKP_501	401846	7607892	1016.30	Hillslope	Lichen		3	7	>120	10
UKP_502	401855	7607867	1015.47	Hillslope	Tussocks	High	7	6	69	20
UKP_503	402067	7607912	998.21	Hillslope	Tussocks	High	20	15	79	10
UKP_505	402485	7608006	960.93	Hillslope	Tussocks	High	10	6	49	10
UKP_507	402884	7608110	926.22	Hillslope	Woody Shrubs		9	11	>120	20
UKP_509	403029	7608152	913.92	Riparian	Sedges		10	35	73	3
UKP_508	403282	7608164	896.44	Hillslope	Tussocks		10	8	59	10
UKP_510	403528	7608297	867.74	Hillslope	0	High	10	13	61	25
UKP_512	403978	7608442	831.54	Hillslope	Sedges	Low	10	5	69	10
UKP_515	404139	7608514	817.74	Riparian	Sedges	Low	11	21	52	25
UKP_516	404240	7608590	817.18	Riparian	Sedges	High	11	12	33	30
UKP_504	402067	7607912	998.21	Hillslope	Tussocks	Low	15	12	46	1
UKP_506	402479	7608075	960.83	Hillslope	Sedges	Low	8	6	50	0
UKP_511	403531	7608324	866.46	Hillslope	Woody Shrubs	Low	13	9	73	3
UKP_513	403966	7608478	830.18	Hillslope	Woody Shrubs	Low	18	6		5
UKP_514	404097	7608494	819.76	Hillslope	0	Low	0	19	87	5
UKP_601	401832	7625636	708.38	Hillslope	Tussocks	High	7	5	56	29
UKP_603	401656	7625562	697.22	Hillslope	Tussocks	High	9	4	49	16.5
UKP_605	401398	7625422	683.11	Hillslope	Tussocks	High	6	23	60	29
UKP_607	401178	7625360	678.77	Hillslope	Tussocks	High	11	16	48	30
UKP_609	400998	7625380	670.95	Hillslope	0	High	8	10	57	18
UKP_611	400418	7625408	654.66	Riparian	Woody Shrubs	High	9	23	39	32
UKP_602	401824	7625652	706.71	Hillslope	Sedges	Low	6	14	69	9.5
UKP_604	401648	7625580	697.01	Hillslope	Tussocks	Low	10	13	54	5
UKP_606	401380	7625448	682.70	Hillslope	Sedges	Low	6	20	73	1
UKP_608	401184	7625393	678.64	Hillslope	Sedges	Low			70	0
UKP_610	400987	7625409	668.85	Hillslope	Sedges	Low	5	13	64	0
UKP_613	400402	7625425	655.06	Hillslope	Sedges	Low	8	19	83	0
UKP_614	400579	7625116	656.97	Hillslope	Tussocks	High	14	10	36	25
SAR18_000	399402	7607770	980.40	Hillslope	Lichen	High	0	0	>120	0
SAR18_001	399367	7607755	977.77	Hillslope	Sedges	Low	0	15	68	6
SAR18_002	399367	7607755	977.77	Hillslope	Tussocks	High	10	8	67	0
SAR18_003	399074	7607725	942.74	Hillslope	Tussocks	High	10	20	71	30
SAR18_004	399074	7607725	942.74	Hillslope	Tussocks	Low	0	27	61	3
SAR18_005	398688	7607646	904.83	Hillslope	Tussocks	High	20	22	42	20
SAR18_006	398688	7607646	904.83	Hillslope	Tussocks	Low	0	44	66	5
SAR18_007	398397	7607647	880.23	Hillslope	Woody Shrubs		0	0	>120	0
SAR18_008	398397	7607647	880.23	Riparian	Sedges	Low	0	14	56	0

SAR18_100	398149	7611921	911.97	Hillslope	Woody Shrubs	High	10	0	56	8
SAR18_101	398149	7611921	911.97	Hillslope	Tussocks	Low	2	23	66	2
SAR18_102	397878	7611853	891.13	Hillslope	Tussocks	High	17	0	48	0
SAR18_103	397878	7611853	891.13	Hillslope	Sedges	Low	15	63	78	0
SAR18_104	397878	7611853	891.13	Hillslope	Sedges	Low	0	15	55	12
SAR18_105	397545	7611920	857.74	Hillslope	Woody Shrubs		19	12	>120	0
SAR18_106	397335	7611919	839.22	Hillslope	Woody Shrubs	High	13	9	68	22
SAR18_107	397335	7611919	839.22	Hillslope	0		17	8	>120	16
SAR18_200	396530	7611635	803.49	Ridge	Lichen		4	0	73	4
SAR18_201	396530	7611635	803.49	Ridge	Sedges	High	19	0	33	19
SAR18_202	396383	7611523	795.44	Hillslope	Tussocks	Low	20	10	45	20
SAR18_203	396379	7611511	795.16	Hillslope	Woody Shrubs	High	10	8	37	18
SAR18_204	396216	7611579	789.15	Hillslope	Sedges	Low	15	5	36	7
SAR18_205	396216	7611579	789.15	Hillslope	Woody Shrubs	High	16	5	37	21
SAR18_206	396015	7611560	782.35	Riparian	Sedges		14	9	33	23
SAR18_207	396015	7611560	782.35	Hillslope	Sedges	Low	13	12	43	5
SAR18_208	396555	7611794	797.15	Hillslope	Woody Shrubs		10	0	65	10
SAR18_209	396580	7611812	795.08	Riparian	Woody Shrubs	Low	11	14	73	25
SAR18_300	398281	7610933	911.58	Hillslope	Tussocks	Low	12	19	59	10
SAR18_301	398291	7610912	912.12	Hillslope	Tussocks		9	0	>120	1
SAR18_302	398110	7610971	894.00	Hillslope	Lichen		1	0	>120	DRY
SAR18_303	398135	7610948	893.94	Hillslope	Tussocks	High	17	9	36	26
SAR18_304	398089	7610929	891.27	Hillslope	Sedges	Low	20	7	82	-5
SAR18_305	398023	7610903	888.65	Hillslope	Lichen		2	0	>120	DRY
SAR18_306	397788	7610881	876.16	Hillslope	Tussocks	High	16	20	40	36
SAR18_307	397763	7601878	870.58	Hillslope	Lichen		4	0	66	DRY
SAR18_308	397565	7610852	858.53	Hillslope	Tussocks	Low	16	24	97	5
SAR18_309	397425	7610888	845.71	Hillslope	Woody Shrubs	High	21	9	30	DRY
SAR18_310	397368	7610881	840.47	Hillslope	Tussocks	Low	12	16	42	12
SAR18_311	397318	7610857	839.55	Hillslope	Lichen		1	0	>120	DRY
SAR18_400L	398644	7608957	924.07	Hillslope	Tussocks	Low	5	18	59	10
SAR18_400H	398644	7608957	924.07	Hillslope	Tussocks	High	10	28	63	28
SAR18_401	398625	7608994	923.16	Hillslope	Lichen		2	0	>120	DRY
SAR18_402	398584	7608897	914.79	Hillslope	Tussocks	High	12	12	85	8
SAR18_403L	398540	7608882	909.73	Hillslope	Tussocks	High	19	19	38	DRY
SAR18_403H	398540	7608882	909.73	Hillslope	Tussocks	Low	5	35	40	0
SAR18_404	398457	7608887	907.49	Hillslope	Lichen		1	0	>120	DRY
SAR18_405	398278	7608920	894.01	Hillslope	Tussocks	High	10	12	56	22
SAR18_406	398026	7609015	877.38	Hillslope	Tussocks	High	21	22	63	21
SAR18_407	398025	7609015	877.38	Hillslope	Lichen		2	0	>120	DRY
SAR18_500	405553	7612653	894.92	Ridge	Tussocks	High	19	11	50	30
SAR18_501	405546	7612665	894.63	Ridge	Woody Shrubs	Low	9	6	69	9
SAR18_502	405547	7612658	895.99	Ridge	Lichen		4	0	81	DRY

SAR18_503	405662	7612720	889.09	Hillslope	Tussocks	Low	8	0	53	7
SAR18_504	405004	7612751	888.46	Hillslope	Tussocks	Low	12	5	48	17
SAR18_505	405670	7612738	889.41	Hillslope	Woody Shrubs	Low	9	8	60	17
SAR18_506	405722	7612736	887.38	Riparian	Sedges	Low	11	30	41	6
SAR18_507	405722	7612736	887.38	Riparian	Sedges	High	19	26	45	19
SAR18_508	405758	7612761	887.30	Riparian	Sedges	High	9	38	47	17
SAR18_509	405756	7612766	887.67	Riparian	Sedges	Low	12	50	62	-5
SAR18_510	405769	7612769	888.26	Riparian	Woody Shrubs	High	17	23	40	DRY
SAR18_511	405857	7612772	890.69	Hillslope	Tussocks	Low	10	15	42	14
SAR18_512	405875	7612701	891.34	Hillslope	Sedges	Low	6	18	49	6
SAR18_513	405875	7612701	891.34	Riparian	Lichen		4	0	70	4
SAR18_600	407161	7613138	959.63	Hillslope	Tussocks	Low	8	10	58	14
SAR18_601	407170	7613177	957.87	Hillslope	Sedges	Low	5	14	81	0
SAR18_602	407032	7613208	946.64	Hillslope	Tussocks	Low	13	4	58	13
SAR18_603	407033	7613222	947.90	Hillslope	Sedges	Low	6	18	61	0
SAR18_604	407021	7613189	946.49	Hillslope	Tussocks	Low	11	6	49	53
SAR18_605	407009	7613216	945.41	Hillslope	Woody Shrubs	Low	7	1	47	8
SAR18_606	407009	7613216	945.41	Hillslope	Woody Shrubs	High	15	4	63	DRY
SAR18_607	406836	7613310	930.32	Hillslope	Woody Shrubs	High	20	20	34	14
SAR18_608	406836	7613310	930.32	Hillslope	Sedges	Low	7	20	81	-2
SAR18_609L	406725	7613332	923.79	Hillslope	Woody Shrubs	Low	5	3	41	DRY
SAR18_609H	406725	7613332	923.79	Hillslope	Woody Shrubs	High	20	27	47	DRY
SAR18_610	406706	7613315	922.29	Hillslope	Woody Shrubs	Low	6	19	74	-2
SAR18_611	406612	7613332	915.59	Riparian	Woody Shrubs	High	13	6	44	19
SAR18_612	406606	7613345	914.97	Hillslope	Sedges	Low	9	12	76	1
SAR18_613	406520	7613317	920.24	Hillslope	Tussocks	Low	7	26	66	10
SAR18_614	406444	7613320	924.53	Hillslope	Lichen		1	4	>120	DRY
SAR18_615	406302	7613308	931.38	Ridge	Lichen		3	0	>120	DRY
SAR18_616	406014	7613242	910.08	Hillslope	Tussocks	High	10	1	52	10
SAR18_617	406009	7613224	909.42	Hillslope	Woody Shrubs	Low	10	7	62	4
SAR18_618	405829	7613201	887.52	Hillslope	Tussocks	High	8	7	61	15
SAR18_619	405827	7613185	888.61	Hillslope	Sedges	Low	7	7	80	0
SAR18_620	405698	7613210	877.03	Riparian	Sedges		10	36	56	7
SAR18_621	405667	7613206	877.91	Riparian	Sedges		7	15	82	22
SAR18_622	405660	7613214	877.69	Riparian	Woody Shrubs	High	17	28	45	DRY
SAR18_623	405596	7613221	882.19	Hillslope	Tussocks	Low	12	10	67	22
SAR18_700	407211	7612977	964.47	Hillslope	Lichen	Low	0	0	89	0
SAR18_701	407213	7612917	964.94	Hillslope	Tussocks	High	14	8	98	15
SAR18_702	407453	7612929	975.20	Hillslope	Tussocks	High	12	8	73	20
SAR18_703	407450	7612927	976.07	Ridge	Tussocks	High	6	-6	63	91
SAR18_704	407184	7612777	961.64	Hillslope	Tussocks	Low	6	1	48	43
SAR18_705	407119	7612763	958.35	Hillslope	Woody Shrubs	High	23	0	73	23

SAR18_706	407120	7612763	958.35	Hillslope	Sedges	Low	10	30	44	10
SAR18_707	407111	7612753	957.75	Hillslope	Sedges	Low	3	66	69	3
SAR18_708	407059	7612751	955.97	Hillslope	Tussocks	High	7	31	78	17
SAR18_709	407057	7612752	956.26	Hillslope	Lichen	Low	0	2	>120	DRY
SAR18_710	407052	7612739	957.17	Hillslope	Tussocks	High	9	21	78	DRY
SAR18_711	406882	7612716	943.24	Hillslope	Tussocks	Low	10	9	60	5
SAR18_712	406741	7612706	934.22	Riparian	Sedges		12	18	65	30
SAR18_800	395644	7616282	739.08	Hillslope	Tussocks	High	20	13	>120	DRY
SAR18_801	395640	7616284	738.66	Hillslope	Tussocks	Low	12	17	58	DRY
SAR18_802	395633	7612085	767.26	Hillslope	Sedges	Low	10	20	70	0
SAR18_803	395651	7616252	739.33	Hillslope	Woody Shrubs	High	27	9	39	DRY
SAR18_804	395588	7616260	737.67	Hillslope	Lichen		3	0	>120	DRY
SAR18_805	395305	7617170	713.67	Hillslope	Sedges		17	44	61	9
SAR18_806	394888	7616472	718.05	Ridge	Woody Shrubs	High	18	0	365	DRY
SAR18_807	394876	7616471	718.05	Ridge	Lichen		1	0	>120	DRY
SAR18_808	395207	7615168	755.74	Hillslope	Tussocks	Low	11	9	54	DRY
SAR18_809	395196	7615159	753.99	Hillslope	Woody Shrubs	High	13	0	54	13
SAR18_900	398232	7611912	918.97	Hillslope	Lichen		3	0	>120	DRY
SAR18_901	398423	7611920	946.93	Hillslope	Woody Shrubs		10	60	373	DRY
SAR18_902	398619	7612014	980.69	Hillslope	Tussocks	Low	3	13	>120	5
SAR18_903				Hillslope	Tussocks	Low	8	6	71	14
SAR18_904				Hillslope	Sedges	Low	0	28	62	0
SAR18_905	398901	7611974	997.20	Ridge	Lichen	Low	0	3	>120	DRY
SAR18_906	398985	7611517	996.61	Ridge	Tussocks	High	15	26	542	41
SAR18_907	398983	7611517	996.61	Ridge	Lichen	Low	0	6	>120	DRY
SAR18_908	399012	7611428	998.72	Ridge	Tussocks	High	13	37	91	20
SAR18_909	399011	7611424	998.77	Ridge	Lichen	Low	1	4	>120	DRY
SAR18_910	399086	7611436	997.90	Ridge	Tussocks	High	10	40	80	48
SAR18_911	399052	7611438	1000.00	Ridge	Lichen	Low	2	5	>120	DRY
SAR18_912	398652	7611299	963.28	Hillslope			2	0	>120	DRY
SAR18_913	398655	7611284	963.99	Hillslope	Woody Shrubs	High	10	60	>120	DRY

Table B2: Measured soil properties data from samples collected during the 2017 and 2018 field campaigns.

Sample Site ID	E [m]	N [m]	Depth [m]	Soil	ϕ [-]	P [g/cm³]	LOI [%]	Sat K [W/mK]	Dry K [W/mK]	K [m/s]	α [1/m]	n [-]	S_r [-]
FVB_12	405742	7612807	0.08	C	0.85	0.14			0.08	4.14E-05			
FVB_16	405740	7612791	0.08	C	0.89	0.20	52			7.69E-04	0.0071	1.319	0
SB_15	405851	7612811	0.08	A	0.92	0.01	100	0.56		3.13E-04	0.0818	1.271	0
SB_30-40cm	405725	7613205	0.35	M	0.31	1.77	4	2.03	0.57	1.85E-07	0.0012	1.374	0
SB_42	405841	7612812	0.08	A	0.81	0.06	89	0.57	0.09	1.66E-03	0.0503	1.453	0.025
SVB_10	405731	7613212	0.05	A	0.88	0.05	100	0.45		4.25E-04	0.0874	1.442	0
SVB_60	405714	7613222	0.08	A	0.92	0.08	100			4.05E-04	0.0235	1.501	0.017
SVB_65	405713	7613204	0.08	A	0.69	0.11				7.68E-04	0.0264	1.314	0.003
SVB_V	405725	7613205	0.33	M	0.61	0.92	4			3.29E-07	0.0033	1.349	0
FVB_04b	405745	7612795	0.18	C	0.78	0.06	100			2.06E-06	0.0534	1.781	0.102
SB_43	405840	7612816	0.03	C	0.79	0.22	70	0.58	0.10	1.93E-07	0.0082	1.677	0.015
UKP_003	402700	7616460	0.23	M	0.64	0.87	15	0.94	0.23	1.16E-08	0.0030	1.274	0
UKP_302	401806	7617439	0.14	M	0.72	0.68	22	0.74	0.12	1.81E-05	0.0066	2.74	0.4
UKP_407	408252	7606212	0.03	A	0.85	0.06	87	0.74	0.08	6.91E-04	0.1853	1.337	0
UKP_508b	403282	7608164	0.33	M	0.30	1.85	3	2.48	0.55	4.47E-06	0.0006	1.386	0
UKP_106	402322	7616101	0.08	A	0.78	0.09	86	0.57	0.09	7.42E-04	0.1242	1.419	0.021
UKP_401	409329	7606554	0.18	C	0.84	0.21	80	0.56	0.07	5.45E-08	0.0148	1.438	0.024
UKP_408	408248	7606217	0.20	C	0.83	0.22	73	0.57	0.09	1.03E-04	0.0121	1.452	0
UKP_604	401648	7625580	0.13	C	0.78	0.14	74	0.57	0.08		0.0192	1.556	0.019
UKP_505	402485	7608006	0.07	C	0.80	0.21	66		0.09	1.05E-06			
UKP_007	403541	7616404	0.18	C	0.80	0.21	67	0.56	0.08	3.17E-05	0.0237	1.336	0
SB_35	405842	7612818	0.03	A	0.72	0.08		0.46	0.07	1.23E-03	0.0365	1.379	0
UKP_508a	403282	7608164	0.13	C	0.82	0.38	45	0.63	0.14	3.24E-06	0.0090	1.68	0.042
Ridge_top_10cm	406341	7613117	0.08	C	0.69	0.40				5.01E-07	0.0061	1.727	0.185
Valley_bottom_40_45	405702	7613112	0.43	C	0.61	0.60					0.0025	1.362	0.003
Midslope_5cm	405997	7613113	0.03	A	0.80	0.10				3.68E-03	0.0847	1.529	0
Valley_bottom_10_15	405702	7613112	0.13	C	0.89	0.17		0.50		4.54E-05	0.0043	2.099	0.176
UKP_614	400579	7625116	0.17	C	0.76	0.31	62				0.0453	1.37	0.228
UKP_411	407901	7606037	0.13	M	0.84	0.17	58				0.0327	1.305	0
SB_32	405844	7612816	0.03	A			100						
SVB_15	405729	7613214	0.03	A			100						
SAR18_108_0_5			0.03		0.77	0.56	21		0.13	3.04E-06			
SAR18_107_10_15	397335	7611919	0.13	A	0.91	0.16			0.05	9.05E-05			
SAR18_102_10_15	397878	7611853	0.13	A	1.06	0.06	93		0.06	2.06E-03			
SAR18_106_20_25	397335	7611919	0.23	M	0.82	0.48	27		0.10	7.18E-07			
SAR18_101_2_7	398149	7611921	0.05	C	0.94	0.15	50		0.05	6.95E-05			
SAR18_105_10_15	397545	7611920	0.13	A	0.85	0.09	95		0.06	4.02E-04			
SAR18_106_15_20	397335	7611919	0.18	C	0.85	0.17	56		0.06	6.75E-05			
SAR18_100_2_7	398149	7611921	0.05	A	0.99	0.08	93			1.82E-03			
SAR18_103_2_7	397878	7611853	0.05	A	0.99	0.04	89		0.08	4.50E-03			
SAR18_102_2_7	397878	7611853	0.05	A	0.90	0.05	96			3.53E-03			

SAR18_105_22_27	397545	7611920	0.25	C	0.88	0.17	64			5.14E-05			
SAR18_104_3_8	397878	7611853	0.06	C	0.92	0.17	46		0.05	5.25E-05			
SAR18_100_15_20	398149	7611921	0.18	M	0.80	0.46	23			1.79E-06			
SAR18_002_15_20	399367	7607755	0.18	C	0.88	0.29	58		0.07	3.01E-06			
SAR18_003_20_25	399074	7607725	0.23	C	0.92	0.23	63		0.05	1.32E-05			
SAR18_003_25_30	399074	7607725	0.28	C	0.86	0.30	52		0.07	4.86E-06			
SAR18_001_0_5	399367	7607755	0.03	C	0.90	0.22			0.06	3.76E-05			
SAR18_005_2_7	398688	7607646	0.05	A	0.98	0.05	92		0.06	2.03E-03			
SAR18_006_15_20	398688	7607646	0.18	C	0.94	0.22	59		0.06	6.13E-06			
SAR18_008_2_7	398397	7607647	0.05	C	0.89	0.19	22		0.06	8.22E-05			
SAR18_004_0_5	399074	7607725	0.03	C	0.98	0.18	51		0.05	4.60E-05			
SAR18_000_0_5	399402	7607770	0.03	C	0.75	0.37	42		0.06	4.50E-04			
SAR18_006_5_10	398688	7607646	0.08	C	0.99	0.14	72		0.05	5.32E-05			
SAR18_006_20_25	398688	7607646	0.23	C	0.88	0.23				4.94E-06			
SAR18_002_0_5	399367	7607755	0.03	A	0.98	0.07	92		0.06	2.03E-03			
SAR18_003_0_5	399074	7607725	0.03	A	1.02	0.07	100		0.06	3.53E-03			
SAR18_206_16_21	396015	7611560	0.19	C	0.85	0.22	64		0.06	1.42E-05			
SAR18_205_20_25	396216	7611579	0.23	M	0.92	0.17	69		0.05	3.17E-05			
SAR18_209_12_17	396580	7611812	0.15	C	0.82	0.36	44		0.09	5.49E-05			
SAR18_102_25_30	397878	7611853	0.28	M	0.59	1.03	9	1.08	0.16	2.97E-06			
SAR18_203_5_10	396379	7611511	0.08	A	0.90	0.10	96	0.57	0.01	1.16E-04			
SAR18_205_0_5	396216	7611579	0.03	A	0.88	0.10	100	0.55	0.04	1.45E-04			
SAR18_208_5_10	396555	7611794	0.08	A	0.94	0.05	83	0.41	0.06	2.25E-03			
SAR18_209_0_5	396580	7611812	0.03	A	0.99	0.07	77	0.24	0.06	1.69E-03			
SAR18_204 (tussok)_0_5	396216	7611579	0.03	A	0.92	0.09		0.46		2.70E-03			
SAR18_204_0_5	396216	7611579	0.03	A	0.92	0.05	90	0.45	0.05	6.38E-04			
SAR18_203_15_20	396379	7611511	0.18	C	0.84	0.14	77	0.58	0.05	7.85E-05			
SAR18_201_15_20	396530	7611635	0.18	A	0.89	0.08		0.47	0.05	2.75E-03			
SAR18_203_20_25	396379	7611511	0.23	M	0.81	0.29	71	0.45	0.08	5.44E-05			
SAR18_202_5_10	396383	7611523	0.08	A	0.98	0.05	82	0.33	0.05	1.88E-03			
SAR18_201_23_28	396530	7611635	0.26	M	0.85	0.33	52	0.58	0.08	4.28E-06			
SAR18_207_10_15	396015	7611560	0.13	C	0.91	0.20	77	0.59	0.06	1.32E-05			
SAR18_202_20_25	396383	7611523	0.23	C	0.84	0.24	52	0.65	0.06	2.39E-04			

SAR18_209_31_36	396580	7611812	0.34	M	0.71	0.74	18	0.83	0.17	5.79E-08			
SAR18_205_30_35	396216	7611579	0.33	M	0.50	1.24	12	1.47	0.28	1.16E-08			
SAR18_512_12_17	405875	7612701	0.15	C	0.89	0.16	85	0.57	0.05	1.58E-05			
SAR18_501_9_14	405546	7612665	0.12	C	0.85	0.20	64	0.59	0.06	1.67E-04			
SAR18_502_10_15	405547	7612658	0.13	M	0.50	1.49		1.85	0.44	1.16E-08			
SAR18_507_15_20	405722	7612736	0.18	C	0.89	0.21	78	0.58	0.05	1.87E-05			
SAR18_508_35_40	405758	7612761	0.38	C	0.73	0.52	46	0.76	0.16	7.33E-06			
SAR18_510_12_17	405769	7612769	0.15	C	0.91	0.19	19	0.55	0.04	1.30E-05			
SAR18_500_5_10	405553	7612653	0.08	A	0.97	0.05	94	0.54	0.05	2.49E-03			
SAR18_506_2_7	405722	7612736	0.05	A	0.91	0.07		0.49	0.04	2.04E-03			
SAR18_503_2_7	405662	7612720	0.05	A	0.91	0.06	94	0.24	0.03	2.64E-03			
SAR18_505_1_6	405670	7612738	0.04	A	1.00	0.05	94	0.57	0.04	2.81E-03			
SAR18_511_1_6	405857	7612772	0.04	A	0.96	0.05	96	0.49	0.04	1.22E-03			
SAR18_507_30_35	405722	7612736	0.33	C	0.81	0.25	70	0.57	0.10	6.83E-06			
SAR18_501_3_8	405546	7612665	0.06	A	0.88	0.06	89	0.58	0.09	1.37E-03			
SAR18_500_20_25	405553	7612653	0.23	C	0.87	0.15	68	0.53	0.09	1.98E-04			
SAR18_508_10_15	405758	7612761	0.13	C	0.88	0.18	79	0.55	0.05	1.47E-05			
SAR18_508_20_25	405758	7612761	0.23	C	0.89	0.22	80	0.50	0.07	5.71E-06			
SAR18_507_22_27	405722	7612736	0.25	C	0.82	0.27	61	0.59	0.07	3.51E-06			
SAR18_505_10_15	405670	7612738	0.13	C	0.84	0.18	68	0.60	0.04	3.95E-05			
SAR18_511_15_20	405857	7612772	0.18	C	0.86	0.22	74	0.60	0.06	6.68E-06			
SAR18_510_23_28	405769	7612769	0.26	C	0.81	0.28	80	0.55	0.07	2.20E-06			
SAR18_510_35_40	405769	7612769	0.38	C	0.60	0.59	36	0.80	0.17	1.39E-07			
SAR18_511_25_30	405857	7612772	0.28	M			9	1.42		5.56E-06			
SAR18_517_10_15			0.13				9						
SAR18_705_55_60	407119	7612763	0.58	M			6	0.62		7.79E-06			
SAR18_702_15_20	407453	7612929	0.18	C	0.85	0.30	41	0.58	0.144	2.43E-05			
SAR18_700_0_5	407211	7612977	0.03	M									
SAR18_707_5_10	407111	7612753	0.08	C	0.91	0.17		0.55	0.08	2.22E-05			
SAR18_701_5_10	407213	7612917	0.08	A	0.96	0.06	95	0.48	0.07	1.38E-03			
SAR18_712_20_25	406741	7612706	0.23	C	0.89	0.17	83	0.34	0.05	1.10E-05			
SAR18_705_25_30	407119	7612763	0.28	M	0.83	0.36	46	0.64	0.11	1.57E-05			
SAR18_711_11_16	406882	7612716	0.14	C	0.88	0.22		0.64	0.06	9.34E-06			
SAR18_707_45_50	407111	7612753	0.48	C	0.91	0.16	76	0.58	0.08	2.05E-05			

SAR18_707_23_28	407111	7612753	0.26	C	0.90	0.20	66	0.60	0.06	1.26E-05			
SAR18_702_5_10	407453	7612929	0.08	A	0.93	0.08	97	0.64	0.06	2.23E-04			
SAR18_705_15_20	407119	7612763	0.18	A	0.95	0.05	94	0.52	0.23	2.86E-03			
SAR18_708_10_15	407059	7612751	0.13	C	0.87	0.19	82	0.55	0.05	9.38E-06			
SAR18_711_0_5	406882	7612716	0.03	A	0.89	0.02	90	0.53	0.16	1.96E-03			
SAR18_708_25_30	407059	7612751	0.28	C	0.87	0.33		1.43	0.09	1.74E-06			
SAR18_711_30_35	406882	7612716	0.33	M	0.63	0.89		2.04	0.16	3.47E-08			
SAR18_200_7_12	396530	7611635	0.10	M	0.36	1.76	3			4.63E-08			
SAR18_513_7_12	405875	7612701	0.10	M	0.38	1.55	4	1.17		1.16E-08			
SAR18_204_25_30	396216	7611579	0.28	M	0.45	1.19	11	1.42	0.39	2.31E-08			
SAR18_208_20_25	396555	7611794	0.23	M	0.36	1.78	2	1.98		1.16E-08			
SAR18_008_14_19	398397	7607647	0.17	M	0.31	1.97	2	2.02		1.16E-08			
SAR18_206_21_26	396015	7611560	0.24	M	0.40	1.59	5	1.84		1.16E-07			
SAR18_701_15_20	407213	7612917	0.18	C	0.81	0.17	54	0.59		2.81E-04			
SAR18_808_5_10	395207	7615168	0.08	A	0.92	0.09	89	0.41		1.12E-03			
SAR18_805_23_28	395305	7617170	0.26	C	0.90	0.16	83	0.59		1.88E-05			
SAR18_800_10_15	395644	7616282	0.13	A	0.87	0.07	91	0.51		8.31E-04			
SAR18_806_10_15	394888	7616472	0.13	A	0.86	0.09		0.30		1.60E-03			
SAR18_802_1_6	395633	7612085	0.04	A	0.86	0.11	80	0.53		2.50E-04			
SAR18_803_30_35	395651	7616252	0.33	C	0.75	0.18	78	0.47		5.71E-06			
SAR18_802_21_26	395633	7612085	0.24	C	0.90	0.18	66	0.57		1.34E-05			
SAR18_701_25_30	407213	7612917	0.28	M	0.65	0.76	5	1.42		1.41E-05			
SAR18_805_34_39	395305	7617170	0.37	C	0.89	0.18	78	0.58		9.90E-06			
SAR18_802_35_40	395633	7612085	0.38	M	0.59	0.82	9	0.60		4.40E-07			
SAR18_800_21_26	395644	7616282	0.24	C	0.91	0.18	72	0.55		1.22E-05			
SAR18_802_33_38	395633	7612085	0.36	M	0.62	0.98	10	1.31		2.31E-08			
SAR18_809_20_25	395196	7615159	0.23	M	0.59	0.99	6	1.28		1.04E-06			
SAR18_712_35_40	406741	7612706	0.38	M	0.34	1.47	5	1.88		8.80E-07			

Table B3: Summary of stratigraphy observations characterized by landscape class.

	Acrotelm Thickness				Catotelm Thickness				Active Layer Thickness				Water Table Depth			
Category	Mean	Std. Dev.	n	T-Test or ANOVA *p*	Mean	Std. Dev.	n	T-Test or ANOVA *p*	Mean	Std. Dev.	n	T-Test or ANOVA *p*	Mean	Std. Dev.	n	T-Test or ANOVA *p*
Landscape Zone																
Hillslope	9.71	5.90	148	0.6406	13.5	12.5	148	0.020697	65.1	19.8	148	0.0086952	23.664	29.094	148	0.15179
Riparian	10.31	6.32	26		19.9	14.8	26		54.2	16.7	26		15.269	13.725	26	
Vegetation Cover Type																
Woody Shrubs	12.4	6.1	45	1.71E-12	12.1	13.2	45	3.78E-10	59.6	21.2	45	0.73759	24.023	25.408	45	1.57E-04
Lichen	1.9	1.5	24		1.3	2.2	24		>120	n/a	24					
Tussocks	10.6	4.9	68		14.4	9.9	68		60.3	17.1	68		21.841	20.061	68	
Sedges	9.7	5.9	48		22.4	15.1	48		62.4	16.3	48		8.1979	11.242	48	
Microtopography																
Local High	12.7	5.4	67	7.95E-08	13.9	11.4	67	0.96729	58.1	18.8	67	0.0003639	28.727	22.231	67	0.35873
Local Low	7.9	5.7	125		14.0	14.0	125		69.2	20.4	125		24.354	34.449	125	
Landscape Zone, Vegetation Cover Type, and Microtopography																
Woody Shrubs - Riparian Zone	10.4	4.9	10	5.00E-12	11.37	10.36	10	9.99E-09	51.9	19.9	10	0.097489	20.1	16.313	10	0.00015182
Woody Shrubs - Hillslope Zone	13.1	6.5	32		12.59	14.36	32		60.9	21.1	32		23.933	25.054	32	
Lichen	1.9	1.5	24		1.29	2.24	24									
Tussock Tundra - Local High	12.0	4.7	38		14.43	9.89	38		61.4	18.1	38		27.153	21.7	38	
Tussock Tundra - Local Low	8.8	4.6	30		14.33	10.11	30		58.8	16.0	30		15.467	16.021	30	
Sedges - Riparian Zone - Local High	13.0	5.3	3		25.22	12.85	3		41.7	7.6	3		22	7	3	
Sedges - Riparian Zone - Local Low	10.1	7.8	12		27.42	14.38	12		57.9	14.6	12		10.5	11.469	12	
Sedges - Hillslope	8.9	5.0	32		20.89	15.32	32		67.1	14.9	32		5.7031	10.541	32	

Table B4: Summary of measured soil properties observation characterized by soil type.

	Mean	Std. Dev.	n	ANOVA *p*
Porosity				
Acrotelm	0.91	0.08	40	2.38E-36
Catotelm	0.85	0.07	61	
High-Organic Mineral	0.69	0.14	16	
Low-Organic Mineral	0.37	0.09	11	
Bulk Density				
Acrotelm	0.07	0.03	40	2.42E-57
Catotelm	0.23	0.10	61	
High-Organic Mineral	0.74	0.34	16	
Low-Organic Mineral	1.62	0.29	11	
Saturated Thermal Conductivity				
Acrotelm	0.57	0.38	28	4.60E-16
Catotelm	0.60	0.16	38	
High-Organic Mineral	1.03	0.35	13	
Low-Organic Mineral	1.79	0.56	11	
Dry Thermal Conductivity				
Acrotelm	0.07	0.04	27	9.64E-28
Catotelm	0.07	0.03	47	
High-Organic Mineral	0.17	0.11	11	
Low-Organic Mineral	0.54	0.03	3	
Saturated Hydraulic Conductivity				
Acrotelm	1.62E-03	1.13E-03	40	3.92E-32
Catotelm	5.67E-05	1.23E-04	58	
High-Organic Mineral	8.55E-06	1.51E-05	16	
Low-Organic Mineral	2.54E-06	4.58E-06	11	
Organic Matter Content				
Acrotelm	0.94	0.08	34	1.60E-25
Catotelm	0.65	0.16	52	
High-Organic Mineral	0.23	0.19	17	
Low-Organic Mineral	0.04	0.01	12	
van Genuchten Alpha				
Acrotelm	7.78E-02	5.23E-02	9	6.19E-04
Catotelm	1.71E-02	1.63E-02	12	
High-Organic Mineral	1.41E-02	1.62E-02	3	
Low-Organic Mineral	1.59E-03	1.17E-03	4	
van Genuchten n				

Acrotelm	1.405	0.086601	9	0.20414
Catotelm	1.5664	0.23452	12	
High-Organic Mineral	1.773	0.83759	3	
Low-Organic Mineral	1.3668	0.01648	4	
van Genuchten θ_r				
Acrotelm	0.007333	0.010488	9	0.12146
Catotelm	0.066167	0.084201	12	
High-Organic Mineral	0.13333	0.23094	3	
Low-Organic Mineral	0	0	4	

Table B5: Predictive equations for selected measured soil properties based on bulk density across all data for all samples.

Dependent Variable	**Predictive model based on ρ_b**
φ	$-0.35\rho_b + 0.93$
LOI	$1.046 * \exp(-2.296\rho_b)$
K	$10\text{^}(-6.68{\rho_b}^{0.2513})$
α	$10\text{^}(-2.631{\rho_b}^{0.2539})$
k	$0.2539\rho_b + 0.024$

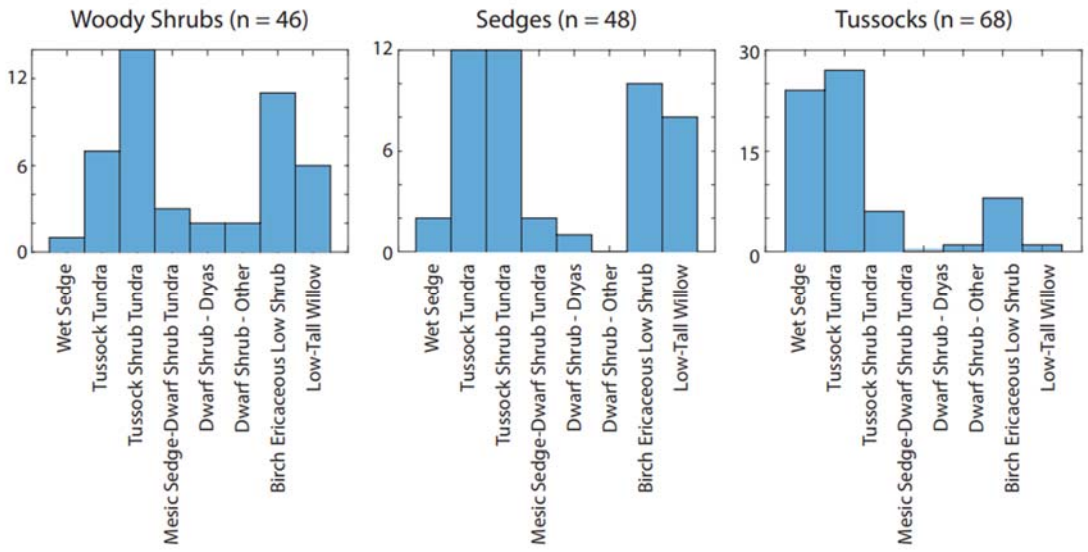

Figure B1: Distributions of the NSSI-defined land cover classes for each of our sites, as they compare to the observed dominant vegetation (Woody Shrubs, Sedge, and Tussock Tundra) at each plot.

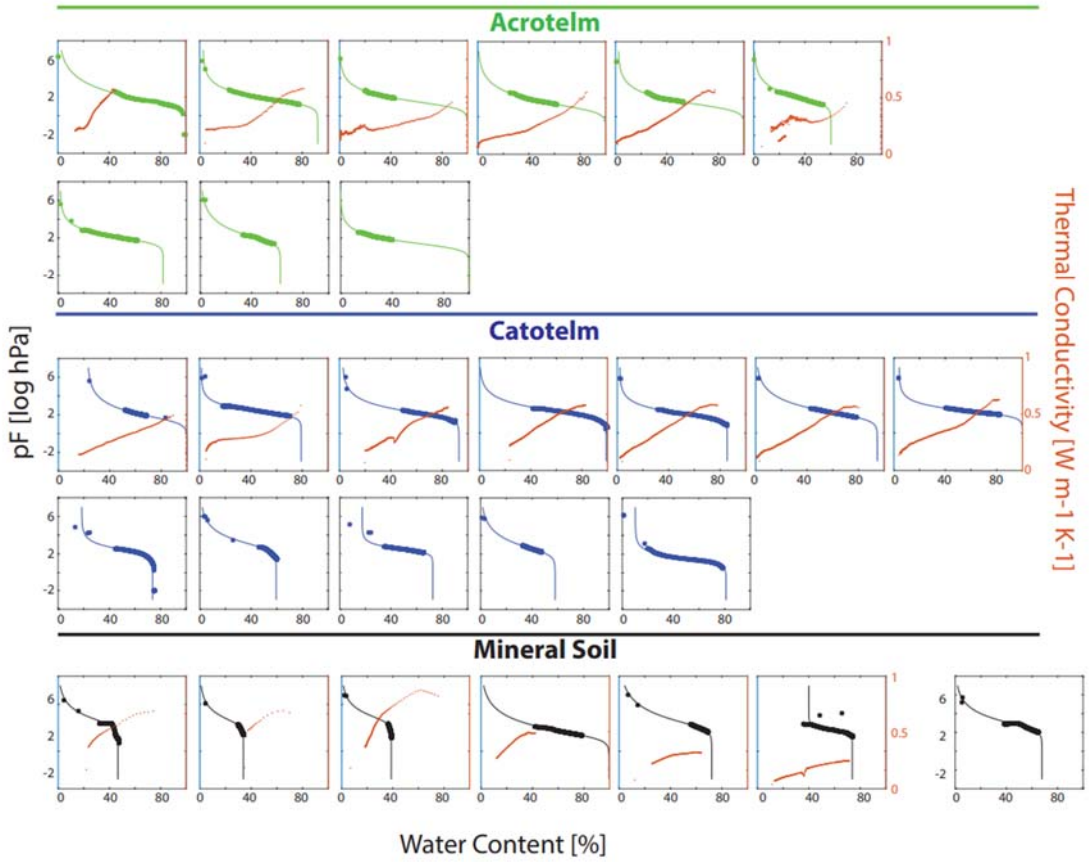

Figure B2: (Left y-axis): Individual soil water retention curves for each soil sample analyzed in the laboratory via the HYPROP (at low soil water suctions) and the WP4 (at high soil water suctions), grouped by soil type. Dots represent measurement values, and lines represent the van Genuchten-fitted soil water retention curve given the measurement values. (Right y-axis): Individual thermal conductivity decay curves simultaneously measurement points collected during using the KD2 during the evaporation experiment.

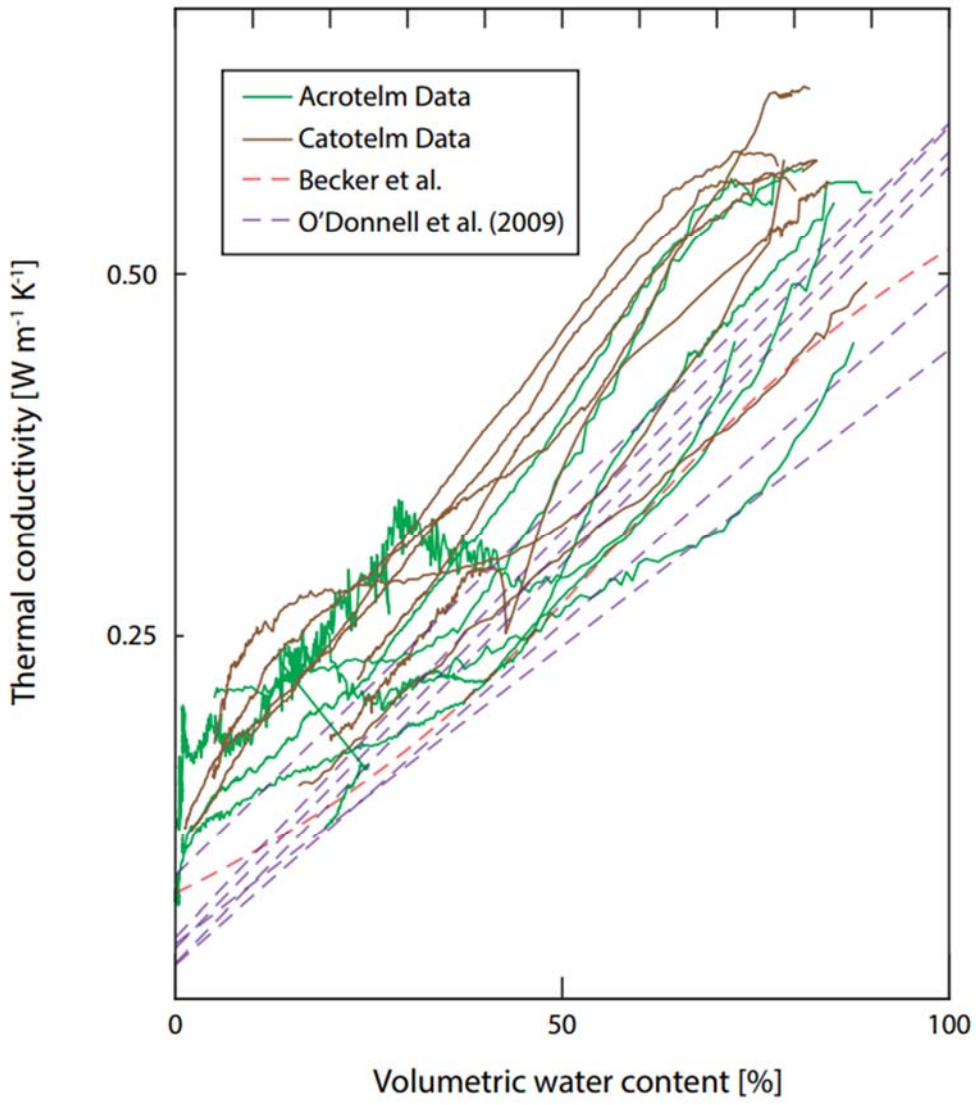

Figure B3: Relationship between effective measured soil thermal conductivity and volumetric water content as determined during HYPROP evaporation experiments.

APPENDIX C: SUPPLEMENTAL MATERIALS FOR CHAPTER 4

Table C1: List of symbols used in numerical modeling work and default model parameters.

Symbol	Physical quantity	ATS unit	Definition or value
φ	Porosity	-	Table 4.1
t	Time	s	Table 4.1
ω_l	Liquid mole fraction	-	1
ω_i	Ice mole fraction	-	1
ω_g	Gas mole fraction	-	Equation 2
$e_{sat}\{T\}$	Saturated vapor pressure as a function of temperature	Pa	Clausius-Clapeyron Equation
p_g	Gas partial pressure	Pa	p_{atm}
η	Molar density	mol m^{-3}	Specified in the periodic table
s	Phase saturation	-	Dependent variable
V_l	Darcy fluid velocity	m s^{-1}	Dependent variable
q	Fluid flow rate	mol m^{-3} s^{-1}	Dependent variable
$k_{r,l}$	Relative permeability	-	Equation 10
k	Intrinsic permeability	m^2	Equation 44
$\mu_l\{T\}$	Dynamic viscosity of water	Pa s	Above 20C: $0.001 * 10^{\left(\frac{1.3272(293.15-T)-0.001053(293.15-T)^2}{T-168.15}\right)}$ Below 20C: $0.001 * 10^{1301\left(\frac{1}{998.333-8.1855(293.15-T)+0.00585(293.15-T)^2}-\frac{1}{998.333}\right)}$
p	Pressure	Pa	Dependent variable
$\rho_l\{T\}$	Mass density of liquid water	kg m^{-3}	$916.724 - 0.147(T - 273.15) - 0.000238(T - 273.15)^2$
g	Acceleration due to gravity	m s^{-2}	9.81
$\hat{z}$	Vertical unit vector	m	1
u	Specific internal energy	J mol^{-1}	$76(T - 273.15)$
$C_{v,soil}$	Volumetric heat capacity of soil matrix	J m^{-3} K^{-1}	$620 * \rho_{soil}$
T	Temperature	K	Dependent variable
h	Specific enthalpy	J mol^{-1}	u
κ_{eff}	Effective thermal conductivity of soil-air-water mixture	W m^{-1} K^{-1}	Equation 11
Ke	Kersten number	[-]	Equations 12 and 13

κ_{sat}	Saturated thermal conductivity of soil matrix	W m^{-1} K^{-1}	Table 4.1
κ_{dry}	Dry thermal conductivity of soil matrix	W m^{-1} K^{-1}	Table 4.1
κ_{water}	Thermal conductivity of water	W m^{-1} K^{-1}	0.6
κ_{air}	Thermal conductivity of air	W m^{-1} K^{-1}	0.03
τ_u	Unfrozen Kersten number fitting parameter	-	0.5
τ_f	Frozen Kersten number fitting parameter	-	1
Q	Thermal source or sink	W m^{-3} or W m^{-2}	Dependent variable or boundary condition
β	Soil colloidal coefficient	-	1
L_f	Latent heat of fusion for melting or freezing snow	J kg^{-1}	334,000
ϑ	Dimensionless temperature	-	$(T - T_0)/T_0$
ϑ_f	Dimensionless freezing point	-	Equation 6
γ_{i-l}	Surface tension between ice and water	N m^{-1}	33.1
γ_{l-g}	Surface tension between water and gas	N m^{-1}	72.7
α	Van Genuchten fitting parameter	L^{-1}	Table 4.1
n	Van Genuchten fitting parameter	-	Table 4.1
m	Van Genuchten fitting parameter	-	$1 - 1/n$
s_r	Residual water content	[-]	Table 4.1
$\chi(T)$	Smoothed step function representing phase transition between ice and water	-	$\cos\left(\frac{2\pi}{\tau}T + \frac{3\pi}{2}\right) * 0.5 + 0.5$
τ	Width of smoothed step function χ	K	0.2
d_w	Ponded water depth	m	Dependent variable
U_w	Surface flow velocity	m s^{-1}	Equation 15
q	Water source or sink	mol m^{-2} s^{-1}	Specified or solved for
N	Manning's roughness coefficient	s $m^{-1/3}$	1

δ	Numerical surface velocities fitting parameter	-	0.01
a	Surface albedo	-	Ice = 0.44, Water = 0.141, Tundra = 0.135
ε_s	Surface emissivity	-	Snow and ice = 0.98, Water = 0.979, Tundra = 0.92
ϵ	Stefan-Boltzman constant	W m^{-2} K^{-4}	5.67E-8
C_p	Specific heat of water	J g^{-1} K^{-1}	4.186
D_{eh}	Turbulent exchange of latent and sensible heat	m s^{-1}	Equation 21
ξ	Atmospheric stability function	-	Equation 22
R_i	Atmospheric stability parameter	-	Equation 23
z_r	Reference height of wind speed measurement	m	3
U_s	Wind speed	m s^{-1}	Forcing data
λ_s	Latent heat of sublimation for snow	J kg^{-1}	2834000
λ_e	Latent heat of evaporation for the ground surface	J kg^{-1}	2497848
E_r	Evaporation resistance	m s^{-1}	Equation 25
R_{air}	Air resistance	s m^{-1}	Equation 26
R_{soil}	Soil resistance	s m^{-1}	Equation 27
e_a	Vapor pressure of air	Pa	Calculated from forcing data
e_s	Vapor pressure of soil or snow	Pa	Dependent variable
p_{atm}	Atmospheric pressure	Pa	Forcing data
L	Length that vapor most travel from the point of evaporation	m	Equation 28
D_0	Molecular diffusion coefficient of water vapor in air	m^2 s^{-1}	2.2E-5
T_a	Air temperature	K	Forcing data
T_s	Surface temperature	K	Dependent variable
z_s	Snowpack or ponded water height	m	Dependent variable
GFW_w	Gram formula weight of water	g mol^{-1}	18.0153
$\rho_{snow,fresh}$	Density of fresh snow	kg m^{-3}	100
H_p	Pressure head	m	Dependent variable
x	Length dimension	m	Specified in model geometry (Figure 4.1)

K	Hydraulic conductivity	$m\ s^{-1}$	Table 4.1
dx	Length of model grid cell	m	10
dz	Height of model grid cell	m	Table 4.1
nx	Number of model grid cells in the x dimension	m	30
nz	Number of model grid cells in the z dimension	m	Figure 4.1

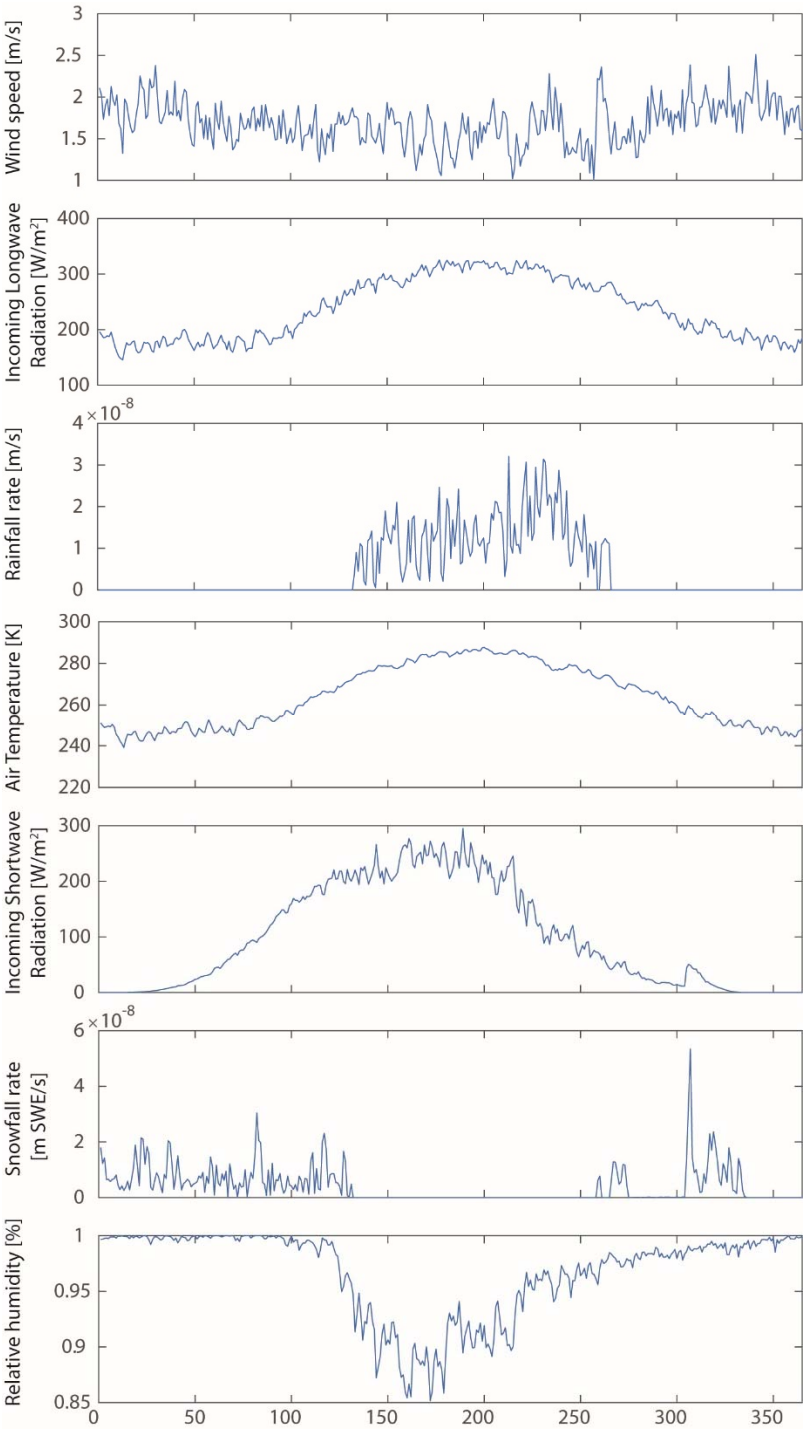

Figure C1: Time-series of the 'average year' meteorological forcing data used to drive ATS simulations. Data acquired from the MIROC5 Global Climate Model (Watanabe et al., 2010).

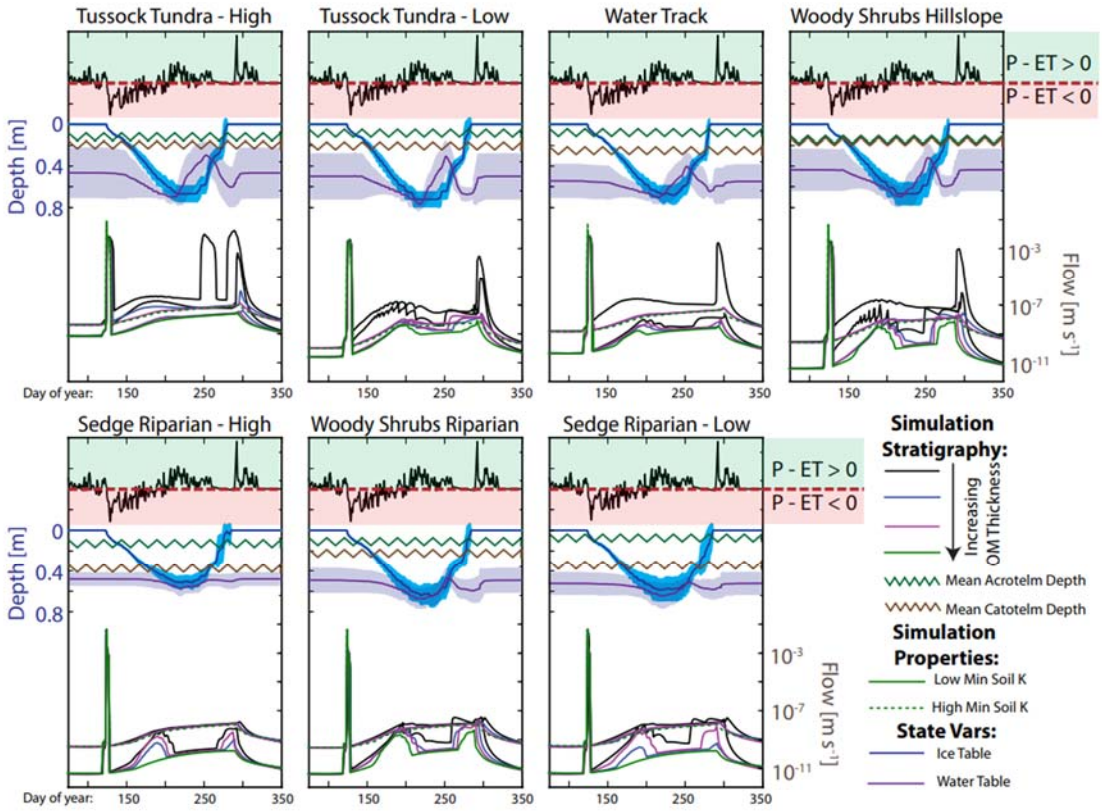

Figure C2: Simulated hydrologic fluxes and state variables for the stratigraphy and properties given in the seven major landscape types in the North Slope Footslope. Top panel: net gain (green shading) or loss (red shading) of water to the subsurface due to precipitation or evaporation. Middle panel: depth to the first fully-frozen cell (blue), approximate b_{ac} (green and jagged), approximate b_{ct} (brown and jagged), and the depth to the first fully-saturated cell (purple). Shading around the ice table and water table depths represent the 95% confidence bounds from the 32 simulations within each landscape class. Bottom panel: lateral groundwater flow from each grid. Line colors denote the organic matter thicknesses, and line dashing denotes either high or low mineral soil K.

References

Abolt, C. J., Young, M. H., Atchley, A. L., & Harp, D. R. (2018). Microtopographic control on the ground thermal regime in ice wedge polygons. *The Cryosphere (Online)*, *12*(6). https://doi.org/10.5194/tc-12-1957-2018

Adams, W. A. (1973). The Effect of Organic Matter on the Bulk and True Densities of Some Uncultivated Podzolic Soils. *Journal of Soil Science*, *24*(1), 10–17. https://doi.org/10.1111/j.1365-2389.1973.tb00737.x

Agus, F., Hairiah, K., & Mulyani, A. (2011). Measuring carbon stock in peat soils. *World Agroforestry Centre (ICRAF) Southeast Asia Regional Program and Indonesian Centre for Agricultural Land Resources Research and Development*.

van Asselen, S., Stouthamer, E., & van Asch, T. W. J. (2009). Effects of peat compaction on delta evolution: A review on processes, responses, measuring and modeling. *Earth-Science Reviews*, *92*(1–2), 35–51. https://doi.org/10.1016/j.earscirev.2008.11.001

Assouline, S. (2006). Modeling the Relationship between Soil Bulk Density and the Hydraulic Conductivity Function. *Vadose Zone Journal*, *5*(2), 697–705. https://doi.org/10.2136/vzj2005.0084

Atchley, A. L., Painter, S. L., Harp, D. R., Coon, E. T., Wilson, C. J., Liljedahl, A. K., & Romanovsky, V. E. (2015). Using field observations to inform thermal hydrology models of permafrost dynamics with ATS (v0.83). *Geosci. Model Dev.*, *8*(9), 2701–2722. https://doi.org/10.5194/gmd-8-2701-2015

Atchley, A. L., Coon, E. T., Painter, S. L., Harp, D. R., & Wilson, C. J. (2016). Influences and interactions of inundation, peat, and snow on active layer thickness. *Geophysical Research Letters*, *43*(10), 5116–5123. https://doi.org/10.1002/2016GL068550

Ball, D. F. (1964). Loss-on-Ignition as an Estimate of Organic Matter and Organic Carbon in Non-Calcareous Soils. *Journal of Soil Science*, *15*(1), 84–92. https://doi.org/10.1111/j.1365-2389.1964.tb00247.x

Becker, B. R., Misra, A., & Fricke, B. A. (1992). Development of correlations for soil thermal conductivity. *International Communications in Heat and Mass Transfer*, *19*(1), 59–68. https://doi.org/10.1016/0735-1933(92)90064-O

Beckwith, C. W., Baird, A. J., & Heathwaite, A. L. (2003a). Anisotropy and depth-related heterogeneity of hydraulic conductivity in a bog peat. I: laboratory measurements. *Hydrological Processes*, *17*(1), 89–101. https://doi.org/10.1002/hyp.1116

Beckwith, C. W., Baird, A. J., & Heathwaite, A. L. (2003b). Anisotropy and depth-related heterogeneity of hydraulic conductivity in a bog peat. I: laboratory measurements. *Hydrological Processes*, *17*(1), 89–101. https://doi.org/10.1002/hyp.1116

Bense, V. F., Kooi, H., Ferguson, G., & Read, T. (2012). Permafrost degradation as a control on hydrogeological regime shifts in a warming climate. *Journal of Geophysical Research: Earth Surface*, *117*(F3). https://doi.org/10.1029/2011JF002143

Blaen, P. J. (2013). Water source dynamics of high Arctic river basins. *Hydrological Processes*. https://doi.org/10.1002/hyp.9891

Bockheim, J. G. (2007). Importance of Cryoturbation in Redistributing Organic Carbon in Permafrost-Affected Soils. *Soil Science Society of America Journal*, *71*(4), 1335. https://doi.org/10.2136/sssaj2006.0414N

Bockheim, J. G., Walker, D. A., Everett, L. R., Nelson, F. E., & Shiklomanov, N. I. (1998a). Soils and Cryoturbation in Moist Nonacidic and Acidic Tundra in the Kuparuk River Basin, Arctic Alaska, U.S.A. *Arctic and Alpine Research*, *30*(2), 166–174. https://doi.org/10.1080/00040851.1998.12002888

Bockheim, J. G., Walker, D. A., Everett, L. R., Nelson, F. E., & Shiklomanov, N. I. (1998b). Soils and cryoturbation in moist nonacidic and acidic tundra in the Kuparuk River Basin, Arctic Alaska, USA. *Arctic and Alpine Research*, 166–174.

Boelter, D. H. (1969). Physical Properties of Peats as Related to Degree of Decomposition. *Soil Science Society of America Journal*, *33*(4), 606–609. https://doi.org/10.2136/sssaj1969.03615995003300040033x

Bouwer, H., & Rice, R. C. (1976). A slug test for determining hydraulic conductivity of unconfined aquifers with completely or partially penetrating wells. *Water Resources Research*, *12*(3), 423–428. https://doi.org/10.1029/WR012i003p00423

Branham, J. E., & Strack, M. (2014). Saturated hydraulic conductivity in Sphagnum-dominated peatlands: do microforms matter? *Hydrological Processes*, *28*(14), 4352–4362. https://doi.org/10.1002/hyp.10228

Bryan, K. (1946). Cryopedology, the study of frozen ground and intensive frost-action, with suggestions on nomenclature. *American Journal of Science*, *244*(9), 622–642. https://doi.org/10.2475/ajs.244.9.622

Cardenas, M. B. (2010). Lessons from and assessment of Boussinesq aquifer modeling of a large fluvial island in a dam-regulated river. *Advances in Water Resources*, *33*(11), 1359–1366. https://doi.org/10.1016/j.advwatres.2010.03.015

Carey, S. K., & DeBeer, C. M. (2008). Rainfall-runoff hydrograph characteristics in a discontinuous permafrost watershed and their relation to ground thaw. In *Proceedings, Ninth International Conference on Permafrost. University of Alaska Fairbanks* (pp. 233–238).

Carman, P. C. (1956). *Flow of gases through porous media*. Academic press.

Clark, M. P., Fan, Y., Lawrence, D. M., Adam, J. C., Bolster, D., Gochis, D. J., et al. (2015). Improving the representation of hydrologic processes in Earth System Models. *Water Resources Research*, *51*(8), 5929–5956. https://doi.org/10.1002/2015WR017096

Coon, E. T., David Moulton, J., & Painter, S. L. (2016). Managing complexity in simulations of land surface and near-surface processes. *Environmental Modelling & Software*, *78*, 134–149. https://doi.org/10.1016/j.envsoft.2015.12.017

Dall'Amico, M. (2010, April 2). *Coupled Water and Heat Transfer in Permafrost Modeling* (phd). University of Trento. Retrieved from http://eprints-phd.biblio.unitn.it/335/

Detterman, R. L., Bowsher, A. L., & Dutro, J. T. (1958). Glaciation on the Arctic Slope of the Brooks Range, Northern Alaska. *Arctic*, *11*(1), 43–61.

Devices, D. (2006). KD2 Pro thermal properties analyzer operator's manual version 4. *Decagon Devices, Pullman, WA*.

Endrizzi, S., Gruber, S., Dall'Amico, M., & Rigon, R. (2014). GEOtop 2.0: simulating the combined energy and water balance at and below the land surface accounting for soil freezing, snow cover and terrain effects. *Geosci. Model Dev.*, *7*(6), 2831–2857. https://doi.org/10.5194/gmd-7-2831-2014

Evans, S., & Ge, S. (2017). Contrasting hydrogeologic responses to warming in permafrost and seasonally frozen ground hillslopes. *Geophysical Research Letters*, *44*(4), 1803–1813. https://doi.org/10.1002/2016GL072009

Everett, K. R. (1980). Soils and Mapping. In-Environmental Engineering and Ecological Baseline Investigations along the Yukon River-Prudhoe Bay Haul Road. J. Brown and RL Berg (Eds.) CRREL Report No. 80-19. Cold Regions Research and Engineering Laboratory. *US Army Corps of Engineers, Hanover, New Hampshire*, 48–52.

Fisher, E. A. (1923). The Freezing of Water in Capillary Systems. *The Journal of Physical Chemistry*, *28*(4), 360–367. https://doi.org/10.1021/j150238a006

Frampton, A., & Destouni, G. (2015). Impact of degrading permafrost on subsurface solute transport pathways and travel times. *Water Resources Research*, n/a-n/a. https://doi.org/10.1002/2014WR016689

Frampton, A., Painter, S., Lyon, S. W., & Destouni, G. (2011). Non-isothermal, three-phase simulations of near-surface flows in a model permafrost system under seasonal variability and climate change. *Journal of Hydrology*, *403*(3–4), 352–359. https://doi.org/10.1016/j.jhydrol.2011.04.010

Freeze, R. A., & Cherry, J. A. (1979). *Groundwater*. Englewood Cliffs, N.J.: Prentice-Hall.

van Genuchten, M. T. (1980). A Closed-form Equation for Predicting the Hydraulic Conductivity of Unsaturated Soils. *Soil Science Society of America Journal*, *44*(5), 892. https://doi.org/10.2136/sssaj1980.03615995004400050002x

Ghanbarian-alavijeh, B., Liaghat, A., Huang, G.-H., & Van genuchten, M. T. (2010). Estimation of the van Genuchten Soil Water Retention Properties from Soil Textural Data. *Pedosphere*, *20*(4), 456–465. https://doi.org/10.1016/S1002-0160(10)60035-5

Gouttevin, I., Menegoz, M., Dominé, F., Krinner, G., Koven, C., Ciais, P., et al. (2012). How the insulating properties of snow affect soil carbon distribution in the continental pan-Arctic area. *Journal of Geophysical Research: Biogeosciences*, *117*(G2). https://doi.org/10.1029/2011JG001916

Hahn, S. C., Oberbauer, S. F., Gebauer, R., Grulke, N. E., Lange, O. L., & Tenhunen, J. D. (1996). Vegetation structure and aboveground carbon and nutrient pools in the Imnavait Creek Watershed. In *Landscape function and disturbance in Arctic tundra* (pp. 109–128). Springer. Retrieved from http://link.springer.com/chapter/10.1007/978-3-662-01145-4_5

Hamilton, T. D. (1982a). A late Pleistocene glacial chronology for the southern Brooks Range: Stratigraphic record and regional significance. *GSA Bulletin*, *93*(8), 700–716. https://doi.org/10.1130/0016-7606(1982)93<700:ALPGCF>2.0.CO;2

Hamilton, T. D. (1982b). A late Pleistocene glacial chronology for the southern Brooks Range: Stratigraphic record and regional significance. *GSA Bulletin*, *93*(8), 700–716. https://doi.org/10.1130/0016-7606(1982)93<700:ALPGCF>2.0.CO;2

Harp, D. R., Atchley, A. L., Painter, S. L., Coon, E. T., Wilson, C. J., Romanovsky, V. E., & Rowland, J. C. (2015). Effect of soil property uncertainties on permafrost thaw projections: a calibration-constrained analysis. *The Cryosphere Discussions*, *9*(3), 3351–3404. https://doi.org/10.5194/tcd-9-3351-2015

Hayashi, M., Goeller, N., Quinton, W. L., & Wright, N. (2007). A simple heat-conduction method for simulating the frost-table depth in hydrological models. *Hydrological Processes*, *21*(19), 2610–2622. https://doi.org/10.1002/hyp.6792

Hillel, D. (1998). *Environmental Soil Physics: Fundamentals, Applications, and Environmental Considerations* (1 edition). San Diego, CA: Academic Press.

Hinkel, K. M., & Nelson, F. E. (2003). Spatial and temporal patterns of active layer thickness at Circumpolar Active Layer Monitoring (CALM) sites in northern Alaska, 1995–2000. *Journal of Geophysical Research: Atmospheres*, *108*(D2), 8168. https://doi.org/10.1029/2001JD000927

Hinzman, L. D., Kane, D. L., Gieck, R. E., & Everett, K. R. (1991). Hydrologic and thermal properties of the active layer in the Alaskan Arctic. *Cold Regions Science and Technology*, *19*(2), 95–110. https://doi.org/10.1016/0165-232X(91)90001-W

Hinzman, L. D., Kane, D. L., Benson, C. S., & Everett, K. R. (1996). Energy Balance and Hydrological Processes in an Arctic Watershed. In P. D. J. F. Reynolds & P. D. J. D. Tenhunen (Eds.), *Landscape Function and Disturbance in Arctic Tundra* (pp. 131–154). Springer Berlin Heidelberg. Retrieved from http://link.springer.com/chapter/10.1007/978-3-662-01145-4_6

Hobbie, J., & Kling, G. (2014). *Alaska's Changing Arctic: Ecological Consequences for Tundra, Streams, and Lakes* (1 edition). Oxford ; New York: Oxford University Press.

Hodson, D. L. R., Keeley, S. P. E., West, A., Ridley, J., Hawkins, E., & Hewitt, H. T. (2013). Identifying uncertainties in Arctic climate change projections. *Climate Dynamics*, *40*(11), 2849–2865. https://doi.org/10.1007/s00382-012-1512-z

Holden, J., & Burt, T. P. (2003). Hydrological studies on blanket peat: the significance of the acrotelm-catotelm model. *Journal of Ecology*, *91*(1), 86–102. https://doi.org/10.1046/j.1365-2745.2003.00748.x

Holden, P. A., & Fierer, N. (2005). Microbial Processes in the Vadose Zone. *Vadose Zone Journal*, *4*(1), 1–21. https://doi.org/10.2136/vzj2005.0001

Hope, C., & Schaefer, K. (2016). Economic impacts of carbon dioxide and methane released from thawing permafrost. *Nature Climate Change*, *6*(1), 56–59. https://doi.org/10.1038/nclimate2807

Huntington, T. G., Johnson, C. E., Johnson, A. H., Siccama, T. G., & Ryan, D. F. (1989). CARBON, ORGANIC MATTER, AND BULK DENSITY RELATIONSHIPS IN A FORESTED SPODOSOL. *Soil Science*, *148*(5), 380.

Jafarov, E., & Schaefer, K. (2015). The importance of a surface organic layer in simulating permafrost thermal and carbon dynamics. *The Cryosphere Discussions*, *9*, 3137–3163. https://doi.org/10.5194/tcd-9-3137-2015

Jan, A., Coon, E. T., Painter, S. L., Garimella, R., & Moulton, J. D. (2018). An intermediate-scale model for thermal hydrology in low-relief permafrost-affected landscapes. *Computational Geosciences*, *22*(1), 163–177.

Jaynes, D. B., & Tyler, E. J. (1984). USING SOIL PHYSICAL PROPERTIES TO ESTIMATE HYDRAULIC CONDUCTIVITY: *Soil Science*, *138*(4), 298–305. https://doi.org/10.1097/00010694-198410000-00007

Kane, D. L., Gieck, R. E., Kitover, D. C., Hinzman, L. D., McNamara, J. P., & Yang, D. (2004). Hydrological cycle on the North Slope of Alaska. *IAHS Publications-Series of Proceedings and Reports*, *290*, 224–236.

Karra, S., Painter, S. L., & Lichtner, P. C. (2014). Three-phase numerical model for subsurface hydrology in permafrost-affected regions (PFLOTRAN-ICE v1.0). *The Cryosphere*, *8*(5), 1935–1950. https://doi.org/https://doi.org/10.5194/tc-8-1935-2014

Kattsov, V. M., Källén, E., Cattle, H. P., Christensen, J., Drange, H., Hanssen-Bauer, I., et al. (2005). Future climate change: modeling and scenarios for the Arctic.

Koch, J., Kikuchi, C., Wickland, K., & Schuster, P. (2014). Runoff sources and flow paths in a partially burned, upland boreal catchment underlain by permafrost. *Water Resources Research*, *50*(10), 8141–8158. https://doi.org/10.1002/2014WR015586

Kollet, S. J., & Maxwell, R. M. (2006). Integrated surface–groundwater flow modeling: A free-surface overland flow boundary condition in a parallel groundwater flow model. *Advances in Water Resources*, *29*(7), 945–958. https://doi.org/10.1016/j.advwatres.2005.08.006

Koopmans, R. W. R., & Miller, R. D. (1966). Soil Freezing and Soil Water Characteristic Curves 1. *Soil Science Society of America Journal*, *30*(6), 680–685. https://doi.org/10.2136/sssaj1966.03615995003000060011x

Koven, C., Friedlingstein, P., Ciais, P., Khvorostyanov, D., Krinner, G., & Tarnocai, C. (2009). On the formation of high-latitude soil carbon stocks: Effects of cryoturbation and insulation by organic matter in a land surface model. *Geophysical Research Letters*, *36*(21).

Koven, C. D., Ringeval, B., Friedlingstein, P., Ciais, P., Cadule, P., Khvorostyanov, D., et al. (2011). Permafrost carbon-climate feedbacks accelerate global warming. *Proceedings of the National Academy of Sciences*, *108*(36), 14769–14774. https://doi.org/10.1073/pnas.1103910108

Kurylyk, B., Hayashi, M., Quinton, W., McKenzie, J., & Voss, C. (2016). Influence of vertical and lateral heat transfer on permafrost thaw, peatland landscape transition, and groundwater flow. *Water Resources Research*, *52*(2), 1286–1305. https://doi.org/10.1002/2015WR018057

Kurylyk, B. L., & Hayashi, M. (2016). Improved Stefan Equation Correction Factors to Accommodate Sensible Heat Storage during Soil Freezing or Thawing.

Permafrost and Periglacial Processes, *27*(2), 189–203. https://doi.org/10.1002/ppp.1865

Kurylyk, B. L., & Watanabe, K. (2013). The mathematical representation of freezing and thawing processes in variably-saturated, non-deformable soils. *Advances in Water Resources*, *60*, 160–177. https://doi.org/10.1016/j.advwatres.2013.07.016

Kurylyk, B. L., Hayashi, M., Quinton, W. L., McKenzie, J. M., & Voss, C. I. (2016). Influence of vertical and lateral heat transfer on permafrost thaw, peatland landscape transition, and groundwater flow. *Water Resources Research*, *52*(2), 1286–1305. https://doi.org/10.1002/2015WR018057

Lawrence, D. M., & Slater, A. G. (2005). A projection of severe near-surface permafrost degradation during the 21st century. *Geophysical Research Letters*, *32*(24), L24401. https://doi.org/10.1029/2005GL025080

Lawrence, D. M., & Slater, A. G. (2008). Incorporating organic soil into a global climate model. *Climate Dynamics*, *30*(2–3), 145–160.

Lawrence, D. M., Slater, A. G., Romanovsky, V. E., & Nicolsky, D. J. (2008). Sensitivity of a model projection of near-surface permafrost degradation to soil column depth and representation of soil organic matter. *Journal of Geophysical Research: Earth Surface*, *113*(F2). https://doi.org/10.1029/2007JF000883

Lawrence, D. M., Slater, A. G., & Swenson, S. C. (2011). Simulation of Present-Day and Future Permafrost and Seasonally Frozen Ground Conditions in CCSM4. *Journal of Climate*, *25*(7), 2207–2225. https://doi.org/10.1175/JCLI-D-11-00334.1

Lawrence, D. M., Koven, C. D., Swenson, S. C., Riley, W. J., & Slater, A. G. (2015). Permafrost thaw and resulting soil moisture changes regulate projected high-latitude CO 2 and CH 4 emissions. *Environmental Research Letters*, *10*(9), 094011. https://doi.org/10.1088/1748-9326/10/9/094011

Leong, E. C., Tripathy, S., & Rahardjo, H. (2003). Total suction measurement of unsaturated soils with a device using the chilled-mirror dew-point technique. *Geotechnique*, *53*(2), 173–182.

Liljedahl, A., & Hinzman, L. (2012). Ice-Wedge Polygon Type Controls Low-Gradient Watershed-Scale Hydrology. *Tenth International Conference on Permafrost Vol. 1: International Contributions*, *1*, 231–236.

Ling, F., & Zhang, T. (2004). A numerical model for surface energy balance and thermal regime of the active layer and permafrost containing unfrozen water. *Cold Regions Science and Technology*, *38*(1), 1–15. https://doi.org/10.1016/S0165-232X(03)00057-0

Liu, Y., Tong, J., & Li, X. (2005). Analysing the silt particles with the Malvern Mastersizer 2000. *Water Conservancy Science and Technology and Economy*, *11*(6), 329–331.

Lu, Y., Lu, S., Horton, R., & Ren, T. (2014). An Empirical Model for Estimating Soil Thermal Conductivity from Texture, Water Content, and Bulk Density. *Soil Science Society of America Journal*, *78*(6), 1859–1868. https://doi.org/10.2136/sssaj2014.05.0218

Martinec, J. (1977). Expected Snow Loads on Structures from Incomplete Hydrological Data. *Journal of Glaciology*, *19*(81), 185–195. https://doi.org/10.3189/S0022143000029270

McKenzie, J. M., & Voss, C. I. (2013). Permafrost thaw in a nested groundwater-flow system. *Hydrogeology Journal*, *21*(1), 299–316. https://doi.org/10.1007/s10040-012-0942-3

McNamara, J. P., Kane, D. L., & Hinzman, L. D. (1997). Hydrograph separations in an arctic watershed using mixing model and graphical techniques. *Water Resources Research*, *33*(7), 1707–1719. https://doi.org/10.1029/97WR01033

McNamara, J. P., Kane, D. L., & Hinzman, L. D. (1999). An analysis of an arctic channel network using a digital elevation model. *Geomorphology*, *29*(3), 339–353. https://doi.org/10.1016/S0169-555X(99)00017-3

Merck, M. F., Neilson, B. T., Cory, R. M., & Kling, G. W. (2012). Variability of in-stream and riparian storage in a beaded arctic stream. *Hydrological Processes*, *26*(19), 2938–2950. https://doi.org/10.1002/hyp.8323

Michaelson, G. J., Ping, C. L., & Kimble, J. M. (1996). Carbon Storage and Distribution in Tundra Soils of Arctic Alaska, U.S.A. *Arctic and Alpine Research*, *28*(4), 414–424. https://doi.org/10.2307/1551852

Morin, P., Porter, C., Cloutier, M., Howat, I., Noh, M.-J., Willis, M., et al. (2016). ArcticDEM; A Publically Available, High Resolution Elevation Model of the Arctic (Vol. 18, pp. EPSC2016-8396). Presented at the EGU General Assembly

Conference Abstracts. Retrieved from http://adsabs.harvard.edu/abs/2016EGUGA..18.8396M

Morris, P. J., Waddington, J. M., Benscoter, B. W., & Turetsky, M. R. (2011). Conceptual frameworks in peatland ecohydrology: looking beyond the two-layered (acrotelm–catotelm) model. *Ecohydrology*, *4*(1), 1–11. https://doi.org/10.1002/eco.191

Morris, P. J., Baird, A. J., & Belyea, L. R. (2015). Bridging the gap between models and measurements of peat hydraulic conductivity. *Water Resources Research*, *51*(7), 5353–5364. https://doi.org/10.1002/2015WR017264

Morris, P. J., Baird, A. J., Eades, P. A., & Surridge, B. W. J. (2019). Controls on Near-Surface Hydraulic Conductivity in a Raised Bog. *Water Resources Research*. https://doi.org/10.1029/2018WR024566

Neilson, B. T., Cardenas, M. B., O'Connor, M. T., Rasmussen, M. T., King, T. V., & Kling, G. W. (2018). Groundwater Flow and Exchange Across the Land Surface Explain Carbon Export Patterns in Continuous Permafrost Watersheds. *Geophysical Research Letters*, *45*(15), 7596–7605. https://doi.org/10.1029/2018GL078140

Nelson, F. E., Shiklomanov, N. I., & Mueller, G. R. (1999). Variability of Active-Layer Thickness at Multiple Spatial Scales, North-Central Alaska, U.S.A. *Arctic, Antarctic, and Alpine Research*, *31*(2), 179–186. https://doi.org/10.2307/1552606

Ochsner, T. E., Horton, R., & Ren, T. (2001). A New Perspective on Soil Thermal Properties. *Soil Science Society of America Journal*, *65*(6), 1641–1647. https://doi.org/10.2136/sssaj2001.1641

O'Connor, M., Cardenas, M. B., Nicholaides, K., Neilson, B., & Kling, G. (2018). Groundwater flow in areas above continuous permafrost: the dynamic effects of stratigraphy, thawing, and micro- and macro-topography.

O'Connor, M., Cardenas, M. B., Nicholaides, K., Mungia, Z., Ferencz, S., Neilson, B., & Kling, G. (2019). The similarity and predictability of soil stratigraphy, hydraulic, and thermal properties of supra-permafrost soils in the arctic Alaska Foothills.

O'donnell, J. A., Romanovsky, V. E., Harden, J. W., & McGuire, A. D. (2009). The effect of moisture content on the thermal conductivity of moss and organic soil horizons from black spruce ecosystems in interior Alaska. *Soil Science*, *174*(12), 646–651.

Omernik, J. M., & Griffith, G. E. (2014). Ecoregions of the Conterminous United States: Evolution of a Hierarchical Spatial Framework. *Environmental Management*, *54*(6), 1249–1266. https://doi.org/10.1007/s00267-014-0364-1

Osterkamp, T. E., & Payne, M. W. (1981). Estimates of permafrost thickness from well logs in northern Alaska. *Cold Regions Science and Technology*, *5*(1), 13–27. https://doi.org/10.1016/0165-232X(81)90037-9

Painter, S. L., & Karra, S. (2014). Constitutive Model for Unfrozen Water Content in Subfreezing Unsaturated Soils. *Vadose Zone Journal*, *13*(4). https://doi.org/10.2136/vzj2013.04.0071

Painter, S. L., Coon, E. T., Atchley, A., Berndt, M., Garimella, R., Moulton, D., et al. (2016). Integrated surface/subsurface permafrost thermal hydrology: Model formulation and proof-of-concept simulations. *Water Resources Research*, n/a-n/a. https://doi.org/10.1002/2015WR018427

Payne, J. (2013, October 30). NSSI Landcover Report: Landcover Mapping for North Slope of Alaska. United States Bureau of Land Management. Retrieved from catalog.northslope.org/catalog/entries/4616-nssi-landcover-report-landcover-mapping-for-n

Périé, C., & Ouimet, R. (2008). Organic carbon, organic matter and bulk density relationships in boreal forest soils. *Canadian Journal of Soil Science*, *88*(3), 315–325. https://doi.org/10.4141/CJSS06008

Ping, C. L., Bockheim, J. G., Kimble, J. M., Michaelson, G. J., & Walker, D. A. (n.d.). Characteristics of cryogenic soils along a latitudinal transect in arctic Alaska. *Journal of Geophysical Research: Atmospheres*, *103*(D22), 28917–28928. https://doi.org/10.1029/98JD02024

Ping, C.-L., Michaelson, G. J., Jorgenson, M. T., Kimble, J. M., Epstein, H., Romanovsky, V. E., & Walker, D. A. (2008). High stocks of soil organic carbon in the North American Arctic region. *Nature Geoscience*, *1*(9), 615–619. https://doi.org/10.1038/ngeo284

Pomeroy, J. W., Gray, D. M., Brown, T., Hedstrom, N. R., Quinton, W. L., Granger, R. J., & Carey, S. K. (2007). The cold regions hydrological model: a platform for

basing process representation and model structure on physical evidence. *Hydrological Processes*, *21*(19), 2650–2667. https://doi.org/10.1002/hyp.6787

Post, W. M., & Kwon, K. C. (2000). Soil carbon sequestration and land-use change: processes and potential. *Global Change Biology*, *6*(3), 317–327. https://doi.org/10.1046/j.1365-2486.2000.00308.x

Prévost, M. (2004). Predicting Soil Properties from Organic Matter Content following Mechanical Site Preparation of Forest Soils. *Soil Science Society of America Journal*, *68*(3), 943–949. https://doi.org/10.2136/sssaj2004.9430

Quinton, W. L., & Gray, D. M. (2003). Subsurface drainage from organic soils in permafrost terrain: the major factors to be represented in a runoff model. In *Proceedings of the Eighth International Conference on Permafrost, Davos, Switzerland, 6pp*.

Quinton, W. L., Gray, D. M., & Marsh, P. (2000a). Subsurface drainage from hummock-covered hillslopes in the Arctic tundra. *Journal of Hydrology*, *237*(1–2), 113–125. https://doi.org/10.1016/S0022-1694(00)00304-8

Quinton, W. L., Gray, D. M., & Marsh, P. (2000b). Subsurface drainage from hummock-covered hillslopes in the Arctic tundra. *Journal of Hydrology*, *237*(1–2), 113–125. https://doi.org/10.1016/S0022-1694(00)00304-8

Quinton, W. L., Carey, S. K., & Goeller, N. T. (2004). Snowmelt runoff from northern alpine tundra hillslopes: major processes and methods of simulation. *Hydrol. Earth Syst. Sci.*, *8*(5), 877–890. https://doi.org/10.5194/hess-8-877-2004

Quinton, W. L., Shirazi, T., Carey, S. K., & Pomeroy, J. W. (2005). Soil water storage and active-layer development in a sub-alpine tundra hillslope, southern Yukon Territory, Canada. *Permafrost and Periglacial Processes*, *16*(4), 369–382.

Quinton, W. L., Hayashi, M., & Carey, S. K. (2008). Peat hydraulic conductivity in cold regions and its relation to pore size and geometry. *Hydrological Processes*, *22*(15), 2829–2837. https://doi.org/10.1002/hyp.7027

Riseborough, D., Shiklomanov, N., Etzelmuller, B., Gruber, S., & Marchenko, S. (2008). Recent advances in permafrost modelling. *Permafrost and Periglacial Processes*, *19*(2), 137–156. https://doi.org/10.1002/ppp.615

Roulet, N. T., Ash, R., Quinton, W., & Moore, T. (2010). Methane flux from drained northern peatlands: Effect of a persistent water table lowering on flux. *Global Biogeochemical Cycles*, *7*(4), 749–769. https://doi.org/10.1029/93GB01931

Rushlow, C. R., & Godsey, S. E. (2017). Rainfall–runoff responses on Arctic hillslopes underlain by continuous permafrost, North Slope, Alaska, USA. *Hydrological Processes*, *31*(23), 4092–4106. https://doi.org/10.1002/hyp.11294

Schaefer, K., Lantuit, H., Romanovsky, V. E., Schuur, E. A. G., & Witt, R. (2014). The impact of the permafrost carbon feedback on global climate. *Environmental Research Letters*, *9*(8), 085003. https://doi.org/10.1088/1748-9326/9/8/085003

Schindler, U., Durner, W., von Unold, G., Mueller, L., & Wieland, R. (2010). The evaporation method: Extending the measurement range of soil hydraulic properties using the air-entry pressure of the ceramic cup. *Journal of Plant*

Nutrition and Soil Science, *173*(4), 563–572. https://doi.org/10.1002/jpln.200900201

Schramm, I., Boike, J., Bolton, W. R., & Hinzman, L. D. (2007). Application of TopoFlow, a spatially distributed hydrological model, to the Imnavait Creek watershed, Alaska. *Journal of Geophysical Research: Biogeosciences*, *112*(G4), G04S46. https://doi.org/10.1029/2006JG000326

Schuh, C., Frampton, A., & Christiansen, H. H. (2017). Soil moisture redistribution and its effect on inter-annual active layer temperature and thickness variations in a dry loess terrace in Adventdalen, Svalbard. *The Cryosphere*, *11*(1), 635–651. https://doi.org/https://doi.org/10.5194/tc-11-635-2017

Schuur, E. a. G., McGuire, A. D., Schädel, C., Grosse, G., Harden, J. W., Hayes, D. J., et al. (2015). Climate change and the permafrost carbon feedback. *Nature*, *520*(7546), 171–179. https://doi.org/10.1038/nature14338

Serreze, M. C., & Barry, R. G. (2011). Processes and impacts of Arctic amplification: A research synthesis. *Global and Planetary Change*, *77*(1), 85–96. https://doi.org/10.1016/j.gloplacha.2011.03.004

Shelef, E., Rowland, J. C., Wilson, C. J., Hilley, G. E., Mishra, U., Altmann, G. L., & Ping, C.-L. (2017). Large uncertainty in permafrost carbon stocks due to hillslope soil deposits. *Geophysical Research Letters*, *44*(12), 2017GL073823. https://doi.org/10.1002/2017GL073823

Smith, S. L., Wolfe, S. A., Riseborough, D. W., & Nixon, F. M. (2009). Active-layer characteristics and summer climatic indices, Mackenzie Valley, Northwest

Territories, Canada. *Permafrost and Periglacial Processes*, *20*(2), 201–220. https://doi.org/10.1002/ppp.651

Stieglitz, M., Shaman, J., McNamara, J., Engel, V., Shanley, J., & Kling, G. W. (2003). An approach to understanding hydrologic connectivity on the hillslope and the implications for nutrient transport. *Global Biogeochemical Cycles*, *17*(4), 1105. https://doi.org/10.1029/2003GB002041

Stow, D. A., Hope, A., McGuire, D., Verbyla, D., Gamon, J., Huemmrich, F., et al. (2004). Remote sensing of vegetation and land-cover change in Arctic Tundra Ecosystems. *Remote Sensing of Environment*, *89*(3), 281–308. https://doi.org/10.1016/j.rse.2003.10.018

Surridge, B. W. J., Baird, A. J., & Heathwaite, A. L. (2005). Evaluating the quality of hydraulic conductivity estimates from piezometer slug tests in peat. *Hydrological Processes*, *19*(6), 1227–1244. https://doi.org/10.1002/hyp.5653

Tarnocai, C., Canadell, J. G., Schuur, E. a. G., Kuhry, P., Mazhitova, G., & Zimov, S. (2009). Soil organic carbon pools in the northern circumpolar permafrost region. *Global Biogeochemical Cycles*, *23*(2), GB2023. https://doi.org/10.1029/2008GB003327

Trexler, J. C., & Travis, J. (1993). Nontraditional regression analyses. *Ecology*, *74*(6), 1629–1637.

Tromp-van Meerveld, H. J., & McDonnell, J. J. (2006). Threshold relations in subsurface stormflow: 2. The fill and spill hypothesis. *Water Resources Research*, *42*(2). Retrieved from http://onlinelibrary.wiley.com/doi/10.1029/2004WR003800/full

Vereecken, H., Maes, J., & Feyen, J. (1990). ESTIMATING UNSATURATED HYDRAULIC CONDUCTIVITY FROM EASILY MEASURED SOIL PROPERTIES. *Soil Science*, *149*(1), 1.

Voytek, E., Rushlow, C., Godsey, S., & Singha, K. (2016). Identifying hydrologic flowpaths on arctic hillslopes using electrical resistivity and self potential. *GEOPHYSICS*, *81*(1), WA225-WA232. https://doi.org/10.1190/geo2015-0172.1

W. J. Rawls, D. Gimenez, & R. Grossman. (1998). USE OF SOIL TEXTURE, BULK DENSITY, AND SLOPE OF THE WATER RETENTION CURVE TO PREDICT SATURATED HYDRAULIC CONDUCTIVITY. *Transactions of the ASAE*, *41*(4), 983–988. https://doi.org/10.13031/2013.17270

Wahrhaftig, C. (1965). *Physiographic divisions of Alaska*. US Government Printing Office.

Walker, D. A., & Everett, K. R. (1991). Loess Ecosystems of Northern Alaska: Regional Gradient and Toposequence at Prudhoe Bay. *Ecological Monographs*, *61*(4), 437–464. https://doi.org/10.2307/2937050

Walker, D. A., & Walker, M. D. (1996). Terrain and vegetation of the Imnavait Creek watershed. In *Landscape Function and Disturbance in Arctic Tundra* (pp. 73–108). Springer. Retrieved from http://link.springer.com/chapter/10.1007/978-3-662-01145-4_4

Walker, D. A., Binnian, E., Evans, B. M., Lederer, N. D., Nordstrand, E., & Webber, P. J. (1989). Terrain, Vegetation and Landscape Evolution of the R4D Research Site, Brooks Range Foothills, Alaska. *Holarctic Ecology*, *12*(3), 238–261.

Walker, D. A., Jia, G. J., Epstein, H. E., Raynolds, M. K., Chapin III, F. S., Copass, C., et al. (2003). Vegetation-soil-thaw-depth relationships along a low-arctic bioclimate gradient, Alaska: synthesis of information from the ATLAS studies. *Permafrost and Periglacial Processes*, *14*(2), 103–123. https://doi.org/10.1002/ppp.452

Walvoord, M. A., & Kurylyk, B. L. (2016). Hydrologic Impacts of Thawing Permafrost—A Review. *Vadose Zone Journal*, *15*(6). https://doi.org/10.2136/vzj2016.01.0010

Walvoord, M. A., & Striegl, R. G. (2007). Increased groundwater to stream discharge from permafrost thawing in the Yukon River basin: Potential impacts on lateral export of carbon and nitrogen. *Geophysical Research Letters*, *34*(12), L12402. https://doi.org/10.1029/2007GL030216

Wang, H. F., & Anderson, M. P. (1995). *Introduction to groundwater modeling: finite difference and finite element methods.* Academic Press.

Watanabe, M., Suzuki, T., O'ishi, R., Komuro, Y., Watanabe, S., Emori, S., et al. (2010). Improved Climate Simulation by MIROC5: Mean States, Variability, and Climate Sensitivity. *Journal of Climate*, *23*(23), 6312–6335. https://doi.org/10.1175/2010JCLI3679.1

Weiss, R., Alm, J., Laiho, R., & Laine, J. (1998). Modeling Moisture Retention in Peat Soils. *Soil Science Society of America Journal*, *62*(2), 305–313. https://doi.org/10.2136/sssaj1998.03615995006200020002x

Woo, M., & Steer, P. (1983). Slope hydrology as influenced by thawing of the active layer, Resolute, N.W.T. *Canadian Journal of Earth Sciences*, *20*(6), 978–986. https://doi.org/10.1139/e83-087

Woo, M.-K., & Marsh, P. (2005a). Snow, frozen soils and permafrost hydrology in Canada, 1999–2002. *Hydrological Processes*, *19*(1), 215–229. https://doi.org/10.1002/hyp.5772

Woo, M.-K., & Marsh, P. (2005b). Snow, frozen soils and permafrost hydrology in Canada, 1999–2002. *Hydrological Processes: An International Journal*, *19*(1), 215–229.

Woo, M.-K., Kane, D. L., Carey, S. K., & Yang, D. (2008). Progress in permafrost hydrology in the new millennium. *Permafrost and Periglacial Processes*, *19*(2), 237–254. https://doi.org/10.1002/ppp.613

Wright, N., Hayashi, M., & Quinton, W. L. (2009). Spatial and temporal variations in active layer thawing and their implication on runoff generation in peat-covered permafrost terrain. *Water Resources Research*, *45*(5), W05414. https://doi.org/10.1029/2008WR006880

Zhang, Y. (2014). Thermal-Hydro-Mechanical Model for Freezing and Thawing of Soils. Retrieved from http://deepblue.lib.umich.edu/handle/2027.42/108828

Zhang, Y., Cheng, G., Li, X., Han, X., Wang, L., Hongyi Li, et al. (2013). Coupling of a simultaneous heat and water model with a distributed hydrological model and evaluation of the combined model in a cold region watershed. *Hydrological Processes*, *27*(25), 3762–3776. https://doi.org/10.1002/hyp.9514

Permanent email: mtoconnor12@gmail.com

This dissertation was typed by Michael Thomas O'Connor